SISSA
Scuola
Internazionale
Superiore di
Studi Avanzati

Physics Area – PhD course in

Statistical Physics

Entanglement, correlations and data-structure in many-body quantum systems

Candidate:
Xhek Turkeshi

Advisor:
Dr. Marcello Dalmonte

Academic Year 2020-21

SCUOLA INTERNAZIONALE SUPERIORE DI STUDI AVANZATI

DOCTORAL THESIS

Entanglement, correlations, and data structure in many-body quantum systems

Author:
Xhek TURKESHI

Supervisor:
Dr. Marcello DALMONTE

A thesis submitted in fulfillment of the requirements for the degree of Doctor of Philosophy

in the

Statistical Physics Group
SISSA

The first principle is that you must not fool yourself – and you are the easiest person to fool.
R.F.

List of Publications

Publications discussed in this thesis

1. **Xhek Turkeshi**, Tiago Mendes-Santos, Giuliano Giudici, and Marcello Dalmonte,
Entanglement guided search for parent Hamiltonians,
Phys. Rev. Lett. **122**, 150606 (2019).

2. **Xhek Turkeshi**, and Marcello Dalmonte,
Parent Hamiltonian Reconstruction of Jastrow-Gutzwiller Wavefunctions,
SciPost Phys. **8**, 042 (2020).

3. **Xhek Turkeshi**, Paola Ruggiero, and Pasquale Calabrese,
Negativity Spectrum in the Random Singlet Phase,
Phys. Rev. B **101**, 064207 (2020).

4. **Xhek Turkeshi**, Paola Ruggiero, Vincenzo Alba, and Pasquale Calabrese,
Entanglement equipartition in critical random spin chains,
Phys. Rev. B **102**, 014455 (2020). *(Editor's Suggestion)*

5. Tiago Mendes-Santos*, **Xhek Turkeshi***, Marcello Dalmonte, and Alex Rodriguez,
Unsupervised learning universal critical behavior via the intrinsic dimension,
Phys. Rev. X **11**, 011040 (2021).

6. **Xhek Turkeshi**, Rosario Fazio, and Marcello Dalmonte,
Measurement-induced criticality in (2+1)-d hybrid quantum circuits,
Phys. Rev. B **102**, 014315 (2020).

7. **Xhek Turkeshi**,
Measurement-induced criticality as a data-structure transition,
arXiv: 2101.06245.

8. **Xhek Turkeshi**, Alberto Biella, Rosario Fazio, Marcello Dalmonte, and Marco Schiró,
Measurement-Induced Entanglement Transitions in the Quantum Ising Chain: From Infinite to Zero Clicks,
Phys. Rev. B **103**, 224210 (2021). *(Editor's Suggestion)*

Publications not discussed in this thesis

9. **Xhek Turkeshi**, and Marco Schiró,
Diffusion and Thermalization in a Boundary-Driven Dephasing Model,
arXiv: 2106.13180.

10. Piotr Sierant, Giuliano Chiriacó, Federica M. Surace, Shraddha Sharma,**Xhek Turkeshi**, Marcello Dalmonte, Rosario Fazio, and Guido Pagano,
Dissipative Floquet Dynamics: from Steady State to Measurement Induced Criticality in Trapped-ion Chains,
arXiv: 2107.05669.

Introduction

Many-body quantum systems are the archetypal framework for the study of collective phenomena and quantum matter at a macroscopic scale [1, 2]. Their complexity stems from the combination of a large number of degrees of freedom, and quantum-mechanical effects, including coherence and entanglement.

The study of many-body systems bridges heterogeneous communities ranging from statistical mechanics [3] to quantum information [4], from high-energy [5] to condensed matter physics [6, 7]. For instance, it covers the study of exotic equilibrium phases of matter, including superconductivity and superfluidity, topological insulators and quantum spin liquids, and out-of-equilibrium phenomena [8], such as quantum thermalization in isolated systems [9, 10], ergodicity [11, 12], and open quantum systems [13, 14].

In the past decades, a variety of new methods and tools have been proven successful to uncover complex patterns of many-body quantum physics. One of the most remarkable developments has been the emergence of entanglement as a tool to characterize and classify states of matter, by quantifying specific forms of non-local correlations in the system [15–18].

Defined as the non-separability of a state in its componing parts, entanglement has been first attached to foundational questions of quantum mechanics and nowadays is an active field of research in a variety of disciplines[19]. From a quantum computing perspective, entanglement is believed to be a fundamental resource in the quantum physics, allowing to perform tasks impossible in a classical world (e.g. teleportation), and providing new technological breakthroughs potentially relevant for everyday life (e.g. quantum cryptography). Furthermore, entanglement plays an important role in condensed matter physics [20], where it serves as a probe of phases and phase transitions. At equilibrium, the ground state of gapped systems exhibits entanglement between a region A with its complementary, proportional to the area of its boundary ∂A . This so-called area law is the reason for the success of numerical methods such as tensor network and density matrix renormalization group [21, 22]. Out of equilibrium, entanglement growth exhibits universal features which are insensible to the microscopic deatails, and depends on the localizing and ergodic properties of the system [23]. For example, thermalizing systems show a linear increase of entanglement entropy with time [24], while many-body localizing phases exhibit a logarithmic relaxation [11]. Lastly, the breakthroughs in cold atoms and trapped ions made it possible to prepare, manipulate and measure atoms with high fidelity, thus allowing to explore the blueprints of entanglement in experiments [25–28].

In parallel to the aformentioned conceptual developments, the technological advancement of algorithmic design, parallel machines and GPUs has largely revolutionized computational methods. Machine learning has become a pillar of modern data science and has been recently applied to classical and quantum physical systems [29–31]. For quantum systems, the main applications are two: to encode complex wave patterns through suitably designed neural network architectures [32] or decode these patterns in intelligible information [33], via unsupervised learning and variational autoencoders. For example, the data structure of statistical and quantum systems has been investigated through unsupervised and supervised learning methods [34, 35]. Similarly, tensor networks have become a standard tool in the exploration of many-body physics [21, 36]. Originally developed on renormalization group ideas, they provide an efficient approximation to certain classes of quantum states, with remarkable successes in fermionic systems, lattice gauge theories, and topological quantum matter. These methods provide alternative, and often complementary, pathways to exact diagonalization and quantum Monte Carlo, which are the main numerical resource for a large class of many-body problems. For instance, exact diagonalization allows the study of highly excited states, thus playing a fundamental role in many-body localization and thermalization [9–11, 37], whereas quantum Monte Carlo allows the study of correlations and entanglement in two (or higher) dimensional bosonic quantum systems [38, 39].

In this thesis, we employ these methods to inquire a variety of many-body problems, ranging from strongly correlated systems at equilibrium, to monitored quantum dynamics in the presence of environment probing. Entanglement, correlations, and data structure – as well as the relationship between them serve as the lens for the investigation of these thematics and constitute the leitmotif of the present thesis. Specifically, we aim to contribute to the following questions: (1) Does a single eigenstate contain the full information on its parent Hamiltonian? (2) How does entanglement behave in the presence of critical disorder? (3) Does the configuration space of a statistical mechanics system directly detect critical behavior? (4) How is the system unitary evolution altered by the presence of a monitoring environment? Following the preceding subjects, for the sake of clarity, we divide the thesis into four chapters; each one presents a detailed introduction on the specific problem and of the literature, and is self-consistent, in that it can be read without the knowledge of the other ones.

In Chapter 1 we propose an entanglement-guided method to address the open problem of finding parent Hamiltonian of variational wavefunctions. The success of variational states is motivated by phenomena as the fractional quantum Hall effect and the high-T_c superconductors, where the microscopic Hamiltonian governing the processes is not known. More in general, this top-down approach which starts from a Hamiltonian and diagonalizes it is not always accessible to quantum spin liquids, which are strongly correlated quantum phases exhibiting topological order and gauge theory structure. Our method is based on the particular structure of the non-local correlation and entanglement, proper of the ground state of Hamiltonian systems, and relies on a well-known field theory result (the Bisognano-Wichmann theorem). The additional assumption is the system should be described by an effective field theory with relativistic invariance.

After general remarks on the nature of the problem, in Chapter 1 we present the algorithm, benchmarking it suitably chosen and known situations, and subsequently apply this technology to reconstruct approximate parent Hamiltonian of the ubiquitous class of Jastrow-Gutzwiller wave function, of which the Laughlin wave function is a particular instance.

In Chapter 2 we investigate entanglement and correlations in critical disordered quantum spin chains. A system with quench disorder is usually difficult to treat analytically and numerically, due to its inhomogeneity which makes the system hard to solve. We consider the random singlet phase, characterizing the ground state properties of the random bond XX and XXZ chain, and study the negativity spectrum and the symmetry resolved entanglement entropy. The negativity spectrum is the spectrum of the partial transposed density matrix of the system, which encodes the entanglement of a mixed state. By itself, the negativity spectrum is not a measure of entanglement, but it can be used to construct via simple algebraic functions, experimentally relevant entanglement witness. The symmetry resolved entanglement entropy is the entanglement content of each symmetry sector for a system displaying an additive symmetry, such as the conservation of total polarization or the number of particles. It has been experimentally estimated for many-body localizing systems with a cold-atoms platform, and for a long-range XX chain in a trapped ions platform.

In particular, we use strong disorder renormalization group methods to compute exactly both negativity spectrum and symmetry resolved entanglement in the scaling limit of large systems, and benchmark our results with ab initio numerical methods and with numerical renormalization group.

In Chapter 3 we study the connection between classical critical phenomena and data structures, by investigating geometric properties of the system configuration space. Specifically, we propose the intrinsic dimension, which is the dimension of the encoding manifold in data-space, as an order parameter for phase transitions. Due to the curse of dimensionality, the precise characterization of the intrinsic dimension is a hard task, as the density of data points in a data manifold is densely packed in its borders. This is the case for partition functions of statistical ensembles, which present a thermodynamic number of configurations for their degrees of freedom, and is naturally present in the exponential nature of quantum data. We use a state-of-the-art algorithm to estimate the intrinsic dimension of a dataset, which assumes the data follows a continuous distribution. This method is independent of the density, and it relies on the ratio between distances of data points. We find the method is not only successful in identifying first- and second-order phase transitions, but can predict with percent level precision a BKT transition already at modest system sizes.

The first three chapters treat equilibrium problems. In Chapter 4 we investigate data structure and entanglement for the dynamics of non-unitary systems. The simplest setting of these systems, on which we

focus in this thesis, is that of a unitary-evolving quantum dynamics coupled to a measuring environment, that stochastically and locally probes the system. The state evolution describes a stochastic process or quantum trajectory in the Hilbert space, driven by the competition between unitary dynamics, that generate entanglement, and local measurement, which due to their collapsing nature, destroy non-local correlations. In particular, the quantum trajectory exhibits different structural properties compared to the average state. As an illustrative example, the von-Neumann entropy over the average state is typically extensive (excluding fine-tuned instances), whereas the conditional average von-Neumann entropy over the trajectories may present extensive or sub-extensive scaling depending on the frequency/strength of the measurements. For low-measurement rates, the stationary state is highly entangled and robust against the probing of the environment which acts as a noise in the system. For these reasons, this dynamical phase is denoted the error-correcting phase. Instead, for high-measurement rates, the system is constantly collapsed to a reduced subspace of the Hilbert space (quantum Zeno phase). We investigate the interplay between unitary dynamics and measurements in Chapter 4 for three different setups. Starting from the results presented in Ch. 3, we consider 1+1D random unitary circuits with stochastic measurements, and explore, employing principal component analysis and intrinsic dimension estimation, how the space encoding the quantum trajectory exhibits (critically) structural changes. We find that the difference between the error-correcting phase and the Zeno phase leaves marks in the behavior of the first principal components, and in the scaling of the intrinsic dimension. We then explore the role of dimensionality in hybrid random circuits by examining the 2+1D Clifford hybrid circuits. To probe the universality of the transition, we consider two protocols, where the environment implements respectively rank-1 or rank-2 local projective measurements. The former has a strong disentangling effect, as the projection is onto a single qubit, whereas the latter presents a remnant entanglement since they project onto a Bell pair. For both these protocols we find a phase transition, with different critical points (which depends on the microscopical detail of the system), but the same critical exponents. Furthermore, our numerical evidence suggests at criticality a scaling with multiplicative logarithmic violations, which resembles the one of Fermi liquids and $U(1)$ lattice gauge theories in 2+1D. Lastly, to understand the role of the measurement, we consider the quantum Ising Hamiltonian coupled to a weakly measuring environment. In this setup, the effective description is in terms of stochastic Schödinger equations. We consider the limit of weak and continuous monitoring, corresponding to independent Brownian stochastic measurements, and the no-click limit, where we post-select only trajectories without any measurement, and the environment acts as a backreaction in the evolution operator. In this limit, the dynamics are generated by a non-Hermitian Hamiltonian. We find that despite quantitative differences, these limits reproduce the same qualitative behavior and pinpoint the same critical transition.

Bibliography

[1] Piers Coleman. *Introduction to Many-Body Physics*. Cambridge University Press, 2015.

[2] Xiao-Gang Wen. *Quantum Field Theory of Many-Body Systems*. Oxford University Press, Sep 2007.

[3] Subir Sachdev. *Quantum Phase Transitions*. Cambridge University Press, 2009.

[4] Bei Zeng, Xie Chen, Duan-Lu Zhou, and Xiao-Gang Wen. *Quantum Information Meets Quantum Matter*. Springer New York, 2019.

[5] Subir Sachdev. *Condensed Matter and AdS/CFT*. Springer Berlin Heidelberg, 2011.

[6] Eduardo Fradkin. *Field Theories of Condensed Matter Physics*. Cambridge University Press, 2013.

[7] Alexander Altland and Ben D. Simons. *Condensed Matter Field Theory*. Cambridge University Press, 2009.

[8] Anatoli Polkovnikov, Krishnendu Sengupta, Alessandro Silva, and Mukund Vengalattore. Colloquium: Nonequilibrium dynamics of closed interacting quantum systems. *Rev. Mod. Phys.*, 83:863–883, Aug 2011.

[9] Joshua M Deutsch. Eigenstate thermalization hypothesis. *Reports on Progress in Physics*, 81(8):082001, Jul 2018.

[10] Mark Srednicki. Chaos and quantum thermalization. *Physical Review E*, 50(2):888–901, Aug 1994.

[11] Dmitry A. Abanin, Ehud Altman, Immanuel Bloch, and Maksym Serbyn. Colloquium: Many-body localization, thermalization, and entanglement. *Rev. Mod. Phys.*, 91:021001, May 2019.

[12] Rahul Nandkishore and David A. Huse. Many-body localization and thermalization in quantum statistical mechanics. *Annual Review of Condensed Matter Physics*, 6(1):15–38, Mar 2015.

[13] Heinz-Peter Breuer and Francesco Petruccione. *The Theory of Open Quantum Systems*. Oxford University Press, Jan 2007.

[14] C. Gardiner, P. Zoller, and P. Zoller. *Quantum Noise: A Handbook of Markovian and Non-Markovian Quantum Stochastic Methods with Applications to Quantum Optics*. Springer Series in Synergetics. Springer, 2004.

[15] Luigi Amico, Rosario Fazio, Andreas Osterloh, and Vlatko Vedral. Entanglement in many-body systems. *Rev. Mod. Phys.*, 80:517–576, May 2008.

[16] Ryszard Horodecki, Paweł Horodecki, Michał Horodecki, and Karol Horodecki. Quantum entanglement. *Rev. Mod. Phys.*, 81:865–942, Jun 2009.

[17] Pasquale Calabrese and John Cardy. Entanglement entropy and quantum field theory. *Journal of Statistical Mechanics: Theory and Experiment*, 2004(06):P06002, Jun 2004.

[18] Pasquale Calabrese and John Cardy. Entanglement entropy and conformal field theory. *Journal of Physics A: Mathematical and Theoretical*, 42(50):504005, Dec 2009.

[19] Michael A. Nielsen and Isaac L. Chuang. *Quantum Computation and Quantum Information*. Cambridge University Press, 2009.

[20] Nicolas Laflorencie. Quantum entanglement in condensed matter systems. *Physics Reports*, 646:1–59, Aug 2016.

[21] Ulrich Schollwöck. The density-matrix renormalization group in the age of matrix product states. *Annals of Physics*, 326(1):96–192, Jan 2011.

[22] J. Eisert, M. Cramer, and M. B. Plenio. Colloquium: Area laws for the entanglement entropy. *Reviews of Modern Physics*, 82(1):277–306, Feb 2010.

[23] Pasquale Calabrese and John Cardy. Quantum quenches in 1+1 dimensional conformal field theories. *Journal of Statistical Mechanics: Theory and Experiment*, 2016(6):064003, Jun 2016.

[24] Adam Nahum, Jonathan Ruhman, Sagar Vijay, and Jeongwan Haah. Quantum entanglement growth under random unitary dynamics. *Physical Review X*, 7(3), Jul 2017.

[25] A. M. Kaufman, M. E. Tai, A. Lukin, M. Rispoli, R. Schittko, P. M. Preiss, and M. Greiner. Quantum thermalization through entanglement in an isolated many-body system. *Science*, 353(6301):794–800, Aug 2016.

[26] Tiff Brydges, Andreas Elben, Petar Jurcevic, Benoît Vermersch, Christine Maier, Ben P. Lanyon, Peter Zoller, Rainer Blatt, and Christian F. Roos. Probing rényi entanglement entropy via randomized measurements. *Science*, 364(6437):260–263, Apr 2019.

[27] Alexander Lukin, Matthew Rispoli, Robert Schittko, M. Eric Tai, Adam M. Kaufman, Soonwon Choi, Vedika Khemani, Julian Léonard, and Markus Greiner. Probing entanglement in a many-body–localized system. *Science*, 364(6437):256–260, 2019.

[28] Andreas Elben, Richard Kueng, Hsin-Yuan (Robert) Huang, Rick van Bijnen, Christian Kokail, Marcello Dalmonte, Pasquale Calabrese, Barbara Kraus, John Preskill, Peter Zoller, and Benoît Vermersch. Mixed-state entanglement from local randomized measurements. *Phys. Rev. Lett.*, 125:200501, Nov 2020.

[29] Pankaj Mehta, Marin Bukov, Ching-Hao Wang, Alexandre G.R. Day, Clint Richardson, Charles K. Fisher, and David J. Schwab. A high-bias, low-variance introduction to machine learning for physicists. *Physics Reports*, 810:1–124, May 2019.

[30] Giuseppe Carleo, Ignacio Cirac, Kyle Cranmer, Laurent Daudet, Maria Schuld, Naftali Tishby, Leslie Vogt-Maranto, and Lenka Zdeborová. Machine learning and the physical sciences. *Rev. Mod. Phys.*, 91:045002, Dec 2019.

[31] Juan Carrasquilla. Machine learning for quantum matter. *Advances in Physics: X*, 5(1):1797528, Jan 2020.

[32] Giuseppe Carleo and Matthias Troyer. Solving the quantum many-body problem with artificial neural networks. *Science*, 355(6325):602–606, Feb 2017.

[33] Giacomo Torlai, Guglielmo Mazzola, Juan Carrasquilla, Matthias Troyer, Roger Melko, and Giuseppe Carleo. Neural-network quantum state tomography. *Nature Physics*, 14(5):447–450, Feb 2018.

[34] Sebastian J. Wetzel. Unsupervised learning of phase transitions: From principal component analysis to variational autoencoders. *Physical Review E*, 96(2), Aug 2017.

[35] Juan Carrasquilla and Roger G. Melko. Machine learning phases of matter. *Nature Physics*, 13(5):431–434, Feb 2017.

[36] Román Orús. Tensor networks for complex quantum systems. *Nature Reviews Physics*, 1(9):538–550, Aug 2019.

[37] Marcos Rigol, Vanja Dunjko, and Maxim Olshanii. Thermalization and its mechanism for generic isolated quantum systems. *Nature*, 452(7189):854–858, Apr 2008.

[38] Anders W. Sandvik, Adolfo Avella, and Ferdinando Mancini. Computational studies of quantum spin systems. 2010.

[39] Federico Becca and Sandro Sorella. *Quantum Monte Carlo Approaches for Correlated Systems*. Cambridge University Press, Nov 2017.

Contents

List of Publications ii

Introduction 1

Bibliography 4

1 Entanglement Guided Search of Parent Hamiltonians 9
1.1 The quest of parent Hamiltonians . . . 9
1.2 Bisognano-Wichmann theorem and parent Hamiltonian reconstruction . . . 11
1.2.1 Bisognano-Wichmann theorem and lattice models . . . 11
1.2.2 Basis of local operators . . . 11
1.2.3 Bisognano-Wichmann Ansatz algorithm and parent Hamiltonian reconstruction . . . 13
1.3 Parent Hamiltonians of conformal, critical and topological phases . . . 14
1.3.1 Parent Hamiltonians of conformal phases . . . 14
1.3.2 Parent Hamiltonian of a symmetry protected topological phase . . . 16
1.3.3 Parent Hamiltonian of a two-dimensional quantum critical point . . . 16
1.4 Parent Hamiltonians of Jastrow-Gutzwiller variational wavefunctions . . . 19
1.4.1 Jastrow-Gutzwiller wave functions . . . 19
1.4.2 Physical properties of the Jastrow-Gutzwiller wave functions . . . 21
1.4.3 Reconstruction of Jastrow-Gutzwiller local parent Hamiltonians . . . 24
1.5 Conclusive remarks . . . 29

Bibliography 31

2 Negativity Spectrum and Entanglement equipartition in Disordered Critical Spin Chains 36
2.1 Introduction . . . 36
2.1.1 Entanglement entropy and entanglement spectrum . . . 37
2.1.2 Negativity and negativity spectrum . . . 37
2.1.3 Symmetry resolved entanglement entropy . . . 38
2.2 Strong Disorder Renormalization Group and the Random Singlet Phase . . . 41
2.2.1 Antiferromagnetic Heisenberg spin chain . . . 41
2.2.2 Strong-Disorder RG and random singlet phase . . . 41
2.2.3 Structure of the reduced density matrix and its partial transpose . . . 43
2.2.4 Scaling of the number of shared singlets and bipartite entanglement . . . 44
2.3 Negativity spectrum . . . 47
2.3.1 Logarithmic negativity and negativity moments . . . 47
2.3.2 Moments $\hat{\mathcal{E}}_\alpha$ and logarithmic negativity . . . 48
2.3.3 Moments $\mathcal{E}_\alpha$ and renewal equation for the negativity spectrum . . . 48
2.3.4 Application to adjacent intervals . . . 50
2.3.5 Numerical tests for adjacent intervals . . . 51
2.4 Symmetry resolved entanglement in the random singlet phase . . . 56
2.4.1 Preliminaries . . . 58
2.4.2 Entanglement equipartition for $\overline{S}_m$ . . . 59
2.4.3 Entanglement equipartition of $\widetilde{S}_m$ . . . 60

2.4.4 Entanglement equipartition for $\widehat{S}_m$ . . . 60
2.4.5 The number entropy and the log-log term . . . 62
2.4.6 Numerical SDRG results . . . 63
2.5 Conclusion . . . 70
2.6 Appendix: Additional detail and results for the negativity spectrum . . . 72
2.6.1 Universality of the SDRG data . . . 72
2.6.2 Fermionic negativity moments . . . 72
2.7 Appendix: Moments of the size of the symmetry block I_m . . . 76

Bibliography **79**

3 Data Structure of Many-Body Systems **90**
3.1 Introduction . . . 90
3.2 Intrinsic Dimension . . . 93
3.3 Models . . . 95
3.3.1 How to characterize partition functions as data sets . . . 96
3.4 Results . . . 97
3.4.1 Second-order phase transitions . . . 97
3.4.2 Berezinskii-Kosterlitz-Thouless (BKT) phase transition . . . 98
3.4.3 First-order phase transitions . . . 100
3.5 Discussion . . . 101
3.5.1 Why the I_d exhibits a singular behavior in the vicinity of T_c? . . . 101
3.5.2 Why I_d exhibit universal scaling behavior? . . . 104
3.6 Conclusions . . . 107
3.7 Appendix . . . 108
3.7.1 The TWO-NN method and comparison with principal component analysis (PCA) . . . 108
3.7.2 Scaling of the I_d with the number of configurations . . . 109
3.7.3 Data collapse . . . 110
3.7.4 Definition of the winding number . . . 113

Bibliography **114**

4 Measurement-Induced Criticality in Non-Unitary Quantum Systems **118**
4.1 Introduction . . . 118
4.1.1 Measurement-induced criticality in hybrid random circuits . . . 120
4.1.2 Measurement-induced criticality in the quantum Ising chain . . . 121
4.2 Stabilizer states and Clifford unitary gates . . . 123
4.3 Measurement-induced criticality as a data-structure transition . . . 125
4.3.1 Hybrid non-unitary dynamics . . . 125
4.3.2 Principal component analysis . . . 125
4.3.3 Intrinsic dimension . . . 127
4.3.4 Conclusion . . . 130
4.4 Measurement-induced criticality in 2+1D hybrid random circuits . . . 131
4.4.1 Model and observables . . . 131
4.4.2 Entanglement dynamical phases and universal criticality . . . 133
4.4.3 Rank-2 measurements . . . 136
4.4.4 Discussion and open questions . . . 137
4.4.5 Conclusion . . . 139
4.5 Measurement-induced entanglement transition in the monitored quantum Ising chain . . . 141
4.5.1 Model and Measurement Protocols . . . 141
4.5.2 Results . . . 144
4.5.3 Conclusion . . . 150

4.6 Appendix 151
4.6.1 Continuous measurements and stochastic Schrödinger equations 151
4.6.2 Free fermion techniques and numerical implementation 155

Bibliography **158**

Chapter 1

Entanglement Guided Search of Parent Hamiltonians

This chapter is based on the following pubblications:

[1] Xhek Turkeshi, Tiago Mendes-Santos, Giuliano Giudici, and Marcello Dalmonte,
Entanglement guided search for parent Hamiltonians,
Phys. Rev. Lett. **122**, 150606 (2019).

[2] Xhek Turkeshi, and Marcello Dalmonte,
Parent Hamiltonian Reconstruction of Jastrow-Gutzwiller Wavefunctions,
SciPost Phys. **8**, 042 (2020).

1.1 The quest of parent Hamiltonians

Which came first: the egg or the chicken?

Variational wave functions have played a pivotal role in the investigation of strongly interacting systems [3–5], where the coordination of long-range entanglement and non-perturbative correlation patterns hinder traditional Hamiltonian methods, such as Monte Carlo simulations [6] and semiclassical approximations [7]. Among the notable examples are the Laughlin wave functions [8, 9], which serve as a phenomenological ansatz for fractional quantum Hall physics [10], and the resonating valence bond states[11–14]. More in general, variational wave functions have been a central tool in exploring quantum spin liquids [7, 15, 16], either with tensor network approaches [17], or in Monte Carlo studies [18–21].

The success of ansatz wave functions has naturally motivated the search for the corresponding parent Hamiltonians [22], with considerable achievements in several context, such as topological matter [23–25] and low-dimensional systems [24, 26–38]. Furthermore, the recent experimental progresses in quantum engineering and synthetic systems [39–43] have opened an additional perspective in the search for parent Hamiltonians: thanks to the high degree of interactions tunability, these experiments provide a clean route toward the realization of tailored quantum simulations.

This has stimulated recent renewed theoretical interest, culminated in a series of work aiming to a systematic reconstruction of Hamiltonians [44–50] having the input state as an *eigenstate*. In these approaches, given an input state $|\Psi\rangle$, the goal is to reconstruct an Hamiltonian H that has the input state as an eigenstate (not necessarily in the low-lying part of the energy spectrum). In this respect, these methodologies have been named *inverse problem*, in contrast to the *forward problem*, which is to find (part of) the spectrum of a given Hamiltonian, and reflects the idea that an eigenstate encodes highly non-trivial content of the full system [51]. A key assumption is that the target Hamiltonian is *local*, *i.e.,* with interactions decaying rapidly with the separation between degrees of freedom: this requirement, which is physically motivated and relevant for certain experimental platforms, rules out fine tuned situations, *e.g.,* the parent Hamiltonian being a non-local projection onto the input state. Within this setup, the techniques introduced in Ref. [44, 46, 50] reconstruct target Hamiltonians in polynomial computational resources, and, remarkably, using only limited information on the state, such as local correlation functions. Interestingly, these method are generic, and has been successfully applied also to disordered systems [44, 48].

procedure RECONSTRUCTION($\Psi, \{O_{\alpha,r}\}$)
  Initialization: $\vec{w}^{(0)}$, error $= 10$, $\eta = 4$
  Compute: $\sum_r r\langle O_{\alpha,r}\rangle_\Psi$
  while error $<$ threshold **do**
    Compute: $\sum_r r\langle O_{\alpha,r}\rangle_{\vec{w}^{(n)}}$
    Compute: $\partial_\alpha S$
    Compute: $\vec{w}^{(n+1)} = \vec{w}^{(n)} - \eta\nabla S$
    if $||\vec{w}^{(n+1)} - \vec{w}^{(n)}|| >$error **then**
      $\eta = \eta/2$
      error $= ||\vec{w}^{(n+1)} - \vec{w}^{(n)}||$
  return $H_{\rm rec} = \sum_{\alpha,r} w_\alpha^{(N)} O_{\alpha,r}$

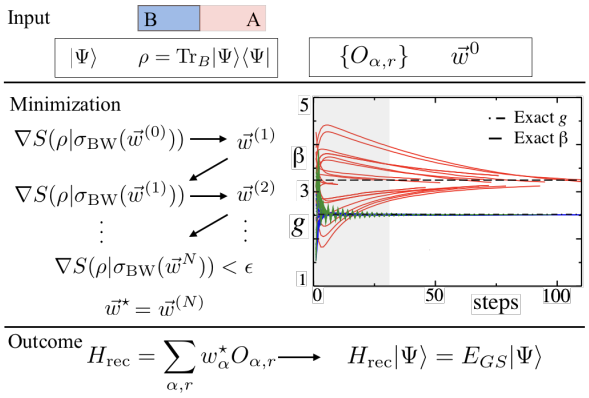

FIGURE 1.1: Schematics of the parent Hamiltonian search. The starting point is the wave-function of interest $|\Psi\rangle$ (with a half-partition reduced density matrix ρ), a set of local operators $\{O_{\alpha,r}\}$, and an initial guess for their coefficients w_α^0. The relative entropy $S(\rho|\sigma_{\rm BW})$ between the state and an ansatz Bisognano-Wichmann reduced density matrix is evaluated at each step of the minimization procedure. The procedure is iterated until convergence with a certain tolerance ϵ: the final outcome are the coupling $w_\alpha^\star$ of the parent Hamiltonian, and the entanglement inverse temperature β. The inset shows a sample of our results for the bilayer Heisenberg model at the critical point (cfr. Sec. 1.3). Different lines corresponds to minimization from different initial values $\vec{w}^0$. Convergence within 0.1% of the correct value of g (interlayer coupling; blue and green) and β (red lines) is typically reached after 30 (grey area) and 200 steps, respectively.

In this chapter we discuss a variation of the inverse problem, where we search Hamiltonians having the input state in the *ground state* manifold. We propose a method to determine parent Hamiltonians guided by Lorentz invariant field theory, which heavily relies on the entanglement structure of the ground states of local Hamiltonians. The first key element of our strategy is to connect the reduced density matrix ρ on a half-partition of $|\Psi\rangle$ to an ansatz inspired by the Bisognano-Wichmann theorem [52–55] adapted to the lattice [56, 57]. As we detail below, and schematically illustrate in Fig. 1.1, this provides an immediate connection between the input vector $|\Psi\rangle$ and its Lorentz invariant parent Hamiltonian H through ρ. The second key element is to combine this ansatz to a minimization procedure based on the relative entropy [58, 59]: this guarantees, for the Bisognano-Wichmann ansatz Hamiltonian a convex optimization scheme, with a unique solution, up to numerical tolerance. (Note, however, that no statement can be made on the convergence rate to the right solution). Furthermore, the entire procedure can be carried out using different theoretical methods, that rely on evaluating expectation values at finite inverse (entanglement) temperature, including finite-temperature density matrix renormalization group (TDMRG) [60, 61] and quantum Monte Carlo methods [62], as we explicitly demonstrate.

Our method is applicable to a broad range of wave functions which can be thought as ground states of lattice Hamiltonians, described at low energies by quantum field theories with emergent Lorentz invariance – thus encompassing physical phenomena as diverse as quantum criticality with $z = 1$, topological matter, and quantum antiferromagnets, to name a few.

This chapter is organized as follows. In Sec. 1.2.1 we discuss the general framework, which we name Bisognano-Wichmann Ansatz (BWA), and illustrate the details of the algorithms. In Sec. 1.3 we benchmark the method by reconstructing the parent Hamiltonian of: (i) conformal phases in the one-dimensional XXZ chain, (ii) the Haldane chain as an epitome of symmetry protected topological phase, and (iii) an example of strongly coupled critical point, the two-dimensional bilayer Heisenberg antiferromagnet. In Sec. 1.4 we instead consider the open problem of determining the parent Hamiltonian of Jastrow-Gutzwiller variational states, which are archetypal of Laughlin wave functions and ubiquitously employed in quantum spin liquids.

1.2 Bisognano-Wichmann theorem and parent Hamiltonian reconstruction

1.2.1 Bisognano-Wichmann theorem and lattice models

The parent Hamiltonian search we propose is guided by a set of field theory results, which go under the name of Bisognano-Wichmann theorem [52, 53]. While it is well known that for local Hamiltonians the ground state contains (potentially complete) information about the Hamiltonian spectrum, this theorem allows to quantitatively establish this correspondence at the field theoretic level. Here we first state the theorem and its consequences, and afterwards, we discuss the Bisognano-Wichmann ansatz we use in lattice models.

Given a pure state $|\Psi\rangle$, and a bipartition $A \cup B$, the reduced density matrix $\rho_A = \mathrm{tr}_B |\Psi\rangle\langle\Psi|$ is a positive operator, which can be parametrized as $\rho_A \sim \exp(-K_A)$. The operator K_A is known as modular or entanglement Hamiltonian, and is in general highly non-local, as it is the logarithm of the non-local operator ρ_A. Remarkably, Bisognano and Wichmann proved that the entanglement Hamiltonian acquire a local density when considering the ground state of a relativistic quantum field theory, when the space is partitioned into two (connected) halves. Moreover, the density of this modular operator is proportional to the density of the Hamiltonian operator of the theory. The statement is the following.

Theorem 1. *Given a local relativistic quantum field theory in $D+1$ spacetime dimensions, described by an Hamiltonian $H = \int d^D x h(x)$, the half-space reduced density matrix of the ground state (vacuum) $|\Omega\rangle$ is*

$$\rho_A = \mathrm{tr}_B |\Omega\rangle\langle\Omega| = \frac{e^{-\beta_{\mathrm{ent}} K_A}}{Z_A},$$
$$K_A = \int_A d^D x x_1 h(x), \qquad Z_A = \mathrm{tr}_A \rho_A. \tag{1.1}$$

Here A and B are respectively the manifolds $A = \{x \in R^D : x_1 \geq 0\}$ and its complementary, Z_A ensures the norm of the density matrix is $\mathrm{tr}_A \rho_A = 1$, while $\beta_{\mathrm{ent}} = 2\pi/v$ is the inverse entanglement temperature, which is inverse proportional to the sound velocity of the relativistic excitations.

More recently, this result has been revisited in the context of holography and many-body physics [63–70], and it has been extended to systems with conformal invariance in $1+1$-dimensions [64], and in $D+1$-dimensions [71, 72].

An important observation is that, when considering lattice systems exhibiting relativistic low-lying excitations, the discretization of Eq. (1.1) gives a fine approximation of the reduced density matrix [56, 57, 73–77], with discrepancies due to the lattice structure disappearing in the scaling limit. (We mention also that for certain model which can be solved through corner transfer matrix, exact solutions exists also at the lattice level [78, 79].) This motivates the core idea behind the BWA method: to find optimal BW entanglement Hamiltonian describing the reduced density matrix of the state of interest. For concreteness, we conclude this subsection with stating the form of the discretized Bisognano-Wichmann Hamiltonian for $D = 1$ with L sites and $A = \{1, \ldots, L/2\}$ (the result extends trivially to $D > 1$)

$$\sigma_A^{\mathrm{BW}} = \frac{e^{-\beta K_A}}{Z_A}, \qquad Z_A = \mathrm{tr}_A \rho_A, \qquad H = \sum_{r=1,\ldots,L/2} h_r$$
$$K_A = \sum_{r=1,\ldots,L/2} r h_r. \tag{1.2}$$

Here r labels the sites, h_r is the lattice density of the Hamiltonian H, while K_A is the corresponding modular operator. Occasionally we omit the partition subscript A when no confusion arises.

1.2.2 Basis of local operators

From Eq. (1.2), it is clear that a fundamental ingredient is the specific choice of the local operators h_r. On one hand, the choice of the basis of operators fixes the concept of locality for the lattice model. On the other,

different choices of such a basis give generally rise to other parent Hamiltonian models. In the following we describe how the basis is defined, and how the Bisognano-Wichmann Hamiltonian Eq. (1.2) reads in this basis. For ease, we consider the $D = 1$ setting, with trivial extensions in $D > 1$ space dimensions.

Following Ref. [44–46], we say an operator is k-local if either (1) it has finite domain k-nearby few body operators, or (2) it is written as a linear combination of the latter. Furthermore, we require k to be constant for any finite system size L we consider. If these conditions are not fulfilled, we say the operator is non-local [1].

We define a basis of k-local operators as the set of matrices $\{O_{\mu,r}\}_{\mu\in I, r\in\Lambda}$. Here I is a set of internal indices, while $\Lambda \subset \Lambda$ is a set of sub-lattice ones. Depending on the values of I and Λ, these basis span different vector spaces of local operators, whose generic element is

$$H = \sum_{\alpha\in I, r\in\Lambda} w_{\alpha,r} O_{\alpha,r}. \tag{1.3}$$

The dimension of these spaces is thus given by the combined cardinality of the label sets $\mathcal{D} = |I||\Lambda|$. For the sake of clarity, we list below few examples of the above notation. First, we consider the Pauli algebra $S^{x/y/z}$ at each site $r \in \Lambda = \Lambda$

$$\mathcal{B}_1 = \{1_r, S^x_r, S^y_r, S^z_r\}_{r\in\Lambda} \quad \text{with} \quad O_{0,r} = 1_r,\ O_{1,r} = S^x_r,\ O_{2,r} = S^y_r,\ O_{3,r} = S^z_r. \tag{1.4}$$

The generic linear combination is

$$H = \sum_{r\in\Lambda}\sum_{\alpha=0}^{3} w_{\alpha,r} O_{\alpha,r}. \tag{1.5}$$

We see the total dimension is $\mathcal{D} = 4L$ in this case. A less trivial example is the two-body nearest neighboring interactions

$$\mathcal{B}_2 = \mathcal{B}_1 \cup \{S^x_r S^x_{r+1}, S^x_r S^y_{r+1}, \dots S^y_r S^y_{r+1}, \dots, S^z_r S^z_{r+1}\}_{r\in\Lambda}. \tag{1.6}$$

Here α covers, in addition to the elements in Eq. (1.4), the following two-body operators at each site r

$$O_{4,r} = S^x_r S^x_{r+1},\ O_{5,r} = S^x_r S^y_{r+1}, \dots,\ O_{10,r} = S^z_r S^y_{r+1},\ O_{11,r} = S^z_r S^z_{r+1}, \tag{1.7}$$

with dimension $\mathcal{D} = 12L$. The basis presented consider different operators for each site, and hosts a operator space which also include inhomogeneous systems [48]. However, for the problem at hand, translational invariance is required by the Bisognano-Wichmann hypothesis. This can be achieved equivalently by either considering a reduced basis, which automatically implement the symmetry constraints, or imposing the constraint at the level of coupling constants, hence viewing the target operator space as embedded in a larger manifold. For notational simplicity, we choose the latter, and replace the couplings $w_{\alpha,r} \mapsto w_\alpha$.

The resulting manifold has dimension $\mathcal{D} \sim \mathcal{O}(k)$ in system size, hence it is independent of the number of sites, and is proportional to the domain of the most extended basis operator. Thus, in the following we are going to consider only translational invariant system and Bisognano-Wichmann Hamiltonians, respectively

$$\text{System}: \quad H = \sum_{\alpha\in I} w_\alpha \sum_{r\in\Lambda} O_{\alpha,r} \equiv \sum_\alpha w_\alpha \tilde{h}_\alpha, \qquad \text{BW}: \quad H = \sum_{\alpha\in I} w_\alpha r \sum_{r\in\Lambda} O_{\alpha,r} \equiv \sum_\alpha w_\alpha \tilde{h}_\alpha. \tag{1.8}$$

In the above equation, we defined the operators $h_\alpha = \sum_r O_{\alpha,r}$ and $\tilde{h}_\alpha = \sum_r r O_{\alpha,r}$.

If additional symmetries are imposed, the number of independent coupling constants is further reduced. For instance, imposing $U(1)$ invariance, and restricting to only interactions at most between nearest neighboring sites, we have

$$\mathcal{B}_k(U(1)) = \left\{S^+_r S^-_{r+k-1} + S^-_r S^+_{r+k-1}, S^z_r S^z_{r+k-1}, S^z_r\right\}_{r\in\Lambda} \tag{1.9}$$

[1] Notice that by this convention, inverse law power-law interacting model are considered non-local; however, as it is the case for such systems, for large value of the exponent governing the interaction, the system is effectively a short-range model. We discuss more about this when treating the Jastrow-Gutzwiller wave functions in Sec. 1.4.

The corresponding target Hamiltonian is still in the form Eq. (1.8), but the index α takes only three values ($\mathcal{D} = 3$).

1.2.3 Bisognano-Wichmann Ansatz algorithm and parent Hamiltonian reconstruction

We are now in position to present the Bisognano-Wichmann Ansatz algorithm. Let ρ_A^{input} be the half-system reduced density matrix of the the input state. Our goal is to minimize a cost function $d(\rho|\sigma)$, and to find optimal coefficients w_α in Eq. (1.8) such that

$$w_\alpha^\star = \arg\min d(\rho_A^{\text{input}}|\sigma_A^{BW}(\{w_\alpha\})) \Rightarrow \rho_A^{\text{input}} \simeq \sigma_A^{BW}(\{w_\alpha^\star\}). \tag{1.10}$$

It is important to stress that the choice of the cost function is a crucial aspect of the algorithm. A simple choice of cost function such as the Kullback-Leibler divergence between participation spectra of the reduced density matrices [80] has the advantage of being trivially implementable in higher spacetime dimensions, but in general fails to guarantee the implication in Eq. (1.10). (However, it guarantees the diagonal parts are the same when the Kullback-Leibler divergence is zero). To simplify the discussion, here we fix the cost function in Eq. (1.10) to have a distance interpretation in the density matrix space. For the class of models described in Eq. (1.6), any convex cost function acting on the space of density matrices leads to a convex optimization problem, hence with a unique solution up to numerical tolerance. Among these, we have found particularly useful for the simple form of the corresponding gradient, the relative entropy

$$S(\rho|\sigma) = \text{tr}(\rho \log \rho) - \text{tr}(\rho \log \sigma). \tag{1.11}$$

This function quantifies the distance between between ρ and σ, it is non-negative $S(\rho|\sigma) \geq 0$ (with the equality holding only if $\rho = \sigma$) and it is jointly convex. In particular, its restriction to a single argument is a convex function. With this choice $d(\rho|\sigma) \equiv S(\rho|\sigma)$, we optimize the relative entropy and obtain the optimal coefficients in Eq. (1.10).

For the numerical implementation, we evaluate a gradient descent on the relative entropy. Introducing the notation $\partial_\alpha = \partial/\partial w_\alpha$ and the expectation values

$$\langle O \rangle_{\text{GS}} \equiv \text{Tr}(O\rho_A), \quad \langle O \rangle_{\text{BW},\vec{w}} \equiv \text{Tr}(O\rho_A^{\text{BW}}(\vec{w})), \tag{1.12}$$

the gradient of the relative entropy reads

$$\partial_\alpha S(\rho_A|\rho_A^{\text{BW}}(\vec{w})) = \langle \tilde{h}_\alpha \rangle_{\text{GS}} - \langle \tilde{h}_\alpha \rangle_{\text{BW},\vec{w}^{(n)}}. \tag{1.13}$$

In the last equation, we used the notation introduced in Eq. (1.8). We conclude this section with few comments. First, we note the actual input needed is just the expectation value over the ground state and over the "thermal" BW density matrix. While the former can sometimes computed analytically (as for the Jastrow-Gutzwiller wave functions in Sec. 1.4), the latter can be implemented with different numerical methods, including quantum Monte Carlo when no sign problem is present. Furthermore, it is easy to prove the convex nature of the problem. In fact, the Hessian of the relative entropy

$$\partial_\alpha S(\rho_A|\rho_A^{\text{BW}}(\vec{w})) = \langle \tilde{h}_\alpha \tilde{h}_\beta \rangle_{\text{BW},\vec{w}^{(n)}} - \langle \tilde{h}_\alpha \rangle_{\text{BW},\vec{w}^{(n)}} \langle \tilde{h}_\beta \rangle_{\text{BW},\vec{w}^{(n)}} \equiv \Xi_{\alpha,\beta}. \tag{1.14}$$

is a quantum covariance matrix, and thus it is a positive semi-definite operator $\Xi \geq 0$.

Lastly, it is worth pointing out that the method is not immediately suited to simple wave functions, where correlations vary at the lattice spacing level (like a product state). This is due to the field theoretical assumption we employ, which might fail in these regimes. Another potential limitation is that it is not possible to capture parent Hamiltonians with quadratic spectra, such as ferromagnets. (See Sec. 1.4 for a discussion in the context of Jastrow-Gutzwiller wavefunctions). Failure is in principle straightforward to diagnose, as the relative entropy minimum will attain a large value, indicating an incorrect result.

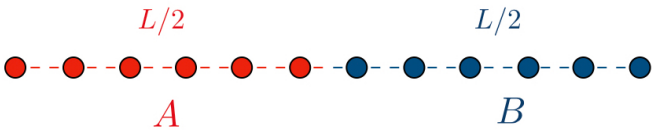

FIGURE 1.2: Spin chain of interest. We compute the reduced density matrix by tracing out the partition B.

1.3 Parent Hamiltonians of conformal, critical and topological phases

In this section we benchmark the BWA algorithm by reconstructing parent Hamiltonian of known states. Specifically, we consider three exemplar model wave functions: (i) the ground state of the XXZ spin-1/2 chain, (ii) the symmetry protected topological (SPT) ground state of the Haldane chain, and the ground state of a two-dimensional quantum critical model, the 2D bilayer Heisenberg model.

1.3.1 Parent Hamiltonians of conformal phases

The class of wave functions we consider are the $c = 1$ conformal field theory (CFT) ground state of the 1D XXZ chain

$$H = \sum_i S_i^x S_{i+1}^x + S_i^y S_{i+1}^y + \Delta S_i^z S_{i+1}^z. \tag{1.15}$$

In the above equation, S_i^α are the spin-1/2 operators acting on the i-th site, whereas the coupling constant Δ control the phase of the system. The model hosts a gapless phase for $-1 < \Delta \leq 1$, described at low-energies by a Luttinger liquid. In addition, it displays a ferromagnetic (antiferromagnetic) phase for $\Delta \leq -1$ ($\Delta > 1$). Both the gapless and the antiferromagnetic phase shall be captured by our approach.

To test our method, we choose as ansatz wave functions the ground state of Eq. (1.15) for various values of Δ, and the basis Eq. (1.6). We define the convergence parameters as $w_\alpha = \beta J_\alpha$, *i.e.* factoring the entanglement temperature, and consider open boundary conditions. We find convenient to vary the internal label index as $\alpha \in \{x, y, z, xx, xy, \ldots, zz\}$, which naturally relate to the operator content (*e.g.*, $w_{xy} \to S_r^x S_r^y$. The reduced density matrix is obtained by tracing half-chain, see cartoon in Fig. 1.2.

Given an initial configuration, we perform the minimization and evaluate the error as

$$\epsilon = ||\eta \nabla S(\rho|\sigma_{\rm BW}(\vec{w})|| \tag{1.16}$$

where η is the control parameter of the gradient descent. For the sake of convenience, we consider a tolerance of 10^{-3} for the error, that we see already return accurate results for the parent Hamiltonian. (In Ref. [1] we present results down to a tolerance 10^{-9}, which does not vary the qualitative results.)

We present the results of the BWA algorithm implemented with exact diagonalization ($L \leq 12$), and TDMRG ($L \leq 24$) in Fig. 1.3. In panel (a), we plot w_α as a function of the steps for different initial guesses $\vec{w}^0$, chosen in the range $w_\alpha^0 \in [2, 6]$: the symmetries of the state are rapidly identified, and the couplings of the parent Hamiltonian converge to the correct ratios after few steps, while the entanglement temperature converges slower. We note that the overall prefactor (the inverse entanglement temperature) is not important at the level of parent Hamiltonian search, as it only sets the energy scale of the model. However, in this section we use it to benchmark the Bisognano-Wichmann hypothesis and hence our method.

The relative entropy indicating vicinity to the exact solution (Fig. 1.3b) displays few plateaux, and eventually converges exponentially fast to the correct solution. In Fig. 1.3c, we plot the converged value of Δ, averaged over initial configurations $\vec{w}^0$, with a relative error with respect to the exact value of percent level. Finally, in Fig. 1.3d we show how the number of steps required for the minimization scale with system size. As the system is enlarged, the field theory predictions become more robust, and the convergence rate is faster. The abrupt change at $\Delta = 1.5$ is an artifact of the minimization and is removed by considering

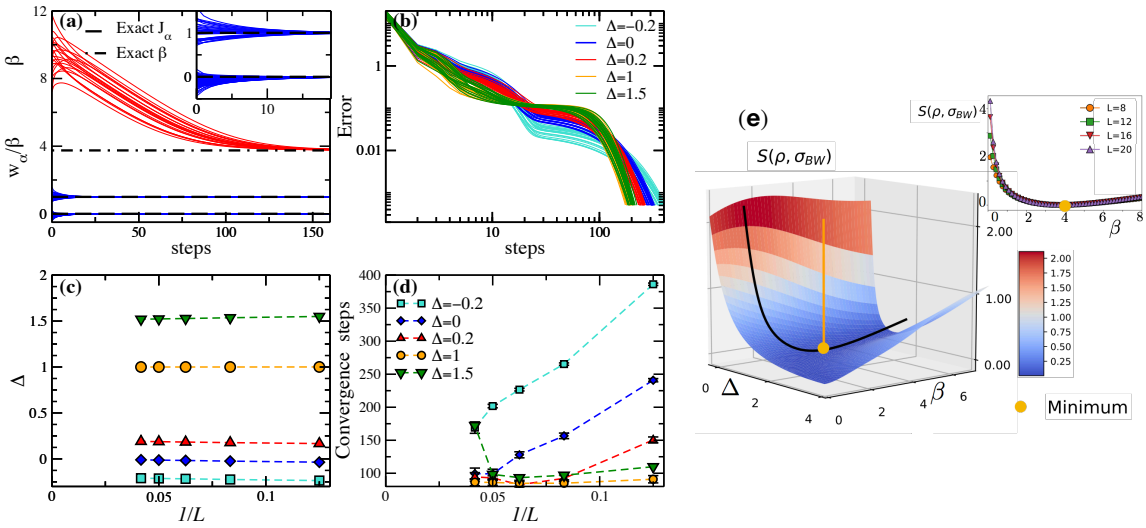

FIGURE 1.3: Parent Hamiltonian search for the XXZ chain using exact diagonalization. (a) Ratios $J_\alpha = w_\alpha/\beta$ (blue lines) and β (red lines) as a function of the minimization steps. We compare with the exact coupling and entanglement temperature. Here, $L = 12$ and $\Delta = 1$. No $U(1)$ symmetry is imposed, hence the number of w_α for the chosen basis is 12. (See text). (b) Error as defined in Eq. (1.16), as a function of the minimization steps; the value Δ label the different input state used, ground state of the respective XXZ Hamiltonian Eq. (1.15). (c) Reconstructed $\Delta = w_{zz}/\beta$ averaged over initial realizations of the coupling constants $\vec{w}^0$, as a function of system size. (d) Average convergence steps over initial realizations of the coupling as a function of system size. The convergence rate typically improves with system size. (e) Landscape of the relative entropy $S(\rho, \sigma_{\rm BW}(\Delta, \beta))$ between the reduced density matrix of the ground state at $\Delta = w_{zz/\beta} = 1$ and the Bisognano-Wichmann Hamiltonian. The insets show a planar cut ($\Delta = 1$) for different system sizes.

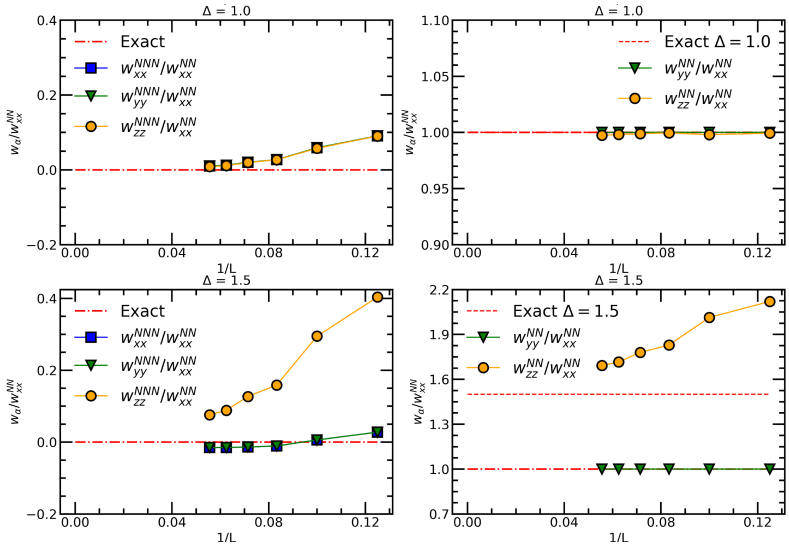

FIGURE 1.4: Converged parameter versus system size for different values of Δ for the XXZ chain. We use exact diagonalization to obtain the data, and average the converged values over the initial guesses $\vec{w}^0$, with elements $w^0_\alpha \in [-1, 1]$ uniformly picked. Other values have been investigated in Ref. [1], but are not presented here to for presentation purposes.

smaller values of the threshold error. Our results are fully consistent with the relative entropy landscape

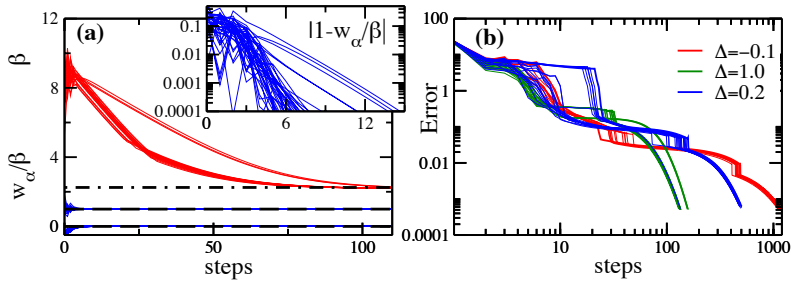

FIGURE 1.5: Parent Hamiltonian search for the Haldane chain with $L = 8$. (a) $J_\alpha = w_\alpha/\beta$ and β as functions of the minimization steps; the initial state is at $\Delta = 1$. The inset shows a magnification up to 14 steps of $|1 - w_\alpha/\beta|$: convergence to the correct solution at a precision of 0.01% is typically achieved achieved after 6 steps. (b) Error as a function of the minimization steps for different values of Δ.

depicted in Fig. 1.3e.

As we have shown above, the coupling associated to the operators in the local basis not sharing the symmetry-content of the chosen input state converge quickly to zero. It is however important to discuss what happens when we enlarge the operator content within the symmetry preserving sectors. We therefore consider the BW Hamiltonian in the basis of nearest neighboring and next nearest neighboring operators. The resulting target BW Hamiltonian we consider is

$$H_{\rm BW} = \sum_{a=x,y,z} \sum_{r\in A} r(w_{ab}^{\rm NN} S_r^a S_{r+1}^a + w_{ab}^{\rm NNN} S_r^a S_{r+2}^a) + w^z \sum_{r\in A} r S_r^z. \tag{1.17}$$

The simulations show that the new next nearest neighboring terms attain a finite value, which is smeared out in the finite size scaling Fig. 1.4. While this trend is rapid in the conformal phase, where the correlation of the system diverges, deeply in the massive case $\Delta = 1.5$ the system presents deviation of order 10% for the system size we reach. This is not unexpected, since for the massive case the ground state has very strong spatial order, and the BWA suffers from slightly larger finite size effects [57].

1.3.2 Parent Hamiltonian of a symmetry protected topological phase

As a model with non-trivial topological phase, we discuss here the Haldane chain [5, 23], described by the Hamiltonian Eq. (1.15) but with spin-1 operators. For $0 < \Delta \lesssim 1.2$, the model supports a Haldane phase. We use exact diagonalization with adaptive gradient descent to determine the parent Hamiltonian for different values of Δ. In this case, we have chosen a subset of the full basis of local hermitian operators up to two body terms $\{O_\alpha, r\} = \{S_r^a S_{r+1}^b, S_r^a\}_{a,b=x,y,z}$ (*i.e.* we do not include spin-1 local operators as $(S_r^\alpha)^2$). The result of the minimization procedure are shown in Fig. 1.5.

In full analogy with the spin-1/2 case, the couplings quickly converge to the correct results, while the entanglement temperature convergence is slower. In all instances we studied, the relative entropy converged faster to 0 in the gapped, topological regime (Fig. 1.5b).

1.3.3 Parent Hamiltonian of a two-dimensional quantum critical point

We finally test our approach on strongly coupled quantum systems, by reconstructing the parent Hamiltonian for the bilayer Heisenberg model characterized by the ratio of inter-to-intra layer coupling g [81]

$$H_{\rm bilayer} = \sum_{l=1,2} \sum_{\langle \vec{i},\vec{j}\rangle} \vec{S}_{\vec{i},l} \cdot \vec{S}_{\vec{j},l} + g \sum_{\vec{i}} \vec{S}_{\vec{i},1} \cdot \vec{S}_{\vec{i},2}. \tag{1.18}$$

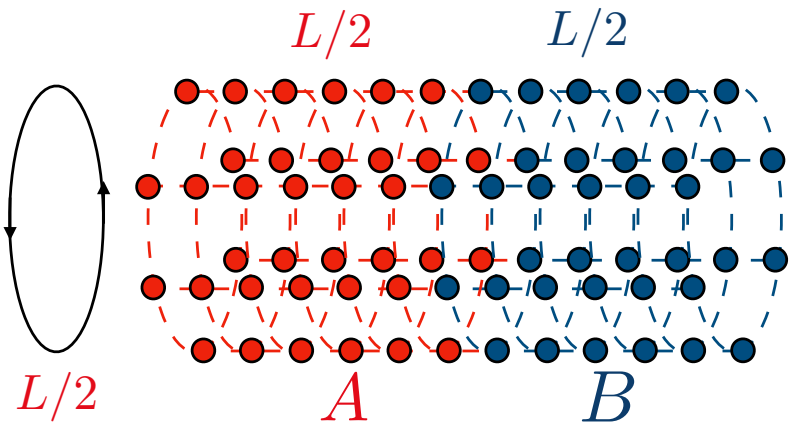

FIGURE 1.6: Cartoon of the two-dimensional geometries employed for the bilayer Heisenberg model.

Here $\vec{i}$ and $\vec{j}$ label the sites within the planes (square lattice), l are the label of the planes, and we introduced the notation $\langle\ ,\ \rangle$ for the sum over nearest neighboring sites. We consider nearest neighboring basis operators $\{O_\alpha, r\} = \{S^a_{\vec{r}} S^a_{\mathrm{neigh}(\vec{r})}\}_{a,b=x,y,z;\vec{r}\in\Lambda}$, with $\mathrm{neigh}(\vec{r})$ denoting the neighboring sites of $\vec{r}$, and consider a lattice which has the cylinder geometry, with size $L \times L/2$ (see cartoon in Fig. 1.6, where we also present the partition considered).

The Hamiltonian Eq. (1.18) at $g = 0$ corresponds to the ground state of two uncoupled planes with antiferromagnetic long-range order, while $g = g_c = 2.52210(5)$ [82] separates the antiferromagnetic phase from a singlet phase. At the criticality, the system is described by a non-linear σ-model.

As previously stated, the input parameters needed for the algorithm to work are the expectation value of the basis operator chosen. Hence, we use stochastic series Monte Carlo with loop updates to compute the expectation values of the operators $\sum_r r S^a_{\vec{r}} S^a_{\mathrm{neigh}(\vec{r})}$ on the ground state (cfr. Eq. (1.14)).

During the gradient descent minimization part, we consider the BW ansatz for the entanglement Hamiltonian of the ground-state half-bipartition

$$H_{\mathrm{BW}} = \beta_c \sum_{l=1,2} \sum_{\vec{i},\delta} i_x \vec{S}_{(i_x,i_y),l} \cdot \vec{S}_{(i_x+\delta,i_y),l} + \beta_c \sum_{l=1,2} \sum_{\vec{i},\delta} (i_x - 1/2) \vec{S}_{(i_x,i_y),l} \vec{S}_{(i_x,i_y),l}$$
$$+ \beta_c g \sum_{l=1,2} \sum_{\vec{i},\delta} (i_x - 1/2) \vec{S}_{\vec{i},l} \vec{S}_{\vec{i},l}, \tag{1.19}$$

where $i_x > 0$ and the shift is done in such a way that the distance from the entanglement cut is computed from the center of the support of the operator.

Before considering the BWA on the bilayer Hamiltonian, we first investigate the convergence to one of the layers of the model at $g = 0$, *i.e.* the Heisenberg model in two-dimensions. Specifically we check the feasibility of the approach in 2D by considering as only free parameter the inverse entanglement temperature. As presented in Fig. 1.7a, the error ϵ features a minimum at the expected value of $\beta = 2\pi/v = 3.792$, weakly dependent on system size.

Next, we switch on the inter-to-intra layer coupling g and preliminary check the relative entropy manifold as a function of g at fixed $\beta = \beta_c = 3.307$ (Fig. 1.7b). We find that the minimum of the error coincide with the correct coupling $g = g_c$ at percent level.

We lastly apply two different procedures: in the first one we fix the entanglement temperature and let the coupling g free (red lines in Fig. 1.7c), while in the second we let both g and β vary (blue lines). In both cases, the error ϵ quickly diminishes (slower in the second case due to more parameters to be optimized). Most importantly, at the end of the minimization, the value of g is close to the correct one at percent level (see Fig. 1.7d), with a finite size scaling with the linear dimension of the system trending toward the expected thermodynamic limit. Given the complexity of the system wave function, this serve as a strong benchmark

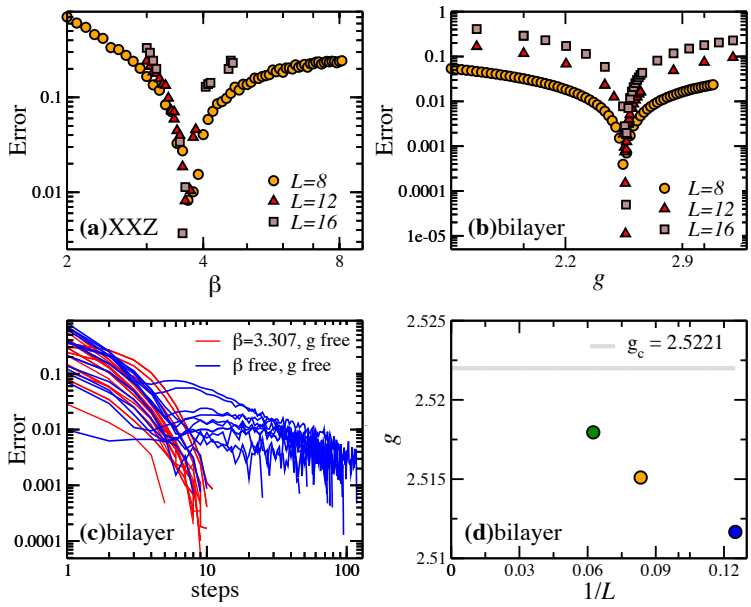

FIGURE 1.7: (a-b) Error between the exact and the BW reduced density matrix as a function of temperature for the 2D Heisenberg model (a), and as a function of g for the bilayer Heisenberg model at $\beta = 3.3$ (b). (c) Error as a function of the minimization step for $L = 8$. (d) Converged inter-to-intra layer coupling versus linear system size.

for our strategy: reconstructing the parent Hamiltonian in this case takes only few tens of steps, each one corresponding to a Monte Carlo simulation of the BW entanglement Hamiltonian.

1.4 Parent Hamiltonians of Jastrow-Gutzwiller variational wavefunctions

In the previous section, to benchmark the Bisognano-Wichmann Ansatz algorithm, we considered a variety of *a priori* known models, and checked if the output reconstructed operator coincided with the initial Hamiltonian. In this section we instead consider an open problem, and apply the BWA to the one-dimensional Jastrow-Gutzwiller (JG) variational wave functions, which are paradigmatic states appearing in several contexts, from integrability to topology, to quantum spin liquids. They are characterized by an extensive superposition of spatially local states, with weights captured by analytic algebraic functions of the basis coordinate, and which in general present long-range correlation patterns. Despite their common appearance, their parent Hamiltonians are not known except for a few fine-tuned cases, amenable to exact solutions.

In the following we first discuss introduce the JG wave functions by analyzing their participation spectrum, their entanglement content and their correlation functions, to preliminary identify a suitable range of applicability of the BWA algorithm. Then, we employ the BWA on different operator basis, and test the results with different proxies. Given the reconstructed Hamiltonian, we compute the relative entropy and the overlap between the input JG state and their ground state, as well as we compare their correlation functions. For the system size considered, we obtain fidelities ranging between 95% and 99%. Finally, we compute the relative error between the ground state energy and the JG variational energy of the reconstructed Hamiltonian. In all the considered cases, the relative error is less than 2%, even in the extrapolated thermodynamic limit. Our finite size analysis suggest the obtained Hamiltonian are approximate, and that the exact parent Hamiltonian require a different operatorial content.

1.4.1 Jastrow-Gutzwiller wave functions

Model wave functions

Throughout this section, we consider a one-dimensional chain Λ of L sites and with periodic boundary conditions. We introduce the variables $n_i \in \{0, 1\}$ defined at each site $i \in \Lambda$. In the basis $\{|n_1 n_2 \dots n_L\rangle\}$, and define the JG wave functions as

$$|\psi_{\mathrm{JG}}\rangle = \sum_{\mathcal{P}_N\{n\}} \psi_\alpha(\{n\})\, |n_1 n_2 \dots n_L\rangle\,,$$
$$\psi_\alpha(\{n\}) = \frac{1}{Z}(-1)^{\sum_{i=1}^{L} i n_i} \prod_{1\le i<j\le L} \sin\left(\frac{\pi}{L}(j-i)\right)^{\alpha n_i n_j}. \tag{1.20}$$

Here the sum is over combinations $\mathcal{P}_N\{n\}$ constrained by $\sum_i n_i = N$. Pictorially, the $\{n_i\}$ variables are occupation numbers of hard-core bosons living on the lattice, with a filling fraction set by $\nu = N/L$. The parameter α and the filling fraction $\nu = N/L$ control the properties of the system, and for fine tuned values of them there exists exact solutions [37, 38, 83, 84]. In the following we fix $\nu = 1/2$ and vary only the parameter α. This is already sufficient to capture both ferromagnetic and antiferromagnetic pattern.

From the form of the wave functions Eq. (1.20), we identify two relevant limit. At $\alpha = 0$, the system is unitary equivalent to an equal weight superposition of all basis states with $\nu = 1/2$, and can be proved to be the ground state of the XXZ chain (cfr. Eq. (1.15)) at $\Delta = -1$. The point $\alpha = 1$ is instead a Slater determinant, which identifies a model of free fermions, or equivalently, the XXZ chain at $\Delta = 0$. A less trivial limit is $\alpha = 2$, where Eq. (1.20) is the ground state of the Haldane-Shastry Hamiltonian [28, 29]

$$H_{\mathrm{HS}} = \frac{\pi^2}{L^2} \sum_{m<n} \frac{\vec{S}_m \cdot \vec{S}_n}{\sin^2(\pi(m-n)/L)}. \tag{1.21}$$

These three points represent the known exactly solvable models for α.

Participation spectroscopy To obtain insights for generic values of α, it is instructive to rephrase Eq. (1.20) in the language of participation spectrum [85–88], *i.e.* rewriting the wave functions in a pseudo-energy fashion

$$\psi_\alpha(\{n\}) = \langle n_1 n_2 \dots n_L | \psi_{\rm JG}\rangle \equiv \frac{e^{-H_\alpha[\{n\}]}}{\sqrt{Z_\alpha}}, \tag{1.22}$$

$$H_\alpha[\{n\}] = \alpha \sum_{1\le i<j\le L} n_i n_j V(i,j) + E_0[\{n\}], \tag{1.23}$$

$$V(i,j) = -\log\left|\sin\left(\frac{\pi}{L}(j-i)\right)\right|, \tag{1.24}$$

$$E_0[\{n\}] = \log\cos\left(\sum \pi i n_i\right). \tag{1.25}$$

We see that H_α is a classical Hamiltonian, with a constant energy shift E_0 and logarithmic interactions between particles $V(i,j)$. Since the sites i, j takes only discrete (integer) values and due to the boundary condition choice, we note that H_α describes a 2D Coulomb gas constrained in a 1D [83, 89]. Analogously, we can introduce the Boltzmann weights and read Z_α in Eq. (1.20) as a partition function

$$p_\alpha(\{n\}) = |\psi_\alpha(\{n\})|^2 = \frac{e^{-2H_\alpha[\{n\}]}}{Z_\alpha}, \tag{1.26}$$

$$Z_\alpha = \sum_{\mathcal{P}_N(\{n\})} p_\alpha(\{n\}) = \sum_{\mathcal{P}_N(\{n\})} e^{-2H_\alpha}. \tag{1.27}$$

Eq. (1.26) suggests the spectrum $\varepsilon(\{n\})$ of H_α determine the relevant weights in the JG wave functions, as well as the sign of the inverse temperature α. For $\alpha > 0$ the Coulomb gas Hamiltonian Eq. (1.23) favors repulsion among particles, whereas for $\alpha < 0$ favors aggregation, modulo the imposition of filling and lattice constraints. Consequently in the limit of large values of α positive and negative the states of the system is easily identified as the following cat states

$$\lim_{\alpha\gg 1} |\psi_{\rm JG}\rangle = \frac{1}{\sqrt{2}}(|01010\dots\rangle + |10101\dots\rangle), \tag{1.28}$$

$$\lim_{\alpha\ll -1} |\psi_{\rm JG}\rangle = \frac{1}{\sqrt{L}}\sum_{i=1}^{L} |\dots 0_{i-1}1_i 1_{i+1}\dots 1_{i+L/2}0_{i+L/2+1}+\dots\rangle, \tag{1.29}$$

where, in the last equation, periodic boundary conditions are implicitly understood. For convenience, we dub the state Eq. (1.28) as Néel cat state (as it is the sum of the Néel and anti-Néel states), and the state Eq. (1.11) as ferromagnetic cat state.

Apart from this limiting regimes, the form of the JG wave function depends on the balance between the competing interactions. However, as we further argue subsequently via entanglement entropy and correlation functions, the qualitatively ferromagnetic nature of the states for $\alpha < 0$ suggest this regime is unsuitable for the BWA algorithm, which in general have a quadratic dispersion relation.

Hence, we focus on the regime $\alpha > 0$ in the remaining of this section. We first compute the participation gap $G = \varepsilon_{\rm min} - \varepsilon_{1^{\rm st}}$ between the ground state and first-excited state of H_α. It is convenient to introduce the number of ferromagnetic domain walls as the number of consecutive occupied/unoccupied sites $N_{\rm dws}$ [2]. The configurations contributing to Eq. (1.28) are the only ones with $N_{\rm dws} = 0$, which also define the $\varepsilon_{\rm min}$. In Fig. 1.8 we present the participation spectrum for $\alpha = 2$ and $\alpha = 6$ at $L = 16$. The participation gap increases with α linearly $G = g_L\alpha$, with g_L a numerical constant whose thermodynamic value is

$$g_\infty = 2\lim_{L\to\infty}\log\left(\frac{\sin(2\pi/L)\prod_{r=1}^{L/2-2}\sin(2r\pi/L)}{\sin(\pi/L)\prod_{r=1}^{L/2-2}\sin((2r+1)\pi/L)}\right) \simeq 0.9031654195\dots. \tag{1.30}$$

[2] For example $N_{\rm dws}(|010101\rangle) = 0$, while $N_{\rm dws}(|011001\rangle) = 2$

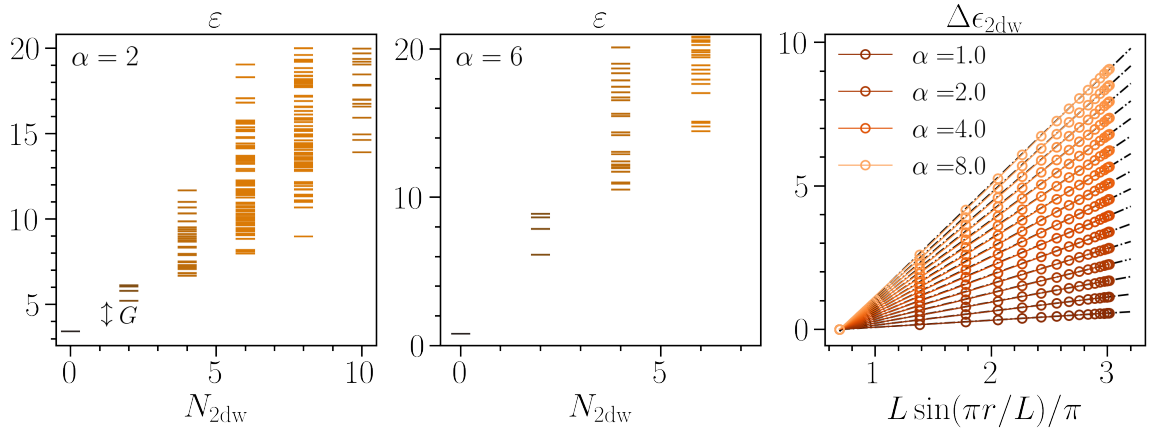

FIGURE 1.8: Participation spectrum ε at $L = 16$ for $\alpha = 2$ (Left), and $\alpha = 6$ (Center). The spectrum is indexed using the number of domain walls N_{dws}, and the color is darker (lighter) for lower (higher) degeneracy of the pseudo-energies. The participation gap G increases linearly with α, with the coefficient g_∞ in the text. (Right) Pseudo-energy differences between two domain walls as a function of wall separation r at $L = 64$. The dashed black lines are the Luttinger liquid prediction [87], with Luttinger parameter $K = 1/\alpha$.

For finite length of the chain, small system size corrections are present which for $L \geq 16$ give $|g_L - g_\infty| < 0.1\%$. These results confirm the previous analytic argument for $\alpha \gg 1$, and suggest that the configuration associated to the excited states of H_α can be captured systematically in a perturbative expansion on domain walls.

Finally, from the substructure of the $N_{\mathrm{dws}} = 2$ sector, we can extract how the domain walls interact. We compute the pseudo-energy difference $\Delta\varepsilon_{2\mathrm{dw}} = \varepsilon_{2\mathrm{dw}}(r) - \varepsilon_{2\mathrm{dw}}(2)$ between domains walls separated by a distance r or close together $(r = 2)$. This quantity has been considered for antiferromagnetic quantum Hamiltonian systems to distinguish between critical and symmetry broken phases of matter. In the former case, the domain walls are logarithmically confined with the separation distance; instead, in the latter this confining is linear. Moreover, the prefactor of this potential is related to the Luttinger parameter for Luttinger liquids [87, 90].

Because of the explicit form of the classical Hamiltonian density H_α, the interaction between two domain walls is always expected logarithmic with their separation distance (Fig. 1.8). We also note the Luttinger parameter $K = 1/\alpha$ describes their logarithmic confining potential, and hence suggests that for $\alpha > 0$ the JG wave functions may host Luttinger liquid states. This hypothesis is supported by CFT arguments [91], and by analysis on the Resta polarization [92]. In the latter study, the author estimate the presence of a Luttinger Liquid phase between $0 < \alpha \leq 4$.

We note that our analysis on the participation spectrum does not show any transition. This is an artifact of the definition of the JG state. While in quantum Hamiltonian systems, symmetry broken phases usually lead to disjoint configurations, in the present setting, the definition of the Jastrow-Gutzwiller wave functions Eq. (1.20) forces coherent superposition on the states. (See also the analysis on the correlation functions below). Furthermore, the participation spectrum is insensitive to coherences, as it is related to the square modulo of the wave function coefficients (In this respect, it plays a similar role to the diagonal ensemble). Next, we discuss the entanglement entropy and the correlation functions, which complement the proposed analysis.

1.4.2 Physical properties of the Jastrow-Gutzwiller wave functions

Entanglement entropy

To investigate the entanglement content of the Jastrow-Gutzwiller wave functions we consider the entanglement entropy [93]. For a given state $|\Psi\rangle$, and a bipartition $\Lambda = A \cup B$, the entanglement entropy is

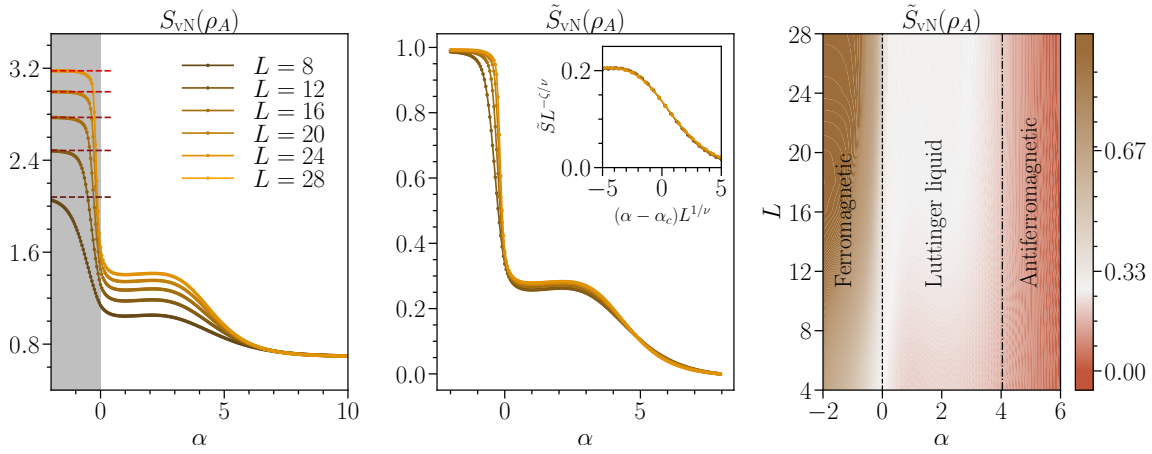

FIGURE 1.9: (Left) Entanglement entropy of the Jastrow-Gutzwiller wave function at different system sizes and values of α. The dashed lines corresponds to the limit $\log L$ (cfr. Eq. (1.32)), whereas at large values of α correspond to $\log 2$ (cfr. Eq. (1.32)). (Center) The rescaled entanglement entropy Eq. (1.35), and its data collapse Eq. (1.36) at $\nu = 4.6(3), \alpha_c = 4.04(5)$ and $\zeta = 0.31(1)$ (inset). (Right) Phase diagram extrapolated from the entanglement entropy.

computed as the von Neumann entropy over the reduced density matrix

$$\rho_A = \text{tr}_B |\Psi\rangle\langle\Psi|, \qquad S_{\text{vN}}(\rho_A) = -\text{tr}_A \rho_A \log \rho_A. \tag{1.31}$$

We compute this quantity numerically through exact diagonalization, and compare with the analytic prediction for the Néel and ferromagnetic cat state

$$S(\rho_A) =_{\alpha \gg 1} \log 2, \qquad S(\rho_A) =_{\alpha \ll -1} \log L. \tag{1.32}$$

The results are plotted in Fig. 1.9. We see a good agreement in the region $\alpha < 0$ even for modest system sizes, whereas the limit large α is reached for the system sizes at handle at $\alpha \simeq 8$.

The region $0 \lesssim \alpha \lesssim 4$ is compatible with a logarithmic scaling

$$S = \frac{c}{3} \log L + \text{const}, \tag{1.33}$$

with coefficient (central charge) $c = 1$. This is expected for $\alpha = 1$ and $\alpha = 2$, as the wave function describes a Luttinger liquid. Our numerical results suggest that this conformal phase is extended in a finite range of values of α, which we determine in the following.

The left limit is $\alpha = 0$, and at this point the system exhibits a jump in the entanglement entropy due to an emergent permutation symmetry. (In fact, as already suggested by the participation spectroscopy, the system at $\alpha = 0$ is in an equal weight superposition of all spin states respecting the constraint $\sum_i n_i = N$). At this point the entanglement entropy can be computed by counting and have the system size scaling

$$S(\rho_A) = \frac{1}{2} \log L + \text{const}, \tag{1.34}$$

which signals an abrupt transition in the entanglement. To determine the right boundary, we consider the variable

$$\tilde{S} = \frac{S - \log 2}{\log L - \log 2}, \tag{1.35}$$

which in the thermodynamic limit decays to zero in the antiferromagnetic region characterized by the Néel cat state, while converge to 1 and 1/3 in the ferromagnetic and conformal phases respectively.

We performe a finite system size scaling, with the hypothesis

$$S(\alpha, L) = L^{\zeta/\nu} f((\alpha - \alpha_c) L^{1/\nu}), \tag{1.36}$$

and obtain the optimal collapse with $\alpha_c = 4.04(5)$, $\nu = 4.6(3)$, $\zeta = 0.31(1)$. The raw and collapsed values of $\tilde{S}(\rho_A)$ are shown in Fig. 1.9(center), where we also present a phase diagram based on the entanglement content Fig. 1.9(right): For $\alpha \leq 0$ the system is ferromagnetic, for $0 < \alpha \leq 4.04$ the system is a Luttinger liquid, while for $\alpha > 4.04$ the system is an antiferromagnet. The analysis on the correlation function supports this picture.

Correlation functions We conclude this subsection by the analysis of the correlation function. We compute the one-body and two-body spin correlation functions of the operators $\{S^z, S^+, S^-\}$. These correlations are needed as input of the BWA algorithm, hence their analytic form is relevant for the reconstruction. Specifically, we consider only $U(1)$ invariant functions, consistently with the symmetry of the JG wave functions. Recalling $S^z = 2n - 1$, with n the number operator we consider

$$\langle S_i^z \rangle = \sum_{\mathcal{P}_N(\{n\})} (2n_i - 1) \big|\psi_\alpha(\{n\})\big|^2, \tag{1.37}$$

$$\langle S_i^z S_j^z \rangle = \sum_{\mathcal{P}_N(\{n\})} (2\delta(n_i, n_j) - 1) \big|\psi_\alpha(\{n\})\big|^2, \tag{1.38}$$

$$\langle \{S_i^+, S_j^-\} \rangle = \sum_{\mathcal{P}_N(\{n\})} (1 - \delta(n_i, n_j)) \psi_\alpha(\{n\}) \psi_\alpha(F_{ij}\{n\}). \tag{1.39}$$

At half-filling Eq. (1.37) is identically zero, while Eq. (1.38) and Eq. (1.39) are non trivial to compute analytically for generic choice of values α, and hence, we obtain numerically.

The correlation length can be extrapolated through finite size scaling of the connected correlation function $\langle S_i^z S_{i+L/2}^z \rangle_c$

$$\langle S_i^z S_j^z \rangle_c \equiv \langle S_i^z S_j^z \rangle - \langle S_i^z \rangle \langle S_j^z \rangle = a \frac{e^{|i-j|/\xi}}{|i-j|^\gamma}, \tag{1.40}$$

$$\frac{1}{\xi} = -\lim_{L\to\infty} \frac{\log\left(\langle S_i^z S_{i+L/2}^z \rangle_c\right)}{L/2} \equiv \lim_{L\to\infty} \frac{1}{\xi_L} \tag{1.41}$$

Here a is a constant, while γ characterizes the algebraic decay, and periodic boundary conditions applies. Let us stress that Eq. (1.40) is well defined only when the cluster decomposition principle holds, and hence is not suited for Schrödinger cat state (as for $\alpha < 0$ and $\alpha > 4$). In fact, the latter exhibits in general an $\mathcal{O}(1)$ correlation function with distance

$$\langle S_0^z S_j^z \rangle_c =_{\alpha<0} = 2\left|1 - \frac{2j}{L}\right| - 1, \qquad \langle S_0^z S_j^z \rangle_c =_{\alpha\gg 1} (-1)^j, \tag{1.42}$$

and it an artifact of their definition. We show the results for the correlation functions and the correlation length in Fig. 1.10. We see the correlation functions decays algebraically in the critical range $0 < \alpha \leq \alpha_c$, in full agreement with the analysis previously proposed through participation spectrum and entanglement entropy.

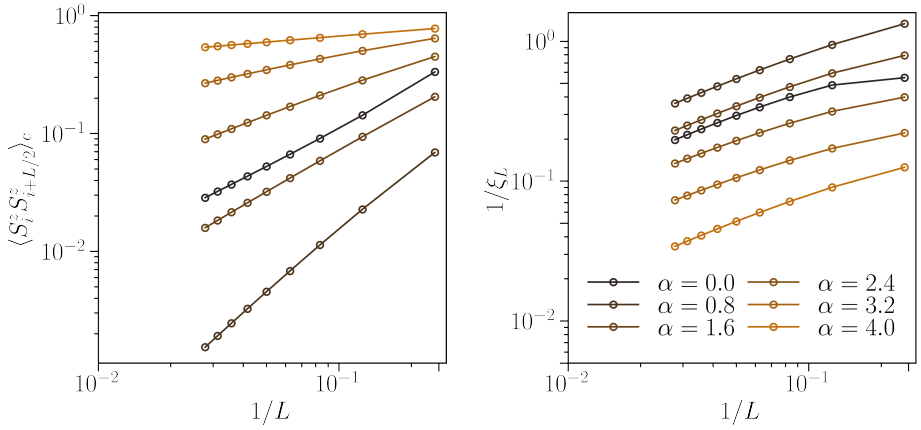

FIGURE 1.10: (Left) Connected correlation function against $1/L$. The seemingly algebraic decay suggests the the cluster decomposition requirement is fulfilled for the considered α. These are chosen representatives of the critical phase. (Right) Inverse correlation length for different values of α in the critical phase. For both plots, we considered chains of lengths $4 \leq L \leq 36$. To avoid odd/even effects, we present only L multiples of four.

1.4.3 Reconstruction of Jastrow-Gutzwiller local parent Hamiltonians

We consider the BWA reconstruction algorithm with Hamiltonians of variable but finite range interactions

$$H_k = \sum_r \sum_{p=1}^{k-1} \frac{J_p}{2} (S^+_r S^-_{r+p} + \text{h.c.}) + \Delta^z_p S^z_r S^z_{r+p}. \tag{1.43}$$

These target Hamiltonian generalize the spin-1/2 XXZ introduced in Eq. (1.11) with the introduction of additional hopping and two-body interaction terms connecting spins at a distance k. For instance $k = 2$ is the XXZ chain, whereas the $k = 3$ encompass as a particular instance, the $J_1 - J_2$ model [20]. We consider an error threshold $\epsilon_{\text{th}} = 10^{-4}$ and initial configurations uniformly drawn in the interval $[-2, 2]$ [3]. Our preliminary analysis in Sec. 1.4.2 has identified the optimal regime for reconstruction $0 < \alpha \leq 4$, where the system shows diverging correlation length and critical entanglement entropy. Within this regime, we employ exact diagonalization to find the parent Hamiltonians of the form Eq. (1.43) for $L \in \{4, \dots 20\}$.

If a p-local Hamiltonian exists, we expect $k > p$ to decay to zero enlarging the system size. When this is not the case, we argue the parent Hamiltonian we find are approximate in the basis chosen, and an exact parent Hamiltonian would require additional operators. We consider the systematic reconstruction for $k = 2, 3, 4$. Throughout this section, we are not interested in the precise value of the inverse entanglement temperature, as it only corresponds to a rescaling of the energy spectrum. Hence, we consider the ratios Δ_p/J_1 and J_p/J_1, where $1 \leq p \leq k-1$. The numerical results of our analysis are given in Fig. 1.11 and Fig. 1.12.

When $k = 2$ the system is the XXZ chain (cfr. Eq. (1.11)). We see that for $0 < \alpha \leq 2$ the system falls in the critical region of the XXZ chain ($-1 < w \leq 1$), while interestingly for $\alpha > 2$ our results shows Hamiltonian in the antiferromagnetic (massive) phase. Combining these findings with our analysis on the entropy Sec. 1.4.2, we conclude that the $\alpha > 2$ require additional couplings.

This intuition is confirmed by the results on $k = 3$ and $k = 4$. For $k = 3$ the J_2/J_1 and Δ_2/J_1 ratios shows finite but small values for $1.5 \leq \alpha \leq 2.5$, while sensibly larger values for $\alpha > 2.5$. This hint that the exact parent Hamiltonian has weak long-range features for $\alpha \lesssim 2.5$, and strong long range features for $\alpha \gtrsim 2.5$. The picture is supported by the $k = 4$ reconstruction, where we see that the converged values of the coupling constants are systematically smaller but finite. Lastly, we notice that at the point $\alpha = 0$ the

[3] We have tested the stability by changing the error threshold in the range $\epsilon = 10^{-3} \div 10^{-6}$ and other distribution of initial couplings, without any qualitative change.

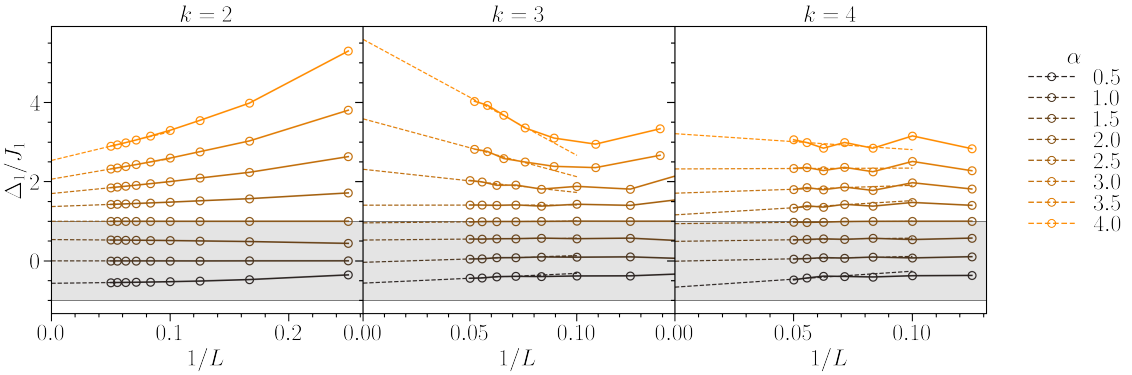

FIGURE 1.11: System size scaling of the output nearest-neighbor coupling for the Hamiltonian H_k in Eq. (1.43) for various values of α. The shaded region corresponds to the XXZ coupling in the critical region $-1 < \Delta_1/J_1 \leq 1$, while the dashed lines correspond to the thermodynamic limit.

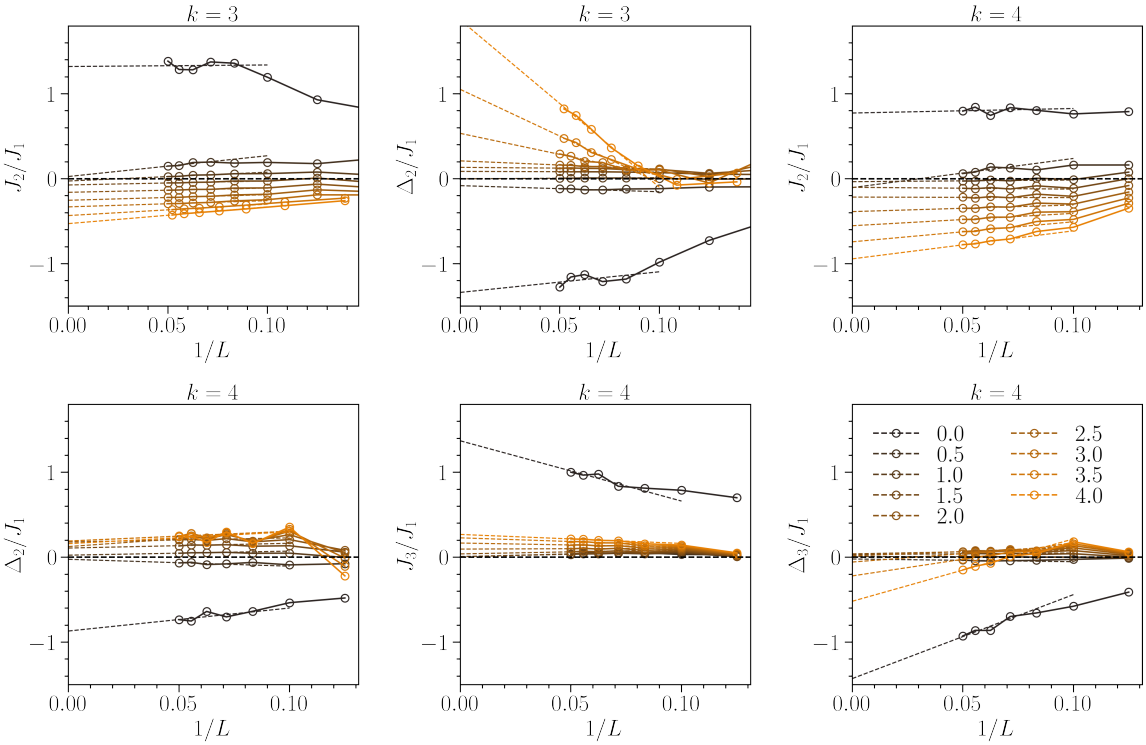

FIGURE 1.12: System size scaling of the ratios of: the converged couplings Δ_2/J_1 and J_2/J_1 for the $k = 3$ and $k = 4$ Hamiltonians in Eq. (1.43); the converged couplings Δ_3/J_1 and J_3/J_1 for H_4. The dashed lines represent the extrapolated thermodynamic limits.

reconstructed coupling constants attain a finite value which is of the same order of magnitude of J_1. At this point, which corresponds to a ferromagnetic regime the BWA is expect to perform worse.

Diagnosis of the reconstruction To verify our results we consider different proxies. First, we evaluate the relative entropy $S(\rho_{\mathrm{JG}}|\sigma_{\mathrm{BW}})$ between the converged Bisognano-Wichmann reduced density matrix and the exact Jastrow-Gutzwiller one (Fig. 1.13). We see a systematic improvement increasing k in the quality of our results. This is consistent with the observed reconstructed coupling $w = \{\Delta_p/J_1, J_p/J_1\}$, and suggest the exact parent Hamiltonian of the JG wave function is long-range.

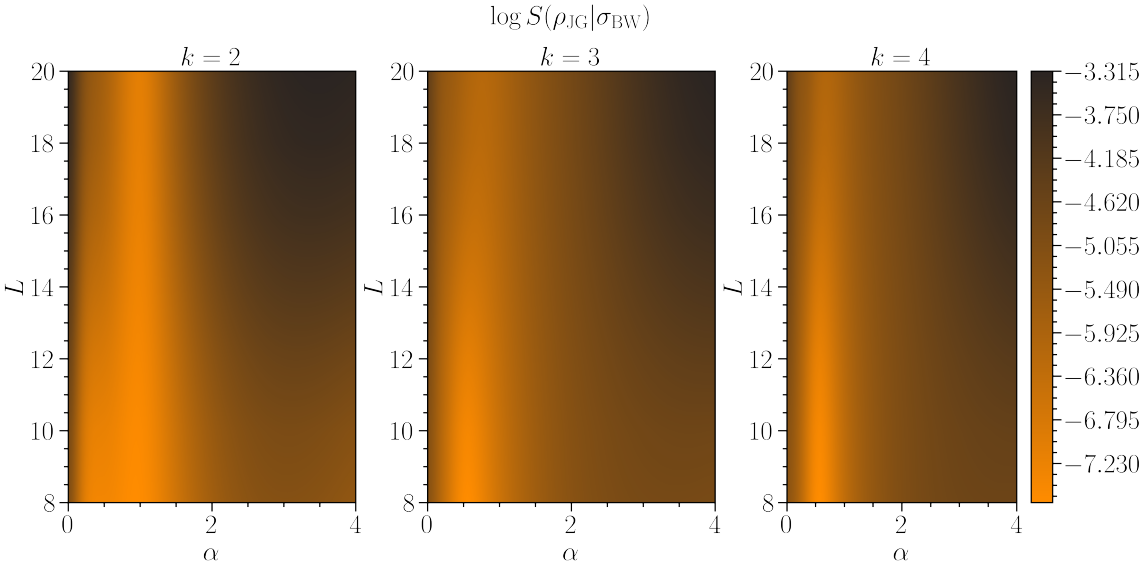

FIGURE 1.13: Relative entropy of the JG reduced density matrix and the BW converged one. We see that enlarging the domain of the operator involved, the quality of the results increases. The line $\alpha = 1$ corresponds to a free fermions gas.

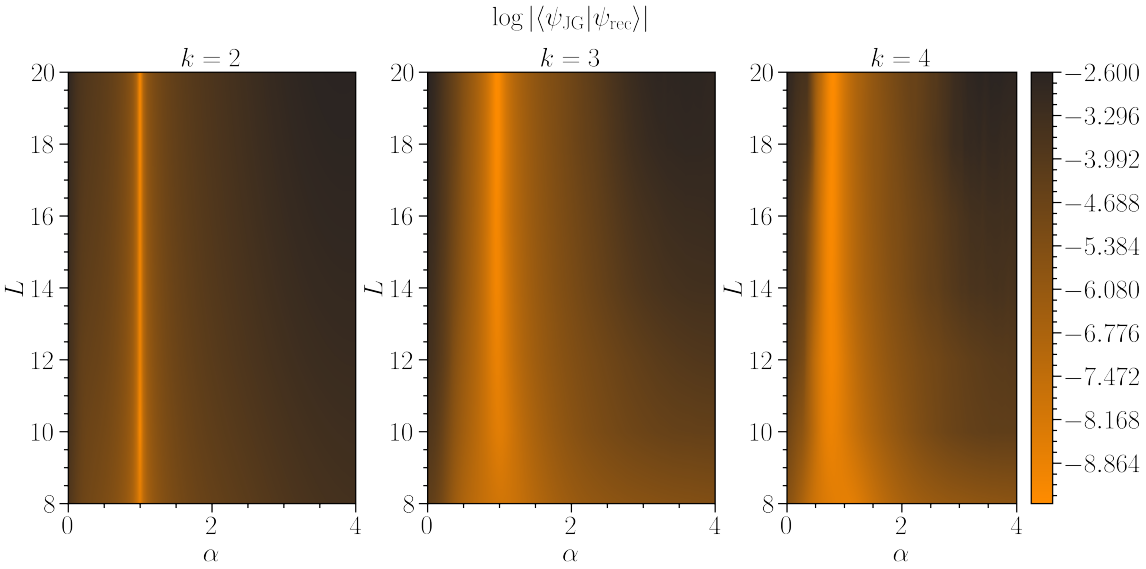

FIGURE 1.14: Superposition between the ground state of the reconstructed parent Hamiltonian and the JG input wave function. We see that enlarging the domain of the operator involved, the quality of the results increases. The line $\alpha = 1$ corresponds to a free fermions gas.

This analysis is also supported by the superposition between the ground state of the reconstructed Hamiltonian $H_{\rm rec}|\psi_{\rm rec}\rangle = E_{\rm gs}|\psi_{\rm rec}\rangle$ and the JS state in Eq. (1.20) (Fig. 1.14). Interestingly, we notice the line $\alpha = 1$ is numerically exact for $k = 2$. This point in fact corresponds to the free fermion limit, which is the exact ground state of the XXZ chain for $\Delta_1 = 0$. The observation is also consistent with the compatibility with zero of the converged couplings at $L \to \infty$ for $\alpha = 1$ and $k > 2$.

We crosscheck these findings with the performance over correlation functions and variational energy. In Fig. 1.15 we compare the exact correlation functions with the numerically computed ones over the ground

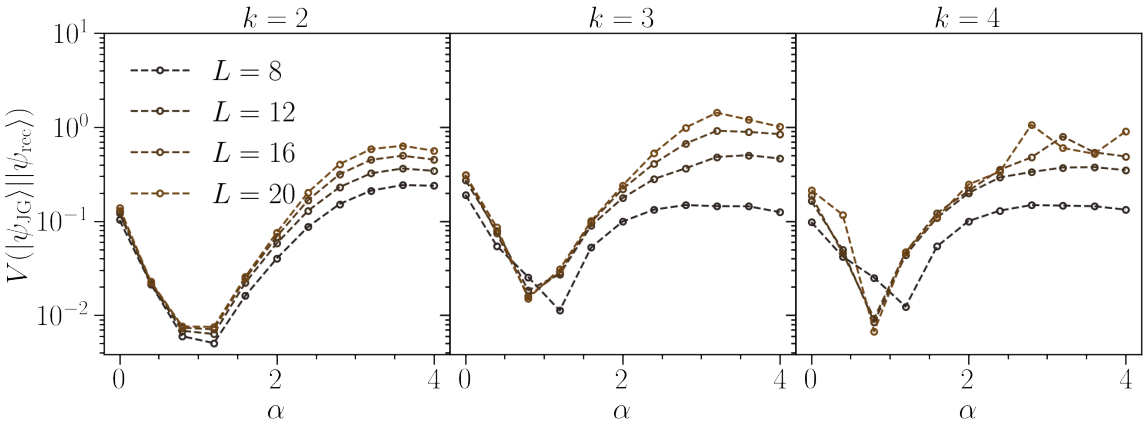

FIGURE 1.15: Eq. (1.44) at various values of α and k, and for different system sizes.

state of the reconstructed Hamiltonian $|\psi_{\rm rec}\rangle$. Specifically we consider the cumulative information

$$V(|\psi_{\rm JG}\rangle||\psi_{\rm rec}\rangle) = \frac{1}{\sqrt{L}}\sqrt{\sum_{j=1}^{L-1}\left(\langle S_0^z S_j^z\rangle_{\rm rec} - \langle S_0^z S_j^z\rangle_{\rm JG}\right)^2}, \tag{1.44}$$

where the factor $1/\sqrt{L}$ renders this object non-extensive. At a fixed value of k, $V(|\psi_{\rm JG}\rangle||\psi_{\rm rec}\rangle)$ seems to saturate at some finite value. Being such an object, a deviation measure from a standard value, it roughly gives how much on percentage the correlation functions change at a fixed site. In the worse scenario of our results, this attains a value of 10%. One may compare our findings with the exact results of the Haldane-Shastry model and the antiferromagnetic Heisenberg chain [28, 29]

$$\langle S_i^z S_j^z\rangle = \begin{cases} j & {\rm JG}(\alpha=2) & {\rm XXZ} \\ 1 & -0.5894 & -0.5908 \\ 2 & 0.225706 & 0.2427. \end{cases} \tag{1.45}$$

From the last equations, we read the relative error of the nearest neighboring correlation functions, and next-nearest neighboring ones, respectively of 2% and of 8%.

Instead, our results show that $V(|\psi_{\rm JG}\rangle||\psi_{\rm rec}\rangle)$ slightly increases when including higher k-terms. This is counterintuitive, since we observe that a larger basis leads to states that are more similar to the JG wave functions (Fig. 1.13 and Fig. 1.14). With the present analysis, we are not able to fully characterize if this trend is due to finite size effects, or it has a more systematic nature. A possible explanation would be hidden in the BWA algorithm: since it optimizes over the short range correlations, the large distance correlation functions are less controlled and subject to frustration effects. Within this interpretation, these discrepancies may suggest that longer range terms are required in the optimization to faithfully reconstruct an exact parent Hamiltonian.

The above interpretation is supported by the study of the relative error between the ground state energy of the reconstructed Hamiltonian $E_{\rm gs}$ and the variational energy of the reconstructed Hamiltonian over the JG wave function

$$E_{\rm var} = \langle\psi_{\rm JG}|H_{\rm rec}|\psi_{\rm JG}\rangle, \tag{1.46}$$

which we compare using the relative error

$${\rm Error}[\%] = \frac{|E_{\rm var} - E_{\rm gs}|}{|E_{\rm gs}|}. \tag{1.47}$$

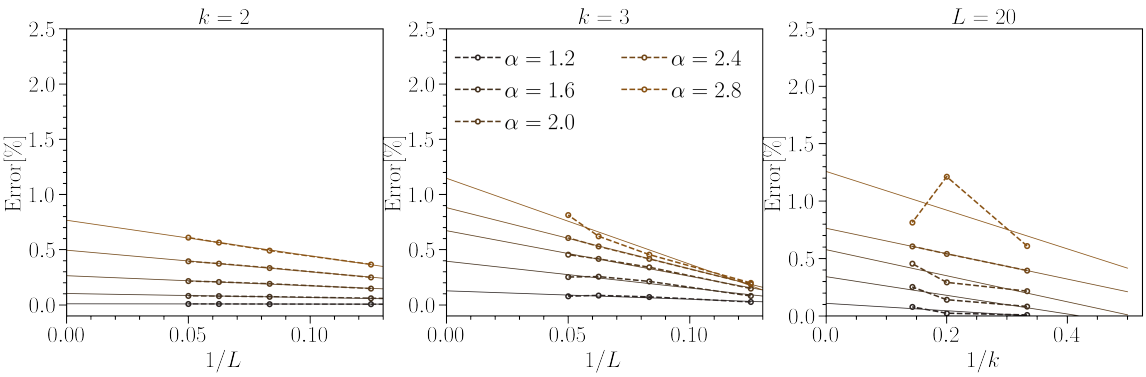

FIGURE 1.16: Relative energy error between the JG variational energy and the ground state energy of the reconstructed parent Hamiltonian for different values of α.

We find (Fig. 1.16) that the frustration effect play a relevant role in the determining the physical properties of the reconstructed model, with the relative error increasing at larger values of k, although bounded at the thermodynamic limit by $1 \div 2\%$.

In conclusion, our analysis suggest that, except for $\alpha = 1$ where a short range Hamiltonian exists and correspond to H_2 with $\Delta_1 = 0$, the exact parent Hamiltonian of the Jastrow-Gutzwiller wave function is presently unknown and most likely long-range in nature, and our findings provide accurate by approximate parent Hamiltonians.

Reconstruction of Jastrow-Gutzwiller parent Hamiltonian with power law interactions We conclude the analysis by considering the model Hamiltonian

$$H_{\mathrm{LR}} = \frac{\pi^2}{L^2} \sum_{r<m} \frac{1}{\sin^2\left(\pi(m-r)/L\right)} \left(\frac{J}{2}(S_r^+ S_m^- + \mathrm{h.c.}) + \Delta S_r^z S_m^z \right). \tag{1.48}$$

This class of Hamiltonians is known to be the exact parent Hamiltonian for $\alpha = 2$ (at the corresponding value $\Delta = 1$), and has been conjectured to be the parent Hamiltonian [83] for generic α JG wave functions for with $\Delta = \Delta(\alpha)$. Our numerical results are summarized in Fig. 1.17. Our comparison with the relative entropy between the converged BW density matrix and the reduced density matrix of the JG wave function show that for $\alpha \simeq 2$ the relative entropy decreases with system size, with a thermodynamic extrapolation compatible with zero, suggesting that in fact, the reconstruction is exact for the Haldane-Shastry model.

Instead, the converged quantity is worse for other values of α, which therefore rule out the possibility of exact reconstruction, and certify only an approximate H_{LR} as approximate parent Hamiltonians for the Jastrow-Gutzwiller wave functions.

Our results suggest the long-range pattern of the exact parent Hamiltonian of the Jastrow-Gutzwiller wave functions is not captured by the long-range XXZ chain, except for $\alpha = 2$ where the Haldane Shastry Hamiltonian is exact.

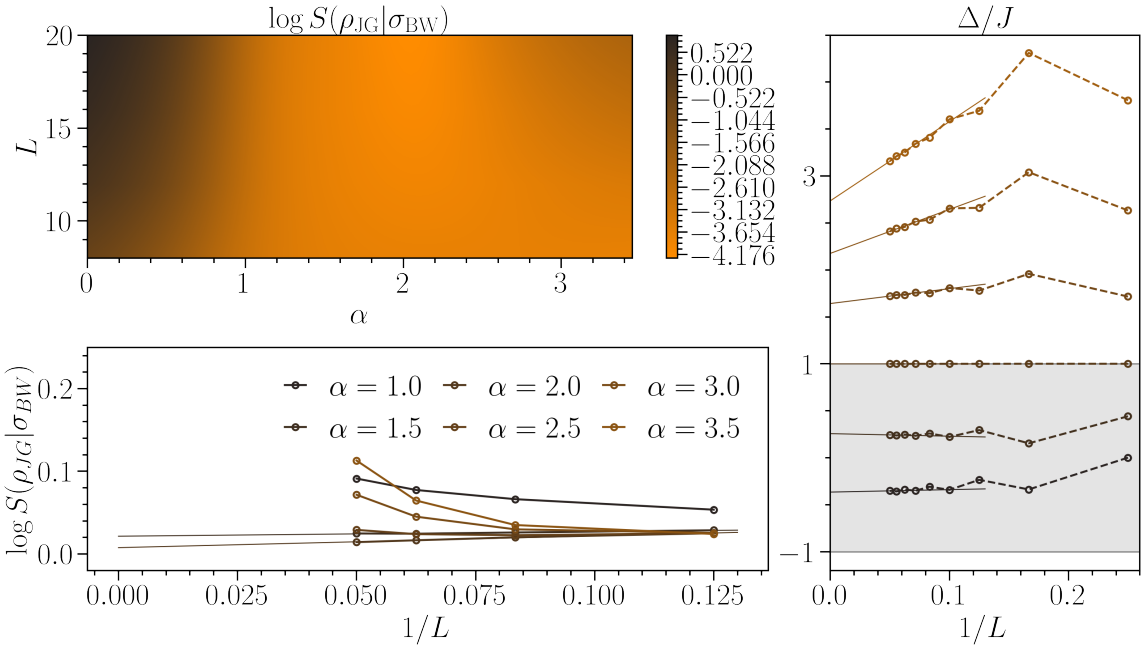

FIGURE 1.17: (Top-Left) Relative entropy landscape at different values of α and L. (Bottom-Left) System size dependence of the relative entropy, with extrapolation to the thermodynamic limit for $\alpha = 1.5$ and $\alpha = 2$. (Right) Converged coupling ratio with system size. The shaded region is the long-range XXZ chain proposed in Ref. [83] as the class of exact parent Hamiltonians for the JG wavefunctions. We see clearly that already at moderate system sizes, the Haldane-Shastry Hamiltonian ($\Delta = 1$) fully captures the physics of the JG wavefunction with $\alpha = 2$.

1.5 Conclusive remarks

In this chapter we introduced an entanglement guided algorithm for parent Hamiltonian reconstructions. The method is based on field theory results, as it relies on the lattice adaptation of the Bisognano-Wichmann theorem.

We have benchmarked the feasibility of our strategy by using several input wave functions, describing conformal phases in 1D and 2D, symmetry protected topological order, or non-linear sigma models.

We then reconstructed approximate parent Hamiltonian for the one-dimensional Jastrow-Gutzwiller wave functions. We have preliminary identified a region in parameter space where the wave functions display critical features compatible with a Luttinger liquid. Outside this interval, the JG wave functions are well described by Schrödinger cat states, either ferromagnetic or antiferromagnetic depending on the sign of the control parameter, and describing symmetry broken phases.

In the critical phase, we reconstructed k-local and power law parent Hamiltonian. The analysis of several quantities show that the reconstruction is approximate for general values of α (exception made for the fine tuned known points), and that the Jastrow-Gutzwiller exhibits non-trivial long-range patterns.

Nevertheless, finite-size results are of value for Hamiltonian engineering and quantum simulations for the present quantum deviced. Indeed, the Bisognano-Wichmann ansatz algorithm provides inherently finite-size optimization and control on the basis chosen and on the quality of the outputs. In particular, one can choose experimentally implementable operator, such as two-body hopping terms. The fact that our technique is easily adaptable to include fully-long-ranged interactions may also be used in a different manner, that is, to certify and validate quantum simulators aimed at finding ground states of spin models including slowly decaying power-law interactions, which are realized in both trapped ions [42], and Rydberg experiments [40].

It will be interesting to check whether the adapted strategy can be connected to Boltzmann machine

methods, due to the form of the Bisognano-Wichmann ansatz, and hence adapt machine learning methodologies to the estimation of parent Hamiltonian reconstruction, or to extend the method to lattice gauge theories, which play a pivotal role in the understanding of a variety of equilibrium and out-of-equilibrium phases of matter. The redundancies due to the gauge symmetry impose additional constraints in the structure of the Bisognano-Wichmann wave functions, which need to be included with more refined approaches.

Concerning the choice of input state, the primary goal is to apply the BWA methods on two-dimensional wave functions, such as the Laughlin wave functions. As we have presented, two-dimensional model can be approached with our method, as far as no sign-problem is present.

Bibliography

[1] X. Turkeshi, T. Mendes-Santos, G. Giudici, and M. Dalmonte. *Entanglement-Guided Search for Parent Hamiltonians*. Phys. Rev. Lett. **122**, 150606 (2019).

[2] X. Turkeshi and M. Dalmonte. *Parent Hamiltonian reconstruction of Jastrow-Gutzwiller wavefunctions*. Scipost Phys. **8**, 042 (2020).

[3] Y. Zhou, K. Kanoda, and T.-K. Ng. *Quantum spin liquid states*. Rev. Mod. Phys. **89**, 025003 (2017).

[4] X.-G. Wen. *Quantum Field Theory of Many-Body Systems* (2007).

[5] E. Fradkin. *Field Theories of Condensed Matter Physics* (2013).

[6] F. Becca and S. Sorella. *Quantum Monte Carlo Approaches for Correlated Systems* (2017).

[7] L. Savary and L. Balents. *Quantum spin liquids: a review*. Rep. Prog. Phys. **80**, 016502 (2016).

[8] R. B. Laughlin. *Anomalous Quantum Hall Effect: An Incompressible Quantum Fluid with Fractionally Charged Excitations*. Phys. Rev. Lett. **50**, 1395–1398 (1983).

[9] V. Kalmeyer and R. B. Laughlin. *Equivalence of the resonating-valence-bond and fractional quantum Hall states*. Phys. Rev. Lett. **59**, 2095–2098 (1987).

[10] D. C. Tsui, H. L. Stormer, and A. C. Gossard. *Two-Dimensional Magnetotransport in the Extreme Quantum Limit*. Phys. Rev. Lett. **48**, 1559–1562 (1982).

[11] P. Anderson. *Resonating valence bonds: A new kind of insulator?* Mater. Res. Bull. **8**, 153–160 (1973).

[12] J. G. Bednorz and K. A. Müller. *Possible high T_c superconductivity in the Ba-La-Cu-O system*. Z. für Phys. B Condens. Matter **64**, 189–193 (1986).

[13] P. W. Anderson. *The Resonating Valence Bond State in La2CuO4 and Superconductivity*. Science **235**, 1196–1198 (1987).

[14] G. Baskaran, Z. Zou, and P. Anderson. *The resonating valence bond state and high-Tc superconductivity - A mean field theory*. Solid State Commun. **63**, 973–976 (1987).

[15] P. A. Lee. *An End to the Drought of Quantum Spin Liquids*. Science **321**, 1306–1307 (2008).

[16] L. Balents. *Spin liquids in frustrated magnets*. Nature **464**, 199–208 (2010).

[17] N. Schuch, I. Cirac, and D. Pérez-García. *PEPS as ground states: Degeneracy and topology*. Ann. Phys. **325**, 2153–2192 (2010).

[18] Y. Iqbal, F. Becca, and D. Poilblanc. *Projected wave function study ofZ2spin liquids on the kagome lattice for the spin-12quantum Heisenberg antiferromagnet*. Phys. Rev. B **84**, 020407 (2011).

[19] W.-J. Hu, F. Becca, A. Parola, and S. Sorella. *Direct evidence for a gapless Z2 spin liquid by frustrating Néel antiferromagnetism*. Phys. Rev. B **88**, 060402 (2013).

[20] Y. Iqbal, D. Poilblanc, and F. Becca. *Spin-1/2 Heisenberg $J_1 - J_2$ antiferromagnet on the kagome lattice*. Phys. Rev. B **91**, 020402 (2015).

[21] Y. Iqbal, W.-J. Hu, R. Thomale, D. Poilblanc, and F. Becca. *Spin liquid nature in the Heisenberg $J_1 - J_2$ triangular antiferromagnet*. Phys. Rev. B **93**, 144411 (2016).

[22] M. Greiter. *Mapping of Parent Hamiltonians*. Springer Tract Mod. Phys. (2011).

[23] F. D. M. Haldane. *Fractional Quantization of the Hall Effect: A Hierarchy of Incompressible Quantum Fluid States*. Phys. Rev. Lett. **51**, 605–608 (1983).

[24] E. Kapit and E. Mueller. *Exact Parent Hamiltonian for the Quantum Hall States in a lattice*. Phys. Rev. Lett. **105**, 215303 (2010).

[25] T. Grover, Y. Zhang, and A. Vishwanath. *Entanglement entropy as a portal to the physics of quantum spin liquids*. New J. Phys. **15**, 025002 (2013).

[26] I. Affleck, T. Kennedy, E. H. Lieb, and H. Tasaki. *Rigorous results on valence-bond ground states in antiferromagnets*. Phys. Rev. Lett. **59**, 799–802 (1987).

[27] F. D. M. Haldane, Z. N. C. Ha, J. C. Talstra, D. Bernard, and V. Pasquier. *Yangian symmetry of integrable quantum chains with long-range interactions and a new description of states in conformal field theory*. Phys. Rev. Lett. **69**, 2021–2025 (1992).

[28] F. D. M. Haldane. *Exact Jastrow-Gutzwiller resonating-valence-bond ground state of the spin-(1/2 antiferromagnetic Heisenberg chain with 1/r2exchange*. Phys. Rev. Lett. **60**, 635–638 (1988).

[29] B. S. Shastry. *Exact solution of anS=1/2 Heisenberg antiferromagnetic chain with long-ranged interactions*. Phys. Rev. Lett. **60**, 639–642 (1988).

[30] G. Moore and N. Read. *Nonabelions in the fractional quantum hall effect*. Nucl. Phys. B **360**, 362–396 (1991).

[31] D. F. Schroeter, E. Kapit, R. Thomale, and M. Greiter. *Spin Hamiltonian for which the Chiral Spin Liquid is the Exact Ground State*. Phys. Rev. Lett. **99**, 097202 (2007).

[32] R. Thomale, E. Kapit, D. F. Schroeter, and M. Greiter. *Parent Hamiltonian for the chiral spin liquid*. Phys. Rev. B **80**, 104406 (2009).

[33] R. Thomale, S. Rachel, P. Schmitteckert, and M. Greiter. *Family of spin-Schain representations of SU(2)kWess-Zumino-Witten models*. Phys. Rev. B **85**, 195149 (2012).

[34] H.-H. Tu, A. E. B. Nielsen, J. I. Cirac, and G. Sierra. *Lattice Laughlin states of bosons and fermions at filling fractions 1/q*. New J. Phys. **16**, 033025 (2014).

[35] M. Greiter, D. F. Schroeter, and R. Thomale. *Parent Hamiltonian for the non-Abelian chiral spin liquid*. Phys. Rev. B **89**, 165125 (2014).

[36] M. A. Nielsen and I. L. Chuang. *Quantum Computation and Quantum Information* (2009).

[37] A. E. B. Nielsen, G. Sierra, and J. I. Cirac. *Local models of fractional quantum Hall states in lattices and physical implementation*. Nat. Commun. **4**, 2864 (2013).

[38] A. E. B. Nielsen. *Anyon braiding in semianalytical fractional quantum Hall lattice models*. Phys. Rev. B **91**, 041106 (2015).

[39] I. Buluta, S. Ashhab, and F. Nori. *Natural and artificial atoms for quantum computation*. Rep. Prog. Phys. **74**, 104401 (2011).

[40] I. Bloch, J. Dalibard, and S. Nascimbène. *Quantum simulations with ultracold quantum gases*. Nat. Phys. **8**, 267–276 (2012).

[41] J. I. Cirac and P. Zoller. *Goals and opportunities in quantum simulation*. Nat. Phys. **8**, 264–266 (2012).

[42] R. Blatt and C. F. Roos. *Quantum simulations with trapped ions*. Nat. Phys. **8**, 277–284 (2012).

[43] I. M. Georgescu, S. Ashhab, and F. Nori. *Quantum simulation*. Rev. Mod. Phys. **86**, 153–185 (2014).

[44] X.-L. Qi and D. Ranard. *Determining a local Hamiltonian from a single eigenstate*. Quantum **3**, 159 (2019).

[45] E. Chertkov and B. K. Clark. *Computational Inverse Method for Constructing Spaces of Quantum Models from Wave Functions*. Phys. Rev. X **8**, 031029 (2018).

[46] E. Bairey, I. Arad, and N. H. Lindner. *Learning a Local Hamiltonian from Local Measurements*. Phys. Rev. Lett. **122**, 020504 (2019).

[47] E. Bairey, C. Guo, D. Poletti, N. H. Lindner, and I. Arad. *Learning the dynamics of open quantum systems from their steady states*. New J. Phys. **22**, 032001 (2020).

[48] M. Dupont and N. Laflorencie. *Many-body localization as a large family of localized ground states*. Phys. Rev. B **99**, 020202 (2019).

[49] M. Greiter, V. Schnells, and R. Thomale. *Method to identify parent Hamiltonians for trial states*. Phys. Rev. B **98**, 081113 (2018).

[50] K. Pakrouski. *Automatic design of Hamiltonians*. Quantum **4**, 315 (2020).

[51] J. R. Garrison and T. Grover. *Does a Single Eigenstate Encode the Full Hamiltonian?* Phys. Rev. X **8**, 021026 (2018).

[52] J. J. Bisognano and E. H. Wichmann. *On the duality condition for a Hermitian scalar field*. J. Math. Phys. **16**, 985–1007 (1975).

[53] J. J. Bisognano. *On the duality condition for quantum fields*. J. Math. Phys. **17**, 303 (1976).

[54] R. Haag. *Local Quantum Physics* (1996).

[55] E. Witten. *APS Medal for Exceptional Achievement in Research: Invited article on entanglement properties of quantum field theory*. Rev. Mod. Phys. **90**, 045003 (2018).

[56] M. Dalmonte, B. Vermersch, and P. Zoller. *Quantum simulation and spectroscopy of entanglement Hamiltonians*. Nat. Phys. **14**, 827–831 (2018).

[57] G. Giudici, T. Mendes-Santos, P. Calabrese, and M. Dalmonte. *Entanglement Hamiltonians of lattice models via the Bisognano-Wichmann theorem*. Phys. Rev. B **98**, 134403 (2018).

[58] V. Vedral. *The role of relative entropy in quantum information theory*. Rev. Mod. Phys. **74**, 197–234 (2002).

[59] H. J. Kappen. *Learning quantum models from quantum or classical data*. 1803.11278 (2020).

[60] S. R. White. *Density matrix formulation for quantum renormalization groups*. Phys. Rev. Lett. **69**, 2863–2866 (1992).

[61] A. E. Feiguin and S. R. White. *Finite-temperature density matrix renormalization using an enlarged Hilbert space*. Phys. Rev. B **72**, 220401 (2005).

[62] R. K. Kaul, R. G. Melko, and A. W. Sandvik. *Bridging Lattice-Scale Physics and Continuum Field Theory with Quantum Monte Carlo Simulations*. Annu. Rev. Condens. Matter Phys. **4**, 179–215 (2013).

[63] B. Swingle and T. Senthil. *Geometric proof of the equality between entanglement and edge spectra*. Phys. Rev. B **86**, 045117 (2012).

[64] J. Cardy and E. Tonni. *Entanglement Hamiltonians in two-dimensional conformal field theory*. J. Stat. Mech. Theory Exp. **2016**, 123103 (2016).

[65] X. Wen, S. Ryu, and A. W. W. Ludwig. *Evolution operators in conformal field theories and conformal mappings: Entanglement Hamiltonian, the sine-square deformation, and others*. Phys. Rev. B **93**, 235119 (2016).

[66] M. Pretko and T. Senthil. *Entanglement entropy ofU(1) quantum spin liquids*. Phys. Rev. B **94**, 125112 (2016).

[67] M. Pretko. *Nodal-line entanglement entropy: Generalized Widom formula from entanglement Hamiltonians*. Phys. Rev. B **95**, 235111 (2017).

[68] H. Casini, E. Testé, and G. Torroba. *Markov Property of the Conformal Field Theory Vacuum and the a Theorem*. Phys. Rev. Lett. **118**, 261602 (2017).

[69] T. Hartman, S. Kundu, and A. Tajdini. *Averaged null energy condition from causality*. J. High Energy Phys. **2017**, 66 (2017).

[70] I. Klich, D. Vaman, and G. Wong. *Entanglement Hamiltonians for Chiral Fermions with Zero Modes*. Phys. Rev. Lett. **119**, 120401 (2017).

[71] H. Casini, M. Huerta, and R. C. Myers. *Towards a derivation of holographic entanglement entropy*. J. High Energy Phys. **2011**, 36 (2011).

[72] H. Casini, M. Huerta, and J. A. Rosabal. *Remarks on entanglement entropy for gauge fields*. Phys. Rev. D **89**, 085012 (2014).

[73] I. Peschel and V. Eisler. *Reduced density matrices and entanglement entropy in free lattice models*. J. Phys. Math. Theor. **42**, 504003 (2009).

[74] P. Kim, H. Katsura, N. Trivedi, and J. H. Han. *Entanglement and corner Hamiltonian spectra of integrable open spin chains*. Phys. Rev. B **94**, 195110 (2016).

[75] V. Eisler and I. Peschel. *Analytical results for the entanglement Hamiltonian of a free-fermion chain*. J. Phys. Math. Theor. **50**, 284003 (2017).

[76] T. Mendes-Santos, G. Giudici, M. Dalmonte, and M. A. Rajabpour. *Entanglement Hamiltonian of quantum critical chains and conformal field theories*. Phys. Rev. B **100**, 155122 (2019).

[77] V. Eisler, E. Tonni, and I. Peschel. *On the continuum limit of the entanglement Hamiltonian*. J. Stat. Mech. Theory Exp. **2019**, 073101 (2019).

[78] H. Itoyama and H. B. Thacker. *Lattice Virasoro algebra and corner transfer matrices in the Baxter eight-vertex model*. Phys. Rev. Lett. **58**, 1395–1398 (1987).

[79] R. J. Baxter. *Exactly Solved Models in Statistical Mechanics*. Integrable Syst. Stat. Mech. , 5–63 (1985).

[80] N. Laflorencie and S. Rachel. *Spin-resolved entanglement spectroscopy of critical spin chains and Luttinger liquids*. J. Stat. Mech. Theory Exp. **2014**, P11013 (2014).

[81] L. Wang, K. S. D. Beach, and A. W. Sandvik. *High-precision finite-size scaling analysis of the quantum-critical point of S=1/2 Heisenberg antiferromagnetic bilayers*. Phys. Rev. B **73**, 014431 (2006).

[82] A. Sen, H. Suwa, and A. W. Sandvik. *Velocity of excitations in ordered, disordered, and critical antiferromagnets*. Phys. Rev. B **92**, 195145 (2015).

[83] O. Narayan and B. S. Shastry. *The 2D Coulomb gas on a 1D lattice*. J. Phys. Math. Gen. **32**, 1131–1146 (1999).

[84] B. Herwerth, G. Sierra, J. I. Cirac, and A. E. B. Nielsen. *Bosonic Gaussian states from conformal field theory*. Phys. Rev. B **98**, 115156 (2018).

[85] J.-M. Stephan, S. Furukawa, G. Misguich, and V. Pasquier. *Shannon and entanglement entropies of one- and two-dimensional critical wave functions*. Phys. Rev. B **80**, 184421 (2009).

[86] J.-M. Stephan, G. Misguich, and V. Pasquier. *Phase transition in the Rényi-Shannon entropy of Luttinger liquids*. Phys. Rev. B **84**, 195128 (2011).

[87] D. J. Luitz, F. Alet, and N. Laflorencie. *Universal Behavior beyond Multifractality in Quantum Many-Body Systems*. Phys. Rev. Lett. **112**, 057203 (2014).

[88] D. J. Luitz, N. Laflorencie, and F. Alet. *Participation spectroscopy and entanglement Hamiltonian of quantum spin models*. J. Stat. Mech. Theory Exp. **2014**, P08007 (2014).

[89] M. Capello, F. Becca, S. Yunoki, and S. Sorella. *Unconventional metal-insulator transition in two dimensions*. Phys. Rev. B **73**, 245116 (2006).

[90] T. Giamarchi. *Quantum Physics in One Dimension* (2003).

[91] J. I. Cirac and G. Sierra. *Infinite matrix product states, conformal field theory, and the Haldane-Shastry model*. Phys. Rev. B **81**, 104431 (2010).

[92] R. Kobayashi, Y. O. Nakagawa, Y. Fukusumi, and M. Oshikawa. *Scaling of the polarization amplitude in quantum many-body systems in one dimension*. Phys. Rev. B **97**, 165133 (2018).

[93] N. Laflorencie. *Quantum entanglement in condensed matter systems*. Phys. Rep. **646**, 1–59 (2016).

Chapter 2

Negativity Spectrum and Entanglement equipartition in Disordered Critical Spin Chains

This chapter is based on the following publications:

[1] Xhek Turkeshi, Paola Ruggiero, and Pasquale Calabrese,
Negativity Spectrum in the Random Singlet Phase,
Phys. Rev. B **101**, 064207 (2020)

[2] Xhek Turkeshi, Paola Ruggiero, Vincenzo Alba, and Pasquale Calabrese,
Entanglement equipartition in critical random spin chains,
Phys. Rev. B **102**, 014455 (2020)

2.1 Introduction

Entanglement plays a fundamental role in characterizing quantum phases of matter [3–6]. For isolated many-body systems at zero temperature, key results have been derived for the entanglement entropy [7–10] and the entanglement spectrum [11–13]. For example, the entanglement entropy of gapped one dimensional systems with local interactions follows an area law, whereas gapless systems present a logarithmic scaling in subsystem size with a universal prefactor related to the central charge of the underlying conformal field theory (CFT).

Entanglement properties have been intensively investigated also in quantum systems with quenched disorder. When considering quenched disorder, static and dynamic properties of a system drastically change compared to the clean case. In fact, randomness usually plays a relevant role in the renormalization group sense. Remarkable examples are Anderson and many-body localization [14–17]. Other well studied systems include a class of quantum spin chains where disorder induces a novel quantum critical phase [18–23]. This phase is characterized by the formation of spin singlets spreading over arbitrarily large distances, and for this reason, it is dubbed random singlet phase (RSP). Its features can be analytically accessed by the strong disorder renormalization group (SDRG) technique [22, 23]. When the low-energy physics of these models is captured by an infinite disorder fixed point, these systems display a logarithmic entanglement entropy scaling which resembles that of a CFT [24–32], although this analogy breaks down in many respects, such as a different scaling of entanglement in other circumstances [33–36] and the absence of a c-theorem [37, 38].

In this Chapter we discuss other information measures in critical systems with quenched disorder. Specifically, we consider the negativity spectrum, an information quantifier for mixed state (see below for details), which extends the entanglement negativity in the same fashion the entanglement spectrum extends the von-Neumann entropy, and the symmetry resolved entanglement entropy, that is the entanglement entropy of each symmetry sector when an additive charge is present. This Chapter is organized as follows. In this Section, we give an overview of key definition and results concerning entanglement in clean and disordered systems. In Sec. 2.2 we given an overview on the physical systems of interest, the random singlet phase, which we derive from the strong disorder renormalization group, starting form the prototypical disordered Heisenberg model. The negativity spectrum is resolved, in the scaling limit, in Sec. 2.3. Our results are tested against numerical simulations, both *ab initio* and through numerical renormalization. The symmetry resolved entanglement entropy is instead presented in Sec. 2.4. As the role of disorder is more subtle for the symmetry resolved quantities, we have considered three different proxies of the statistical

properties of the system, and prove they fulfill entanglement equipartition. Our conclusion are summarized in Sec. 2.5, where we also present some outlooks. In the Appendix 2.6 we give additional details for the negativity spectrum: we give some numerical evidence of the universality of the SDRG, and we present the fermionic negativity spectrum. In Appendix 2.7 we detail the main computation for the analytical results for the symmetry resolved entanglement entropy.

2.1.1 Entanglement entropy and entanglement spectrum

By partitioning a system into two parts $A \cup B$, the bipartite entanglement of a pure state $|\Psi\rangle$ is fully encoded in its reduced density matrix $\rho_A = \mathrm{tr}_B\left(|\Psi\rangle\langle\Psi|\right)$. The spectrum of ρ_A, known as entanglement spectrum, has been proven of fundamental value in a variety of frameworks, including topological properties of quantum matter [11, 39–48], symmetry-broken phases [49–53] and many-body localization [54–56]. For one-dimensional critical systems with an underlying conformal invariance, the distribution of eigenvalues of ρ_A obeys a universal scaling law, depending only on the central charge [12, 13, 57–60]. This distribution is of high importance to understand the effectiveness of some tensor network algorithms [61–63]. The entanglement spectrum can be accessed by studying the scaling of the Rényi entropies [12, 64], which correspond to the momentum of the eigenvalue distribution of ρ_A:

$$S_m(\rho_A) = \frac{1}{1-m} \ln \mathrm{tr}_A\left(\rho_A^m\right), \tag{2.1}$$

that for $m \to 1$ provide the renowned von Neumann (entanglement) entropy

$$S(\rho_A) \equiv \lim_{m\to 1} S_m(\rho_A) = -\mathrm{tr}_A\left(\rho_A \log \rho_A\right). \tag{2.2}$$

For one-dimensional quantum systems in the scaling limit, the above can be computed using the replica trick [4, 9]. In 1+1d CFT (with central charge c), explicit results can be obtained in many different situations. When A is a finite interval of length ℓ embedded in an infinite line, one has the well known formula [7–10]

$$S_m^{\mathrm{CFT}}(\rho_A) = \frac{c}{6}\frac{m+1}{m} \ln \ell + O(\ell^0), \tag{2.3}$$

The subleading terms are in general non-universal. Using conformal transformations, Eq. (2.3) can be generalized to finite systems [9], finite temperature [9], and quench dynamics as well [65].

2.1.2 Negativity and negativity spectrum

The situation is more complicated when considering a bipartition of a system in a mixed state. Here the Rényi entropies Eq. (2.1) do not distinguish between classical and quantum correlations, and thus, they fail to characterize entanglement. The same issue arises when considering the mutual entanglement between subregions of a multipartite pure state. For concreteness, let us consider a tripartition $A_1 \cup A_2 \cup B$ of a pure state $|\Psi\rangle \in \mathcal{H} = \mathcal{H}_{A_1} \otimes \mathcal{H}_{A_2} \otimes \mathcal{H}_B$. Tracing out B, we obtain the reduced density matrix ρ_A describing the subsystem $A = A_1 \cup A_2$. The quantum correlations between A_1 and A_2 are encoded in the partially transposed reduced density matrix [66–72] $\rho_A^{T_2}$ and in its negative eigenvalues. The definition of $\rho_A^{T_2}$ is $\langle uv|\rho_A^{T_2}|u'v'\rangle \equiv \langle uv'|\rho_A|u'v\rangle$, with $\{u\}$ and $\{v\}$ being local bases of respectively $\mathcal{H}_{A_1}$ and $\mathcal{H}_{A_2}$. From $\rho_A^{T_2}$ one can extract measures of mutual entanglement such as the entanglement negativity $\mathcal{N}$ and the logarithmic negativity $\mathcal{E}$ [73–76]

$$\mathcal{N} = \frac{\left|\left|\rho_A^{T_2}\right|\right| - 1}{2}, \quad \mathcal{E} = \log\left|\left|\rho_A^{T_2}\right|\right|, \tag{2.4}$$

where $\left|\left|\rho\right|\right| = \mathrm{tr}\sqrt{\rho\rho^\dagger}$ is the trace norm. For any given state, clearly $\mathcal{E} = \log(2\mathcal{N}+1)$. The (logarithmic) negativity has been studied in several contexts, ranging from harmonic chains and lattices [77–86] to quantum spin models [87–98], from conformal and integrable field theories [99–108] to non-equilibrium situations [103, 109–114] and intrinsic and symmetry-protected topological orders [115–121, 121–123].

For fermionic models, it has been shown that a similar operation known as partial time-reversal transpose is a more appropriate object to characterise the entanglement in mixed states [122–131]. Finally, also experimental proposals for the measurement of negativity have recently appeared [132, 133].

It is not a surprise that the spectral density of $\rho_A^{T_2}$ contains more information about the entanglement between A_1 and A_2 than the negativities in Eq. (2.4). Such spectral density is usually referred to as *negativity spectrum* [134] and is fully characterized through the moments

$$M_\alpha^{T_2} = \mathrm{tr}\left(\rho_A^{T_2}\right)^\alpha. \tag{2.5}$$

In the following we will refer to $M_\alpha^{T_2}$ as *negativity moments*. Notice that the trace norm in Eq. (2.4) may be obtained as the replica limit [99, 100] $\left|\left|\rho_A^{T_2}\right|\right| = \lim_{\alpha\to 1/2} M_{2\alpha}^{T_2}$.

The negativity spectrum has been investigated in clean systems in Ref. [134–136]. In Sec. 2.3 we extend these consideration to the disordered case, by focusing on the random singlet phase. In the spirit of Ref. [34] we use renewal equations to find analytic formulae for the negativity moments. In particular, we work out analytic results for the the case of adjacent intervals which we test against a numerical implementation of the SDRG for the XXX model and against *ab-initio* simulations for the random XX spin-chain. Among the other results, we find that the logarithm and the average disorder do not commute, in the sense that $\overline{\log M_{2\alpha}^{T_2}} \neq \log \overline{M_{2\alpha}^{T_2}}$ even in the limit $\alpha \to 1/2$. A maybe surprising consequence is that the negativity and its logarithmic analogue are not trivially related after disorder average in the RSP. This is in contrast with the case of the entanglement entropy, where the logarithm and the disorder average commute in the replica limit $\alpha \to 1$ [34].

2.1.3 Symmetry resolved entanglement entropy

For a system with additive conservation laws, it is possible to probe different contributions to the entanglement, directly related to the entanglement within different symmetry sectors [137] (see below for details).

Consider a system possessing a global *additive* conserved charge Q. For instance, this symmetry could be abelian such as the total magnetization in spin systems. The reduced density matrix of a subsystem can be decomposed into a direct sum of orthogonal sectors. To be specific, let us consider a bipartition of the system as $A \cup B$ and a state ρ in a given representation of Q. The additivity of Q implies that $Q = Q_A \otimes \mathbf{1}_B + \mathbf{1}_A \otimes Q_B$ and can be used to show that

$$[\rho_A, Q_A] = 0. \tag{2.6}$$

Thus the reduced density matrix is block diagonal in the quantum numbers of Q_A. Denoting with Π_q the projector into the subspace relative to the eigenvalue q, we have

$$\rho_A = \oplus_q \left(\Pi_q \rho_A \Pi_q\right) = \oplus_q p_A(q)\rho_A(q). \tag{2.7}$$

In the last equality we factorized the term $p_A(q) = \mathrm{tr}_A(\Pi_q \rho_A)$, and defined

$$\rho_A(q) \equiv \frac{\Pi_q \rho_A \Pi_q}{p_A(q)}, \quad \mathrm{tr}(\rho_A(q)) = 1. \tag{2.8}$$

Here $p_A(q)$ is the probability for the subsystem to be in a specific symmetry sector. In fact, only the global state possesses a definite charge, while the subsystem fluctuates between the Q_A-sectors due to quantum effects.

The total von Neumann entanglement entropy of the system naturally splits in two parts

$$S(\rho_A) = S^{\mathrm{Q}} + S^{\mathrm{conf}}, \tag{2.9}$$

with

$$S^{\mathrm{Q}} = -\sum_q p_A(q)\log p_A(q), \tag{2.10}$$

$$S^{\mathrm{conf}} = \sum_q p_A(q) S(q), \tag{2.11}$$

Here $S(q) \equiv -\mathrm{Tr}\rho_A(q)\ln\rho_A(q)$ defines the symmetry-resolved entanglement entropy, meaning the contribution to the entanglement entropy of the q-sector. S^{Q} is known as the number (or fluctuation) entropy, since it is related to the number of excitations carrying a quantum of symmetry charge, which fluctuates in a subsystem. Despite its classical Shannon form, it originates from tunneling effects [137]. We mention here that the link between entanglement and subsystem's fluctuations (for instance, of spin or particle number in lattice models with a $U(1)$ current) has been widely studied [138–151]. S^{conf} is named configurational entropy, as it depends on the many-body coherence pattern of the subsystem configurations in a given symmetry sector.

Similarly, one can define the symmetry-resolved Rényi entropies, $S_m(q)$. First, we introduce the symmetry-resolved moments:

$$Z_m(q) \equiv p^m(q)\mathrm{Tr}(\rho_A^m(q)). \tag{2.12}$$

Note that $Z_1(q) = p_A(q)$. Then, we have

$$S_m(q) = \frac{1}{1-m}\log\left(\frac{Z_m(q)}{Z_1^m(q)}\right). \tag{2.13}$$

They are related to $S(q)$ by the usual limit $m \to 1$.

Such symmetry resolution is natural in computational methods like exact diagonalization and tensor network, and has been discussed in earlier papers [57, 152]. In particular, the authors of Ref. [152] suggested, using a quantum-thermal correspondence argument, that the entanglement entropy in Luttinger liquids is the same for all symmetry sectors. Lately, this conjecture has been dubbed *entanglement equipartition* and it has has been proven for conformal [153] and integrable systems [154]. Computing $Z_m(q)$ is in general a non-trivial task. A fundamental observation for its derivation is that $Z_m(q)$ is the Fourier transform of the charged moment $\mathcal{Z}_m(\alpha) = \mathrm{tr}_A\left(\rho_A^m e^{iQ_A\alpha}\right)$ [155], i.e.,

$$\mathcal{Z}_m(\alpha) = \sum_q e^{iq\alpha} Z_m(q), \quad Z_m(q) = \int_{-\pi}^{\pi}\frac{d\alpha}{2\pi}\mathcal{Z}_m(\alpha). \tag{2.14}$$

In some setting, the calculation of $\mathcal{Z}_m(\alpha)$ can be easily performed and then, by Fourier transform, symmetry-resolved Rényi entropies are obtained. This is the case for example for 1+1d CFTs, where the charged moments are easily expressed in path integral language [155]. For Luttinger liquids, a particular class of CFTs with central charge $c = 1$ and characterized by a parameter K (Luttinger parameter), one finds

$$Z_m(q) \simeq \ell^{-\frac{1}{6}(m-\frac{1}{m})}\sqrt{\frac{n\pi}{2K\ln\ell}}e^{-\frac{n\pi^2 q^2}{2K\ln\ell}}, \tag{2.15}$$

leading to

$$S_m(q) = S_m^{\mathrm{CFT}} - \frac{1}{2}\ln(K\ln\ell) + O(\ell^0). \tag{2.16}$$

Here S_m^{CFT} is given by (2.3). Eq. (2.16) shows that the entanglement entropies of the different symmetry sectors are the same at leading orders in the subsystem size ℓ, i.e., Luttinger liquids exhibit entanglement equipartition. Corrections to this scaling are in general non-universal and model dependent [154, 156, 157].

The symmetry resolution of entanglement has been copiously discussed in several context for clean systems [57, 152–154, 154–156, 156–168]. In Sec. 2.4 we study the symmetry resolved entanglement for the random singlet phase, and prove that an entanglement equipartition theorem holds.

2.2 Strong Disorder Renormalization Group and the Random Singlet Phase

In this Section we discuss the strong disorder renormalization group and the key characterizations of the random singlet phase. For concreteness, we consider the antiferromagnetic disordered Heisenberg spin chain (Sec. 2.2.1) as a representative model for the phase, and discuss how through real-space renormalization we can access the random singlet phase (Sec. 2.2.2). In particular, we discuss the structure of the density matrix (Sec. 2.2.3), which factorizes in a product of arbitrary distant singlets. The scaling of the number of shared singlets between two partitions, which governs the entanglement properties of the phase, is detailed in Sec.2.2.4.

2.2.1 Antiferromagnetic Heisenberg spin chain

The spin-$1/2$ antiferromagnetic Heisenberg chain is defined by the Hamiltonian

$$H_L = \sum_{i=1}^{L} J_i (S_i^x S_{i+1}^x + S_i^y S_{i+1}^y + \Delta S_i^z S_{i+1}^z), \tag{2.17}$$

where Δ is the anisotropy parameter, and $S_i^{x,y,z}$ are spin-$1/2$ operators. Here J_i are positive random couplings distributed according to a given distribution $P(J)$. In the absence of disorder, i.e., $P(J) \sim \delta(J - J_0)$ for some fixed value J_0, the ground state of the model is in a Luttinger liquid phase at any $-1 < \Delta \leq 1$. Thus, the scaling of the ground-state entanglement entropy is described by the CFT formula Eq. (2.3) with $c = 1$. In the presence of random antiferromagnetic couplings J_i, the ground state of the system is described by an Infinite-Randomness Fixed Point (IRFP), irrespective of the initial distribution $P(J)$ and, therefore, of the initial disorder strength [169]. More generally, all the long-wavelength properties of the disordered Heisenberg chain are expected to be universal. The ground state of Eq. (2.17) is in the random singlet phase (RSP), which is the simplest example of IRFP. The structure of the RSP can be understood by using the SDRG method.

2.2.2 Strong-Disorder RG and random singlet phase

For disordered spin systems, the usual space-block decimation [170] fails due to the inhomogeneity in the Hamiltonian (see *e.g.* Eq.(2.17)) within a single disorder realization. A better rationale is instead to decimate through an energetic principle, where, at each renormalization step, the sites connected by the strongest coupling are projected onto their local ground state, i.e., the singlet state. These are effectively decoupled by the rest of the system, while the edge sites are connected by a renormalized coupling.

We illustrate this decimation procedure, which allows us to obtain the low-energy description of our model. We start by considering a 4-sites isotropic Heisenberg Hamiltonian (cf. (2.17), with $\Delta = 1$). We split H as

$$H \equiv H_2^{(0)} + H_2^{(1)}, \tag{2.18}$$

$$H_2^{(0)} = \Omega \vec{S}_2 \vec{S}_3, \tag{2.19}$$

$$H_2^{(1)} = J_L \vec{S}_1 \vec{S}_2 + J_R \vec{S}_3 \vec{S}_4. \tag{2.20}$$

Here we assume that $\Omega > J_L, J_R$ is the strongest coupling. Then we can treat the Hamiltonian $H_2^{(1)}$ as a perturbation to $H_2^{(0)}$. The spins in sites $(2, 3)$ bond forming a singlet (the local ground state)

$$|s\rangle = \frac{|\uparrow\downarrow\rangle - |\downarrow\uparrow\rangle}{\sqrt{2}}. \tag{2.21}$$

This also provides an effective coupling for spins $(1,4)$. Indeed, using second order perturbation theory we obtain an effective Hamiltonian H_2^{eff} for spins $(1,4)$

$$H_2^{\text{eff}} = \langle s|H_2^{(0)} + H_2^{(1)}|s\rangle + \sum_t \frac{|\langle t|H_2^{(1)}|s\rangle|^2}{E_s - E_t} \tag{2.22}$$

$$= E_0 + \tilde{J}\vec{S}_1\vec{S}_4, \qquad \tilde{J} = \eta\frac{J_L J_R}{\Omega}, \tag{2.23}$$

where the sum is over the triplet states of two spins, $|t\rangle = |\uparrow\uparrow\rangle, |\downarrow\downarrow\rangle, (|\uparrow\downarrow\rangle + |\downarrow\uparrow\rangle)/\sqrt{2}$, and $E_t = \Omega/4$, $E_s = -3\Omega/4$. E_0 is an unimportant energy constant, and $\eta = 1$ for $\Delta = 0$, whereas $\eta = 1/2$ for $0 < \Delta \leq 1$. Note that H_2^{eff} in (2.23) is still Heisenberg-like, so that the previous steps translate in an effective renormalization of the couplings.

The procedure can then be easily generalized to a many-body hamiltonian with L spins such as Eq. (2.17). At each renormalization step, the pair interacting through the strongest coupling $\Omega = \max\{J_i\}$ forms a singlet which is decimated, and the set of couplings changes according to

$$(\dots, J_L, \Omega, J_R, \dots)_L \to \left(\dots, \eta\frac{J_L J_R}{\Omega}, \dots\right)_{L-2}. \tag{2.24}$$

This is known as Ma-Dasgupta rule [18, 19]. In Eq. (2.24) we specified that the chain length reduced from L to $L-2$ in one renormalization step. Therefore, for a finite chain, the RG terminates when all sites are decimated. The resulting state, known as random singlet phase (RSP),, is a product of singlets ranging arbitrary far in the system and approximates the ground state of the system. Its structure is the same irrespective of the chain anisotropy Δ, i.e., chains with different Δ belong to the same universality class. In the scaling limit $L \to \infty$, the SDRG procedure is asymptotically exact and a flow equation emerges. For convenience, we introduce the variables

$$\beta_i^m = \log\frac{\Omega^{(m)}}{J_i^{(m)}}, \quad \Gamma^{(m)} = -\log\Omega^{(m)}. \tag{2.25}$$

Here $\Omega^{(m)}$ and $J_i^{(m)}$ are respectively the strongest bond and the couplings at site i at renormalization step m. Intuitively, Γ set the energy scale of the strongest coupling at a successive step, while β is a measure of the broadness of the coupling distribution around it.

The Ma-Dasgupta rule (2.24) rewritten in terms of the β variables is $\tilde{\beta} = \beta_{\text{L}} + \beta_{\text{R}} + \log\eta$. It induces a flow for the probability distribution of the couplings $P(\beta,\Gamma)$

$$\frac{d}{d\Gamma}P(\beta,\Gamma) = \frac{\partial}{\partial\beta}P(\beta,\Gamma) + P(0,\Gamma)\int_0^\infty d\beta_2\int_0^\infty d\beta_1\delta(\beta_1+\beta_2+\log\eta-\beta)P(\beta_1,\Gamma)P(\beta_2,\Gamma). \tag{2.26}$$

Iterating the renormalization procedure, β grows indefinitely and it is safe to drop out the factor $\log\eta$ in the above equation. Within this assumption, Eq. (2.26) can be solved analytically [20], leading to

$$P_\star(\beta,\Gamma) = \frac{e^{-\beta/\Gamma}}{\Gamma}. \tag{2.27}$$

This function is a *universal attractor*, irrespective of the distribution of the couplings [20, 21, 30]. Moreover, variables distributed according to Eq. (2.27) are closely packed around $J_\star \simeq 0^+$, and this *a posteriori* justifies the perturbative treatment. To conclude, we note that Eq. (2.27) is independent from η in Eq. (2.24), hence the phase is the same for $\Delta > 0$ (interacting many-body system) and $\Delta = 0$, which is a quadratic system and can be exactly diagonalized within polynomial times.

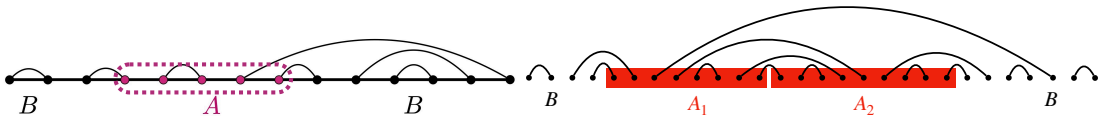

FIGURE 2.1: Pictorial illustration of the Random Single Phase (RSP). The links connect the spins forming a singlet. (Left) We show the bipartition $A \cup B$. The entanglement entropy S is proportional to the number of singlets shared between A and B. (Right) Cartoon of the random singlet phase in a tripartite setting $A_1 \cup A_2 \cup B$. The special case of two adjacent intervals (in red) embedded in a larger system is depicted.

2.2.3 Structure of the reduced density matrix and its partial transpose

The RSP emerges naturally as an infinite disorder critical point, and it is characterized by singlets spreading among arbitrary far regions of the system (see Fig. 2.1). Below we introduce the elementary building blocks of the associated density matrix and its partially transpose. They are (i) the density matrix of a singlet, $\rho_{2\mathrm{s}}$, (ii) its reduced density matrix for one of the spins, ρ_{s}, (iii) the partial transpose of $\rho_{2\mathrm{s}}$ with respect to one of the sites, $\rho_{2\mathrm{s}}^{T_2}$. In the basis $|\uparrow\uparrow\rangle$, $|\uparrow\downarrow\rangle$, $|\downarrow\uparrow\rangle$, and $|\downarrow\downarrow\rangle$, the above objects read

$$\rho_{2\mathrm{s}} = \frac{1}{2}\begin{pmatrix} 0 & 0 & 0 & 0 \\ 0 & 1 & -1 & 0 \\ 0 & -1 & 1 & 0 \\ 0 & 0 & 0 & 0 \end{pmatrix}, \qquad \rho_{\mathrm{s}} = \frac{1}{2}\begin{pmatrix} 1 & 0 \\ 0 & 1 \end{pmatrix}, \qquad \rho_{2\mathrm{s}}^{T_2} = \frac{1}{2}\begin{pmatrix} 0 & 0 & 0 & -1 \\ 0 & 1 & 0 & 0 \\ 0 & 0 & 1 & 0 \\ -1 & 0 & 0 & 0 \end{pmatrix}. \tag{2.28}$$

For concreteness, we consider the partition of the system $B \cup A$. We denote with $n_{X:Y}$ the number of singlets shared between X and Y. This is symmetric $n_{X:Y} = n_{Y:X}$ and additive $n_{X:Y\cup Z} = n_{X:Y} + n_{X:Z}$. The density matrix of the RSP takes the form

$$\rho_{\mathrm{RSP}} = \bigotimes_{m=1}^{n_{A:A}} \rho_{2\mathrm{s}} \bigotimes_{n=1}^{n_{A:B}} \rho_{2\mathrm{s}} \bigotimes_{l=1}^{n_{B:B}} \rho_{2\mathrm{s}}. \tag{2.29}$$

Tracing out B does not affect the $n_{A:A}$ singlets within A, but affects the spins of the $n_{A:B}$ shared singlets. We obtain

$$\rho_A = \bigotimes_{m=1}^{n_{A:A}} \rho_{2\mathrm{s}} \bigotimes_{n=1}^{n_{A:B}} \rho_{\mathrm{s}}, \tag{2.30}$$

which is depicted in Fig. 2.1 (Left). The eigenvalues of this density matrix are equal to $1/2$, with a degeneracy that depends on the number of in-out singlets. In particular, it is evident that for each realization one has

$$S_m = S = n_{A:B} \ln 2. \tag{2.31}$$

For later convenience, let us define $\rho_{\mathrm{in/out}}$ as

$$\rho_{\mathrm{in/out}} = \bigotimes_{n=1}^{n_{A:B}} \rho_{\mathrm{s}}. \tag{2.32}$$

The definition Eq. (2.32) will be useful in Sec. 2.4 when we discuss the symmetry resolution.

If instead we consider a tripartite system with $A\cup B$ and $A = A_1 \cup A_2$ (Fig. 2.1 (Right)), after tracing out B and obtaining Eq. (2.30), we can compute the partial traspose over one of the partitions. For concreteness we consider the partial transpose over A_2, which results in

$$\rho_A^{T_2} = \bigotimes_{q=1}^{n_{A_1:A_1}} \rho_{2\mathrm{s}} \bigotimes_{r=1}^{n_{A_2:A_2}} \rho_{2\mathrm{s}} \bigotimes_{p=1}^{n_{A_1:A_2}} \rho_{2\mathrm{s}}^{T_2} \bigotimes_{n=1}^{n_{A:B}} \rho_{\mathrm{s}}. \tag{2.33}$$

Here we have used the fact that $\rho_{\rm s}^{T_2} = \rho_{\rm s}$ for a single site, and that $\rho_{2{\rm s}}^{T_2} = \rho_{2{\rm s}}$ when both the ends of a bond are in the same subsystem A_i $(i = 1, 2)$. The spectrum of Eq. (2.33) is denoted as negativity spectrum and is discussed in Sec. 2.3.

2.2.4 Scaling of the number of shared singlets and bipartite entanglement

The density matrix of a single random configuration and all the quantities that can be derived from it are fully characterized by the number of shared singlets $n_{X:Y}$. Occasionally we refer to this quantity as the number of in-out bonds. Consequently, the scaling of these quantities is crucial in the study of the spectrum of the reduced density matrix of the RSP and of its partial transpose. The knowledge of all the $n_{X:Y}$ can be extracted through the solution of a simple set of linear equations, relying on the additivity property of $n_{X:Y}$. Hereafter we denote by ℓ_X the length of an interval X, and X_c its complement. Consider a $2k$-multipartite system $\bigcup_{X\in\mathcal{G}_0} X$ with $\mathcal{G}_0 = \{A_1, B_1, \ldots, A_k, B_k\}$. We define $\mathcal{G}$ as the set of all possible compact subintervals of the chain. For each $X \in \mathcal{G}$ one can decompose the number of singlets $n_{X:X_c}$ as

$$n_{X:X_c} = \sum_{Y,Z\in\mathcal{G}} n_{X\cap Y:X_c\cap Z}. \tag{2.34}$$

Despite these relations hold for any single disorder realization, a great dealt of information can be extracted by their statistical proxies. In particular, many of our results require the disorder average; after this operation denoted throughout this Chapter with $\overline{\circ}$ or $\langle\circ\rangle$, we have a set of linear equations, whose solution gives $\overline{n}_{X:W}$ for any $X, W \in \mathcal{G}_0$

$$\overline{n}_{X:X_c} = \sum_{Y,Z\in\mathcal{G}} \overline{n}_{X\cap Y:X_c\cap Z}. \tag{2.35}$$

The left hand side has been previously computed within the RSP [24]

$$\overline{n}_{X:X_c} = \frac{b_{X:X_c}}{6}\log\ell_X + k, \tag{2.36}$$

where $b_{X:X_c}$ is the number of edges shared by X and X_c, and k is a non-universal constant of order $\mathcal{O}(1)$ in the subsystem size ℓ_X. For the leading logarithmic term, we then have

$$\frac{b_{X:X_c}}{6}\log\ell_X = \sum_{Y,Z\in\mathcal{G}} \overline{n}_{X\cap Y:X_c\cap Z}. \tag{2.37}$$

This set of equations can be straightforwardly solved for the variables $\overline{n}$, and a unique solution can be extracted for any partition of the system. (See Ref. [35] for several explicit examples.) For concreteness we recall the result for the partition in Fig. 2.1 (Left)

$$\langle n_{A:B}\rangle = \frac{1}{3}\ln\ell + O(\ell^0). \tag{2.38}$$

More refined insights are instead obtained from the generating function of the stochastic variable $n_{A:B}$, defined as

$$g(\sigma) = \sum_{n_{A:B}} P(n_{A:B}) e^{-n_{A:B}\sigma}, \tag{2.39}$$

where σ is real parameter and $P(n_{A:B})$ is the full distribution of the shared singlets. Specifically, from (2.39), we can compute any moment

$$\langle n_{A:B}^k\rangle = \left.\frac{d^k g(\sigma)}{d\sigma^k}\right|_{\sigma=0}. \tag{2.40}$$

Note that after replacing the summation with an integral, Eq. (2.39) is the Laplace transform of $P(n_{A:B})$.

Importantly, in the scaling limit of large ℓ, $g(\sigma)$ can be calculated within the SDRG framework (by using a renewal-equation approach, see Ref. [34] for details). The result reads

$$g(\sigma) = e^{-3/2\mu}\left[\cosh\left(\frac{\sqrt{5+4e^{-\sigma}}}{2}\mu\right) + \frac{3}{\sqrt{5+4e^{-\sigma}}}\sinh\left(\frac{\sqrt{5+4e^{-\sigma}}}{2}\mu\right)\right], \tag{2.41}$$

where

$$\mu = 3\langle n_{A:B}\rangle + \frac{1}{3}. \tag{2.42}$$

Eq. (2.41) holds in the scaling limit $\ell \to \infty$. Away from the scaling limit, corrections due to finite ℓ are expected [34].

We now discuss the consequences for the entanglement entropies. In particular, we introduce two different definitions of disorder-averaged entropies. In the first, the average over the disorder is taken after the logarithm of the moments of the reduced density matrix, i.e., we average Eq. (2.1). This defines the entropies $\overline{S}$ and $\overline{S}_m$ as

$$\overline{S} \equiv -\langle \mathrm{tr}_A \rho_A \ln \rho_A\rangle, \tag{2.43}$$

$$\overline{S}_m \equiv \frac{1}{1-m}\langle \ln \mathrm{tr}_A \rho_A^m\rangle. \tag{2.44}$$

with $\langle \bullet \rangle = \sum_{n=0}^{\infty} P(n)\,\bullet$ being the disorder average. It is straightforward to see that there is a trivial dependence on the Rényi index m, i.e,

$$\overline{S}_m = \overline{S} \quad \forall m. \tag{2.45}$$

Moreover, Eq. (2.31) depends only on the average number of shared singlets $n_{A:B}$. Therefore, by using Eq. (2.38), we get

$$\overline{S}_m = \langle n_{A:B}\rangle \ln 2 = \frac{\ln 2}{3}\ln \ell + O(\ell^0). \tag{2.46}$$

The disorder averaged version of eq. (2.1), is not sufficient to study the full entanglement spectrum [34]. To further investigate the entanglement structure of random singlet phase, it is custom to define

$$\widetilde{S}_m \equiv \frac{1}{1-m}\ln\langle \mathrm{tr}_A \rho_A^m\rangle, \tag{2.47}$$

where the average is taken before the logarithm, i.e., it is the logarithm of the averaged partition function. Now, $\widetilde{S}_m$ depend on the full distribution of in-out singlets $P(n_{A:B})$, which encodes the full entanglement content of the random singlet phase. Note that, by making use of the following identity

$$\lim_{m\to 1}\frac{1}{1-m}\ln f(m) = -\partial_m f(m)|_{m=1}, \tag{2.48}$$

valid for any function $f(m)$ such that $f(1) = 1$, one can show that, in the limit $m \to 1$, $\widetilde{S}_m$ and $\overline{S}_m$ coincide, i.e.

$$\lim_{m\to 1}\widetilde{S}_m = \lim_{m\to 1}\overline{S}_m = \overline{S}. \tag{2.49}$$

More generally, from the definition of $g(s)$ in Eq. (2.39), it is straightforward to obtain the Rényi entropies in Eq. (2.47) as

$$\widetilde{S}_m = \frac{1}{1-m}\ln g((m-1)\ln 2). \tag{2.50}$$

By using $g(s)$ in Eq. (2.41), we obtain

$$\widetilde{S}_m = \frac{\sqrt{5+2^{3-m}}-3}{2(1-m)}\ln \ell + O(\ell^0). \tag{2.51}$$

The subleading term is non-universal and disorder dependent. Importantly, from (2.51), we recover

$$\lim_{m\to 1} \widetilde{S}_m = \frac{\ln 2}{3} \ln \ell + O(\ell^0), \tag{2.52}$$

which is consistent with (2.49).

We mention that SDRG methods can be used also to derive predictions for the entanglement scaling in other phases of matter more complicated than RSP [171–180].

2.3 Negativity spectrum

2.3.1 Logarithmic negativity and negativity moments

The central object of this Section is the spectral density of the operator $\rho_A^{T_2}$ in Eq. (2.33)

$$\mathbb{P}(\lambda) = \sum_i \delta(\lambda - \lambda_i), \tag{2.53}$$

where the sum is over the eigenvalues of $\rho_A^{T_2}$. From the knowledge of $\mathbb{P}(\lambda)$, we can infer the negativity moments (2.5)

$$\mathrm{tr}(\rho_A^{T_2})^\alpha = \sum_i \lambda_i^\alpha = \int d\lambda\, \mathbb{P}(\lambda)\lambda^\alpha. \tag{2.54}$$

The converse is also true, in that the knowledge of all the negativity moments gives access to the function $\lambda\mathbb{P}(\lambda)$ through an inverse Stieltjes transform [134, 136]. For this reason, with a slight but standard abuse of language, we will refer also to the whole set of moments as the negativity spectrum.

Most of the derivations presented in this Section are valid for a very general tripartition $A_1 \cup A_2 \cup B$ of an infinite chain (with some caveat which will be clearer in the course of the calculation). For concreteness and benchmarks, in Sec. 2.3.4 we will specialize to the usual partition depicted in Fig. 2.1 (Right) with two adjacent blocks.

Within a single disorder realization, the negativity moments depends only on $n_{A:B}$ and $n_{A_1:A_2}$. The partial transpose $\rho_A^{T_2}$ in Eq. (2.33) is straightforwardly diagonalized and the eigenvalues are

$$\lambda_\pm = \pm 2^{-n_{A:B}-n_{A_1:A_2}}, \tag{2.55}$$

with degeneracies

$$d_- = 2^{n_{A:B}+n_{A_1:A_2}-1}(2^{n_{A_1:A_2}} - 1), \tag{2.56}$$

$$d_+ = 2^{n_{A:B}+2n_{A_1:A_2}} - d_-. \tag{2.57}$$

Consequently, the negativity moments for this given disorder realization are

$$M_\alpha^{T_2} = 2^{(n_{A:B}+n_{A_1:A_2})(1-\alpha)} \begin{cases} 2^{n_{A_1:A_2}} & \alpha \text{ even} \\ 1 & \alpha \text{ odd.} \end{cases} \tag{2.58}$$

Notice that the moments $M_\alpha^{T_2}$ depends on both $n_{A:B}$ and $n_{A_1:A_2}$. Hence, as well known, they are not direct measures of the mutual entanglement between A_1 and A_2. However, the dependence on $n_{A:B}$ cancels in the limit $2\alpha \to 1$, as a consequence of the fact that the negativity is a good entanglement measure also in the RSP [35].

Nevertheless, in the same spirit of the entanglement spectrum compared to the entanglement entropy [11], the moments (2.58) encode more information about the mutual entanglement than the (logarithmic) negativity itself, as we shall see.

Till now we have been discussing what happens for a single disorder realization, but the physical relevant quantities are the averages over the quench disorder. From the knowledge of the moments, we can define two different averaged quantities, each one providing useful information about the entanglement. Indeed, since the average of the logarithm and the logarithm of the average are not at all equivalent, we can define

$$\hat{\mathcal{E}}_\alpha = \overline{\log M_\alpha^{T_2}}, \tag{2.59}$$

$$\mathcal{E}_\alpha = \log \overline{M_\alpha^{T_2}}. \tag{2.60}$$

These two quantities are expected to behave very differently, as it happens for the analogous averages for the entanglement spectrum [34] (i.e. $\overline{\log \mathrm{tr}\rho_A^\alpha}$ and $\log \overline{\mathrm{tr}\rho_A^\alpha}$). Anyhow, we are going to show that $\hat{\mathcal{E}}_\alpha$ and $\mathcal{E}_\alpha$

are related through a linear transformation at the leading order in ℓ.

2.3.2 Moments $\hat{\mathcal{E}}_\alpha$ and logarithmic negativity

We start by considering the average of the logarithm of the moments $\hat{\mathcal{E}}_\alpha$ ($\alpha > 0$) in Eq. (2.59). This is the easiest quantity to calculate because it depends linearly on $\overline{n}_{A:B}$ and $\overline{n}_{A_1:A_2}$. Hence, straightforwardly from Eq. (2.58), we get

$$\hat{\mathcal{E}}_\alpha = \log 2 \begin{cases} (1-\alpha)\overline{n}_{A:B} + (2-\alpha)\overline{n}_{A_1:A_2} & \alpha \text{ even}, \\ (1-\alpha)(\overline{n}_{A:B} + \overline{n}_{A_1:A_2}) & \alpha \text{ odd}. \end{cases} \tag{2.61}$$

We observe that, because of the linear structure, $\hat{\mathcal{E}}_\alpha$ depends only on the averages $\bar{n}_{X:Y}$ and not on the full distribution of the singlets shared between the partitions. We recall that one of the main reasons why we are interested in $\hat{\mathcal{E}}_\alpha$ is that they are the replica quantities to access the average logarithmic negativity [35]

$$\mathcal{E} = \lim_{\alpha \to 1/2} \hat{\mathcal{E}}_{2\alpha} = \overline{n}_{A_1:A_2} \log 2. \tag{2.62}$$

We stress that (2.61) are valid for arbitrary tripartition of the chain and not only for adjacent intervals. Notice that since the moments $\hat{\mathcal{E}}_\alpha$ depend only on the averages $\bar{n}_{X:Y}$, they do not encode more information than the entanglement negativity and entropy.

2.3.3 Moments $\mathcal{E}_\alpha$ and renewal equation for the negativity spectrum

The logarithm of the average of the moments in Eq. (2.60) is the quantity more directly related to the true negativity spectrum (i.e. the distribution of eigenvalues of the partial transpose). Its calculation is, however, much more cumbersome compared to $\hat{\mathcal{E}}_\alpha$ because of the non-linear dependence on $n_{X:Y}$: it requires the knowledge of the entire distribution of singlets and not only of the average. We focus on the tripartition $A = A_1 \cup A_2$ and $B = A_c$. Denoting as $P(n_{A:B}, n_{A_1:A_2})$ the joint probability distribution of $n_{A:B}$ and $n_{A_1:A_2}$, we introduce the generating function for the probability distribution of in-out bonds [34, 181].

$$g(t,s) \equiv \log\langle e^{t n_{A:B} + s n_{A_1:A_2}} \rangle = \log \sum_{n_{A:B}, n_{A_1:A_2}} e^{n_{A:B} t + n_{A_1:A_2} s} P(n_{A:B}, n_{A_1:A_2}). \tag{2.63}$$

The knowledge of $g(t,s)$ is equivalent to that of the negativity spectrum, in the sense that it univocally determines the negativity moments.

The asymptotic behavior of generating function $g(t,s)$ (in a RG sense that will be clearer later on) may be accessed following the phenomenological approach introduced in Ref. [34] for the entanglement spectrum. The starting observation is that, within SDRG, the singlets form at a constant rate with respect to the RG time μ. This rate is responsible for the logarithmic scaling of $\overline{n}_{X:X_c}$ for a single interval X. The probability distribution of waiting times for a decimation to occur across a bond since the last decimation is [24]

$$f(\mu) = \frac{1}{\sqrt{5}} \left(e^{-\frac{3-\sqrt{5}}{2}\mu} - e^{-\frac{3+\sqrt{5}}{2}\mu} \right). \tag{2.64}$$

This expression is true only for asymptotically large μ because non-universal terms related to the initial distribution of disorder have been neglected in its derivation [24]. For the following, it is useful to explicitly introduce $\tilde{f}(x)$ as the Laplace transform of $f(\mu)$

$$\tilde{f}(x) = \frac{1}{\sqrt{5}} \left(\frac{1}{x + \frac{3-\sqrt{5}}{2}} - \frac{1}{x + \frac{3+\sqrt{5}}{2}} \right). \tag{2.65}$$

At this point, in order to compute $g(t,s)$ one would need to know and quantify all the possible processes between two RG times. The renormalization flow generate several of these processes, but the most probable one is clearly the formation of isolated singlets [34]. Thus, in a first approximation, expected to be correct

in the limit of large μ, we can write a renewal equation for the generating function Eq. (2.63), considering only formations of in-out isolated singlets

$$\langle e^{nt+sm}\rangle_\mu = \int_\mu^\infty d\xi f(\xi) + pe^t \int_0^\mu d\xi f(\xi)\langle e^{nt+sm}\rangle_{\mu-\xi} + qe^s \int_0^\mu d\xi f(\xi)\langle e^{nt+sm}\rangle_{\mu-\xi}. \tag{2.66}$$

Here, for notational convenience, we express the disorder average at RG time μ with $\langle\cdot\rangle_\mu$ while n and m are just shorthands for $n_{A:B}$ and $n_{A_1:A_2}$ respectively. The constants p and $q = 1-p$ are, respectively, the asymptotic probability of increasing n and m by one unit. In a general setting p and q can depend on the RG time μ and can have activation times depending on the tripartition, here we are only interested in the limit of large μ and hence neglect these corrections that can be important when comparing with numerics. The *fundamental assumption* here is that p and q have a non-zero limit as $\mu \to \infty$. The renewal equation Eq. (2.66) represents an educated conjecture generalizing the one for $n_{A:B}$ in Ref. [34] to two kinds of singlets ($n_{A:B}$ and $n_{A_1:A_2}$) with probability p and q. The correctness of all our (reasonable) assumptions can be tested only a posteriori with numerical simulations. In fact, as for the analogous equation for the entanglement spectrum in Ref. [34], the renewal equatio Eq. (2.66) does not take into account many subleading processes. For example, processes like multiple decimations (which require higher order terms in p and q), the RG dependence of the variables p and q, and memory effects beyond the first order are all neglected in Eq. (2.66) and their inclusion in the renewal equation requires the addition of new convolution terms. It is difficult to identify the most relevant corrections among all the possible ones; anyhow in most cases they lead to equations which are hard, if not impossible, to solve.

The renewal equation Eq. (2.66) can be solved through Laplace transform. Indeed, after some simple algebra we get

$$g_\mu(t,s) = \log\left[\mathcal{L}^{-1}\left(\frac{1}{x}\frac{1-\tilde{f}(x)}{1-(pe^t+qe^s)\tilde{f}(x)}\right)(\mu)\right]. \tag{2.67}$$

The inverse transform $\mathcal{L}^{-1}$ can be computed analytically and gives, at large μ

$$e^{g_\mu(t,s)} \overset{\mu\gg 1}{\simeq} \left(\frac{1}{2} + \frac{3}{2\sqrt{5+4(pe^t+qe^s)}}\right)\exp\left(\frac{\sqrt{5+4(pe^t+qe^s)}-3}{2}\mu\right). \tag{2.68}$$

From the definition Eq. (2.63), we have

$$\overline{n}_{A_1:A_2} = \partial_s g(0,0) \overset{\mu\gg 1}{=} \frac{q}{9}(3\mu-1), \tag{2.69}$$

$$\overline{n}_{A:B} = \partial_t g(0,0) \overset{\mu\gg 1}{=} \frac{p}{9}(3\mu-1), \tag{2.70}$$

and in particular

$$\frac{\overline{n}_{A_1:A_2}}{\overline{n}_{A:B}} = \frac{q}{p} = \frac{q}{1-q}. \tag{2.71}$$

The last three equations must be used to extract p and $q = 1-p$ in a self-consistent way. Indeed, the average number of singlets between complementary sets is univocally fixed by the set of equations Eq. (2.37). Thus, for a chosen partitioning $\mathcal{G}_0$, one first solves Eq. (2.37), then uses the solutions to determine the probabilities p and q via Eq. (2.71), and finally plug them in Eq. (2.67) determining the asymptotics of $g(t,s)$ for large μ. Notice that in Eqs. (2.69) and (2.70) we kept the $O(1)$ term in μ to show that Eq. (2.71) is valid also at the first subleading order.

At this point, Eq. (2.58) allows to write the desired averaged negativity moments as function of $g(t,s)$ as

$$\mathcal{E}_\alpha = g(t_\alpha, s_\alpha), \tag{2.72}$$

with

$$t_\alpha \equiv (1-\alpha)\log 2, \tag{2.73}$$

$$s_\alpha \equiv \begin{cases} (2-\alpha)\log 2 & \alpha \text{ even}, \\ (1-\alpha)\log 2 & \alpha \text{ odd}. \end{cases} \tag{2.74}$$

The leading term in μ (and hence in $\overline{n}$ or equivalently in ℓ) comes from the exponential term in Eq. (2.68). We have two different results for α even and odd that we denote respectively as $\mathcal{E}^e_\alpha$ and $\mathcal{E}^o_\alpha$. By simple algebra we obtain

$$\mathcal{E}^e_\alpha = \frac{\sqrt{5+(1+q)2^{3-\alpha}}-3}{2}\mu + \dots, \tag{2.75}$$

and

$$\mathcal{E}^o_\alpha = \frac{\sqrt{5+2^{3-\alpha}}-3}{2}\mu + \dots, \tag{2.76}$$

where the dots stands for subleading non-universal terms in μ. Notice that in Eqs. (2.75) and (2.76) all the dependence on the partition is encoded in the constant q and in μ. However, since μ is proportional to the logarithm of the length involved in the problem, the universal prefactor of this logarithm depends on the partition only through q. Hence, the odd moments have the same scaling factor for any tripartition of the chain with $q \neq 0, 1$.

Eqs. (2.75) and (2.76) are the main analytic results of this manuscript and we recall that *they are valid for any tripartition of the infinite chain* as long as $p, q \neq 0$.

Importantly, they depend on the entire distribution of shared singlets and not only on their averaged values, showing indeed that the negativity moments provide more information than the logarithmic negativity and the entanglement entropy.

A trivial consistency check is that $\mathcal{E}^o_1 = 0$, as it should. An important consequence of Eq. (2.75) is that the replica limit $\mathcal{E}^e_1 = \lim_{\alpha\to 1}\mathcal{E}_{2\alpha}$ does not converge to the logarithmic negativity Eq. (2.62) (which is the limit of $\hat{\mathcal{E}}_{2\alpha}$) for any $q > 0$. This means that *the average negativity is not related trivially to the average logarithmic negativity* as instead happens for a clean system, i.e. $\overline{\mathcal{E}} \neq \log(2\overline{\mathcal{N}} - 1)$ as average over disorder. Not only, we also have that $\mathcal{E}^e_1 > \hat{\mathcal{E}}^e_1$ for all $q > 0$, as expected since the logarithm is a concave function. It is also true that $\mathcal{E}_\alpha > \hat{\mathcal{E}}_\alpha$ for any α.

Since both $\mathcal{E}_\alpha$ and $\hat{\mathcal{E}}_\alpha$ are proportional to μ, it is instructive also to write a relation between the two at fixed α. Simply combining Eqs. (2.75) and (2.76) with (2.61), we obtain

$$\mathcal{E}_\alpha = A_\alpha \hat{\mathcal{E}}_\alpha + K^{(\alpha)}, \tag{2.77}$$

were $K^{(\alpha)}$ are a non-universal constants and function A_α takes two different values for even and odd α:

$$A^e_\alpha = 3\frac{\sqrt{5+(1+q)2^{3-\alpha}}-3}{2(1-\alpha+q)\log 2}, \tag{2.78}$$

$$A^o_\alpha = 3\frac{\sqrt{5+2^{3-\alpha}}-3}{2(1-\alpha)\log 2}. \tag{2.79}$$

2.3.4 Application to adjacent intervals

In this subsection we specialize the results of the previous one to the case of adjacent intervals of length ℓ_1 and ℓ_2 as in Fig. 2.1 (Right). In this case the set of equations Eq. (2.37) admits the following solution at the leading order in the lengths [35]

$$\overline{n}_{A_1:A_2} = \frac{1}{6}\log\left(\frac{\ell_{A_1}\ell_{A_2}}{\ell_{A_1}+\ell_{A_2}}\right), \tag{2.80}$$

$$\overline{n}_{A:B} = \frac{1}{3}\log(\ell_{A_1}+\ell_{A_2}). \tag{2.81}$$

The ratio Eq.(2.71) seems a complicated function of ℓ_1 and ℓ_2. However, we are interested in the regime of $\ell_1 \propto \ell_2 \gg 1$ when $\overline{n}_{A_1:A_2}/\overline{n}_{A:B} = 1/2 + \ldots$, where the dots stand for subleading logarithmic corrections to the scaling (which may be important in the analysis of the numerical data). Hence, in the regime $\ell_{1,2} \gg 1$, from Eq. (2.71) we get

$$q = \frac{1}{3}, \quad \text{and} \quad p = \frac{2}{3}. \tag{2.82}$$

Summarizing, plugging Eq. (2.82) in Eqs. (2.61), (2.75) and (2.76), the final results for $\hat{\mathcal{E}}_\alpha$ and $\mathcal{E}_\alpha$ for adjacent intervals are

$$\hat{\mathcal{E}}^e_\alpha = (4-3\alpha)\frac{\log 2}{6}\log \ell + \ldots, \tag{2.83}$$

$$\hat{\mathcal{E}}^o_\alpha = (1-\alpha)\frac{\log 2}{2}\log \ell + \ldots, \tag{2.84}$$

$$\mathcal{E}^e_\alpha = 3\frac{\sqrt{5+2^{5-\alpha}/3}-3}{4}\log \ell + \ldots, \tag{2.85}$$

$$\mathcal{E}^o_\alpha = 3\frac{\sqrt{5+2^{3-\alpha}}-3}{4}\log \ell + \ldots, \tag{2.86}$$

where we posed $\ell = \ell_1 = x\ell_2$ (with x finite) and the dots stand (again) for non-universal additive constants (with a partial and universal dependence on x).

The relation between $\hat{\mathcal{E}}_\alpha$ and $\mathcal{E}_\alpha$ is always given by Eq. (2.77) with A^o_α given by Eq. (2.79) and A^e_α equal to

$$A^e_\alpha = 9\frac{\sqrt{5+2^{5-\alpha}/3}-3}{2(4-3\alpha)\log 2}. \tag{2.87}$$

The above results straightforwardly generalize to more involved tripartitions and can be used to access universal features of the negativity spectrum in the RSP. Let us recapitulate what one has to do in the most general case: (i) choose the partition, (ii) compute the average in-out singlets number solving the set of equations Eq. (2.37), (iii) find the values of p and q using Eq. (2.71), (iv) if $p, q \neq 0$, then the negativity moments are just given by Eqs. (2.75) and (2.76). The results will be valid only in the scaling regime of all length-scales of the same order and much larger than 1.

2.3.5 Numerical tests for adjacent intervals

In this section we numerically test the predictions reported above and in particular we compare our numerical simulations with the analytic formulas (2.83-2.86) for the negativity moments of adjacent intervals. We present two benchmarks of our results. First we focus on the XX chain for which we can exploit known free fermion techniques to easily access the integer moments $M^{T_2}_\alpha$ with ab-initio simulations [103, 109, 182, 183]. This kind of computations does not rely on the random singlet phase structure and thus represents a robust non-trivial check of our findings. Moreover we implement numerically the SDRG for the XXX chain, providing another numerical benchmark which allows to explore much larger system sizes and easily access also the two analytic continuations of the moments to non-integer values. All these simulations are extremely important in view of the several (reasonable) assumptions we made in writing down the renewal equation (2.66): only the very good agreement between the predictions from its solution and the numerics represents a definitive confirmation for the correctness of these assumptions, at least for asymptotically large RG time.

Free fermions and negativity spectrum

We review the mapping between the XX chain and free fermions on the line. Within the free fermions formalism, we can express the reduced density matrix and its partial transpose in the spin variables as a sum

of Gaussian operators with known Majorana correlation matrices. The negativity moments are computed through a product rule for Gaussian matrices [182–184].

The Hamiltonian of the random XX chain is Eq. (2.17) at $\Delta = 0$

$$H = \sum_{i=1}^{L-1} J_i (S_i^x S_{i+1}^x + S_i^y S_{i+1}^y). \tag{2.88}$$

Here we consider a chain of length L. The Jordan-Wigner transformation

$$c_i = \left(\prod_{m=1}^{i-1} S_m^z \right) \frac{S_i^x - i S_i^y}{2}, \tag{2.89}$$

maps the Hamiltonian (2.88) in the free-fermion one

$$H = \frac{1}{2} \sum_{i=1}^{L-1} J_i (c_i^\dagger c_{i+1} + c_{i+1}^\dagger c_i) \equiv \sum_{i,j=1}^{L-1} c_i^\dagger h_{i,j} c_j. \tag{2.90}$$

The c_i are fermion annihilation operator, satisfying the canonical anti-commutation relations $\{c_m, c_n^\dagger\} = \delta_{mn}$. At the free fermion point the many-body eigenfunctions of H can be expressed in terms of the single-particle ones $\{\phi_q(i)\}$; the same is true for the many-body spectrum. Indeed, the eigenstates of the Hamiltonian (2.90) are obtained by applying an arbitrary number of single-particle creation operators

$$\eta_q^\dagger = \sum_i \phi_q(i) c_i^\dagger, \tag{2.91}$$

to the (fermonic) vacuum $|0\rangle$. The ground state of (2.88) corresponds to half-filling in fermionic language, that is the $N = L/2$ lowest energy levels are occupied

$$|\mathrm{GS}\rangle = \eta_{q_N}^\dagger \cdots \eta_{q_1}^\dagger |0\rangle. \tag{2.92}$$

The correlation matrix takes the form

$$C_{ij} \equiv \langle c_i^\dagger c_j \rangle = \sum_q \phi_q^*(i) \phi_q(j), \tag{2.93}$$

where the sum is over the occupied single-particle excitations in the ground state. The reduced correlation matrix to a given subsystem A with ℓ sites, C_A, is a $\ell \times \ell$ matrix whose elements are defined by the restriction of Eq. (2.93) to $i, j \in A$. For later convenience we also introduce the Majorana fermions

$$a_{2m-1} = c_m^\dagger + c_m, \quad a_{2m} = i(c_m^\dagger - c_m), \tag{2.94}$$

and the corresponding $2\ell \times 2\ell$ Majorana correlation matrix Γ_A with matrix elements

$$(\Gamma_A)_{nm} \equiv \langle a_m a_n \rangle - \delta_{mn}. \tag{2.95}$$

It is clear that there is a direct relation between the entries of Γ_A and those of C_A.

Crucially, reduced density matrices associated with a single interval are Gaussian operators [185]

$$\rho_A = \frac{1}{Z_\Omega} \exp\left(\frac{1}{4} \sum_{n,m} a_n \Omega_{nm} a_m \right), \tag{2.96}$$

(Z_Ω being a normalization) and the matrix Ω may be written in terms of Γ_A as

$$\Gamma_A \equiv \tanh\left(\frac{\Omega}{2}\right). \tag{2.97}$$

However, when the subsystem A consists of more than one interval, the reduced density matrix is not gaussian [186, 187], and so also its partial transpose [124, 183]. Still, in both cases, the corresponding operator is the sum of gaussian terms. For instance, in the case of two disjoint intervals $A = A_1 \cup A_2$, ρ_A is the sum of two Gaussian operators ρ_{Γ_i} associated by Eqs. (2.96) and (2.97) to distinct covariance matrices Γ_i.

With free fermion techniques is not straightforward to calculate the eigenvalues of the sum of Gaussian operators (see anyhow Ref. [188] for a brute force approach). Instead, the traces of arbitrary integer powers of sums of (even non-commuting) gaussian operators can be calculated with, by now, standard methods [182, 184]. These methods heave been exploited already many times also for the calculation of negativity in spin chains [105, 124, 131, 183]. Since the associated machinery is quite involved, here we just summarize the results and refer to the literature for further details [124, 183]. Let us denote by ρ_Γ the gaussian operator associated to the covariance matrix Γ. Given Γ and Γ', we define the following product rule

$$\rho_\Gamma \rho_{\Gamma'} = \mathrm{Tr}\left[\rho_\Gamma \rho_{\Gamma'}\right] \ \rho_{\Gamma\times\Gamma'}, \tag{2.98}$$

where [182]

$$\Gamma \times \Gamma' \equiv 1 - (1-\Gamma')\frac{1}{1+\Gamma\Gamma'}(1-\Gamma), \tag{2.99}$$

relating the covariance matrices of two gaussian operators to the one associated to their product. The trace on the right hand side of (2.98) is [182, 184]

$$\{\Gamma, \Gamma'\} \equiv \mathrm{Tr}\left(\rho_\Gamma \rho_{\Gamma'}\right) = \prod_{\mu\in\sigma(\Gamma\Gamma')/2} \frac{1+\mu}{2}, \tag{2.100}$$

with the product being over half of the spectrum $\sigma(\Gamma\Gamma')$, which is doubly-degenerate. Moreover, by associativity, one can extend this relation to more than two gaussian operators

$$\prod_{i=1}^{n} \rho_{\Gamma_{\alpha_i}} = \{\Gamma_{\alpha_1}, \cdots, \Gamma_{\alpha_n}\} \rho_{\Gamma_1\times\cdots\times\Gamma_{\alpha_n}}, \tag{2.101}$$

where

$$\{\Gamma_{\alpha_1}, \Gamma_{\alpha_2}, \cdots, \Gamma_{\alpha_n}\} \equiv \mathrm{Tr}\left(\rho_{\Gamma_{\alpha_1}} \rho_{\Gamma_{\alpha_2}} \cdots \rho_{\Gamma_{\alpha_n}}\right) = \{\Gamma_{\alpha_1}, \Gamma_{\alpha_2}\}\{\Gamma_{\alpha_1} \times \Gamma_{\alpha_2}, \cdots, \Gamma_{\alpha_n}\}. \tag{2.102}$$

The above equation can be used iteratively to evaluate traces of arbitrary products of gaussian operators.

In our case we need to identify the gaussian operators whose sum gives the partially transposed density matrix. Let us specialize to the system studied in Sec. 2.3.4 with two adjacent intervals A_1 and A_2, when there are major simplifications compared to the case of disjoint intervals [124, 183].

Denoting with Γ_{AA} the correlation matrix within $A = A_1 \cup A_2$, we further define the four building blocks

$$\Gamma_1 = \Gamma_{AA}, \quad \Gamma_2 = P\Gamma_1 P, \tag{2.103}$$

$$\tilde{\Gamma}_k = \tilde{P}\Gamma_k\tilde{P}, \quad k = 1, 2, \tag{2.104}$$

where

$$P = \begin{pmatrix} \mathbf{1}_\ell & 0 \\ 0 & -\mathbf{1}_\ell \end{pmatrix}, \quad \text{and} \quad \tilde{P} = \begin{pmatrix} \mathbf{1}_\ell & 0 \\ 0 & i\mathbf{1}_\ell \end{pmatrix}. \tag{2.105}$$

Here $\mathbf{1}_\ell$ is an identity matrix of dimension $\ell \times \ell$. The integer negativity moments may be written in terms

of these building blocks [183]. For convenience, we report here the cases of $\alpha = 2, 3, 4$ which we use in the following

$$M_2^{T_2} = \{\tilde{\Gamma}_1, \tilde{\Gamma}_2\}, \tag{2.106}$$

$$M_3^{T_2} = -\frac{1}{2}\{\tilde{\Gamma}_1, \tilde{\Gamma}_1, \tilde{\Gamma}_1\} + \frac{3}{2}\{\tilde{\Gamma}_1, \tilde{\Gamma}_1, \tilde{\Gamma}_2\}, \tag{2.107}$$

$$M_4^{T_2} = -\frac{1}{2}\{\tilde{\Gamma}_1, \tilde{\Gamma}_1, \tilde{\Gamma}_1, \tilde{\Gamma}_1\} + \frac{1}{2}\{\tilde{\Gamma}_1, \tilde{\Gamma}_2, \tilde{\Gamma}_1, \tilde{\Gamma}_2\} + \{\tilde{\Gamma}_1, \tilde{\Gamma}_1, \tilde{\Gamma}_2, \tilde{\Gamma}_2\}. \tag{2.108}$$

The above equations are used to numerically compute the disorder average of the negativity moments. The recipe is the following: (i) we choose a disorder realization of the free fermion single-particle Hamiltonian (2.90) with $J_i \sim P(J)$, (ii) we derive the correlation matrix for Majorana fermions Γ_{AA}, (iii) we construct Γ_i and $\tilde{\Gamma}_i$ from the latter, (iv) we compute the moments Eq. (2.106-2.108), and finally (v) iterating the process for many disorder realizations, we calculate the average.

Numerical results for adjacent intervals

We are finally ready to test numerically the predictions reported in Sec. 2.3.4, as we do in the following. Throughout this subsection we consider a uniform coupling distribution $P(J) = 1$ with $J \in [0, 1]$, although, as stressed in Sec. 2.2, the results are distribution independent because of the universality of the RSP. In order to perform the numerical calculations, we must consider a finite chain of length L and, for simplicity, we choose to work with open boundary conditions. In order to reduce the finite size and boundary effects we take the two adjacent intervals placed at the center of the chain. We also limit our attention to the case of two intervals of equal length ℓ, because all the universal factors may be extracted from this partition.

First we consider the *ab-initio* method for XX chain, reviewed in the previous subsection. We focus on $\alpha = 2, 3, 4$. We consider different system sizes $L = 200, 400, 800$ and we vary the intervals length ℓ between $\ell \in \{1, \dots, L/4\}$. We consider 10^5 disorder realizations and we compute the disorder averages (2.59) and (2.60). The obtained numerical data are reported in Fig. 2.2. It is evident that all $\mathcal{E}_\alpha$ grow logarithmically with ℓ as predicted. The logarithmic growth is compared with the analytic predictions in Eqs. (2.83-2.86). The agreement between the numerical data and SDRG is perfect already for moderate values of ℓ. In the plots the non-universal additive constants (not specified in Eqs. (2.83-2.86)) have been fitted.

A byproduct of these ab-initio numerical simulations is an *indirect* test of the SDRG scaling for the logarithmic negativity obtained in Ref. [35]. In fact, the latter is not efficiently accessed through free fermion techniques, because, as already stressed many times, the partially transposed reduced density matrix is not a non-gaussian operator. Therefore, via replica trick, the computation of $\hat{\mathcal{E}}_{2\alpha}$ provides an indirect check for the scaling of the logarithmic negativity as well. This complement the numerical results obtained by SDRG and density matrix renormalization group in Ref. [35].

We now implement numerically the SDRG for finite spin chains, defined by the Ma-Dasgupta rule (2.24) for the XXX chain, which works as follows: (i) pick up a random disorder realization with a list random couplings $J_i \sim P(J)$; (ii) iterate the Ma-Dasgupta rule (i.e. choose the strongest bond, build a singlet between them, remove the two sites, renormalize the coupling according to (2.24)) until all spins are paired up in singlets; at each step keep track of the location of the singlet and of the removed spins; (iii) count the in-out singlets formed between the partitions of interest; (iv) evaluate the negativity moments for the single realization using their form in terms of the number of singlets in Eq. (2.58); (v) perform the average over all realizations. We vary the parameter α, total length L, and the subsystem size ℓ. Here the disorder average is taken over 10^6 realizations. Since we are using Eq. (2.58) as operative definition of the negativity moments in the random singlet phase, we have direct access to the analytic continuations of all four families moments $\mathcal{E}_\alpha^{e/o}$ and $\hat{\mathcal{E}}_\alpha^{e/o}$ to even, odd and arbitrary non-integer values of α. From these numerical averages, we extract

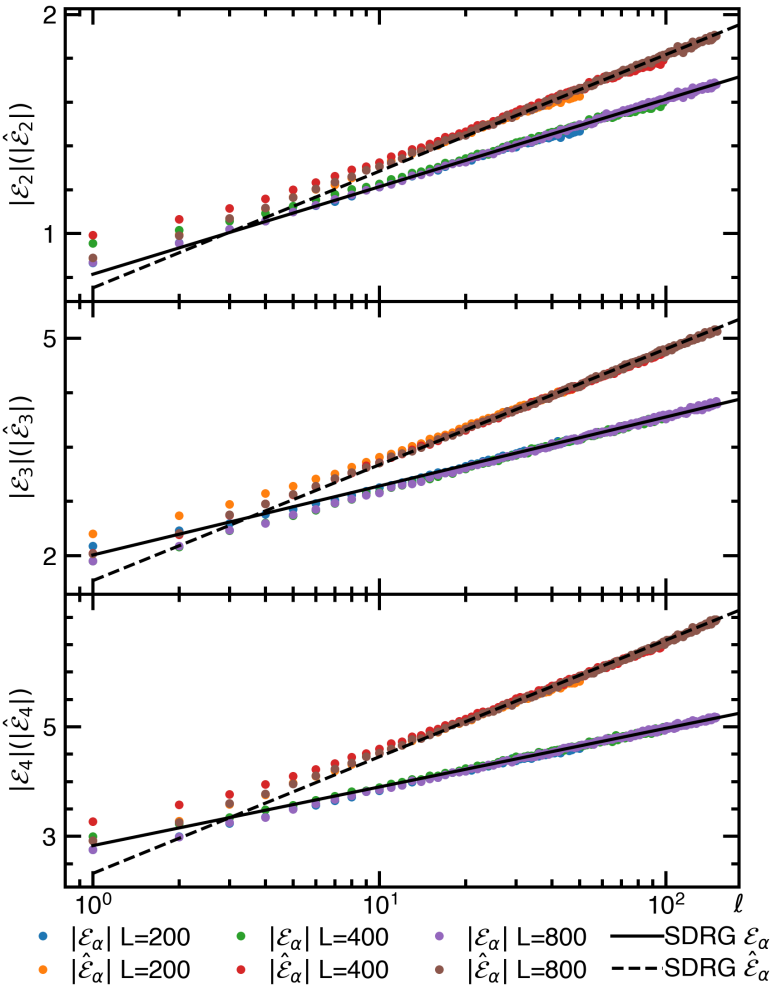

FIGURE 2.2: Negativity moments $\mathcal{E}_\alpha$ and $\hat{\mathcal{E}}_\alpha$ for the random XX chain: results of the *ab initio* computations for two adjacent intervals of equal length ℓ. We report the absolute values, since for the considered values of α, they are all negative quantities (i.e. the moments $M_\alpha^{T_2}$ are smaller than 1). The symbols correspond to the numerical data while the continuous lines are the analytic SDRG predictions Eqs. (2.83-2.86), with a best fit for the unknown non-universal additive constants. The agreement between the simulation and SDRG predictions is excellent already for moderate values of ℓ.

the prefactor of the logarithm for all the negativity moments for several values of α fitting the averages with

$$\begin{aligned} \hat{\mathcal{E}}_\alpha^{e/o} &= \hat{\varepsilon}_\alpha^{e/o} \log \ell + \hat{k}_\alpha^{e/o}, \\ \mathcal{E}_\alpha^{e/o} &= \varepsilon_\alpha^{e/o} \log \ell + k_\alpha^{e/o}. \end{aligned} \tag{2.109}$$

We restrict the fits to the windows of ℓ for which a logarithmic scaling is observed before finite size corrections kick in. The results for these four universal prefactors as function of α are reported in Fig. 2.3. The agreement between the analytic predictions in Eqs. (2.83-2.86) and the simulations is extremely good for the four moments and for all considered values of α (although some small finite size corrections are evident for the larger considered α). These SDRG results provide a test not only for the integer negativity moments, but also for their analytical continuations (2.83-2.86). In

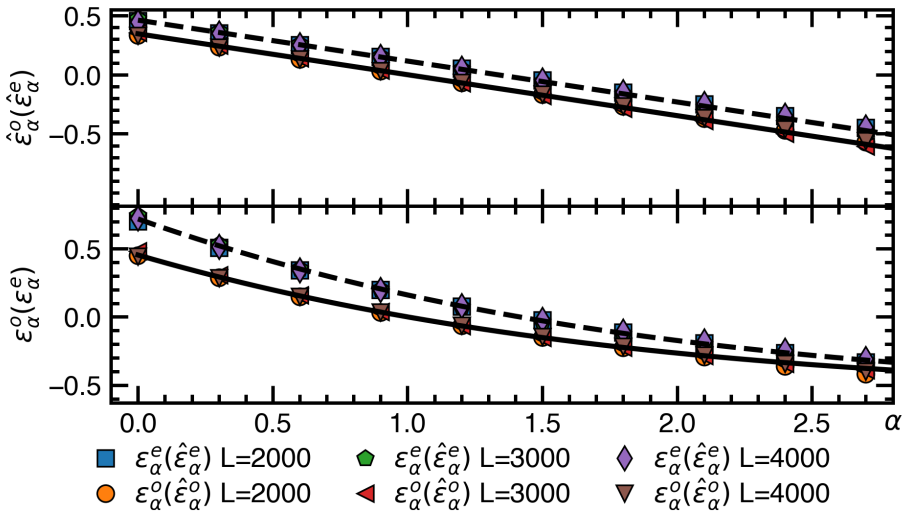

FIGURE 2.3: SDRG simulations for the negativity moments. Here we plot, as function of α, the prefactor of the logarithm $\varepsilon_\alpha^{e/o}$ (cf. (2.109)), as obtained by a fit of the numerical data. The symbols are the corresponding numerical data while the continuous lines are the analytic predictions in Eqs. (2.83-2.86). The plots show an extremely good agreement between numerical data and analytic predictions.

2.4 Symmetry resolved entanglement in the random singlet phase

In this Section we study the symmetry-resolved entanglement in the random singlet phase. Also in the presence of disorder, the Heisenberg chain for arbitrary Δ is $U(1)$ symmetric because of the conservation of the total magnetization $S^z_{\rm tot} = \sum_i S^z_i = S^z_A \otimes \mathbf{1}_B + \mathbf{1}_A \otimes S^z_B$. Indeed each hamiltonian term in (2.17) commutes with $S^z_{\rm tot}$, i.e.,

$$[J_i(S^x_i S^x_{i+1} + S^y_i S^y_{i+1} + \Delta S^z_i S^z_{i+1}), S^z_i + S^z_{i+1}] = 0. \tag{2.110}$$

At the isotropic point, the symmetry is enlarged to $SU(2)$, but here we focus on the more ubiquitous $U(1)$ symmetry.

In the following, we introduce the shorthand $n \equiv n_{A:B}$, with, as usual, $n_{A:B}$ the number of singlets shared between A and B. In order to find the internal structure of ρ_A, the first trivial observation is that the singlets within A do not contribute to the subsystem magnetization. Hence, the possible values of such magnetization only depend on shared singlets. Each shared singlet can provide either $+1/2$ or $-1/2$ and consequently the $(n+1)$ possible values which we denote by s are $s \in \{-n/2, -n/2+1, \dots, n/2\}$. Consequently, throughout this Section, s stands for the possible eigenvalue of the conserved charge within A, i.e., the quantity denoted by q in Sec. 2.1.3.

As it should be clear at this point, entanglement properties of the random singlet phase can be extracted by only looking at the reduced density matrix $\rho_{\rm in/out}$ (cf. (2.32)). This is true in particular for the contributions from different symmetry sectors. Now, $\rho_{\rm in/out}$ is of size $2^n \times 2^n$ and has a block structure, with $(n+1)$ blocks with charge $s \in \{-n/2, \dots, n/2\}$. The dimension of the block corresponding to s is

$$d_s = \binom{n}{n/2+s}. \tag{2.111}$$

The sum rule $\sum_s d_s = 2^n$ holds true from Newton binomial theorem.

The main ingredient to study the symmetry-resolved entanglement is the resolved partition function $Z_m(s)$ defined as

$$Z_m(s) \equiv {\rm Tr}\,(\Pi_s \rho_A^m) = {\rm Tr}\,(\Pi_s \rho^m_{\rm in/out})\,, \tag{2.112}$$

where Π_s here denotes the projection in the sector with magnetization s. In the singlet basis, all the blocks of $\rho_{\rm in/out}$ are diagonal with equal diagonal elements 2^{-n}. Consequently, a simple computation gives the symmetry-resolved moments (2.112) as

$$Z_m(s) = d_s 2^{-mn} = \binom{n}{n/2+s} 2^{-mn}. \tag{2.113}$$

We recall that, in terms of $Z_m(s)$, the symmetry-resolved Rényi entropies are

$$S_m(s) = \frac{1}{1-m} \ln \left[\frac{Z_m(s)}{Z_1^m(s)} \right], \tag{2.114}$$

which holds *for a given disorder realization*.

In principle, the distribution of Eq. (2.113) provide entirely the symmetry resolved quantum information properties in the random singlet phase. However, accessing such distribution is extremely hard; for this reason we consider different averages of the single disorder realization entanglement (2.114): this will allow to get indirect information about the entire distribution function.

Specifically, in the following we introduce three different quantities. All these observables are accessible to the cold-atom experiments like the one in Ref. [137]. In fact, in these experiments, one can access the single-disorder realizations of the symmetry resolved entropy, and consequently, perform all possible averages. We recall that, in the singlet language, the explicit meaning of the average is $\langle \bullet \rangle = \sum_{n=0}^{\infty} P(n) \bullet$.

The first one is

$$\overline{S}_m(s) = \frac{1}{1-m} \left\langle \ln \left[\frac{Z_m(s)}{Z_1^m(s)} \right] \right\rangle, \tag{2.115}$$

which is a genuine average of the symmetry resolved entropies. It is analogous to Eq. (2.44) for each symmetry sector. Although this is the most natural quantity, it is the less interesting one from a theoretical perspective, i.e., from the point of view of the information that is encoded into it.

The second one is

$$\widetilde{S}_m(s) = \frac{1}{1-m} \ln \left\langle \frac{Z_m(s)}{Z_1^m(s)} \right\rangle, \tag{2.116}$$

which represents the logarithm of the average of the m-th moment. It is the symmetry resolved version of Eq. (2.47) and it is the most suitable quantity to access the symmetry resolved entanglement spectrum.

Finally we also have

$$\widehat{S}_m(s) = \frac{1}{1-m} \ln \left[\frac{\langle Z_m(s) \rangle}{\langle Z_1(s) \rangle^m} \right], \tag{2.117}$$

which is the ratio of the averages of the symmetry resolved partitions. $\widehat{S}_m(s)$ has no equivalent in the definitions of total entropies, but it is the quantity naturally related to the Fourier transforms of charged entropies, as we shall also see in more details in the following. Hence it is the average that is closely related to clean systems.

Our main result, which we are going to show soon, is that all the entropies defined in Eqs. (2.115), (2.116) and (2.117) satisfy the same equipartition law for the leading and first subleading orders for large subsystem size ℓ. The violations of entanglement equipartition at higher-order are non-universal.

Before proceeding, some observations are in order to set up the calculations. First, plugging Eq. (2.113) into Eq. (2.115), we obtain that $\overline{S}_m(s)$ reads as

$$\overline{S}_m(s) = \left\langle \ln \binom{n}{n/2+s} \right\rangle. \tag{2.118}$$

Note that similarly to Eq. (2.46), $\overline{S}_m(s)$ does not depend on m. For $\widetilde{S}_m(s)$, plugging Eq. (2.113) into Eq. (2.116), one has the similar expression

$$\widetilde{S}_m(s) = \frac{1}{1-m} \ln \left\langle \binom{n}{n/2+s}^{(1-m)} \right\rangle . \tag{2.119}$$

Using Eq. (2.48), it is straightforward to see that Eq. (2.119) and (2.118) coincide in the limit $m \to 1$, leading to

$$\overline{S}(s) = \widetilde{S}(s) = \left\langle \ln \binom{n}{n/2+s} \right\rangle . \tag{2.120}$$

This result is also in full analogy with the total entropy where the two limits of Eq. (2.44) and (2.47) coincide at $m = 1$.

Conversely, $\widehat{S}_m(s)$ provides a different limit for $m \to 1$, Indeed, plugging Eq. (2.113) into Eq. (2.117) we have

$$\widehat{S}_m(s) = \frac{1}{1-m} \ln \frac{\left\langle 2^{-mn} \binom{n}{n/2+s} \right\rangle}{\left\langle 2^{-n} \binom{n}{n/2+s} \right\rangle^m}, \tag{2.121}$$

that in the limit $m \to 1$ becomes

$$\widehat{S}(s) = \frac{\left\langle n\, 2^{-n} \binom{n}{n/2+s} \right\rangle}{\left\langle 2^{-n} \binom{n}{n/2+s} \right\rangle} \ln 2 + \ln \left\langle 2^{-n} \binom{n}{n/2+s} \right\rangle , \tag{2.122}$$

where we used again the identity (2.48). Finally, it is important to notice that only the calculation of $\widehat{S}_m(s)$ involves explicitly $\langle Z_m(s) \rangle$.

2.4.1 Preliminaries

Before embarking into the specific calculations of the various entropies, we discuss the asymptotic limit in which we are interested and the simplifications taking place in such a limit. First of all, we observe that the main ingredient for the computation of symmetry resolved entropies are the averaged integer (negative) powers of the size d_s of block at fixed symmetry resolution s. We introduce the quantity $I_m(s)$ as

$$I_m(s) \equiv \langle d_s^{1-m} \rangle = \sum_{n=0}^{\infty} P(n) \binom{n}{n/2+s}^{(1-m)} , \tag{2.123}$$

which is directly related to the entropy $\widetilde{S}_m(s)$ as

$$\widetilde{S}_m(s) = \frac{\ln(I_m(s))}{1-m}. \tag{2.124}$$

The calculation of the average $I_m(s)$ at finite size is a hard task (likely impossible), since it requires a precise knowledge of the probability distribution $P(n)$. However, we are only interested in the scaling limit with large ℓ. In this case, the mean number of singlets $\langle n \rangle$ is large (cf. Eq (2.38)). Thus, for the average in Eq. (2.123), we can focus on the large n limit, using the Stirling approximation to expand the Newton binomial in Eq. (2.123) to obtain:

$$\binom{n}{n/2+s}^{1-m} = 2^{n(1-m)} \left(\frac{\pi n}{2}\right)^{\frac{m-1}{2}} \sum_{k=0}^{\infty} Q_k(n) \left(\frac{s}{n}\right)^{2k}, \tag{2.125}$$

where $Q_k(n)$ are algebraic functions in n. For instance, one has:

$$Q_0(n) = 1 + O\left(\frac{1}{n}\right), \tag{2.126}$$

$$Q_1(n) = 2(m-1)n + O(1). \tag{2.127}$$

We are interested in small values of s since they are those with a significant contribution to the total entropy (the probability $p(s)$ is expected to decay very quickly with s, as we self-consistently show). Then, in the limit of $n \gg s$, the only relevant term is the one with $k = 0$ in Eq. (2.125), i.e.,

$$\binom{n}{n/2+s}^{1-m} \simeq \left(\frac{\pi n}{2}\right)^{\frac{m-1}{2}} 2^{n(1-m)}. \tag{2.128}$$

Recalling that $g(\sigma) \equiv \langle e^{-n\sigma}\rangle$ (cf. Eq. (2.39)), the average over the disorder of Eq. (2.128) for m odd is straightforwardly related to the derivative of $g(\sigma)$. Consequently we have

$$I_m(s) \simeq \langle 2^{n(1-m)}(\pi n/2)^{\frac{m-1}{2}}\rangle = \left(\frac{\pi}{2}\right)^{\frac{m-1}{2}} \frac{\partial^a g(\sigma)}{\partial(-\sigma)^a}\bigg|_{\sigma=(m-1)\ln 2, a=\frac{m-1}{2}}. \tag{2.129}$$

One can easily perform explicitly the a-th derivative (at leading order), obtaining after simple algebra

$$I_m(s) \simeq I_m^{(0)} \equiv \frac{1}{2} e^{-\frac{1}{2}(3-\sqrt{5+2^{3-m}})\mu}\left(1 + \frac{3}{\sqrt{5+2^{3-m}}}\right)\left(\frac{\pi 2^{-m}\mu}{\sqrt{5+2^{3-m}}}\right)^{\frac{m-1}{2}}, \tag{2.130}$$

where $\mu = \ln \ell + \dots$ is the same as in Eq. (2.42). At this point, we have an analytic expression for odd m. It is very reasonable to assume that the same expression indeed provides the correct result for even m. An explicit calculation valid for arbitrary real m can be performed by exploiting the Laplace transform of Eq. (2.123) for large n. The calculation is very cumbersome, although it employs only standard techniques of complex integration. To maintain a clear exposition of our results, we report the details in Appendix 2.7 and just state here that such a complex calculation reproduces Eq. (2.130) at the leading order (but suggests that some deviations are present at subleading ones).

Let us quickly discuss what Eq. (2.125) suggests for the correction to the leading behavior in Eq. (2.130). The first corrections comes from the term with $k = 1$ that for large n multiplies the leading factor by a term $\propto s^2/n$. This implies that such a correction term is proportional to $\langle 2^{n(1-m)} n^{\frac{m-1}{2}-1}\rangle$. Once again, using the derivative trick in Eq. (2.129), we quickly obtain that this correction is $\propto I_m^0/\mu$. Recalling that $\mu = \ln \ell + O(\ell^0)$, we conclude that

$$I_m(s) = I_m^{(0)}\left(1 + (m-1)2^m\sqrt{5+2^{3-m}}\,\frac{s^2}{\ln \ell} + \dots\right), \tag{2.131}$$

where we explicitly work out the constant multiplying $s^2/\ln \ell$. This analysis suggests that the first term that breaks equipartition in $I_m(s)$ is proportional to $s^2/\ln \ell$. This is reminiscent of what observed for clean systems in few different situations [156, 161]. However, we must stress that Eq. (2.131) should be taken with a grain of salt. Indeed, it assumes the validity of the form (2.41) for $g(\sigma)$ also for the subleading term. It is however known that subleading non-universal terms, not encoded in $g(\sigma)$, are present; they are model-dependent and more difficult to calculate (see Ref. [34] for an in-depth discussion).

2.4.2 Entanglement equipartition for $\overline{S}_m$

The first case we consider is the symmetry resolved entropy $\overline{S}_m(s)$ defined in Eq. (2.115) and given by the mean value of $\ln d_s$, cf. Eq. (2.118). This logarithm is simply deduced by exploiting

$$\left\langle \ln \binom{n}{n/2+s} \right\rangle = -\frac{\partial}{\partial m} I_m(s)\bigg|_{m=1}, \tag{2.132}$$

and using the zeroth order approximation for $I_m(s)$ in Eq. (2.130). Keeping the subleading terms up to $O(\ell^0)$, we obtain

$$\begin{aligned}\overline{S}_m(s) &= \frac{\ln 2}{3}\mu - \frac{1}{2}\ln\left(\frac{\pi}{6}\mu\right) - \frac{\ln 2}{9} + O(\mu^{-1}) \\ &= \overline{S} - \frac{1}{2}\ln\left(\frac{\pi}{6}\mu\right) + O(\mu^{-1}) = \overline{S} - \frac{1}{2}\ln\ln\ell + \dots .\end{aligned} \tag{2.133}$$

Equation (2.133) is the first main result of this Section: it shows the entanglement equipartition of the random singlet phase for the entropy $\overline{S}_m(s)$. The leading contributions to these Rényi entropies are the same for all the symmetry sectors. The first term is just the total entanglement. We will discuss the origin of $-1/2\ln\ln\ell$ at the end of the section, because the same term will appear in all other entropies we consider. The $O(1)$ term is not universal, but we reported it here for some comparisons we will do later on.

Let us briefly discuss the corrections to this leading behavior. Exploiting Eq. (2.131), i.e., considering only those coming from Eq. (2.125), we simply have that the first term breaking equipartition should behave as $s^2/\ln\ell$. More quantitatively, from Eq. (2.131) we have

$$\overline{S}_m(s) - \overline{S}_m(0) = -6\frac{s^2}{\mu}. \tag{2.134}$$

Accordingly, at least at this order and within these approximations, $\overline{S}_m(s)$ is a monotonous *decreasing* function of $|s|$.

2.4.3 Entanglement equipartition of $\widetilde{S}_m$

Here we show the entanglement equipartition for the Rényi entropies $\widetilde{S}_m$ for arbitrary m. The integral $I_m(s)$ is directly related to $\widetilde{S}_m(s)$ as $\widetilde{S}_m(s) = (\ln I_m(s))/(1-m)$. Hence, we have

$$\begin{aligned}\widetilde{S}_m(s) &= \frac{\sqrt{2^{3-m}+5}-3}{2(1-m)}\mu - \frac{1}{2}\ln\frac{2^{-m}\pi\mu}{\sqrt{2^{3-m}+5}} + \frac{1}{1-m}\ln\left(\frac{3}{2\sqrt{2^{3-m}+5}} + \frac{1}{2}\right) + O(\mu^{-1}) \\ &= \widetilde{S}_m - \frac{1}{2}\ln\frac{2^{-m}\pi\mu}{\sqrt{2^{3-m}+5}} + O(\mu^{-1}) = \widetilde{S}_m - \frac{1}{2}\ln\ln\ell + \dots .\end{aligned} \tag{2.135}$$

The leading logarithmic term is the same as in the total Rényi entropy $\widetilde{S}_m$. Again, there is an additional universal double-logarithmic term in ℓ which is not present in the total entropy. Both these terms are independent of the symmetry sector s, i.e., the symmetry-resolved Rényi entropies $\widetilde{S}_m(s)$ exhibit equipartition. In both Eqs. (2.135) and (2.133), we have been very careful to write the entire subleading term at order $O(\ell^0)$. This has been done to show their relationship with the $O(\ell^0)$ terms in the total entropies from Ref. [34]. We stress however that they have all been obtained with the assumptions used to derive $g(\sigma)$ in Ref. [34].

Even for this entanglement measure, from Eq. (2.131), we expect subleading logarithmic corrections to Eq. (2.135) to violate equipartition as $s^2/\ln\ell$. Specifically, from Eq. (2.131) we have

$$\widetilde{S}_m(s) - \widetilde{S}_m(0) = -2^m\sqrt{2^{3-m}+5}\frac{s^2}{\mu}. \tag{2.136}$$

Once again, at least at this order and within these approximations, $\widetilde{S}_m(s)$ is a monotonous *decreasing* function of $|s|$ for all values of m.

2.4.4 Entanglement equipartition for $\widehat{S}_m$

In this section we explicitly compute $\widehat{S}_m(s)$ and show that entanglement equipartition holds also for it. Moreover, we will show that also the double logarithnmic term is the same as for $\widetilde{S}_m(s)$ and $\overline{S}_m(s)$.

The main ingredient to compute $\widehat{S}_m(s)$ is the average $\langle Z_m(s)\rangle$. Here the strategy is to first evaluate the disorder average of the charged moments $\langle \mathcal{Z}_m(\alpha)\rangle$ and then to perform a Fourier transform (cfr. Eq. (2.14)). *En passant* this will give access to the probability $p(s)$ characterizing each sector's population.

In a given disorder realization with n shared singlets, the charged moment $\mathcal{Z}_m(\alpha)$ reads

$$\mathcal{Z}_m(\alpha) = \sum_{s=-n/2}^{n/2} 2^{-mn} \binom{n}{n/2+s} e^{i\alpha(s-n)/2} \left[2^{(1-m)} \cos\left(\frac{\alpha}{2}\right)\right]^n , \tag{2.137}$$

and consequently its disorder average is

$$\langle \mathcal{Z}_m(\alpha)\rangle = g\left(2^{(1-m)} \cos\left(\frac{\alpha}{2}\right)\right), \tag{2.138}$$

where $g(\sigma)$ is the generating function in (2.39). Incidentally for $m = 1$, $\langle \mathcal{Z}_1(\alpha)\rangle$ is the full counting statistic generating function of this disordered model.

Exploiting the explicit knowledge of $g(\sigma)$ in Eq. (2.41), the Fourier transform of Eq. (2.138) can be computed by using the saddle point approximation in the scaling limit $\ell \gg 1$ (equivalently $\mu \gg 1$, cfr. Eq. (2.42)), obtaining

$$\langle Z_m(s)\rangle = \left(\frac{1}{2} + \frac{3}{2\sqrt{5+2^{3-m}}}\right) e^{-\frac{3}{2}\mu + \frac{\sqrt{5+2^{3-m}}}{2}\mu} \sqrt{\frac{2^m\sqrt{5+2^{3-m}}}{\pi\mu}} \exp\left[-\frac{2^m\sqrt{5+2^{3-m}}}{\mu} s^2\right]. \tag{2.139}$$

Interestingly, in this approximation $\langle Z_m(s)\rangle$ has the very same structure of conformal result, cf. Eq. (2.15), i.e., it is gaussian with variance $\propto \mu$. From Eq. (2.139) we can directly read out the probability for the subsystem magnetization to be equal to s as

$$p(s) = \langle Z_1(s)\rangle = \sqrt{\frac{6}{\pi\mu}} \exp\left[-\frac{6s^2}{\mu}\right]. \tag{2.140}$$

Finally, we plug the partition function (2.139) into the definition (2.117), to get the entropy $\widehat{S}_m(s)$ as

$$\begin{aligned} \widehat{S}_m(s) &= \widetilde{S}_m(s) + \frac{m}{2(m-1)} \ln\left(\frac{2^m}{6}\sqrt{2^{3-m}+5}\right) + O(\mu^{-1}) \\ &= \frac{\sqrt{2^{3-m}+5}-3}{2-2m} \ln\ell - \frac{1}{2}\ln\ln\ell + \dots \\ &= \widetilde{S}_m - \frac{1}{2}\ln\ln\ell + \dots . \end{aligned} \tag{2.141}$$

We see that at leading universal orders $\widehat{S}_m(s) = \widetilde{S}_m(s)$ (and the same holds in the limit $m \to 1$), with a non-universal $O(\ell^0)$ difference in the thermodynamic limit.

We close this subsection with the highlight of a peculiar phenomenon which characterizes the s-dependence of the entropies $\widehat{S}_m(s)$. From Eq. (2.139), the equipartition is again broken at order s^2/μ. Anyhow, this subleading term breaking equipartition has not a definite sign with m, as an important difference with all considered cases, not only in this Section, but in the entire literature. This phenomenon can be easily seen by analyzing the difference $\widehat{S}_m(s) - \widehat{S}_m(0)$, i.e.,

$$\widehat{S}_m(s) - \widehat{S}_m(0) = \frac{(6m - 2^m\sqrt{2^{3-m}+5})}{1-m} \frac{s^2}{\mu}, \tag{2.142}$$

where to get the rhs we explicitly used Eq. (2.139). The coefficient of the term multiplying s^2 is negative for $m < m^* = 2.695\dots$ and positive for $m > m^*$. This change of sign causes the Rényi entropy to be a monotonous *decreasing* function of $|s|$ for $m < m^*$, as all the cases considered so far in the literature, while it is a monotonous *increasing* function of $|s|$ for $m > m^*$. It is natural to wonder whether and how

this intriguing phenomenon survives to the effect of the further subleading corrections that are not taken into account by $g(\sigma)$ in Eq. (2.41). We will answer this question with the analysis of the numerical data in Sec. 2.4.6.

2.4.5 The number entropy and the log-log term

In this subsection we heuristically discuss about the number entropy and its relation with the first subleading term in the symmetry resolved entanglement. Eq. (2.9) guarantees that for each realization of the disorder (let us say r) it holds

$$S_r = -\sum_s p_r(s) \ln p_r(s) + \sum_s p_r(s) S_r(s) \,. \tag{2.143}$$

Taking the average over the disorder means to mediate only *after* the sum over s has been performed.

If we assume *self-averaging*, we can invert the two sums/averages, obtaining

$$\overline{S} = -\sum_s p(s) \log p(s) + \sum_s p(s) \overline{S}(s), \tag{2.144}$$

where $p(s)$ is the average probability of configurations with subsystem magnetization s given in Eq. (2.140). Within this assumption, the number entropy is

$$S_{\rm Q} = -\int ds p(s) \ln p(s) = \frac{1}{2}\Big(1 + \ln \frac{\pi\mu}{6}\Big) \,, \tag{2.145}$$

i.e., it diverges like $\ln \mu$ for large μ, i.e., like $\ln \ln \ell$. This $\ln \mu$ divergence is identical to the one that appears in the symmetry resolved entropy $\overline{S}(s)$. Indeed, since at this order in μ the symmetry resolved entropy $\overline{S}(s)$ does not show any s-dependence, we have $\sum_s p(s)\overline{S}(s) = \overline{S}(s)$ and the term $\ln \mu$ (absent in the total entropy $\overline{S}$) should be compensated by an identical term in $\overline{S}(s)$.

The above equivalence between number entropy and subleading term in the symmetry resolved one takes place in a very similar form also for clean system described by a Luttinger liquid. There the subleading term $\frac{1}{2}\ln(K \ln \ell)$ reflects that the charge fluctuations of the subsystem are proportional to [139, 189, 190] $K \ln \ell$ (cfr. (2.15)). The prefactor is again $1/2$ and also cancels in the total entropy when summing number and symmetry resolved ones.

This is not the end of the story. For clean systems, also the $O(1)$ term in the symmetry resolved entropies is independent of s. Hence it is also equal to the one for the total entropy (modulo the shift in the number entropy as in (2.145)). By comparing carefully Eqs. (2.133), (2.144), and (2.145) this *does not seems to be the case for random systems*. Most likely this mismatch is due to the lack of self averaging for the subleading term. Another possible explanation could be also the presence of s-dependent $O(1)$ terms in the symmetry resolved entropy which are not captured by $g(\sigma)$ in Eq. (2.41) (that, as we stressed, ignores several subleading effects).

Finally, we have found the same term $-\frac{1}{2}\ln \mu$ to be present in *all* symmetry resolved entropies independently also of the Rényi index. This fact can be understood reasoning similarly to what done above. First, for $m = 1$ it is sufficient to assume self-averaging for the entropy of interest. Instead for $m \neq 1$, Eq. (2.9) for the splitting in number and configurational entropy does not hold. It is also not possible to rewrite a similar form using only the probability $p(s)$. However, we can exploit the recent result [161] for a different splitting involving the generalized probabilities $p_m \equiv Z_m(s)/Z_m$ (Z_m is the exponential of the total Rényi entropies). The complete check is straightforward and not very illuminating, one just needs to assume self averaging for all the quantities of interest. In conclusion, this argument explains why the term $-\frac{1}{2}\ln \mu$ is present in all the quantities we considered with the same prefactor, in spite the coefficient of the leading term (in $\mu = \ln \ell + \dots$) is not the same.

2.4.6 Numerical SDRG results

In this section we present numerical simulations supporting our analytic results. We implement numerically the SDRG method for a finite-size Heisenberg chain. Specifically, the method works according to the following steps. We initialize a list of length L with the chain couplings J_i. We take the $\{J_i\}$ to be independent random variables with $J_i \in [0,1]$ and extracted from the probability distribution

$$p(J) = \frac{1}{\delta} J^{-1+1/\delta}. \tag{2.146}$$

Here $\delta > 0$ is a parameter characterizing the strength of the randomness: $\delta = 1$ is the uniform distribution, while $\delta \to \infty$ correspond to strong disorder (i.e., to the RG fixed point). We implement the Ma-Dasgupta decimation rule, Eq. (2.24), which is iterated on the list of couplings until all the spins are decimated. During the iteration the algorithm keeps track of all the singlets that are formed. The method is repeated for many random realizations of the couplings. From the spatial information about the singlets, it is straightforward to calculate the von Neumann and Rényi entropies. Given a bipartition of the system as $A \cup B$, these are obtained by counting the number of shared singlets between the subsystems and by applying (2.31). The symmetry-resolved entanglement entropies can be calculated in a similar way. In fact, in a given disorder realization the SDRG method produces n shared singlets. This means that there are $(n+1)$ blocks. Each block, labelled by the quantum number s, is diagonal, and has dimension d_s (cf. (2.111)). Thus, from the spatial configuration of singlets it is straightforward to calculate the symmetry-resolved entropies for each disorder realization and their averages $\overline{S}_m(s)$, $\widetilde{S}_m(s)$, and $\widehat{S}_m(s)$ according to the specific rules in Eqs. (2.118), (2.119) (2.121), respectively.

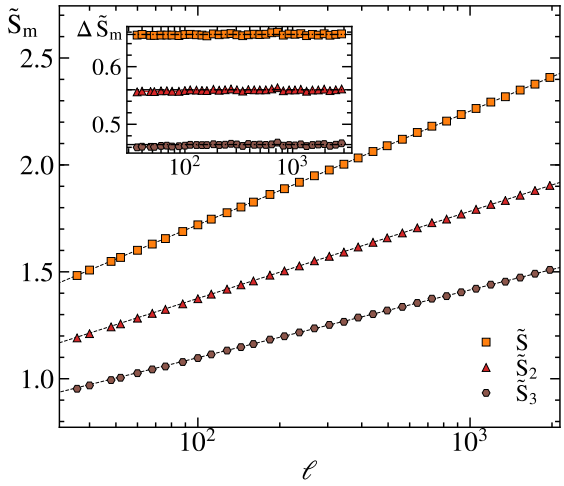

FIGURE 2.4: Total Rényi entropies $\tilde{S}_m$ in the disordered Heisenberg chain, plotted against the subsystem size ℓ. Symbols represent numerical SDRG simulation with system size $L = 16384$, disorder strength $\delta = 5$, and average over $N \approx 10^6$ disorder configurations. Different symbols and colors correspond to different Rényi index $m = 1, 2, 3$. Dashed lines are the analytical predictions, Eq. (2.147). In the inset we report $\Delta\tilde{S}_m$ in Eq. (2.148) clearly showing that the leading corrections are $O(\ell^0)$.

Preliminary benchmarks

Before presenting the numerical results for the symmetry-resolved entanglement, it is important to reanalyze the behavior of the total, i.e., non symmetry-resolved, von Neumann and Rényi entropies. In fact, a striking feature of the symmetry-resolved entropies is that they possess subleading double-logarithmic corrections that are not present in the total ones. Thus it is worth reanalyzing the total entanglement to exclude log-log terms also here and to emphasize the differences with the symmetry resolved ones.

Our results for the von Neumann entropy and for the Rényi entropies $\widetilde{S}_m$ ($m = 1, 2, 3$) are shown in Fig. 2.4. The symbols are numerical data for a chain with $L = 16384$ sites (finite size scaling is discussed later) and for a disorder strength $\delta = 5$ (other values of δ provide equivalent result, as discussed for the symmetry resolved ones). The data are obtained by averaging over $N \approx 10^6$ disorder realizations. The continuous lines are the theory predictions obtained as a fit of the form

$$\widetilde{S}_m = \frac{\sqrt{5 + 2^{3-m}} - 3}{2(1-m)} \ln \ell + a, \tag{2.147}$$

in which a is the only fitting parameter. The agreement between the SDRG results and (2.147) is good for all the entropies. However, in order to have a better feeling of the subleading term, in the inset we plot the subtracted entropy

$$\Delta\widetilde{S}_m \equiv \widetilde{S}_m - \frac{\sqrt{5 + 2^{3-m}} - 3}{2(1-m)} \ln \ell \,. \tag{2.148}$$

This inset provides a strong evidence that the leading correction to the entropy is $O(\ell^0)$, ruling out the presence of a log-log term.

We do not report the numerics for $\overline{S}_m$ because they coincide with $\widetilde{S} = \widetilde{S}_1$ by definition (see the discussion in Sec. 2.4.2).

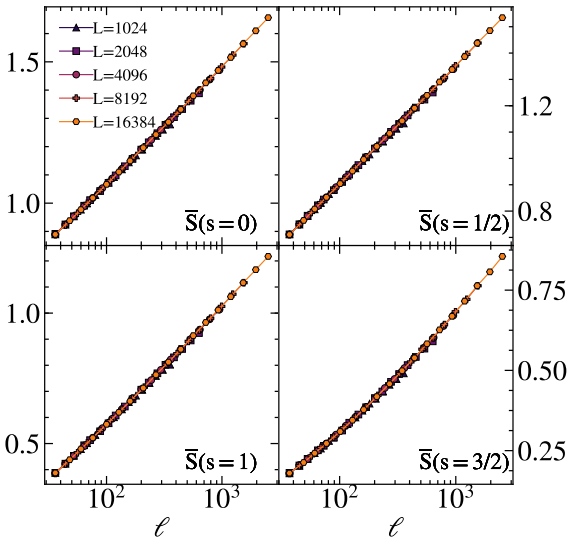

FIGURE 2.5: Finite size behavior of the disorder averaged symmetry resolved entropies $\overline{S}(s)$. We report the numerical data for L from 1024 to 16384. The four panels are for $s = 0, 1/2, 1, 3/2$. All data correspond to disorder strength $\delta = 1$ (uniform distribution) and are averaged over 10^6 disorder realizations. For the considered values of ℓ there are no visible finite size corrections.

Symmetry-resolved von Neumann entropy

We now discuss the symmetry-resolved von Neumann entropy in the random singlet phase. We will consider both $\overline{S}(s)$ in Eq. (2.120) and $\widehat{S}(s)$ in Eq. (2.122). We recall that $\overline{S}(s)$ is the limit $m \to 1$ of both $\overline{S}_m(s)$ and $\widetilde{S}_m(s)$.

We start with the analysis of the finite size behavior. In Fig. 2.5 we report the numerical data for $\overline{S}(s)$ at fixed disorder $\delta = 1$ for $L = 1024, 2048, 4096, 8192, 16384$. The averages are over $\approx 10^6$ disorder realizations. The subsystem magnetization s can assume both integer of semi-integer values, depending on the parity of ℓ. Hence, hereafter the data for $s = 0, 1, 2$ correspond to even ℓ, while the data for $s = 1/2, 3/2$ are for odd ℓ (everywhere for each even ℓ considered, we also plot $\ell + 1$). In Fig. 2.5, the data for all reported values of ℓ are on top of each other and there is no visible finite size correction for any s. Then in

the following, we will work mainly at $L = 16384$ and consider values of ℓ up to ~ 3000 for which there are no appreciable corrections. We checked that this feature is universal, i.e., does not depend either on disorder strength δ or on the considered entropy. In all this Section, we only report positive values of s, but we tested that for $s \to -s$ we get exactly the same results.

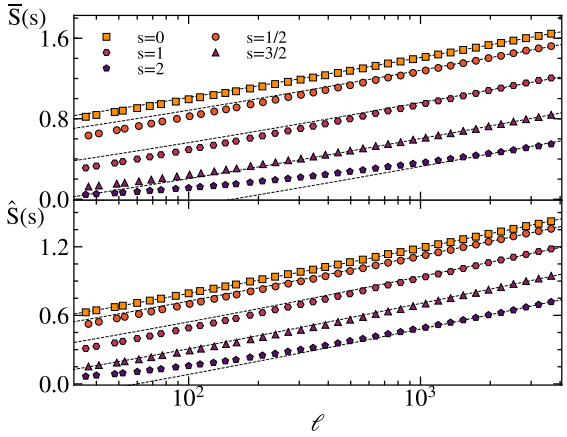

FIGURE 2.6: Symmetry resolved entanglement entropy $\overline{S}(s)$ (top) and $\widehat{S}(s)$ (bottom) in the disordered Heisenberg chain, against the subsystem size ℓ. Symbols are numerical results using the SDRG method with system size $L = 16384$ and average over $N \approx 10^6$ disorder realizations with disorder strength $\delta = 5$. Different symbols and colors correspond to different symmetry sectors $s = 0, 1/2, 1, 3/2, 2$. The dashed lines represent the theory prediction (2.149) in which a has been adjusted to fit the data.

We are now ready to start our analysis of the symmetry resolved entropies. In Fig. 2.6 we compare our analytical formulas with numerical SDRG results. The data are for a chain with $L = 16384$ sites and are obtained by averaging over $N \approx 10^6$ disorder realizations. Data are plotted as function of ℓ. The different symbols correspond to the different symmetry sectors s. We report the data for both $\overline{S}(s)$ (top panel) and $\widehat{S}(s)$ (bottom panel). For large ℓ all curves become parallel, showing asymptotic equipartition, as we theoretically derived in the previous section. The curves however are not superimposed, manifesting that the subleading corrections do depend on s. Furthermore we find that the various curves are monotonously decreasing function of $|s|$, as theoretically predicted in the previous section. In this respect, it is important that non-universal terms not included in the approximations that led to Eqs. (2.134) and (2.142) do not spoil such a result.

The dashed lines in figure 2.6 are fit to the form

$$\frac{\ln(2)}{3} \ln \ell - \frac{1}{2} \ln \ln \ell + a, \tag{2.149}$$

with a single free parameter a. We use the same form for both $\overline{S}(s)$ and $\widehat{S}(s)$ since in SDRG they show the same asymptotic scaling (cf. Eq. (2.141)) with a different $O(\ell^0)$ term, i.e., with a different a in the above equation. The fit is performed only with the data for large ℓ. The agreement is really good taking into account that we only have one parameter in the fit. It is clear that the corrections to the scaling become more important for larger values of $|s|$, as it was expected on the bases of the result of the previous section. Needless to say that the presence of the term $-1/2 \ln \ln \ell$ in Eq. (2.149) is fundamental to have such agreement.

However, proceeding in this way, we would have the additive constant a which does depend on s. Conversely, the SDRG results in Eqs. (2.134) and (2.142) suggest that this is not the case. It is also true that our SDRG treatment ignores some non-universal processes that do not alter the two leading terms, but at least in principle can affect the constant. On the other hand, within SDRG we have also shown the presence of s-dependent terms behaving like $s^2/\ln \ell$ (indeed these log-corrections are typical features of symmetry resolved entanglement entropies also in clean systems [156, 161]). Can these corrections be responsible for

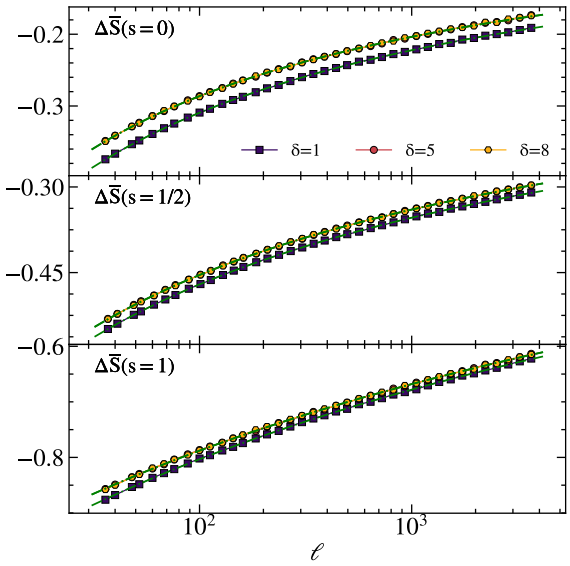

FIGURE 2.7: Subtracted symmetry resolved entanglement entropy $\Delta S(s)$ in Eq. (2.150) for $s = 0, 1/2, 1$ (from top to bottom) in the disordered Heisenberg chain, against the subsystem size ℓ. Symbols are numerical results using the SDRG method with system size $L = 16384$ and average over $N \approx 10^6$ disorder realizations. Different symbols and colors correspond to different disorder strength $\delta = 1, 5, 8$. The data are slowly approaching 0 according to the law (2.151). The fits are reported as lines and perfectly match the data.

a seemingly s-dependent additive constant? To answer this question we study the difference

$$\Delta\overline{S}(s) \equiv \overline{S}(s) - \overline{S} + \frac{1}{2}\ln\left(\frac{\pi}{6}\ln\ell\right). \tag{2.150}$$

This subtraction is motivated by the fact that the additive constant not only is s independent, but also equal the one for the total entropy (modulo the additive factor within the number entropy). Hence, according to our SDRG results, $\Delta\overline{S}(s)$ should decay to zero for large ℓ as

$$\Delta\overline{S}(s) \simeq \frac{b}{\ln\ell + c}, \tag{2.151}$$

where b and c are free non-universal parameter that may (and actually do) depend on s. We analyze the SDRG data for $\Delta\overline{S}(s)$ in Fig. 2.7 where we consider three different disorder distributions with strength $\delta = 1, 5, 8$ to rule out the possibility of some weak disorder effect. It is evident that δ only mildly influences the data and for $\delta = 5$ and $\delta = 8$ there are no differences at all. The three panels in the figure correspond to $s = 0, 1/2, 1$. The numerical data are fit to the form (2.151). The agreement is truly impressive when one thinks that we are fitting curves that asymptotically tend to zero, but we are working in a regime where they are still far from it. Increasing the values of s, subleading terms, e.g. going like $s^2/(\ln\ell)^2$ or $s^4/(\ln\ell)^\alpha$, becomes important and it is more difficult to fit the data with (2.151) at the available values of ℓ. Finally we mention that we repeated the same analysis also for the entropy $\widehat{S}(s)$ finding equivalent results for the equipartition.

Concluding, Fig. 2.7 is a very strong and convincing evidence that the prediction from SDRG in Eq. (2.134) survives the inclusion of non-universal effects and that there is equipartition of entanglement at the order $O(\ell^0)$ also in the random singlet phase. The first term breaking equipartition $s^2/\ln\ell$ is also correctly captured by SDRG in Eq. (2.134).

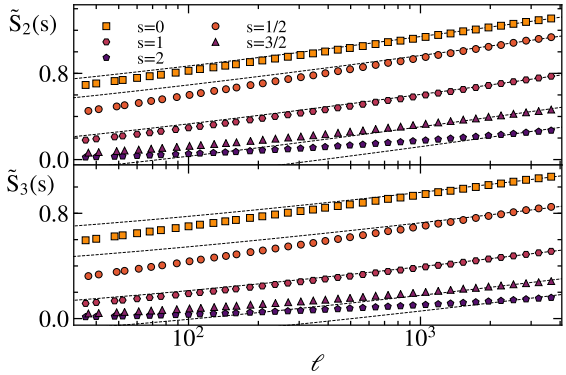

FIGURE 2.8: Symmetry-resolved Rényi entropies $\widetilde{S}_m(s)$ for $m = 2$ (top) and $m = 3$ (bottom). The symbols are SDRG results for the Heisenberg chain with $L = 16384$ sites. The average is over 10^6 disorder realizations with strength $\delta = 5$. Different symbols and colors correspond to different subsystem magnetization $s = 0, 1/2, 1, 3/2, 1$. The dashed lines are fits to the form (2.152).

Symmetry-resolved Rényi entropies

We now discuss the symmetry-resolved Rényi entropies. For many aspects the analysis is identical to the one of the previous section for the von Neumann one and we will not repeat all details.

We first consider $\widetilde{S}_m(s)$ (since $\overline{S}_m(s)$ do not depend on m, there is no reason to discuss them). In Fig. 2.8 we plot SDRG data for $m = 2, 3$. In the scaling limit all the Rényi entropies exhibit equipartition and are described by

$$\widetilde{S}_m(s) = \frac{\sqrt{2^{3-m}+5}-3}{2(1-m)} \ln \ell - \frac{1}{2} \ln \ln \ell + a + \dots . \tag{2.152}$$

Again, the first term in (2.152) is the result for the total Rényi entropies, $\widetilde{S}_m$. Note that the subleading term $1/2 \ln \ln \ell$ is the same as for the von Neumann entropy. For large ℓ all curves at fixed m become parallel, showing asymptotic equipartition. Anyhow, they are not on top of each other, manifesting that the subleading corrections do depend on s.

The first check to test the asymptotic behavior is to perform a simple fit of the data to the form (2.152) allowing a to depend on s. These fits are shown in Fig. 2.8 as continuous lines. The agreement is excellent and, as expected, it slowly deteriorates increasing $|s|$. We have performed an analysis like the one in Fig. 2.7 for the von Neumann entropy to convince ourselves that the differences between the various curves at fixed s are, as SDRG predicts in Eq. (2.136), only due to subleading term as $s^2/\ln \ell$. The analysis shows that this is likely, but the corrections are much larger than for $m = 1$ and so more difficult to treat. This is not unexpected: Eq. (2.136) predicts that the coefficient of $s^2/\ln \ell$ grows exponentially with m (being ~ 6 at $m = 1$, ~ 10.6 at $m = 2$, and ~ 20 at $m = 3$) and so the data soon become difficult to handle as m increases.

Finally, we discuss the Rényi entropies $\widehat{S}_m(s)$, focusing on $m = 2, 3$. Before discussing the scaling behavior of the entanglement entropies, it is useful to consider the partition functions $\langle Z_m(s) \rangle$, being the main ingredient to construct $\widehat{S}_m(s)$ and being per se interesting (for $m = 1$, $\langle Z_1(s) \rangle$ is the average probability $p(s)$ of having subsystem magnetisation s, cf. Eq. (2.140), while for other m are related to generalized probability distributions [161]).

In Fig. 2.9, we present a quantitative comparison for $\langle \mathcal{Z}_m(\alpha) \rangle$ and $\langle Z_m(s) \rangle$ between the numerics and the analytic predictions, respectively in Eqs. (2.138) and (2.139). The additive constant in μ (cfr. Eq. (2.42)) appearing in both formulas is preliminary fitted only once for all data. The numerical data are obtained by averaging Eq. (2.137) for $\langle \mathcal{Z}_m(\alpha) \rangle$ and Eq. (2.113) for $\langle Z_m(s) \rangle$. For $\langle \mathcal{Z}_m(\alpha) \rangle$, we observe a fair agreement between our data and the analytic expressions, although finite size corrections are present as $\alpha \to \pm\pi$ (the plot is in log scale). The discrepancies at the boundaries of the Brillouin zone are well known for clean systems [156, 157, 168] and are physically due to the fact that such charged entropies must

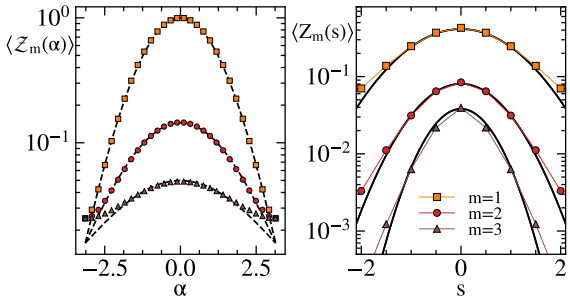

FIGURE 2.9: Charged (left) and symmetry-resolved (right) moments, $\langle \mathcal{Z}_m(\alpha)\rangle$ and $\langle Z_m(s)\rangle$. Symbols represent numerical SDRG simulation with system and subsystem sizes $L = 8192$ and $\ell = 3722$, respectively. The average is over $N \approx 10^6$ disorder configurations and the strength of the disorder is $\delta = 1$. Different symbols and colors correspond to different index $m = 1, 2, 3$. Dashed and full lines are the analytic predictions, Eq. (2.138) and Eq. (2.139), respectively.

be periodic of period 2π. Then they should be present in lattice disorder systems as well. Also the data for $\langle Z_m(s)\rangle$ are remarkably reproduced by SDRG predictions, with corrections to the scaling that become larger as $|s|$ increases, as it is the case for all the quantities considered so far. Incidentally, we did not yet mention that, very generically, deviations at higher s are expected, because populating higher sectors requires exponentially larger system sizes.

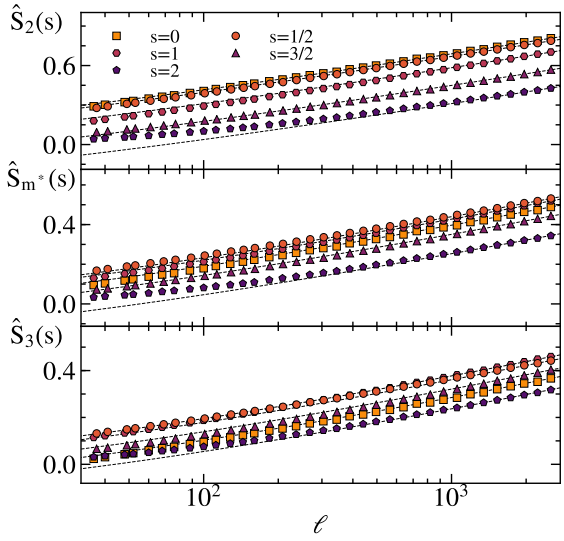

FIGURE 2.10: Symmetry-resolved Rényi entropies $\widehat{S}_m(s)$ for $m = 2$, $m = m^* = 2.69\ldots$, and $m = 3$ (from top to bottom). The symbols are SDRG results for the Heisenberg chain with $L = 16384$ sites and disorder strength $\delta = 5$. The average is over 10^6 disorder realizations. Different symbols and colors correspond to different subsystem magnetization $s = 0, 1/2, 1$. The lines are fits to the theoretical result (2.153). Notice that the entropies are ordered as monotonically decreasing function of s for $m = 2$, are mixed up at $m = m^*$, and start inverting their order for $m = 3$.

We are then ready to analyze the symmetry-resolved entropies $\widehat{S}_m(s)$ which are plotted in Fig. 2.10. Again, for asymptotic large ℓ the various curves for different s at fixed m become parallel, manifesting equipartition. As done for all other entropies, we first check the correctness of the leading scaling term that in SDRG is given by Eq. (2.141). In Fig. 2.10, the continuous lines are fit of the data with

$$\widehat{S}_m = \frac{\sqrt{2^{3-m}+5}-3}{2(1-m)} \ln \ell - \frac{1}{2} \ln \ln \ell + a + \ldots \tag{2.153}$$

where we allow a to depend on s. We observe a good asymptotic agreement in Fig. 2.10 confirming the correctness of the leading term.

We now move to the corrections. In this case the analysis is very difficult because of the peculiar non-monotonic features we highlighted at the end of Sec. 2.4.4 in Eq. (2.142). Indeed while they are always of the form $s^2/\ln \ell$, the prefactor is negative for $m < m^*$ (as in all other cases observed so far here and in the literature) and it is positive for $m > m^*$. Close to m^*, the subsubleading terms become important and larger than the ones under scrutiny that instead vanish at $m = m^*$. Exactly for this reason in the Fig. 2.10 we report $m = 2$, $m = m^*$, and $m = 3$. We observe that the entropies are ordered as monotonically decreasing function of s for $m = 2$, they are mixed up at $m = m^*$ (which is the point where the leading corrections to the scaling vanish in SDRG) and they tend to reverse their order for $m = 3$, although they are not in increasing order in s, likely because of subleading corrections (m^* is very close to 3). We found extremely remarkable that this unusual effect predicted by SDRG is not spoiled by non-universal effects as well as by other universal RG processes that have not been included in the derivation of $g(\sigma)$ in Eq. (2.41) presented in Ref. [34].

2.5 Conclusion

In this Chapter we have studied the negativity spectrum and the symmetry resolved entanglement entropy in the random singlet phase.

For the negativity spectrum, our results are based on the Ma-Dasgupta decimation rule, which leads to a renewal equation for the probability distribution of in-out singlets in a tripartition of an infinite disordered spin chain in the random singlet phase. This procedure assumes that the most relevant renormalization effect is a single decimation occurring at a specific bond. The distribution resulting from the solution of the renewal equation provides analytic results for the negativity moments in the RSP and for their analytic continuations. We focused on the case of adjacent intervals and the results have been numerically tested by means of *ab-initio* simulations and numerical strong disorder renormalization group techniques, finding perfect agreement. While the logarithmic negativity depends only on the average value of the singlets forming in the system, we find that the negativity spectrum depends on their full probability distribution. Therefore, an important consequence is that our analytic results can be used to reconstruct the full probability distribution of the number of singles $n_{A_1:A_2}$ between two generic subsystems. This generalizes the same result for the distribution $n_{A:B}$ for complementary subsystems, which follows from the knowledge of the entanglement spectrum. A second intriguing result of our analysis is that the negativity and logarithmic negativity are not trivially related after the average over the disorder: this can be understood as a consequence of the well-known different scaling of *average* and *typical* (i.e. most probable) correlations in this class of disordered models.

Our analysis naturally rises a few questions deserving further investigations. The first one is that the true negativity spectrum (i.e. the full distribution of eigenvalues of $\rho_A^{T_2}$) has not yet been derived. Indeed, this is still and open issue also for the entanglement spectrum [34] for which the calculation should be much simpler. A second natural question is to wonder whether it is possible to calculate the negativity moments for other infinite randomness fixed points that have been described in the literature.

Finally, the dynamical evolution of the entanglement in random spin systems has been also subject to intensive investigation, especially in relation to many-body localized phases [16, 191–197]. A crucial aspect so far, even from the experimental side [198, 199], has been to establish a quantitative understanding of the growth of the entanglement entropy. It would be interesting to generalize some of these results to the negativity and negativity spectrum.

For the symmetry resolved Rényi entropies, we then have considered different proxies that we give in Eqs. (2.115), (2.116), and (2.117). Two of them ((2.115) and (2.116)) become equal in the von Neumann limit. We compute the asymptotic behavior of these entropies in the large ℓ limit using well established techniques within SDRG. Our main result is that the three definitions all provide entanglement entropies that satisfy equipartition at the leading universal orders. We confirmed these results numerically and showed the presence of subleading non-universal terms breaking equipartition. The order of such corrections, $s^2/\ln \ell$, is also correctly characterized by analytic SDRG techniques. We finally point out that the double logarithmic term in the symmetry resolved entanglement is related to the number entropy, in full analogy with clean systems [156]. There are also few quantitative remarkable SDRG predictions about the subleading terms that are confirmed by numerics. The first is that the $O(\ell^0)$ term in the symmetry resolved entanglement, not only is s-independent (a remarkable fact by itself), but it is also the same as in the total entropy (modulo a contribution from the number entropy). Another one is that for almost all entropies the corrections are monotonically decreasing function of $|s|$, but for the one defined in Eq. (2.117) there is a switch as the Rényi index grows.

An important test of our results that is still to be performed consists in checking some of our predictions in microscopic models with ab-initio methods. However, it is a numerically demanding problem to reach the large system sizes required to minimize the effect of the subleading corrections, even for disordered free-fermion models and exploiting well established techniques [26, 34].

A fundamental generalization for our work concerns symmetry resolved entanglement and equipartition for disordered systems out of equilibrium. Indeed, there is already a large literature about the time evolution of the total entanglement entropy [25, 137, 191–197, 199–201], that provided insights also about the celebrated many body localization. Only in recent experiments [137], the importance of symmetry resolution

has been highlighted also to shed light on the slow growth of the total entanglement entropy. However, many aspects of the problem still require to be studied deeply.

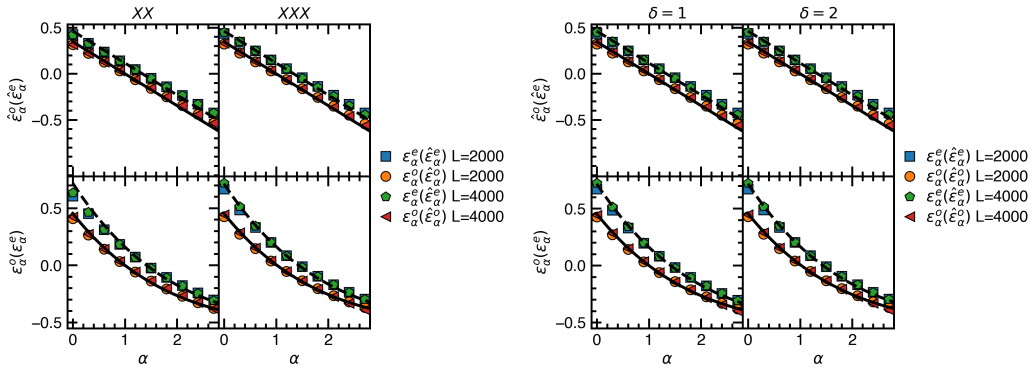

FIGURE 2.11: (Left) Comparison between the SDRG simulations using the Ma-Dasgupta rule respectively for the XX chain eq. (**??**) and the XXX chains eq. (**??**). Similarly to Fig. 2.3, we plot, as function of α, the prefactor of the logarithm $\varepsilon_\alpha^{e/o}$ (cf. (2.109)), as obtained by a fit of the numerical data. The continuous lines are the analytic predictions in Eqs. (2.83-2.86). The plots show an extremely good agreement between numerical data and analytic predictions. (Right) Numerical comparison between the SDRG simulation for the XXX model using the initial coupling distribution eq. (2.154) with $\delta = 1$ and $\delta = 2$. Similarly to Fig. 2.3 and Fig. 2.11, we plot, as function of α, the prefactor of the logarithm $\varepsilon_\alpha^{e/o}$ (cf. (2.109)), as obtained by a fit of the numerical data. The continuous lines are the analytic predictions in Eqs. (2.83-2.86). Analogous results holds for other values of δ, and suggests the independence of the SDRG procedure with respect to the initial distribution of the couplings.

2.6 Appendix: Additional detail and results for the negativity spectrum

2.6.1 Universality of the SDRG data

In this section we provide numerical evidence for the universality of the SDRG. In Fig. 2.11 (Left) we present a comparison between the SDRG results of Sec. 2.3.5 for the XXX model and the same numerical implementation for the XX chain. The small discrepancies are due to finite size effects.

Furthermore we check our data are independent of the initial distribution by considering various initial coupling distributions of the form:

$$P_\delta(J) = \frac{J^{-1+1/\delta}}{\delta}, \qquad J \in [0,1]. \tag{2.154}$$

$\delta = 1$ coincides with the flat distribution in Sec. 2.3.5, $\delta \to 0$ is the clean case, while $\delta \to \infty$ is the infinite randomness fixed-point. We considered different values of δ. In particular, in Fig. 2.11 (Right) we compare the results for $\delta = 1$ and $\delta = 2$ for the XXX model, leaving the other parameter identical to those discussed in Sec. 2.3.5. From the figure we can appreciate the independence from the disorder distribution.

2.6.2 Fermionic negativity moments

The RSP describes also fermionic systems with random hoppings. However it has been shown was shown that the entanglement in the fermion variables is better captured by a *fermionic negativity*, introduced in Ref. [128] and related to a partial time reversal operation. The associated spectrum has been studied for disorder-free fermions [136]. Therefore it is interesting to understand this spectrum in random systems and particularly in the RSP. In this appendix, we recall the definition of the two possible density matrices for fermionic negativity and determine them in the random singlet phase.

For interacting fermions, the hamiltonian is obtained from the XXZ hamiltonian Eq. (2.17), via a Jordan-Wigner trasformation

$$H = \sum_j J_j \left(c_j^\dagger c_{j+1} + c_{j+1}^\dagger c_j - \Delta n_j + \Delta n_j n_{j+1} \right), \tag{2.155}$$

where $c_j, c_j^\dagger$ are spinless fermionic operators and $n_j = c_j^\dagger c_j$ the occupation number of the j-th site of the chain. The non-locality of such transformation points at a modification of the SDRG prescription to take into account the fermionic nature of the particles. It was shown [202] that this can be implemented through a simple modification of the RG prescription as

$$\tilde{J} = -\frac{J_L J_R}{\Omega}. \tag{2.156}$$

Eq. (2.156) implies that the hoppings can now be either positive or negative. When they are positive, a singlet-type bond is established between two sites, of the form $|\psi_-\rangle \propto |01\rangle - |10\rangle$, written in the occupation number basis of the fermions. If the hopping is negative, the corresponding triplet-type anti-bond is established $|\psi_+\rangle \propto |01\rangle + |10\rangle$. A crucial point is that the two types of bonds share many properties, such as entanglement. In particular, the spectrum of the associated density matrices is the same, $\sigma(\rho_+) = \sigma(\rho_-)$, where $\rho_\pm = |\psi_\pm\rangle\langle\psi_\pm|$. The same is true for the corresponding (standard) partial transpose, $\sigma(\rho_+^{T_2}) = \sigma(\rho_-^{T_2})$. Therefore, for our purpose, the ground state in the RSP can be written as

$$|GS\rangle = \prod_i |\psi_-\rangle_i. \tag{2.157}$$

In the occupation number basis, the fermionic partial trasponse differs from the standard partial transpose just by a phase $e^{i\pi\phi}$, with

$$\phi(\{n_j\},\{\bar{n}_j\}) = \frac{\tau_1(\tau_1+1)}{2} + \frac{\bar{\tau}_1(\bar{\tau}_1+1)}{2} + \tau_2\bar{\tau}_2 + \tau_1\tau_2 + \bar{\tau}_1\bar{\tau}_2 + (\tau_1+\tau_2)(\bar{\tau}_1+\bar{\tau}_2). \tag{2.158}$$

Here $\tau_s = \sum_{i\in A_s} n_i$, $\bar{\tau} = \sum_{i\in A_s}\bar{n}_i$ and refer to the ket $|\{n_j\}\rangle$ and bra $\langle\{\bar{n}_j\}|$ state, respectively. See Ref. [128] for details. In particular, applying the definition to our building block ρ_-, with the two subsystems consisting of a single site each, leads to

$$\rho_-^{R_2} = \frac{1}{2}\begin{pmatrix} 0 & 0 & 0 & -i \\ 0 & 1 & 0 & 0 \\ 0 & 0 & 1 & 0 \\ -i & 0 & 0 & 0 \end{pmatrix}, \tag{2.159}$$

whose spectrum is given by $\{i/2, -i/2, 1/2, 1/2\}$.

We can now apply Eq. (2.159) to the reduced density matrix of the RSP, after tracing B, i.e.,

$$\rho_A = \bigotimes_{m=1}^{n_{A:A}} \rho_{2\mathrm{s}} \bigotimes_{n=1}^{n_{A:B}} \rho_{\mathrm{s}},$$

where here $\rho_{2\mathrm{s}} = \rho_-$ and $\rho_{\mathrm{s}} = \mathrm{tr}_s\rho_-$ (with the trace being on one of the two sites). We obtain

$$\rho_A^{R_2} = \left\{ \prod_{k=1,2} \bigotimes_{p=1}^{n_{A_k:A_k}} \rho_{2\mathrm{s}} \right\} \bigotimes_{q=1}^{n_{A_1:A_2}} \rho_{2\mathrm{s}}^{R_2} \left\{ \prod_{k=1,2} \bigotimes_{r=1}^{n_{A_k:B}} \rho_{\mathrm{s}} \right\}. \tag{2.160}$$

Here we have used the fact that $\rho_{\mathrm{s}}^{R_2} = \rho_{\mathrm{s}}$ for a single site, and that $\rho_{2\mathrm{s}}^{R_2} = \rho_{2\mathrm{s}}$ when both the ends of a bond are in the same subsystem A_i $(i = 1, 2)$.

There are 4 different non-zero eigenvalues

$$\lambda_k = 2^{-n_{A:B}-n_{A_1:A_2}} e^{ik\pi/2},\ k = 0, \pm 1, 2. \tag{2.161}$$

These come with degeneracies d_k given by

$$\begin{aligned} d_{\pm 1} &= 2^{n_{A:B}+n_{A_1:A_2}-2}\left(2^{n_{A_1:A_2}}\right), \\ d_0 &= 2^{n_{A:B}+n_{A_1:A_2}-2}\left(2^{n_{A_1:A_2}}+2\right), \\ d_2 &= 2^{n_{A:B}+n_{A_1:A_2}-2}\left(2^{n_{A_1:A_2}}-2\right). \end{aligned} \tag{2.162}$$

From (2.161) and (2.162) we notice that the moments, $M_\alpha^{R_2} \equiv \mathrm{tr}\left(\rho_A^{R_2}\right)^\alpha$ have three different analytic continuations when restricting to α integer

$$M_\alpha^{R_2} = 2^{(n_{A:B}+n_{A_1:A_2})(1-\alpha)} \begin{cases} 1 & \alpha = 2p+1, \\ 2^{n_{A_1:A_2}} & \alpha = 4p, \\ 0 & \alpha = 4p+2, \end{cases} \tag{2.163}$$

with p integer. This more complicated periodicity has already been observed in the translational invariant setting [136]. As a check, from the odd sequence in (2.163) we recover the proper normalization $\mathrm{tr}\rho_A^{R_2} = \lim_{\alpha\to 1} M_\alpha^{R_2} = 1$.

This was dubbed *untwisted* negativity spectrum in Ref. [136], with the important difference with respect to the standard negativity spectrum of spin and bosonic models, of being complex. On the other hand, also for fermions one can introduce a hermitian partial transpose, more suitable to define another fermionic negativity due to its real spectrum. This is done by considering the composite operator $\rho_\times \equiv (\rho_A^{R_2})^\dagger \rho_A^{R_2}$ and by noting that $\rho_\times = (\rho_A^{\tilde{R}_2})^2$, where we introduced the *twisted* partial transpose $\rho_A^{\tilde{R}_2} \equiv \rho_A^{R_2}(-1)^{F_2}$ of Ref. [136]. Here $(-1)^{F_2}$ is the fermion number parity in A_2, since $F_2 = \sum_{j\in A_2} n_j$.

For the RSP, the twisted partial transposed reads

$$\rho_A^{\tilde{R}_2} = \left\{ \prod_{k=1,2} \bigotimes_{p=1}^{n_{A_k:A_k}} \rho_{2\mathrm{s}} \right\} \bigotimes_{q=1}^{n_{A_1:A_2}} \rho_{2\mathrm{s}}^{\tilde{R}_2} \left\{ \prod_{k=1,2} \bigotimes_{r=1}^{n_{A_k:B}} \rho_{\mathrm{s}} \right\}. \tag{2.164}$$

It has two non-zero eigenvalues

$$\tilde{\lambda}_\pm = \pm 2^{-n_{A:B}-n_{A_1:A_2}}, \tag{2.165}$$

with equal degeneracy

$$\tilde{d}_\pm = 2^{n_{A:B}+2n_{A_1:A_2}-1}. \tag{2.166}$$

Therefore, the associated moments, $M_\alpha^{\tilde{R}_2} \equiv \mathrm{tr}\left(\rho_A^{\tilde{R}_2}\right)^\alpha$, are given by

$$M_\alpha^{\tilde{R}_2} = \begin{cases} 0 & \alpha \text{ odd} \\ 2^{(n_{A:B}+n_{A_1:A_2})(1-\alpha)} 2^{n_{A_1:A_2}} & \alpha \text{ even}. \end{cases} \tag{2.167}$$

The negativity is obtained from Eq. (2.167) via replica limit as

$$\mathcal{E} = \lim_{\alpha\to 1/2} \overline{\log M_{2\alpha}^{\tilde{R}_2}} = \overline{n_{A_1:A_2}} \log 2. \tag{2.168}$$

Actually, in this case, Eq. (2.163) also implies that

$$\mathcal{E} = \lim_{\alpha\to 1/4} \overline{\log M_{4\alpha}^{R_2}} = \overline{n_{A_1:A_2}} \log 2. \tag{2.169}$$

Note that, as already shown numerically in Ref. [128], this means that in the case of fermions we recover the result obtained for the equivalent spin system in Ref. [35].

From Eqs. (2.163) and (2.167), it is clear that the fermionic negativity spectrum is different from the corresponding one in the spin variables. In fact, there are integer values of α for which they are trivial,

i.e. are exactly vanishing. Nevertheless, the non-trivial moments have the same functional forms of the moments (2.58). As such, the same techniques employed in Section 2.3 may be used to obtain SDRG results for the disordered-average moments associated to twisted and untwisted density matrices. For example, within the same assumptions of Sec. 2.3, the non-trivial untwisted moments reads

$$\log \overline{M_\alpha^{R_2}} = \begin{cases} \dfrac{\sqrt{5+2^{3-\alpha}}-3}{2}\mu + \dots & \alpha = 2p+1, \\ \dfrac{\sqrt{5+(1+q)2^{3-\alpha}}-3}{2}\mu + \dots & \alpha = 4p, \end{cases} \tag{2.170}$$

while the non-trivial twisted ones are

$$\log \overline{M_\alpha^{\tilde{R}_2}} = \frac{\sqrt{5+(1+q)2^{3-\alpha}}-3}{2}\mu, \qquad \alpha \text{ even.} \tag{2.171}$$

2.7 Appendix: Moments of the size of the symmetry block I_m

In this appendix we show how to use the Laplace transform techniques to rigorously calculate the leading behavior of $I_m(s)$. First of all we notice that for large n, the sum in Eq. (2.123) can be replaced by an integral, and we can exploit the closed-form expression for the generating function $g(\sigma)$ of the moments of n (cf. Eq. (2.39)), which is the Laplace transform of the probability distribution, i.e., $g(\sigma) = \mathcal{L}_n[P(n)](\sigma)$.

Thus, to evaluate Eq. (2.123), we first introduce the following Laplace transform

$$f(\sigma; s) \equiv \mathcal{L}_n \left[\binom{n}{n/2+s}^{(1-m)} \right]. \tag{2.172}$$

Then, by using the rule for the Laplace transform of a product, Eq. (2.123) can be written, in the scaling regime of large n, as

$$I_m(s) = \lim_{T\to\infty} \frac{1}{2\pi i} \int_{a-iT}^{a+iT} g(\sigma) f(-\sigma; s) d\sigma, \tag{2.173}$$

where a is a real number that guarantees convergence of the integral and $g(\sigma)$ is the generating function of the moments of the distribution of the number of shared singlets defined in Eq. (2.39).

The Laplace transform of (2.128) with respect to n can be calculated order by order by using that

$$\mathcal{L}_\sigma(2^{n(1-m)} n^{\frac{m}{2}} n^{-2k-\frac{1}{2}} n^{\beta}) = \Gamma\Big(\frac{1+m}{2} - 2k + \beta\Big)(\sigma + (m-1)\ln 2)^{2k-\beta-\frac{m+1}{2}}. \tag{2.174}$$

We now observe that the generating function $g(s)$ is analytic in the complex plane. On the other hand, Eq. (2.174) shows that if m is even $f(-\sigma; s)$ has an algebraic branch point at $\sigma^* = (m-1)\ln 2$. Instead, for m odd there is a pole at σ^* when $2k - \beta - (m+1)/2 < 0$, which is the reason why it becomes just a derivative, as in the main text.

The integral (2.173) can be performed by considering the contour integration along the path in Fig. 2.12 (we report m even, for m odd it is slightly simpler). The red dashed line is the branch cut starting at the algebraic branch point singularity at $\sigma^* = (m-1)\ln 2$. Since there are no singularities in the region enclosed by the contour, the integral is zero, i.e.,

$$\frac{1}{2\pi i} \int_{\mathcal{C}} g(\sigma) f(-\sigma; s) d\sigma = I_m + I^+ + I^- + I^{+,T} + I^{-,T} + I^\epsilon = 0. \tag{2.175}$$

Here I_m is the integral (2.173), where we set $a = 0$, $I^\pm$ are the integrals on the paths $\mathcal{C}^\pm$, $\mathcal{C}^{\pm,T}$ are contributions of the large semicircle, and I^ϵ is the contribution of $\mathcal{C}^\epsilon$.

We are interested in the limit $T \to \infty$ (T is the radius of the semicircle). It is straightforward to show that in this limit the contribution of $I^{+,T} + I^{-,T}$ vanishes. We should also observe that for odd m the two terms $I^\pm$ cancel out because the singularity at σ^* is a pole. Here, not to loose generality, we consider the case of m even, while odd can be deduced as a special case.

From Eqs. (2.173) and (2.174), the integrals in (2.175) are of the form

$$\mathcal{I}_{\mathcal{C}'} = \frac{1}{2\pi i} \int_{\mathcal{C}'} \frac{g(u-\sigma^*)}{(-u)^\omega} du, \tag{2.176}$$

where $\mathcal{C}'$ denotes the different paths forming the contour in Fig. 2.12, and we defined

$$u \equiv \sigma - \sigma^*, \tag{2.177}$$

$$\omega \equiv (m+1)/2 - 2k + \beta. \tag{2.178}$$

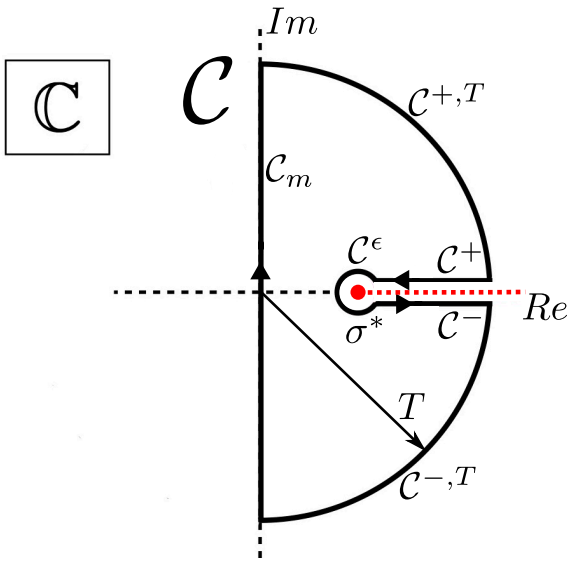

FIGURE 2.12: Contour $\mathcal{C}$ to evaluate the integral in Eq. (2.173). The integral on $\mathcal{C}_m$ is (2.173). For even values of the Rényi index m there is a branch cut starting at $\sigma^* = (m-1)\ln(2)$. For odd m the contributions of $\mathcal{C}^{\pm}$ cancel out and one has a pole at σ^*. The contributions of the semicircle $C^{\pm,T}$ vanishes.

Here we are interested in the limit $\ell \to \infty$, which implies $\mu \to \infty$ (cf. (2.42)). In this limit we can simplify the expression for the generating function $g(\sigma)$ as

$$g(\sigma) \simeq \frac{1}{2} e^{-\frac{1}{2}(3-\sqrt{5+4e^{-\sigma}})\mu} \Big[1 + \frac{3}{\sqrt{5+4e^{-\sigma}}}\Big]. \tag{2.179}$$

The integral (2.176) is difficult to compute in general. However, in the limit $\mu \to \infty$ on can use the saddle point method. Let us start discussing the contribution of the path $\mathcal{C}^+$:

$$\mathcal{I}_{\mathcal{C}^+} = -\frac{1}{2\pi i} \int_{\epsilon}^{T'} \frac{e^{-\frac{1}{2}(3-\sqrt{5+2^{3-m}e^{-u}})\mu}}{2(-u)^{\omega}} \Big[1 + \frac{3}{\sqrt{5+2^{3-m}e^{-u}}}\Big] du, \tag{2.180}$$

where $T' = T - \sigma^*$. A standard saddle point analysis of this integrals in the large μ limit gives the leading contribution as

$$\mathcal{I}^{(0)}_{\mathcal{C}^+} = \frac{e^{-\frac{1}{2}(3-\gamma_m)\mu}}{4\pi i(-1)^{\omega}} \Big(1 + \frac{3}{\gamma_m}\Big) \Big(\frac{2^{1-m}\mu}{\gamma_m}\Big)^{\omega-1} \Gamma\Big(1-\omega, \frac{2^{1-m}u}{\gamma_m}\Big)\Big|_{\mu\epsilon}^{\mu T'}, \tag{2.181}$$

where Γ is the incomplete Gamma function and we introduced

$$\gamma_m = \sqrt{5 + 2^{3-m}}. \tag{2.182}$$

Saddle point corrections to Eq. (2.181) are $\mathcal{O}(1/\sqrt{\mu})$. First, we should observe that the contribution at $T' \to \infty$ in Eq. (2.181) vanishes. However, the contribution of $\mu\epsilon$ diverges in the limit $\epsilon \to 0$. We anticipate that this divergence is regularised by the contribution of $\mathcal{C}^{\epsilon}$ (see Fig. 2.12). Precisely, one has

$$\Gamma(\omega, x) \approx \Gamma(\omega) - \frac{x^{\omega}}{\omega} + \frac{x^{\omega+1}}{1+\omega}, \quad \text{for } x \to 0. \tag{2.183}$$

Note that the number of singular terms depends on ω. The first correction to the saddle point result can be easily derived, yielding

$$\mathcal{I}^{(1)}_{\mathcal{C}^+} = \frac{e^{-\frac{1}{2}(3-\gamma_m)\mu} 2^m}{2\pi i(-1)^\omega \mu^2} \Big\{ \frac{2^{m-1}3\gamma_m}{(8+2^m 5)} \Gamma\Big(2-\omega, \frac{2^{1-m}u}{\gamma_m}\Big) + \frac{(2^m 5+4)\,(3\,2^m\gamma_m + 2^m 5 + 8)}{2^4(8+2^m 5)} \Gamma\Big(3-\omega, \frac{2^{1-m}u}{\gamma_m}\Big)\Big) \Big\}\Big|_{\mu\epsilon}^{\mu T'} \times \left(\frac{2^{1-m}\mu}{\gamma_m}\right)^\omega + \mathcal{O}(\mu^{\omega-3}). \quad (2.184)$$

We now observe that in both (2.181) and (2.184) in the limit $T' \to \infty$, we have $\Gamma(\omega, T') \to 0$. For $\epsilon \to 0$ similar divergences as for (2.181) arise, which are removed by the integral on $\mathcal{C}^\epsilon$.

Before discussing the integral on $\mathcal{C}^\epsilon$, we focus on $\mathcal{I}_{\mathcal{C}^-}$ (see (2.176)). The calculation is similar, the only difference is the phase factor due to the presence of the branch cut. Precisely, one has

$$\mathcal{I}_{\mathcal{C}^-} = -\mathcal{I}_{\mathcal{C}^+} e^{-2\pi\omega i}. \quad (2.185)$$

From that (2.177), for even m one obtains that $\mathcal{I}_{\mathcal{C}^+} = \mathcal{I}_{\mathcal{C}^-}$ (whereas for odd m the two integrals cancel out).

Finally, we briefly discuss the integral on the inner circle $\mathcal{C}^\epsilon$ around the branch cut. One has $u = \epsilon e^{i\theta}$. Therefore the integral to evaluate is

$$\mathcal{I}_{\mathcal{C}^\epsilon} = \frac{\epsilon^{1-\omega}}{4\pi(-1)^\omega} \int_0^{2\pi} d\theta \frac{e^{-\frac{1}{2}(3-\sqrt{5+2^{3-m}e^{-\epsilon e^{i\theta}}})\mu}}{e^{i(\omega-1)\theta}} \Big[1 + \frac{3}{\sqrt{5+2^{3-m}e^{-\epsilon e^{i\theta}}}}\Big]. \quad (2.186)$$

Since we are interested in the limit $\epsilon \to 0$, we can expand the integrand. After performing the integral over θ, we obtain that at the leading order in ϵ one has

$$\mathcal{I}_{\mathcal{C}^\epsilon} = \frac{\epsilon^{1-\omega} e^{-2i\pi\omega}}{2\pi(\omega-1)} \Big(1 + \frac{3}{\gamma_m}\Big) e^{-\frac{1}{2}(3-\gamma_m)\mu} \sin(\pi\omega). \quad (2.187)$$

At the leading order the contribution of (2.187) cancels the most divergent term in $\mathcal{I}^{(0)}_{\mathcal{C}^+} + \mathcal{I}^{(0)}_{\mathcal{C}^-}$ (see (2.181)). We checked that higher order terms cancel higher order divergences in (2.181) and (2.184).

It is now straightforward to derive the result for the integral I_m in (2.173). We focus on the leading order in μ. At the leading order $\omega = (m+1)/2$, from (2.181), (2.185), and the expression for Q_0 (cf. (2.126)) one obtains that

$$I_m = \frac{1}{2} e^{-\frac{1}{2}(3-\gamma_m)\mu} \Big(1 + \frac{3}{\gamma_m}\Big) \Big(\frac{2}{\pi}\Big)^{\frac{1-m}{2}} \Big(\frac{2^{1-m}\mu}{\gamma_m}\Big)^{\frac{m-1}{2}}. \quad (2.188)$$

Here we also used that the factor $\Gamma((m+1)/2)$ in (2.174) cancels out with the $\Gamma((1-m)/2)$ obtained from (2.181) in the limit $\epsilon \to 0$ (see (4.19)) using Euler's reflection formula

$$\Gamma(x)\Gamma(1-x) = \frac{\pi}{\sin(\pi x)}, \quad x \notin \mathbb{Z}. \quad (2.189)$$

Finally, we stress that the result (2.188) coincides, at least to leading order, with the result in the main text (2.130) obtained by taking the derivative of $g(\sigma)$ for odd m.

Bibliography

[1] Xhek Turkeshi, Paola Ruggiero, and Pasquale Calabrese. Negativity spectrum in the random singlet phase. *Physical Review B*, 101(6):064207, Feb 2020.

[2] Xhek Turkeshi, Paola Ruggiero, Vincenzo Alba, and Pasquale Calabrese. Entanglement equipartition in critical random spin chains. *Physical Review B*, 102(1):014455, Jul 2020.

[3] L. Amico, R. Fazio, A. Osterloh, and V. Vedral. *Entanglement in many-body systems*. *Rev. Mod. Phys.* ***80****, 517 (2008).*

[4] P. Calabrese, J. Cardy and B. Doyon. *Entanglement entropy in extended quantum systems*. *J. Phys. A* ***42****, 500301 (2009).*

[5] N. Laflorencie. *Quantum entanglement in condensed matter systems*. *Phys. Rep.* **646***, 1 (2016).*

[6] J. Eisert, M. Cramer and M. B. Plenio. *Area laws for the entanglement entropy*. *Rev. Mod. Phys.* ***82****, 277 (2010).*

[7] G. Vidal, J.I. Latorre, E. Rico and A. Kitaev. *Entanglement in quantum critical phenomena*. *Phys. Rev. Lett.* ***90****, 227902 (2003).*

[8] J. I. Latorre, E. Rico and G. Vidal. *Ground state entanglement in quantum spin chains*. *Quant. Inf. Comp.* ***4****, 048 (2004).*

[9] P. Calabrese and J. Cardy. *Entanglement entropy and quantum field theory*. *J. Stat. Mech.* ***2004****, P06002 (2004).*

[10] P. Calabrese and J. Cardy. *Entanglement entropy and conformal field theory*. *J. Phys. A* ***42****, 504005 (2009).*

[11] H. Li and F. D. M. Haldane. *Entanglement Spectrum as a Generalization of Entanglement Entropy: Identification of Topological Order in Non-Abelian Fractional Quantum Hall Effect States*. *Phys. Rev. Lett.* ***101****, 010504 (2008).*

[12] P. Calabrese and A. Lefevre. *Entanglement spectrum in one-dimensional systems*. *Phys. Rev. A* ***78****, 032329 (2008).*

[13] F. Pollmann and J. E. Moore. *Entanglement spectra of critical and near-critical systems in one dimension*. *New J. Phys.* ***12****, 025006 (2010).*

[14] P.W. Anderson. *Absence of Diffusion in Certain Random Lattices*. *Phys. Rev.* ***109****, 1492 (1958).*

[15] E. Abrahams. *50 Years of Anderson Localization*. *World Scientific (2010).*

[16] R. Nandkishore and D. A. Huse. *Many body localization and thermalization in quantum statistical mechanics*. *Ann. Review of Cond. Mat. Phys.* ***6****, 15 (2015).*

[17] D.A. Abanin, E. Altman, I. Bloch, and M. Serbyn. *Colloquium: Many-body localization, thermalization, and entanglement*. *Rev. Mod. Phys.* ***91****, 021001 (2019).*

[18] S.-K. Ma, C. Dasgupta, and C.-k. Hu. *Random Antiferromagnetic Chain*. *Phys. Rev. Lett.* ***43****, 1434 (1979).*

[19] C. Dasgupta and S.-K. Ma. *Low-temperature properties of the random Heisenberg antiferromagnetic chain*. *Phys. Rev. B* ***22****, 1305 (1980).*

[20] D. S. Fisher. *Random transverse field Ising spin chains*. *Phys. Rev. Lett.* ***69****, 534 (1992).*

[21] D. S. Fisher. *Critical behavior of random transverse-field Ising spin chains*. *Phys. Rev. B* ***51****, 6411 (1995).*

[22] F. Iglói and C. Monthus. *Strong disorder RG approach of random systems*. *Phys. Rep.* ***412****, 277 (2005).*

[23] F. Igloi and C. Monthus. *Strong Disorder RG approach - a short review of recent developments*. *Eur. Phys. J. B* ***91****, 290 (2018).*

[24] G. Refael and J. E. Moore. *Entanglement Entropy of Random Quantum Critical Points in One Dimension*. *Phys. Rev. Lett.* **93***, 260602 (2004).*

[25] G. De Chiara, S. Montangero, P. Calabrese, and R. Fazio. *Entanglement entropy dynamics of Heisenberg chains*. *J. Stat. Mech. P03001 (2006).*

[26] N. Laflorencie. *Scaling of entanglement entropy in the random singlet phase*. *Phys. Rev. B* **72***, 140408(R) (2005).*

[27] G. Refael and J. E. Moore. *Entanglement entropy of the random s=1 Heisenberg chain*. *Phys. Rev. B* **76***, 024419 (2007).*

[28] J. A. Hoyos, A. P. Vieira, N. Laflorencie, and E. Miranda. *Correlation amplitude and entanglement entropy in random spin chains*. *Phys. Rev. B* **76***, 174425 (2007).*

[29] N. E. Bonesteel and K. Yang. *Infinite-Randomness Fixed Points for Chains of Non-Abelian Quasiparticles*. *Phys. Rev. Lett.* **99***, 140405 (2007).*

[30] G. Refael and J. E. Moore. *Criticality and entanglement in random quantum systems*. *J. Phys. A* **42***, 504010 (2009).*

[31] D. Binosi, G. De Chiara, S. Montangero, and A. Recati. *Increasing entanglement through engineered disorder in the random Ising chain*. *Phys. Rev. B* **76***, 140405 (2007).*

[32] J. C. Getelina, F. C. Alcaraz, and J. A. Hoyos. *Entanglement properties of correlated random spin chains and similarities with conformally invariant systems*. *Phys. Rev. B* **93***, 045136 (2016).*

[33] F. Igloi and Y.-C. Lin. *Finite-size scaling of the entanglement entropy of the quantum Ising chain with homogeneous, periodically modulated and random couplings*. *J. Stat. Mech. P06004 (2008).*

[34] M. Fagotti, P. Calabrese and J. E. Moore. *Entanglement spectrum of random-singlet quantum critical points*. *Phys. Rev. B* **83***, 045110 (2011).*

[35] P. Ruggiero, V. Alba and P. Calabrese. *Entanglement negativity in random spin chains*. *Phys. Rev. B* ***94****, 035152 (2016).*

[36] G. Ramirez, J. Rodriguez-Laguna, and G. Sierra. *Entanglement in low-energy states of the random-hopping model*. *J. Stat. Mech. P07003 (2014).*

[37] R. Santachiara. *Increasing of entanglement entropy from pure to random quantum critical chains*. *J. Stat. Mech. L06002 (2006).*

[38] L. Fidkowski, G. Refael, N. E. Bonesteel, and J. E. Moore. *c-theorem violation for effective central charge of infinite-randomness fixed points*. *Phys. Rev. B* **78***, 224204 (2008).*

[39] N. Regnault, B. A. Bernevig and F. D. M. Haldane. *Topological Entanglement and Clustering of Jain Hierarchy States*. *Phys. Rev. Lett.* ***103***, *016801 (2009)*.

[40] L. Fidkowski. *Entanglement Spectrum of Topological Insulators and Superconductors*. *Phys. Rev. Lett.* ***104***, *130502 (2010)*.

[41] A. M. Läuchli, E. J. Bergholtz, J. Suorsa and M. Haque. *Disentangling Entanglement Spectra of Fractional Quantum Hall States on Torus Geometries*. *Phys. Rev. Lett.* ***104***, *156404 (2010)*.

[42] H. Yao and X.-L. Qi. *Entanglement Entropy and Entanglement Spectrum of the Kitaev Model*. *Phys. Rev. Lett.* ***105***, *080501 (2010)*.

[43] F. Pollmann, A. M. Turner, E. Berg and M. Oshikawa. *Entanglement spectrum of a topological phase in one dimension*. *Phys. Rev. B* ***81***, *064439 (2010)*.

[44] J. Dubail and N. Read. *Entanglement Spectra of Complex Paired Superfluids*. *Phys. Rev. Lett.* ***107***, *157001 (2011)*.

[45] X.-L. Qi, H. Katsura and A. W. W. Ludwig. *General Relationship between the Entanglement Spectrum and the Edge State Spectrum of Topological Quantum States*. *Phys. Rev. Lett.* ***108***, *196402 (2012)*.

[46] D. Poilblanc, N. Schuch, D. Pérez-García and J. I. Cirac. *Topological and entanglement properties of resonating valence bond wave functions*. *Phys. Rev. B* ***86***, *014404 (2012)*.

[47] L. Cincio and G. Vidal. *Characterizing Topological Order by Studying the Ground States on an Infinite Cylinder*. *Phys. Rev. Lett.* ***110***, *067208 (2013)*.

[48] R. Lundgren, J. Blair, P. Laurell, N. Regnault, G.A. Fiete, M. Greiter and R. Thomale. *Universal entanglement spectra in critical spin chains*. *Phys. Rev. B* ***94***, *081112 (2016)*.

[49] M. A. Metlitski and T. Grover. *Entanglement Entropy of Systems with Spontaneously Broken Continuous Symmetry*. *arXiv:1112.5166 (2011)*.

[50] V. Alba, M. Haque and A. M. Läuchli. *Entanglement Spectrum of the Two-Dimensional Bose-Hubbard Model*. *Phys. Rev. Lett.* ***110***, *260403 (2013)*.

[51] N. M. Tubman and D. C. Yang. *Calculating the entanglement spectrum in quantum Monte Carlo with application to ab initio Hamiltonians*. *Phys. Rev. B* ***90***, *081116 (2014)*.

[52] F. Kolley, S. Depenbrock, I. P. McCulloch, U. Schollwöck and V. Alba. *Entanglement spectroscopy of SU(2)-broken phases in two dimensions*. *Phys. Rev. B* ***88***, *144426 (2013)*.

[53] I. Frérot and T. Roscilde. *Entanglement Entropy across the Superfluid-Insulator Transition: A Signature of Bosonic Criticality*. *Phys. Rev. Lett.* ***116***, *190401 (2016)*.

[54] Z.-C. Yang, C. Chamon, A. Hamma and E. R. Mucciolo. *Two-Component Structure in the Entanglement Spectrum of Highly Excited States*. *Phys. Rev. Lett.* ***115***, *267206 (2015)*.

[55] S. D. Geraedts, R. Nandkishore and N. Regnault. *Many-body localization and thermalization: Insights from the entanglement spectrum*. *Phys. Rev. B* ***93***, *174202 (2016)*.

[56] M. Serbyn, A. A. Michailidis, D. A. Abanin and Z. Papic. *Power-Law Entanglement Spectrum in Many-Body Localized Phases*. *Phys. Rev. Lett.* ***117***, *160601 (2016)*.

[57] A. M. Läuchli. *Operator content of real-space entanglement spectra at conformal critical points*. *arXiv:1303.0741 (2013)*.

[58] Y.O. Nakagawa and S. Furukawa. *Capacity of entanglement and distribution of density matrix eigenvalues in gapless systems*. *Phys. Rev. B* ***96****, 205108 (2017).*

[59] M. Goldstein and E. Sela. *Symmetry-Resolved Entanglement in Many-Body Systems*. *Phys. Rev. Lett.* **120***, 200602 (2018).*

[60] V. Alba, P. Calabrese and E. Tonni. *Entanglement spectrum degeneracy and the Cardy formula in 1+1 dimensional conformal field theories*. *J. Phys. A* ***51****, 024001 (2018).*

[61] L. Tagliacozzo, T. R. de Oliveira, S. Iblisdir and J. I. Latorre. *Scaling of entanglement support for matrix product states*. *Phys. Rev. B* ***78****, 024410 (2008).*

[62] F. Pollmann, S. Mukerjee, A. M. Turner and J. E. Moore. *Theory of Finite-Entanglement Scaling at One-Dimensional Quantum Critical Points*. *Phys. Rev. Lett.* ***102****, 255701 (2009).*

[63] B. Pirvu, G. Vidal, F. Verstraete and L. Tagliacozzo. *Matrix product states for critical spin chains: Finite-size versus finite-entanglement scaling*. *Phys. Rev. B* ***86****, 075117 (2012).*

[64] V. Alba, P. Calabrese, and E. Tonni. *Entanglement spectrum degeneracy and Cardy formula in 1+1 dimensional conformal field theories*. *J. Phys. A* **51***, 024001 (2018).*

[65] P. Calabrese and J. Cardy. *Evolution of Entanglement Entropy in One-Dimensional Systems*. *J. Stat. Mech. (2005) P04010.*

[66] A. Peres. *Separability Criterion for Density Matrices*. *Phys. Rev. Lett.* ***77****, 1413 (1996).*

[67] M. Horodecki, P. Horodecki and R. Horodecki. *Separability of mixed states: necessary and sufficient*, journal = conditions.

[68] R. Simon. *Peres-Horodecki Separability Criterion for Continuous Variable*, journal = Systems.

[69] R. F. Werner and M. M. Wolf. *Bound Entangled Gaussian States*. *Phys. Rev. Lett.* ***86****, 3658 (2001).*

[70] G. Giedke, B. Kraus, M. Lewenstein and J. I. Cirac. *Entanglement Criteria for All Bipartite Gaussian States*. *Phys. Rev. Lett.* ***87****, 167904 (2001).*

[71] K Zyczkowski, P. Horodecki, A. Sanpera, and M. Lewenstein. *Volume of the set of separable states*. *Phys. Rev. A* ***58****, 883 (1998).*

[72] K Zyczkowski. *Volume of the set of separable states. II*. *Phys. Rev. A* ***60****, 3496 (1999).*

[73] J. Eisert and M. B. Plenio. *A comparison of entanglement measures*. *J. Mod. Opt.* ***46****, 145 (1999).*

[74] J. Lee, M. S. Kim, Y. J. Park, and S. Lee. *Partial teleportation of entanglement in a noisy environment*. *J. Mod. Opt.* ***47****, 2151 (2000).*

[75] G. Vidal and R. F. Werner. *Computable measure of entanglement*. *Phys. Rev. A* **65***, 032314 (2002).*

[76] M. B. Plenio. *Logarithmic Negativity: A Full Entanglement Monotone That is not Convex*. *Phys. Rev. Lett.* ***95****, 090503 (2005).*

[77] K. Audenaert, J. Eisert, M. B. Plenio and R. F. Werner. *Entanglement properties of the harmonic chain*. *Phys. Rev. A* ***66****, 042327 (2002).*

[78] A. Ferraro, D. Cavalcanti, A. García-Saez and A. Acín. *Thermal Bound Entanglement in Macroscopic Systems and Area Law*. *Phys. Rev. Lett.* ***100****, 080502 (2008).*

[79] D. Cavalcanti, A. Ferraro, A. García-Saez and A. Acín. *Distillable entanglement and area laws in spin and harmonic-oscillator systems*. *Phys. Rev. A* ***78****, 012335 (2008).*

[80] J. Anders and W. Andreas. *Entanglement and separability of quantum harmonic oscillator systems at finite temperature*. *Quantum Info. Comput.* ***8***, *0245 (2008).*

[81] J. Anders. *Thermal state entanglement in harmonic lattices*. *Phys. Rev. A* ***77***, *062102 (2008).*

[82] S. Marcovitch, A. Retzker, M. B. Plenio and B. Reznik. *Critical and noncritical long-range entanglement in Klein-Gordon fields*. *Phys. Rev. A* ***80***, *012325 (2009).*

[83] N. E. Sherman, T. Devakul, M. B. Hastings and R. R. P. Singh. *Nonzero-temperature entanglement negativity of quantum spin models: Area law, linked cluster expansions, and sudden death*. *Phys. Rev. E* ***93***, *022128 (2016).*

[84] C. D. Nobili, A. Coser and E. Tonni. *Entanglement negativity in a two dimensional harmonic lattice: area law and corner contributions*. *J. Stat. Mech. 083102 (2016).*

[85] V. Eisler and Z. Zimboras. *Entanglement negativity in two-dimensional free lattice models*. *Phys. Rev. B* **93**, *115148 (2016).*

[86] M R. M. Mozaffar and A. Mollabashi. *Logarithmic negativity in Lifshitz harmonic models*. *J. Stat. Mech. (2018) 053113.*

[87] H. Wichterich, J. Molina-Vilaplana and S. Bose. *Scaling of entanglement between separated blocks in spin chains at criticality*. *Phys. Rev. A* ***80***, *010304 (2009).*

[88] A. Bayat, S. Bose and P. Sodano. *Entanglement Routers Using Macroscopic Singlets*. *Phys. Rev. Lett.* ***105***, *187204 (2010).*

[89] A. Bayat, P. Sodano and S. Bose. *Negativity as the entanglement measure to probe the Kondo regime in the spin-chain Kondo model*. *Phys. Rev. B* ***81***, *064429 (2010).*

[90] A. Bayat, S. Bose, P. Sodano and H. Johannesson. *Entanglement Probe of Two-Impurity Kondo Physics in a Spin Chain*. *Phys. Rev. Lett.* ***109***, *066403 (2012).*

[91] H. Wichterich, J. Vidal and S. Bose. *Universality of the negativity in the Lipkin-Meshkov-Glick model*. *Phys. Rev. A* ***81***, *032311 (2010).*

[92] R. A. Santos, V. Korepin and S. Bose. *Negativity for two blocks in the one-dimensional spin-1 Affleck-Kennedy-Lieb-Tasaki model*. *Phys. Rev. A* ***84***, *062307 (2011).*

[93] T.-C. Lu and T. Grover. *Singularity in Entanglement Negativity Across Finite Temperature Phase Transitions*. *arXiv:1808.04381 (2018).*

[94] Y. Javanmard, D. Trapin, S. Bera, J. H. Bardarson and M. Heyl. *Sharp entanglement thresholds in the logarithmic negativity of disjoint blocks in the transverse-field Ising chain*. *New J. Phys.* ***20***, *083032 (2018).*

[95] J. Gray, A. Bayat, A. Pal, and S. Bose. *Scale Invariant Entanglement Negativity at the Many-Body Localization Transition*. *ArXiv:1908.02761.*

[96] E. Cornfeld, M. Goldstein, and E. Sela. *Imbalance entanglement: Symmetry decomposition of negativity*. *Phys. Rev. A* **98**, *032302 (2018).*

[97] N. E. Sherman, T. Devakul, M. B. Hastings, and R. R. P. Singh. *Nonzero-temperature entanglement negativity of quantum spin models: Area law, linked cluster expansions, and sudden death*. *Phys. Rev. E* **93**, *022128 (2016).*

[98] J. Kudler-Flam, H. Shapourian, and S. Ryu. *The negativity contour: a quasi-local measure of entanglement for mixed states*. *ArXiv:1908.07540.*

[99] P. Calabrese, J. Cardy and E. Tonni. *Entanglement Negativity in Quantum Field Theory*. *Phys. Rev. Lett.* ***109***, *130502 (2012)*.

[100] P. Calabrese, J. Cardy and E. Tonni. *Entanglement negativity in extended systems: a field theoretical approach*. *J. Stat. Mech. P02008 (2013)*.

[101] P. Calabrese, L. Tagliacozzo and E. Tonni. *Entanglement negativity in the critical Ising chain*. *J. Stat. Mech. P05002 (2013)*.

[102] V. Alba. *Entanglement negativity and conformal field theory: a Monte Carlo study*. *J. Stat. Mech. P05013 (2013)*.

[103] A. Coser, E. Tonni and P. Calabrese. *Entanglement negativity after a global quantum quench*. *J. Stat. Mech. P12017 (2014)*.

[104] P. Calabrese, J. Cardy and E. Tonni. *Finite temperature entanglement negativity in conformal field theory*. *J. Phys. A* ***48***, *015006 (2015)*.

[105] C. D. Nobili, A. Coser and E. Tonni. *Entanglement entropy and negativity of disjoint intervals in CFT: some numerical extrapolations*. *J. Stat. Mech. P06021 (2015)*.

[106] M. Kulaxizi, A. Parnachev and G. Policastro. *Conformal blocks and negativity at large central charge*. *J. High Ener. Phys. 09 010 (2014)*.

[107] O. Blondeau-Fournier, O. A. Castro-Alvaredo and B. Doyon. *Universal scaling of the logarithmic negativity in massive quantum field theory*. *J. Phys. A* ***49***, *125401 (2016)*.

[108] D. Bianchini and O. A. Castro-Alvaredo. *Branch point twist field correlators in the massive free Boson theory*. *Nuc. Phys. B* ***913***, *879 (2016)*.

[109] V. Eisler and Z. Zimborás. *Entanglement negativity in the harmonic chain out of equilibrium*. *New J. Phys.* ***16***, *123020 (2014)*.

[110] V. Alba and P. Calabrese. *Quantum information dynamics in multipartite integrable*, journal = systems.

[111] M. Hoogeveen and B. Doyon. *Entanglement negativity and entropy in non-equilibrium conformal field theory*. *Nuc. Phys. B* ***898***, *78 (2015)*.

[112] X. Wen, P.-Y. Chang and S. Ryu. *Entanglement negativity after a local quantum quench in conformal field theories*. *Phys. Rev. B* ***92***, *075109 (2015)*.

[113] M. J. Gullans and D. A. Huse. *Entanglement Structure of Current-Driven Diffusive Fermion Systems*. *Phys. Rev. X* ***9***, *021007 (2019)*.

[114] J. Kudler-Flam, M. Nozaki, S. Ryu, and M. T. Tan. *Quantum vs. classical information: operator negativity as a probe of scrambling*. *arXiv:1906.07639*.

[115] X. Wen, S. Matsuura and S. Ryu. *Edge theory approach to topological entanglement entropy, mutual information, and entanglement negativity in Chern-Simons theories*. *Phys. Rev. B* ***93***, *245140 (2016)*.

[116] X. Wen, P.-Y. Chang and S. Ryu. *Topological entanglement negativity in Chern-Simons theories*. *JHEP 09, 012 (2016)*.

[117] C. Castelnovo. *Negativity and topological order in the toric code*. *Phys. Rev. A* ***88***, *042319 (2013)*.

[118] Y. A. Lee and G. Vidal. *Entanglement negativity and topological order*. *Phys. Rev. A* ***88***, *042318 (2013)*.

[119] O. Hart and C. Castelnovo. *Entanglement negativity and sudden death in the toric code at finite temperature*. *Phys. Rev. B* ***97****, 144410 (2018).*

[120] F. Pollmann and A. M. Turner. *Detection of symmetry-protected topological phases in one dimension*. *Phys. Rev. B* ***86****, 125441 (2012).*

[121] K. Shiozaki and S. Ryu. *Matrix product states and equivariant topological field theories for bosonic symmetry-protected topological phases in (1+1) dimensions*. *JHEP 04, 100 (2017).*

[122] H. Shapourian, K. Shiozaki and S. Ryu. *Many-Body Topological Invariants for Fermionic Symmetry-Protected Topological Phases*. *Phys. Rev. Lett.* ***118****, 216402 (2017).*

[123] K. Shiozaki, H. Shapourian, K. Gomi and S. Ryu. *Many-body topological invariants for fermionic short-range entangled topological phases protected by antiunitary symmetries*. *Phys. Rev. B* ***98****, 035151 (2018).*

[124] V. Eisler and Z. Zimboras. *On the partial transpose of fermionic Gaussian states*. *New J. Phys.* **17**, *053048 (2015).*

[125] P.-Y. Chang and X. Wen. *Entanglement negativity in free-fermion systems: An overlap matrix approach*. *Phys. Rev. B* ***93****, 195140 (2016).*

[126] C. P. Herzog and Y. Wang. *Estimation for entanglement negativity of free fermions*. *J. Stat. Mech. 073102 (2016).*

[127] J. Eisert, V. Eisler and Z. Zimborás. *Entanglement negativity bounds for fermionic Gaussian states*. *Phys. Rev. B* ***97****, 165123 (2018).*

[128] H. Shapourian, K. Shiozaki and S. Ryu. *Partial time-reversal transformation and entanglement negativity in fermionic systems*. *Phys. Rev. B* ***95****, 165101 (2017).*

[129] H. Shapourian and S. Ryu. *Entanglement negativity of fermions: Monotonicity, Separability criterion, and classification of few-mode states*. *Phys. Rev. A* ***99****, 022310 (2019).*

[130] H. Shapourian and S. Ryu. *Finite-temperature entanglement negativity of free fermions*. *J. Stat. Mech. 043106 (2019).*

[131] A. Coser, E. Tonni and P. Calabrese. *Towards the entanglement negativity of two disjoint intervals for a one dimensional free fermion*. *J. Stat. Mech. 033116 (2016).*

[132] J. Gray, L. Banchi, A. Bayat and S. Bose. *Machine-Learning-Assisted Many-Body Entanglement Measurement*. *Phys. Rev. Lett.* ***121****, 150503 (2018).*

[133] E. Cornfeld, E. Sela and M. Goldstein. *Measuring Fermionic Entanglement: Entropy, Negativity, and Spin Structure*. *Phys. Rev. A* **99**, *062309 (2019).*

[134] P. Ruggiero, V. Alba and P. Calabrese. *Negativity spectrum of one-dimensional conformal field theories*. *Phys. Rev. B* ***94****, 195121 (2016).*

[135] G. B. Mbeng, V. Alba and P. Calabrese. *Negativity spectrum in 1D gapped phases of matter*. *J. Phys. A* ***50****, 194001 (2017).*

[136] H. Shapourian, P. Ruggiero, S. Ryu, and P. Calabrese. *Twisted and untwisted negativity spectrum of free fermions*. *arxiv:1906.04211 (2019).*

[137] A. Lukin, M. Rispoli, R. Schittko, M.E. Tai, A.M. Kaufman, S. Choi, V. Khemani, J. Leonard and M.Z. Greiner. *Probing entanglement in a many-body localized system*. *Science* ***364****, 6437 (2019).*

[138] H. F. Song, S. Rachel, C. Flindt, I. Klich, N. Laflorencie, and K. Le Hur. *Bipartite fluctuations as a probe of many-body entanglement*. *Phys. Rev. B* **85**, *035409 (2012)*.

[139] H. F. Song, S. Rachel, and K. Le Hur. *General relation between entanglement and fluctuations in one dimension*. *Phys. Rev. B* **82**, *012405 (2010)*.

[140] S. Rachel, N. Laflorencie, H. F. Song, and K. Le Hur. *Detecting Quantum Critical Points Using Bipartite Fluctuations*. *Phys. Rev. Lett.* **108**, *116401 (2012)*.

[141] I. Klich and L. Levitov. *Quantum Noise as an Entanglement Meter*. *Phys. Rev. Lett.* **102**, *100502 (2009)*.

[142] H. F. Song, C. Flindt, S. Rachel, I. Klich, and K. Le Hur. *Entanglement entropy from charge statistics: Exact relations for noninteracting many-body systems*. *Phys. Rev. B* **83**, *161408(R) (2011)*.

[143] A. Petrescu, H. F. Song, S. Rachel, Z. Ristivojevic, C. Flindt, N. Laflorencie, I. Klich, N. Regnault and K. Le Hur. *Fluctuations and entanglement spectrum in quantum Hall states*. *J. Stat. Mech. (2014) P10005*.

[144] H. M. Wiseman and J. A. Vaccaro. *Entanglement of Indistinguishable Particles Shared between Two Parties*. *Phys. Rev. Lett.* **91**, *097902 (2003)*.

[145] H. Barghathi, C. M. Herdman, and A. Del Maestro. *Rényi generalization of the operational entanglement entropy*. *Phys. Rev. Lett.* **121**, *150501 (2018)*.

[146] H. Barghathi, E. Casiano-Diaz, and A. Del Maestro. *Operationally accessible entanglement of one-dimensional spinless fermions*. *Phys. Rev. A* **100**, *022324 (2019)*.

[147] M. Kiefer-Emmanouilidis, R. Unanyan, J. Sirker, and M. Fleischhauer. *Bounds on the entanglement entropy by the number entropy in non-interacting fermionic systems*. *arXiv:2003.03112*.

[148] M. Kiefer-Emmanouilidis, R. Unanyan, J. Sirker, and M. Fleischhauer. *Evidence for unbounded growth of the number entropy in many-body localized phases*. *arXiv:2003.04849*.

[149] P. Calabrese, M. Mintchev and E. Vicari. *Exact relations between particle fluctuations and entanglement in Fermi gases*. *EPL* **98**, *20003 (2012)*.

[150] R. Susstrunk and D. A. Ivanov. *Free fermions on a line: Asymptotics of the entanglement entropy and entanglement spectrum from full counting statistics*. *EPL* **100**, *60009 (2012)*.

[151] P. Calabrese, P. Le Doussal, and S. N. Majumdar. *Random matrices and entanglement entropy of trapped Fermi gases*. *Phys. Rev. A* **91**, *012303 (2015)*.

[152] N. Laflorencie and S. Rachel. *Spin-resolved entanglement spectroscopy of critical spin chains and Luttinger liquids*. *J. Stat. Mech. P11013 (2014)*.

[153] J.C. Xavier, F.C. Alcaraz and G. Sierra. *Equipartition of the entanglement entropy*. *Phys. Rev. B* ***98***, *041106 (2018)*.

[154] S. Murciano, G. Di Giulio and P. Calabrese. *Symmetry resolved entanglement in gapped integrable systems: a corner transfer matrix approach*. *SciPost Phys.* **8**, *046 (2020)*.

[155] M. Goldstein and E. Sela. *Symmetry-Resolved Entanglement in Many-Body Systems*. *Phys. Rev. Lett.* ***120***, *200602 (2018)*.

[156] R. Bonsignori, P. Ruggiero and P. Calabrese. *Symmetry resolved entanglement in free fermionic systems*. *J. Phys. A* ***52***, *475302 (2019)*.

[157] S. Fraenkel and M. Goldstein. *Symmetry resolved entanglement: Exact results in 1D and beyond*. *J. Stat. Mech. (2020) 033106*.

[158] M. Goldstein and E. Sela. *Imbalance Entanglement: Symmetry Decomposition of Negativity*. *Phys. Rev. A **98**, 032302 (2018)*.

[159] N Feldman and M. Goldstein. *Dynamics of Charge-Resolved Entanglement after a Local Quench*. *Phys. Rev. **B** 100, 235146 (2019)*.

[160] P. Calabrese, M. Collura, G. Di Giulio and S. Murciano. *Full counting statistics in the gapped XXZ spin chain*. *EPL **129**, 60007 (2020)*.

[161] L. Capizzi, P. Ruggiero, and P. Calabrese. *Symmetry resolved entanglement entropy of excited states in a CFT*. *arXiv:2003.04670 (2020)*.

[162] H. Shapourian, P. Ruggiero, S. Ryu, and P. Calabrese. *Twisted and untwisted negativity spectrum of free fermions*. *SciPost Phys. **7**, 037 (2019)*.

[163] E. Cornfeld, L. A. Landau, K. Shtengel, and E. Sela. *Entanglement spectroscopy of non-Abelian anyons: Reading off quantum dimensions of individual anyons*. *Phys. Rev. B **99**, 115429 (2019)*.

[164] P. Caputa, G. Mandal, and R. Sinha. *Dynamical entanglement entropy with angular momentum and U(1) charge*. *JHEP 11 (2013) 052*.

[165] J. S. Dowker. *Conformal weights of charged Rényi entropy twist operators for free scalar fields in arbitrary dimensions*. *J. Phys. A **49**, 145401 (2016);*
.

[166] A. Belin, L.-Y. Hung, A. Maloney, S. Matsuura, R. C. Myers, and T. Sierens. *Holographic charged Rényi entropies*. *JHEP **12** (2013) 059*.

[167] P. Caputa, M. Nozaki, and T. Numasawa. *Charged Entanglement Entropy of Local Operators*. *Phys. Rev. D **93**, 105032 (2016)*.

[168] S. Murciano, P. Ruggiero, and P. Calabrese. *Symmetry resolved entanglement in two-dimensional systems via dimensional reduction*. *arXiv:2003.11453 (2020)*.

[169] D. Fisher. *Random antiferromagnetic quantum spin chains*. *Phys. Rev. B **50**, 3799 (1994)*.

[170] J. Cardy. *Scaling and Renormalization in Statistical Physics*. *CUP, Cambridge, UK (2015)*.

[171] Y.-C. Lin, F. Igloi, and H. Rieger. *Entanglement Entropy at Infinite-Randomness Fixed Points in Higher Dimensions*. *Phys. Rev. Lett. **99**, 147202 (2007)*.

[172] R. Yu, H. Saleur, and S. Haas. *Entanglement entropy in the two-dimensional random transverse field Ising model*. *Phys. Rev. B **77**, 140402 (2008)*.

[173] I. A. Kovacs, and F. Igloi. *Critical behavior and entanglement of the random transverse-field Ising model between one and two dimensions*. *Phys. Rev. B **80**, 214416 (2009)*.

[174] I. A. Kovacs, and F. Igloi. *Universal logarithmic terms in the entanglement entropy of 2d, 3d and 4d random transverse-field Ising models*. *Europhys. Lett **97**, 67009 (2012)*.

[175] J. Rodriguez-Laguna, S. N. Santalla, G. Ramirez, and G. Sierra. *Entanglement in correlated random spin chains, RNA folding and kinetic roughening*. *New J. Phys. **18**, 073025 (2016)*.

[176] V. Alba, S. N. Santalla, P. Ruggiero, J. Rodriguez-Laguna, P. Calabrese, and G. Sierra. *Unusual area-law violation in random inhomogeneous systems*. *J. Stat. Mech. 023105 (2019)*.

[177] S. Pappalardi, P. Calabrese, and G. Parisi. *Entanglement entropy of the long-range Dyson hierarchical model*. *J. Stat. Mech. 073102 (2019).*

[178] C. Monthus. *Properties of the simplest inhomogeneous and homogeneous Tree-Tensor-States for Long-Ranged Quantum Spin Chains with or without disorder*. *arXiv:2001.10731*.

[179] R. Vasseur, A. Roshani, S. Haas, and H. Saleur. *Healing of Defects in Random Antiferromagnetic Spin Chains*. *EPL* **119**, *50004 (2017).*

[180] R. Vasseur, J. L. Jacobsen, and H. Saleur. *Universal entanglement crossover of coupled quantum wires*. *Phys. Rev. Lett.* **112**, *106601 (2014).*

[181] R. Vasseur and J.E. Moore. *Multifractal orthogonality catastrophe in one-dimensional random quantum critical points*. *Phys. Rev. B* **92**, *054203 (2015).*

[182] M. Fagotti and P. Calabrese. *Entanglement entropy of two disjoint blocks in XY chains*. *J. Stat. Mech. P04016 (2010).*

[183] A. Coser, E. Tonni and P. Calabrese. *Partial transpose of two disjoint blocks in XY spin chains*. *J. Stat. Mech. P08005 (2015).*

[184] R. Balian and E. Brezin. *Nonunitary Bogoliubov transformations and extension of Wick's theorem*. *Il Nuovo Cimento B* **64**, *37 (1969).*

[185] I. Peschel and V. Eisler. *Reduced density matrices and entanglement entropy in free lattice models*. *J. Phys. A* **42**, *504003 (2009).*

[186] F. Igloi and I. Peschel. *On reduced density matrices for disjoint subsystems*. *EPL* **89**, *40001 (2010).*

[187] V. Alba, L. Tagliacozzo, and P. Calabrese. *Entanglement entropy of two disjoint blocks in critical Ising models*. *Phys. Rev. B* **81**, *060411 (2010).*

[188] J. Zhang, P. Ruggiero, and P. Calabrese. *Subsystem trace distance in low-lying states of (1+1)-dimensional conformal field theories*. *arXiv:1907.04332 (2019).*

[189] M. Bortz, J. Sato, and M. Shiroishi. *String correlation functions of the spin-1/2 Heisenberg XXZ chain*. *J. Phys. A* **40**, *4253 (2007).*

[190] D. B. Abraham, F. H. L. Essler, and A. Maciolek. *Effective Forces Induced by a Fluctuating Interface: Exact Results*. *Phys. Rev. Lett.* **98**, *170602 (2007).*

[191] M. Serbyn, Z. Papic, and D. A. Abanin. *Universal Slow Growth of Entanglement in Interacting Strongly Disordered Systems*. *Phys. Rev. Lett.* **110**, *260601 (2013).*

[192] R. Vosk and E. Altman. *Dynamical Quantum Phase Transitions in Random Spin Chains*. *Phys. Rev. Lett.* **112**, *217204 (2014).*

[193] E. Altman and R. Vosk. *Universal dynamics and renormalization in many body localized systems*. *Ann. Review of Cond. Mat. Phys. 6, 383 (2015).*

[194] S. A. Parameswaran, A. C. Potter and R. Vasseur. *Eigenstate phase transitions and the emergence of universal dynamics in highly excited states*. *Annalen der Physik 529, 1600302 (2017).*

[195] D. A. Abanin, E. Altman, I. Bloch and M. Serbyn. *Ergodicity, Entanglement and Many-Body Localization*. *Rev. Mod. Phys.* ***91***, *021001 (2019).*

[196] D. Pekker, G. Refael, E. Altman, E. Demler, and V. Oganesyan. *Hilbert-Glass Transition: New Universality of Temperature-Tuned Many-Body Dynamical Quantum Criticality*. *Phys. Rev. X* **4**, *011052 (2014).*

[197] Y. Zhao, F. Andraschko, and J. Sirker. *Entanglement entropy of disordered quantum chains following a global quench*. *Phys. Rev. B* **93**, *205146 (2016)*.

[198] A. Lukin, M. Rispoli, R. Schittko, M. E. Tai, A. M. Kaufman, S. Choi, V. Khemani, J. Leonard, and M. Greiner. *Probing entanglement in a many-body localized system*. *Science* **364**, *6437 (2019)*.

[199] B. Chiaro et. al. *Growth and preservation of entanglement in a many-body localized system*. *arXiv:1910.06024*.

[200] M. Znidaric, T. Prosen, and P. Prelovsek. *Many body localization in Heisenberg XXZ magnet in a random field*. *Phys. Rev. B* **77**, *064426 (2008)*.

[201] J. H. Bardarson, F. Pollmann, and J. E. Moore. *Unbounded Growth of Entanglement in Models of Many-Body Localization*. *Phys. Rev. Lett.* **109**, *017202 (2012)*.

[202] G. Ramirez, J. Rodriguez-Laguna and G. Sierra. *Entanglement over the rainbow*. *J. Stat. Mech. P06002 (2015)*.

Chapter 3

Data Structure of Many-Body Systems

This chapter is based on the following pubblications:

[1] Tiago Mendes-Santos*, Xhek Turkeshi*, Marcello Dalmonte, and Alex Rodriguez, *Unsupervised learning universal critical behavior via the intrinsic dimension*, Phys. Rev. X **11**, 011040 (2021).

3.1 Introduction

The growing field of machine learning (ML) is rapidly expanding our capabilities of analyzing and describing high-dimensional data sets [2–5]. With the increasing understanding of these methods, the community is becoming convinced that their outstanding performance is mostly due to the fact that this *high-dimensionality* is applicable only to the embedding space, while the data sets lay in a manifold that can be twisted and topologically complex but whose intrinsic dimension, I_d, is typically much smaller than the large number of coordinates of the system [6, 7](see graphics in Fig. 3.1 (A)). The determination of this I_d is an active field of research [6, 8, 9] in unsupervised learning (UL), i.e., the branch of machine learning that aims to uncover the internal structure of a data set without the need of any label.

Recently, ML ideas have encountered fruitful applications in the context of statistical physics [10–12]. Such applications have ranged from the determination of physical properties [13–21], to the formulation of novel classes of variational ansätze [22–25]. These progress leveraged on analyzing and exploiting the results of dimensional reduction, and using a variety of tools to analyze (or employ) the final representation (or truncation) obtained in this way. In various contexts, results obtained via these methods have remarkably shown to be already competitive with more traditional approaches [10].

Here, we pursue an alternative approach: our main purpose is to show that, from a ML perspective, physically relevant and universal information can be gathered by analyzing the very same embedding procedure that carries out the dimensional reduction, rather than focusing on its final result. In particular, we show how the intrinsic dimension correspondent to the partition function of statistical mechanics models displays universal scaling behavior in the vicinity of phase transitions, and it behaves as an order parameter for a corresponding structural transition in data space. Differently from previous works [13, 26–32], our approach is thus focused on *data mining* the data set as a whole, and thus, does not leverage on any kind of projection. At the technical level, this is achieved by employing a cutting-edge nearest-neighbor estimator of the I_d, which is suitably designed to deal with non-linear data sets, i.e. data sets lying on non-linear manifolds [9].

In order to access the complex data structure at phase boundaries, we study numerically instances of first-order, second-order (conformal), and Berezinskii-Kosterlitz-Thouless (BKT) transitions in two-dimensional (2D) classical spin systems. In all cases, I_d displays a universal scaling behavior correspondent with the transition properties of the underlying lattice model. (i) For first-order transitions, I_d peaks at the critical point due to the coexistence of different orders, and the finite-size corrections of the transition temperature are dictated by trivial scaling exponents. (ii) For both second-order and topological transitions, we observe *universal scaling collapse*, with transition temperature and critical exponents determined to the percent level. (iii) Most importantly, we provide compelling evidence that the I_d is an ideal tool to underpin topological transitions in an unsupervised fashion: as an example, we extract the critical temperature of the 2D XY model with 1% confidence even at modest system sizes.

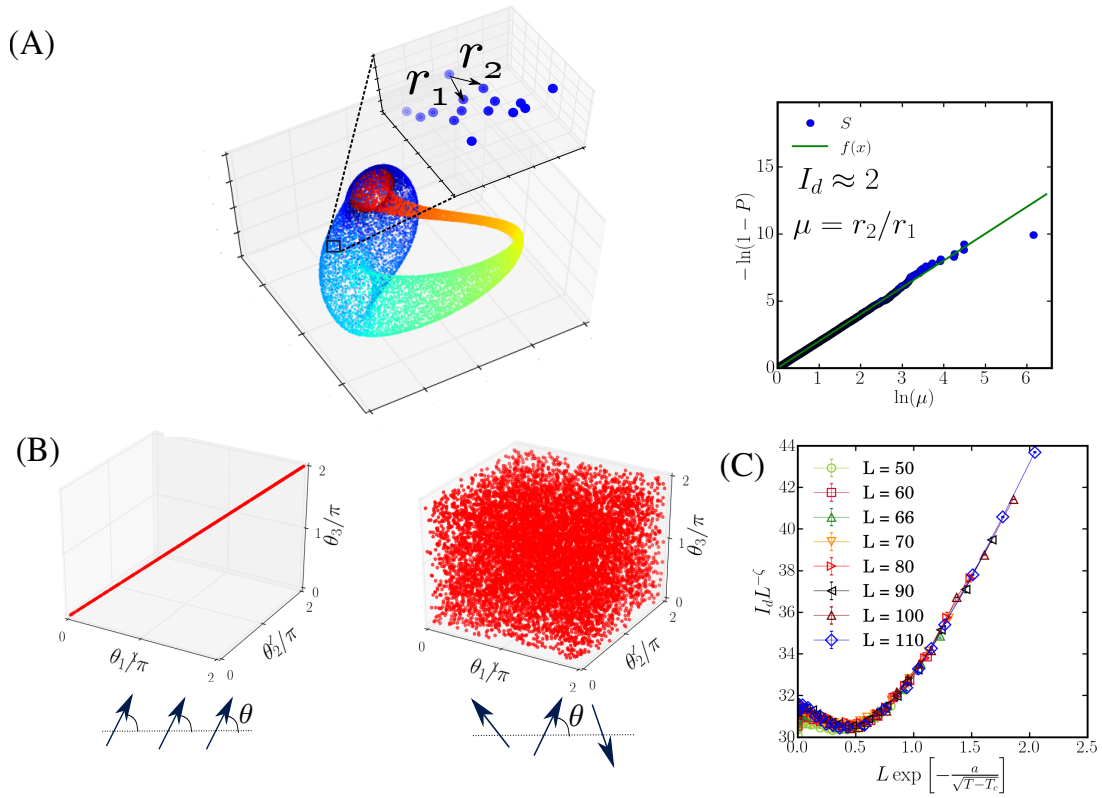

FIGURE 3.1: Panel (A): *Schematics of the intrinsic dimension, I_d.* The important content of a data set typically lays in a manifold whose I_d is much lower than the number of coordinates. In the example, despite the synthetic data set (Klein's bottle-shaped) is embedded in a three-dimensional space, it can be effectively described by a twisted manifold whose $I_d = 2$. The key ingredients to compute the I_d are the first- and the second-nearest neighbor distances, r_1 and r_2, of each point of the data set. The computation of the I_d is based on the fitting of the *empirical* cumulative distribution function (CDF) of the ratio $\mu = r_2/r_1$, $P(\mu)$ [see text and Eq. (3.2)]. Panels (B): *Low- and high-temperature data sets of a 3-site model in configuration space.* The points represent the 3-site XY model configurations: $\vec{\theta} = (\theta_1, \theta_2, \theta_3)$. The high- and zero-temperature cases show simple data structures: for $T = 100$, I_d is equal to the number of spins, while for $T = 0$, $I_d = 1$. Panel(C): *Intrinsic dimension in the vicinity of a phase transition.* The I_d in the intermediate temperature regime, representative of phase transitions in larger systems, is considerably more complex. The temperature dependence of I_d can be used to signalize and characterize critical points. As an example, we show the universal data collapse of the I_d at the Berezinskii-Kosterlitz-Thouless described by the 2D XY model.

We then develop a theoretical framework in support of the fact that I_d has characteristic features at transition points, that are governed by scaling theory. First, we show how several instances of the data set, in particular, the distribution of distances between sampled configurations, are already revealing striking features about critical behavior for all classes of phase transitions. The basic idea there is that the data space naturally clusters configurations characterized by similar physical properties (e.g., magnetization and winding number). The fact that the intrinsic dimension has strong features at phase transition then follows from its 'local' nature (related to changes of scale in configuration space, in a sense that we specify below). Then, we discuss how, for the type of data sets we are interested in, the intrinsic dimension can be connected directly to a set of arbitrary-many-body correlation functions, that, following the finite-size scaling hypothesis, justifies its scaling behavior in the vicinity of transition points. We then check *a posteriori* the validity of some of the assumptions at the basis of this framework.

Before diving into the main part of this Chapter, we provide a simplified picture that qualitatively captures how the intrinsic dimension is connected to the physical information obtained by sampling a partition

function via Monte Carlo methods. The basic intuition behind the I_d of data sets generated in the low- and high-temperature regimes of a simple 3-site XY model is drawn in Fig. 3.1 (B). At low temperature (left graphics of Fig. 3.1 (B)), most of the spin configurations sampled during the Markov chain correspond to fully ferromagnetic spin arrangements (see cartoon). In the limiting case $T = 0$, the ground states are given by XY ferromagnetic configurations, i.e., $\theta_1 = \theta_2 = \theta_3$, and the data set is described by a manifold that lays in a line ($I_d = 1$). Oppositely, in the high temperatures regime, the data set is described by a manifold whose $I_d = 3$: each new Monte Carlo configuration corresponds to an arbitrary arrangement of the three spins, so that the structure of the data set is that of a homogeneously occupied three-dimensional space. This simple example demonstrate how transitions in parameter space are accompanied by structural transitions in data space. Due to its collective origin, the transition region requires the computation of I_d in very high dimensional data space: in Fig. 3.1 (C), we show a sample of our results, illustrating the scaling collapse of the intrinsic dimension correspondent of the 2D XY model in the vicinity of its BKT transition point.

3.2 Intrinsic Dimension

Before addressing the analysis of concrete statistical mechanics models, we present here a self-contained discussion on the intrinsic dimension and its state-of-the-art estimators. This section is propaedeutic to the critical identification of the best estimator to be used in our applications below.

The I_d is a concept that arises from the observation that, in natural data sets, the correlations between the input variables induce a structure, modifying the dimensionality of the manifold in which the data lie. In order to visualize this, one can imagine a data set with the Cartesian coordinates of points extracted from a circle. Although the input coordinates are two, they are strongly correlated and the manifold in which the points lie has a $I_d = 1$. Therefore, in simple cases like this, or the one shown in Fig. 3.1B, it roughly corresponds with the minimum number of variables needed to describe a data set [8, 9].

Information about the I_d is important to determine if dimensional reduction of high-dimensional data sets incurs information loss or not. Moreover, it can be used as an UL approach to characterize a system. Just to mention a few examples: in biological physics, the I_d can be used to determine the number of independent directions a protein can have during a sequence evolution [33], in image analysis, to distinguish between different kind of image structures [34], in astrophysics, to estimate the amount of information available in spectropolarimetric data [35], in theoretical machine learning, to understand the properties of deep neural networks [36], and in ecology, to characterize the minimum number of independent axes of variation that adequately describes the functional variation among plants [37].

Different approaches have been developed to estimate the I_d, see Ref. [8] for review. For example, dimensional reduction techniques, such as principal component analysis (PCA) [38], Multidimensional Scaling [39], Isomap [40], Locally Linear Embedding [41], Autoencoders [42], t-distributed stochastic neighbor embedding (t-SNE) [43] or Uniform Manifold Approximation and Projection (UMAP) [44] to mention some of them, search for a lower dimensional space to project the data set by minimizing a projection error. The dimension of the identified subspace is viewed as an estimation of I_d. However, identifying this dimension is far from trivial. For instance, in the PCA case, one should take into consideration the spectrum of the eigenvalues of the covariance matrix and look either for a gap or decide *ad hoc* a cut-off parameter. It is worth saying that, for PCA, this strategy will not work if the manifold of lower dimensionality is curved. Furthermore some of the above mentioned methods, like t-SNE, are focused on visualization and assume that the dimension of the projection space is lower than the I_d. Therefore, these projection algorithms aim to alleviate the problems that this dimension mismatch cause in the visualization, not being well suited for I_d detection.

A closely related quantity is the fractal dimension [45], whose estimation relies on the scaling of the number of neighbors with the distance from a given point. This approach is largely employed in the study of percolation transitions [46], but it suffers from serious limitations when the density distribution of points is not uniform.

These limitations lead to the development of nearest neighbors methods, in which it is assumed that nearest-neighborhood points can be considered as uniformly drawn from small enough I_d-dimensional hyperspheres (not all the data set) [6, 8]. Indeed, the avoidance of any projection step and the smoothing on the condition of data uniformity (from the full data set to a small neighborhood around each point) are key features for obtaining good results in highly non-uniform, non-linear data sets even at really high dimensions (a regime at which all the purely geometrical methods present a bias due to the curse of dimensionality).

The TWO-NN method employed in this Chapter belongs to this type of methods, with the particularity that by focusing only on the first two nearest neighbors (see Fig. 3.1 A), the size of the I_d-dimensional hyperspheres at which the density is assumed constant is reduced to its minimum expression. The method is rooted in computing the distribution functions of neighborhood distances, which are function of I_d. More specifically, for each point $\vec{x}$ in the data set, we consider its first and second nearest-neighbors distances $r_1(\vec{x})$ and $r_2(\vec{x})$, respectively. Under the condition that the data set is locally uniform in the range of second nearest-neighbors, it has been shown in Ref. [9] that the the distribution function of $\mu = r_2(\vec{x})/r_1(\vec{x})$ is

$$f(\mu) = I_d \mu^{-I_d - 1}. \tag{3.1}$$

ove, being a purely g
oints needed to have a
(3.2) was derived a
nt support implies sc
hall happen when tv

3.3 Models

Our approach focuses on the high-dimensional data sets associated with the equilibrium configuration states of a partition function. Such states are sampled with Markov Chain Monte Carlo simulations from the thermal weight $\rho(E) \sim e^{-E(\vec{x})/T}$, where $E(\vec{x})$ is the energy of an independent configuration $\vec{x}$ and T is the temperature. We employ Wolff's cluster algorithm [47, 48], and for each data set, we consider N_r configurations.

We consider partition-function data sets of several models in the vicinity of various types of phase transitions [49, 50]. The first example is the well known Ising model in two-dimensions

$$E(\vec{s}) = -\sum_{\langle i,j \rangle} s_i s_j, \tag{3.3}$$

where the spin degrees of freedom are $s_i = \pm 1$, and $\langle i, j \rangle$ are the nearest neighboring bonds of a square lattice, with $N_s = L \times L$ spins and periodic boundary condition. The Ising configuration states are defined as

$$\vec{s} = (s_1, s_2, ..., s_{N_s}). \tag{3.4}$$

This model describes a second-order phase transition characterized by the breaking of a Z_2 symmetry at the critical temperature $T_c = 2/\ln(1+\sqrt{2})$. In the vicinity of T_c, the spin correlation length diverge as $\xi \sim (T - T_c)^{-\nu}$, where the critical exponent is $\nu = 1$.

We also consider the first- and second-order phase transitions described by the q-states Potts model (qPM)

$$E(\vec{\sigma}) = -\sum_{\langle i,j \rangle} \delta_{\sigma_i,\sigma_j}, \tag{3.5}$$

where the spin $\sigma_i = 0, 1, 2, ..., q-1$, and $\delta_{\sigma_i,\sigma_j}$ is the delta function. In particular, the $q = 2$ Potts model can be mapped into the Ising model. The Potts configuration states are defined by

$$\vec{\sigma} = (\sigma_1, \sigma_2, ..., \sigma_{N_s}). \tag{3.6}$$

The qPM is characterized by a discrete Z_q symmetry that is broken at the critical temperature $T_c = 1/\ln(1+\sqrt{q})$. Importantly, this class of models displays a second-order phase transition for $q \leq 4$, and a first-order one for $q > 4$. We examine both these regime: the second-order transition described by the $q = 3$ PM (with correlation length critical exponent $\nu = 4/5$), and the first-order transition described by the $q = 8$ PM [51, 52].

Finally, as a representative of the BKT universality class, we investigate the two-dimensional XY model[53, 54]

$$E(\vec{\theta}) = -\sum_{\langle i,j \rangle} \vec{S}_i \cdot \vec{S}_j, \tag{3.7}$$

where $\vec{S}_i = (\cos(\theta_i), \sin(\theta_i))$, $\cos(\theta_i)$ and $\sin(\theta_i)$ being the projection of the spin at site i in the x and y directions, respectively, and $\theta_i \in [0, 2\pi[$. The XY configurations are defined as

$$\vec{\theta} = [\cos(\theta_1), \sin(\theta_1), ..., \cos(\theta_{N_s}), \sin(\theta_{N_s})]. \tag{3.8}$$

This model is characterized by a continuous $U(1)$ symmetry and describes a phase transition between a high-temperature phase with exponentially decaying spin correlations, and a low-temperature quasi-ordered phase characterized by power-law decaying correlations. The BKT critical temperature, T_{BKT}, is not known exactly; state-of-the-art estimations based on the analysis of the spin stiffness of lattices of order $O(10^6)$ spins give $T_{BKT} = 0.8935(1)$ [55].

The detection of the BKT critical point is hindered by the fact that it cannot be characterized by conventional local order parameters, as in the examples discussed previously, and due to the exponential growth of the correlation length near T_{BKT}. Hence, the BKT transition represents a key challenging test for any UL method.

3.3.1 How to characterize partition functions as data sets

Before proceeding to the discussion of the results, we point out some important aspects of the Ising, Potts and XY data sets (see Eqs. (3.4), (3.6) and (3.8), respectively.). First, a crucial step to obtain the I_d (cfr. Eq. (3.2)) is to consider a proper metric; the distance $r(\vec{x^i}, \vec{x^j})$ between two configuration states $\vec{x^i}$ and $\vec{x^j}$ must be non-negative, equal to zero only for identical configurations, symmetric, and satisfy the triangular inequality.

For the XY data sets the distance is defined as the the Euclidean distance:

$$r(\vec{\theta^i}, \vec{\theta^j}) = \sqrt{2 \sum_{k=1}^{N_s} \left(1 - \vec{S}_k^i \cdot \vec{S}_k^j\right)}. \tag{3.9}$$

This distance properly takes into account the periodicity of the configuration states in the interval $\theta_i \in [0, 2\pi[$.

For both Ising and Potts configuration states, we consider the Hamming distance, i.e., $r(\vec{s^i}, \vec{s^j})$ (or $r(\vec{\sigma^i}, \vec{\sigma^j})$) is given by the number of positions in the state vectors ($\vec{s^i}$ and $\vec{s^j}$) for which the corresponding coordinates are different. The choice of the Hamming distance is motivated by the fact that the energy difference between two spins in the model of interest is given by a delta function.

As mentioned in the previous section, the two-NN method fails when two or more sampled configurations of the data set have identical coordinates. This issue typically occurs in the discrete-variables Ising and Potts data sets, when the total number of independent configuration states, N_c, is smaller or of the same order of the number of configurations used in the data set, N_r. For instance, for both Ising and Potts data sets, identical ferromagnetic configurations are sampled in most of the Monte Carlo steps when $T \ll T_c$. However, in the regime that we focus here (i.e., T close to T_c and $L > 10$), as $N_c \gg N_r$, this issue is irrelevant (we have explicitly checked this in our data sets).

Finally, we mention that data sets generated by the XY configuration states lie typically in nonlinear manifolds, which can be noted by the fact that linear dimension reduction methods, such as PCA, fails to describe XY data sets, see Ref. [30]. In fact, even for the simple data set shown in Fig.3.1 (B), linear PCA fails in estimating the true I_d of the system when the proper distance between the configurations are taken into account, see the Appendix 3.7.1. This feature of the XY data sets reveals the necessity of using state-of-the-art I_d-estimators (such as the two-NN method considered here) that properly takes into account nonlinearities.

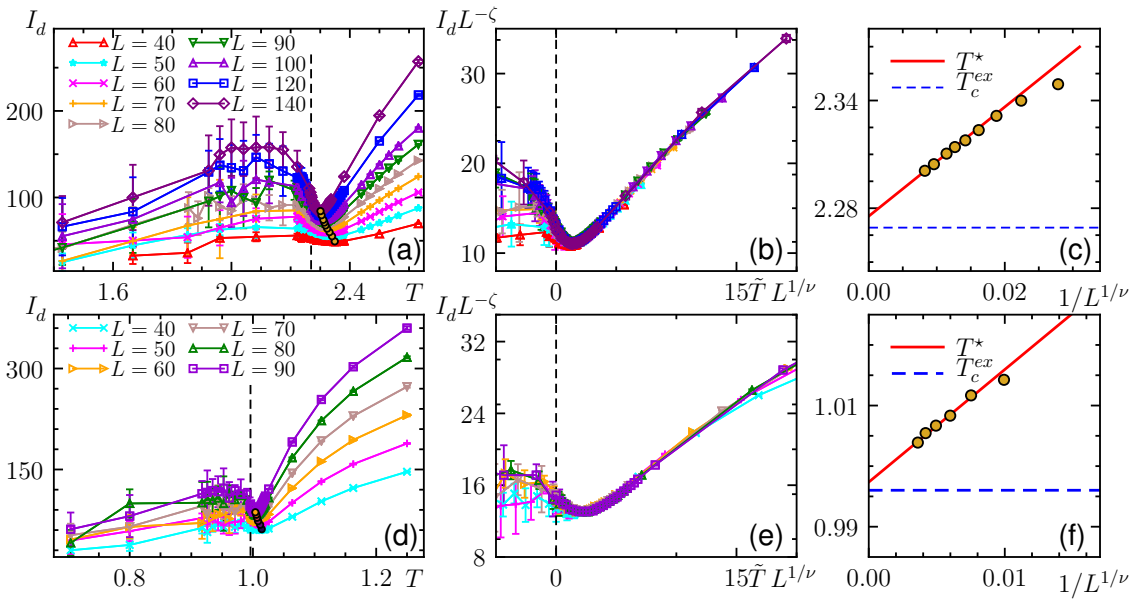

FIGURE 3.2: *Second-order phase transition. Panels (a-c): Ising model. Panels (d-f): $q = 3$ Potts model.* Panels (a,d): I_d as a function of T for the Ising model. Errorbars are standard deviation associated to a distributions of n realizations of I_d (we typically consider $n \geq 5$). Panel (b,e): data collapse of I_d based on the FSS discussed in main text. The best data collapse of the results give $T_c = 2.283(2)$, $\nu = 1.02(2)$ and $\zeta = 0.410(5)$ for the case of the Ising model, and $T_c = 0.996(2)$, $\nu = 0.805(5)$, and $\zeta = 0.420(2)$ for the case of the Potts model. Panels (c,f): finite size (FSS) scaling of the minimum temperature T^* (see text); the horizontal line is the exact result for T_c. The extrapolation returns $T_c = 2.2784(2)$ and $T_c = 0.9970(3)$ for the Ising and Potts cases, respectively.

3.4 Results

3.4.1 Second-order phase transitions

We start our discussion considering second-order phase transitions (2PTs) described by the Ising and the 3-states Potts (3PM) models, see Fig. 3.2. We consider data sets formed by $N_r = 5 \times 10^4$ configuration states. Overall, far from the transition, I_d is an increasing function of T. For low-T, the computation of I_d is affected by the discreteness of the Potts (Ising) configurations; which reflects on the larger error bars. However, this issue is mitigated close to the critical point, T_c. Remarkably, I_d exhibits a non-monotonic behavior in the vicinity of the critical point (see Figs. 3.2 (a1) and (b1)) which can be used to locate and characterize the transition point itself.

As conventionally done in the analyses of physical observables, e.g., magnetic susceptibility and heat capacity, we now consider a finite-size scaling (FSS) theory for I_d. First, based on the FSS hypothesis and postulating that I_d behaves as an order parameter for the transition, one has $I_d = L^{\zeta} f(\xi/L)$, where the correlation length diverges as $\xi \sim (T - T_c)^{-\nu}$, ν is a critical exponent, and ζ is a scaling exponent associated with the divergence of I_d at T_c. Figs. 3.2 (a2) and (b2) show the universal data collapse for Ising and 3PM, respectively. The values obtained for T_c and ν have a discrepancy with exact results of less than 0.5% and 4%, respectively. For Ising we obtain: $T_c = 2.283(2)$, $\nu = 1.02(2)$, and $\zeta = 0.410(5)$, while for 3PM: $T_c = 0.996(2)$, $\nu = 0.805(5)$, and $\zeta = 0.420(2)$. See the Appendix 3.7.3, for the discussion about the details of the data-collapse procedure.

Further, we consider the size scaling of the shift of the local minimum of $I_d(T)$ (i.e., the temperature $T^*(L)$),

$$T^*(L) - T_c \sim \frac{1}{L^{1/\nu}}. \tag{3.10}$$

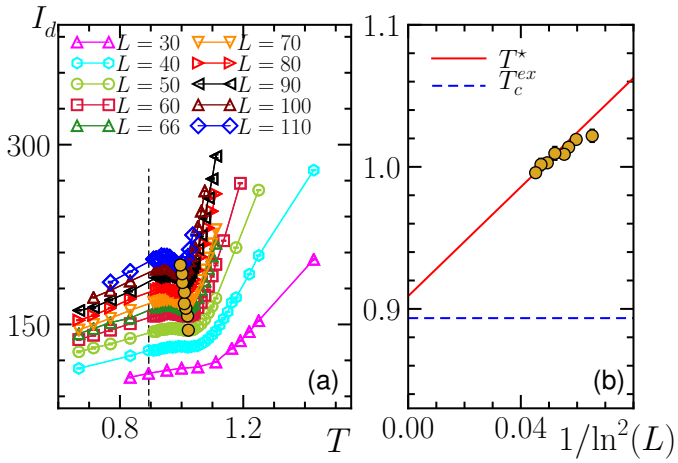

FIGURE 3.3: *Berezinskii-Kosterlitz-Thouless transition.* Panel (a) shows the temperature dependence of I_d for different values of L. The dashed line indicates the value of the BKT critical temperature obtained in Ref. [55] using conventional methods, $T_{BKT} = 0.8935(1)$. For each point, we harvested approximated 10 instances of the data set and average the resulting estimates for the I_d. The error bars are the standard deviation of such set of results. The scaling collapse obtained with these data sets is depicted in Fig. 3.1 (c). Panel (b) shows the finite-size scaling of T^* based on Eq. (3.11). Fitting the results for $L = 80, 90, 100$ and 110, we obtain $T_{BKT} = 0.909 \pm 0.015$. In the text, we discuss how we obtain the local minimum of I_d, T^*. We compute the I_d of manifolds with $N_r = 5 \times 10^4$ configurations.

We note that $T^*(L)$ is reminiscent of the universal scaling behavior of singular features of physical observables close to T_c (e.g., the peak of the magnetic susceptibility) [56]. In order to compute T_c, we employ the following procedure: (i) we obtain $T^*(L)$ by fitting the results in an interval close to $T^*(L)$ with a cubic function; the fitting is performed with a jackknife procedure, which allows establishing an error bar for $T^*(L)$. We then (ii) consider the aforementioned FSS to compute T_c; the fitting is performed considering different sets of points. This method provides a coherent error propagation for T_c. We obtain, $T_c = 2.2784(2)$ for the Ising model and $0.9970(3)$ for the 3 state Potts model. Their discrepancies with the exact values are respectively of order 0.4% and 0.2%.

The results of this analysis confirm the validity of our original assumption, that is, that the intrinsic dimension is a valid order parameter describing the transition in data space as a structural transition. We remark that this is validated at two steps - firstly, via the quality of the scaling collapse, and secondly, by the scaling of the transition temperature obtained by analysis a single feature of the I_d dependence with respect to the temperature. Those represent two fundamental tests that any valid order parameter shall satisfy at transition points.

3.4.2 Berezinskii-Kosterlitz-Thouless (BKT) phase transition

Unsupervised learning of phase transitions associated with the break of a symmetry, as discussed in the previous section, can also be performed with other unsupervised methods, such as PCA [13, 28, 57] and variational autoencoder (VAE) [26]. For example, the critical temperature of the Ising model can be obtained with an accuracy similar to the ones obtained here. Furthermore, the latent parameters of the VAE can be used to learn the local order parameter associated to both discrete and continuous symmetry-breaking transitions [26]. Those methods are based on a dimension reduction, and thus, differ on a fundamental way from our unsupervised approach, which is based solely on the analysis of the I_d. As we discuss in this section, our approach can be extended to transitions that are characterized by non-local order parameters, such as the topological BKT phase transition, that are treated on the same footing of second order transitions.

The difficulties in learning the BKT transition from raw XY configurations occur in both supervised [58] and unsupervised [28] ML approaches. Recent progress based on diffusion maps [30, 59] or topological data

analysis[60] have been made to solve this problem, typically considering problem-specific insights (such as the structure of topological excitations). These approaches have shown how considerable qualitative insight can be gathered on the nature of the BKT transition. However, it is presently unclear if the raw data structure corresponding to topological transitions can exhibit universal features, and if so, if unsupervised approaches can be used to detect the critical temperature with an accuracy that is comparable with conventional methods (that typically rely on the a priori knowledge of the order parameter).

In Fig. 3.3 (a), we show the temperature dependence of I_d in the transition region. The intrinsic dimension clearly distinguishes the low-T regime, characterized by bound vortex-antivortex pairs, from the unbinding high-T regime. In the vicinity of the BKT critical point, T_{BKT}, the behavior of I_d resembles the one observed for the second-order phase transitions, i.e., I_d exhibits a local minimum at $T^*(L)$ (observed for $L > 30$), which is a signature of the BKT transition. Note that the minimum is clearly visible already for lattices of order $L = 50$; at these sizes, the spin stiffness is instead featuring a very smooth behavior, as considerably larger systems are required to appreciate a qualitative jump in the latter.

We consider the conventional FSS for BKT transition, $I_d(T, L) = L^{\zeta} f(\xi(T)/L)$, where the singular value of the correlation length diverge exponentially, i.e., $\xi \sim \exp\left(a/\sqrt{T - T_c}\right)$. In Fig. (3.1) (C), we show the universal data collapse for different values of L, where a, T_{BKT} and ζ are treated as free-parameters in the collapse procedure; see the Appendix 3.7.3. The value obtained, $T_{BKT} = 0.92(1)$, is in good agreement with estimations of T_{BKT} obtained on Ref. [56].

A more accurate estimation of T_{BKT} is based on the finite-size scaling of $T^*(L)$. This approach relies on the computation of $T^*(L)$, which is performed with the same procedure described in the previous section, and the finite size scaling ansatz [56]:

$$T^*(L) - T_{BKT} \sim \frac{1}{\ln^2 L}. \tag{3.11}$$

As discussed before this procedure allows us to establish an error bar for the calculated T_{BKT}. We obtain $T_{BKT} = 0.909 \pm 0.015$, that is compatible within error bars with Ref. [55] where simulations with up to $O(10^6)$ spins were carried out. For comparison, the best alternative method [30] utilizing unsupervised learning techniques reported relative errors of the order of 5%.

Conventionally, T_{BKT} is obtained with the aid of the so-called Nelson-Kosterlitz universal jump of the spin wave stiffness [61], which allows to determine the finite-site critical temperature, $T^*_{BKT}(L)$. The FSS [Eq. (3.11)] is then used to determine BKT critical point at the thermodynamic limit. Remarkably, here we observe that the intrinsic dimension of raw XY data sets exhibit a clear signature of the finite-site T_{BKT}, even for moderate system sizes we have considered.

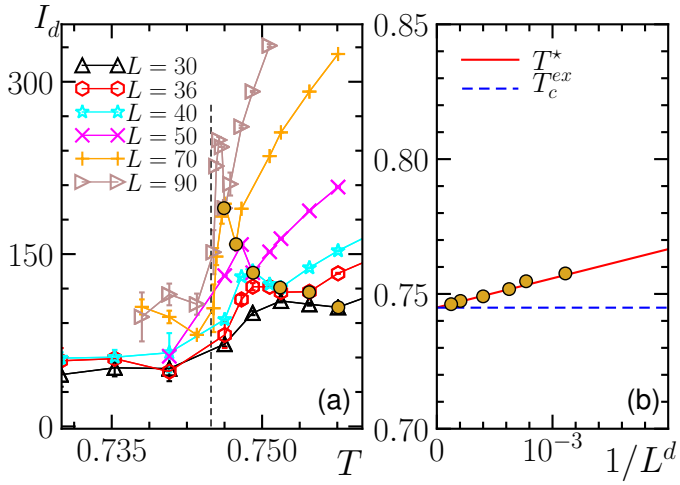

FIGURE 3.4: *First-order phase transition.* Panel (a) shows I_d as function of T for the 8-states Potts model. Panel (b) shows the finite size (FSS) scaling of T^*, where $d = 2$ (see text).

3.4.3 First-order phase transitions

Finally, we consider an example of first-order phase transition (1PT): the 8-state Potts model (8PM). As is typical of 1PT the system exhibit a finite-size correlation length at T_c, $\xi_8 = 23.9$ [62]. For $L > \xi_8$, the transition can be described by trivial and generic critical exponents, e.g., $\nu = 1/d$, d being the system dimension [52, 63, 64]. Furthermore, the finite-size shift of the critical temperature, $T_c(L)$, conventionally detected, for example, by the maximum value of the magnetic susceptibility, scales as $T_c(L) - T_c \sim 1/L^d$.

Fig. 3.4 shows that I_d also exhibit a clear signature of the 1PT, featured by a peak at T_c for $L \gg \xi_8$. For $L \approx \xi_8$, the temperature dependence of I_d resembles the one observed for 2PTs in Fig. 3.2; i.e., I_d exhibit a local minimum at a temperature T^*. Interesting, the FSS of T^* is in agreement with first-order transitions, see Fig. 3.4 (b) [63, 64]; the discrepancy of the calculated $T_c = 0.7448(1)$ with the exact value is less the 0.05%

3.5 Discussion

Our results so far support the fact that, in the vicinity of a phase transition, the intrinsic dimension displays universal behavior at both first, second-order and BKT transition, and works as a order parameter signalling a transition between different data structures in configuration space. Within this framework, the position of the transition is always identified with the scaling of the minimum of the intrinsic dimension.

In continuous phase transitions, collective behavior is captured by only a handful of parameters. This suggests that the amount of information required to describe the system is parametrically simpler at the critical point when compared to its vicinity, as the latter region requires additional information on the operators required to perturb away from criticality. This emergent simplicity may have several consequences at the data structure level. The most direct consequence is that one expects a simplified data structure to be described by a minimum of the intrinsic dimension at the transition point. This is exactly what we have observed at both second-order and BKT transitions. We note that this expectation is not related to the number of states sampled by the partition function (this number is, in our case, fixed by N_r are configurations are never repeated). The discussion of how our results change with N_r is reported in Appendix 3.7.2.

For first-order transitions, the above reasoning is not applicable as it relies on universal behavior, and thus the existence of a continuum limit. In these cases, one expects that the data space in the vicinity the transition point shall feature two separate regions, each of them composed of states representing the two phases meeting at T_c. Exactly at the transition point, one expects an abrupt change in the data structure: indeed, the MC sampling will access a large number of configurations corresponding to both phases (in analogy to metastability), and thus display a sharp increase (see Fig. 3.4 (a)). Approaching the transition point from the disordered phase will feature instead of a minimum, that scales to the transition point.

The arguments above serve as a qualitative guideline behind the basic picture we put forward: the simplified field theory description applicable at transition points reflects directly into the data structure of the problem. We now provide a data-driven discussion in support of this picture, that specifically emphasize the connection between the data set and correlations in the system via the (generic) definition of distance we employ. For the sake of concreteness, we first elaborate on the presence of distinctive features in the vicinity of T_c, and then connect to universal scaling.

3.5.1 Why the I_d exhibits a singular behavior in the vicinity of T_c?

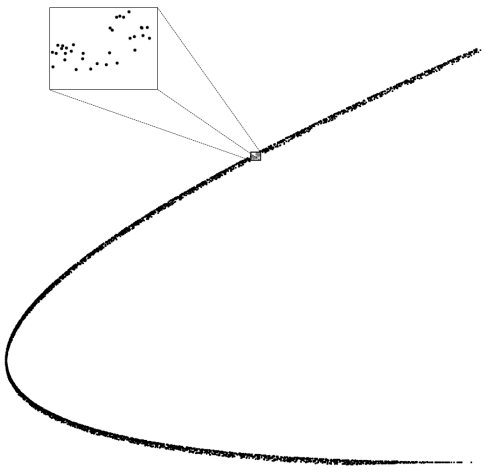

FIGURE 3.5: *Scale dependence of ID*. The data set shown presents an $I_d = 1$ or $I_d = 2$ depending on the scale that is considered.

The I_d is a *scale* dependent quantity [8]. This can be intuitively understood by looking at example depicted in Fig. 3.5, where an approximately one dimensional object appears as two dimensional when

looking at a different scale by zooming. The scale of the data set, as estimated with two-NN, is fixed by N_r for a given T, since it fixes the actual meaning of first and second nearest neighbors [9]; here we always consider $N_r = 5 \times 10^4$. In the following, we will show how changes in the scale of the data (configuration) space appear when there is a phase transition, leading to the emergence of features in the I_d.

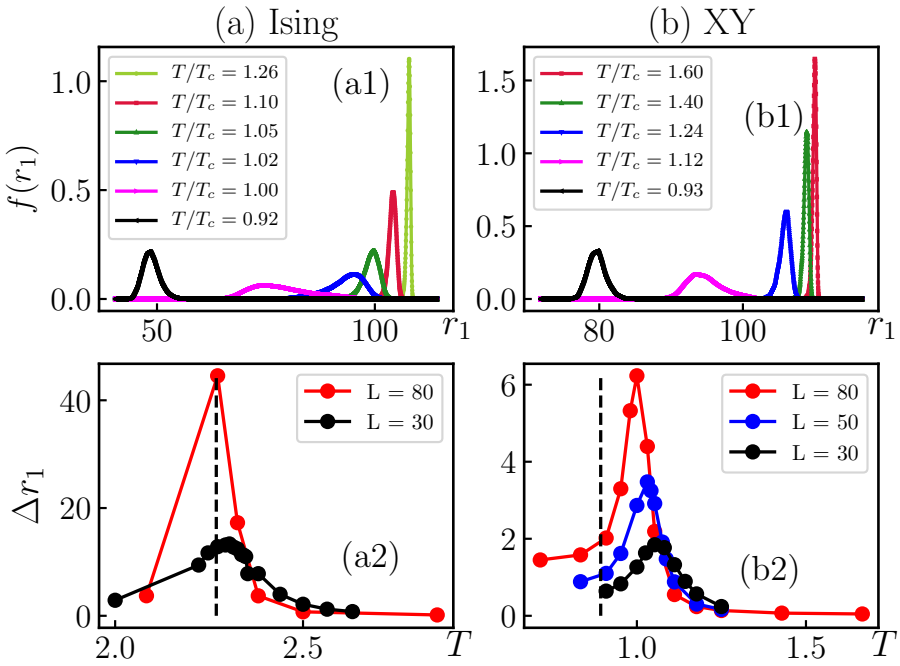

FIGURE 3.6: *Statistics of first nearest-neighbor distances,* r_1. In panels (a1) and (b1) we show the Kernel density estimation of the probability density function of r_1 for the Ising and XY data sets, respectively. All the results have $L = 80$. Panels (b1) and (b2) show the temperature dependence of the variance associated to the distribution functions show in (a) for different system sizes. Results for the second nearest-neighbor distances, r_2, are qualitatively the same.

A first test is to check that these changes in the scale effectively occur. To this end, we analyze the statistics of r_1 and r_2. For example, the distribution function of the first-neighbor distances, $f(r_1)$, changes for both Ising and BKT critical points, see Figs. 3.6 (a1) and (b1). The position of the peak of $f(r_1)$ sharply decreases as one crosses the transition, and the variance associated to $f(r_1)$, Δr_1, has a peak close to the transition, see Fig. 3.6 (a2) and (b2). Interestingly, our results indicate that the quantity Δr_1 also exhibit universal scaling behavior at Ising and BKT critical points. Moreover, the results for both Ising and XY data sets are qualitatively the same, highlighting that data-wise, symmetry-breaking and topological transitions are treated on the same footing. However, it is important to stress that, contrary to what happens in the case of I_d, the peak in Δr_1 is not expected to present features when the data sets are not homogeneous in density, since the relevant distances will be also affected due to these inhomogeneities (see ref. 9 for a further discussion on why two-NN is only mildly affected by this problem). In this sense, the intrinsic dimension, being solely sensitive to changes of scale and not local density features, provides a considerably more reliable probe for phase transitions.

In order to understand the underlying cause to this change of scale, we first focus on discrete symmetry-breaking transitions. In those cases, PCA provides an understanding of the data structure emerging at critical points [13, 28]. For instance, the Ising data set features clusters characterized by configurations with positive, $+M$, and negative, $-M$, total magnetization for $T < T_c$. In contrast, a single cluster is formed for $T > T_c$, see Figs. 3.7 (a1) and (a2). This clustering structure allow us to understand the connectivity between neighboring configurations in the Ising data set. For $T > T_c$, the magnetization of neighbors is completely random. In contrast, configurations connect to first and second neighbors with the

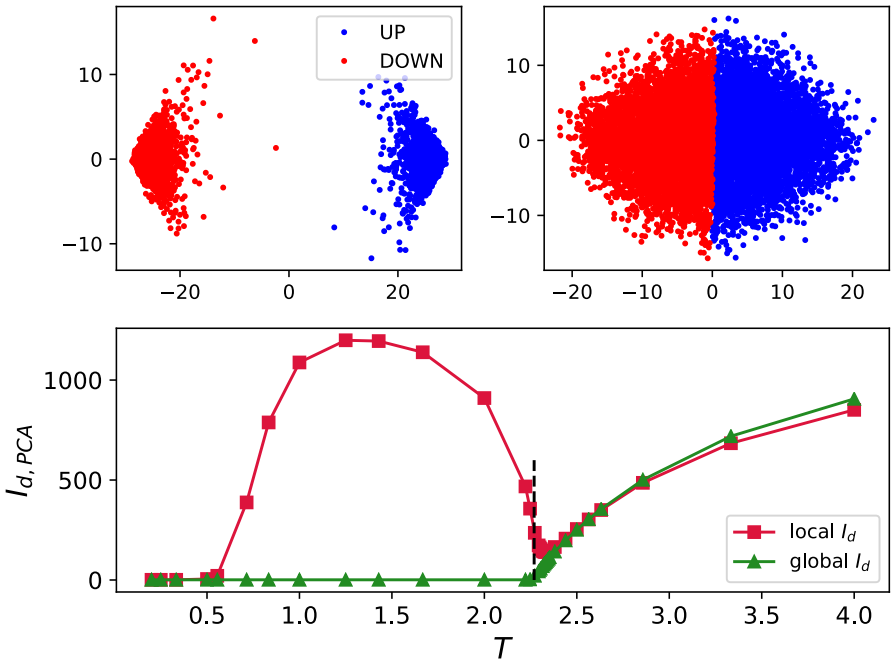

FIGURE 3.7: *I_d obtained with PCA.* Panel (a1) and (a2) show the projection of the Ising data set in the two leading principal components for $T/T_c \approx 0.94$ and $T/T_c \approx 1.10$, respectively. Configurations with total magnetization $M > 0$ are represented by the blue points, while ones with $M \leq 0$ by the red points. Panel (b) shows the PCA estimation of the I_d considering the full Ising data set (global I_d) and the data set generated by configurations with total magnetization $M > 0$ ("local" I_d). For all the results, $L = 60$.

same magnetization sign for $T < T_c$; see Fig. 3.8 (a). Equivalent reasoning based on PCA is applicable to the Potts data sets.

To illustrate how the locality (and the the connectivity between neighboring configurations) affects the behavior of the I_d, we consider two estimates of the I_d provided by PCA. In the first case, we employ all the configurations of the Ising data set, $I_{d,PCA}$ (global) while, in the second, we consider just configurations with M > 0, $I_{d,PCA}$ (local); see the Appendix 3.7.1 for more details. The latter quantity provides a local estimate (within the range scale of a single cluster) for $T < T_c$, which is analogous to the local measure of the I_d provided by the TWO-NN method. As shown in Fig. 7 (b), the global $I_{d,PCA}$ sharply goes to 1 below T_c, while the local $I_{d,PCA}$ exhibits the same non-monotonic behavior close to T_c observed in Fig. 3.2. This result highlights that the locality of the I_d is the crucial element to understand its non-monotonic behavior close to T_c.

The connectivity between neighboring configurations is also related to the physical properties of the BKT transition. In this case, the most suitable quantity to characterize configurations and the corresponding clustering structure in phase space is the winding number, w (see Appendix 3.7.4), as excitations have topological (global) nature [30]. Above the BKT transition, vortex-antivortex pairs are unbounded. Due to this, MC simulation samples configurations with different w. By contrast, in the quasi-long-range-order regime ($T < T_{BKT}$), most of the configurations have $w = (0, 0)$. This feature of the BKT transition affects the connectivity between neighboring configurations. In particular, the fraction of configurations whose first two neighbors are connected to points with the same w, F_w, is negligible for $T > T_{BKT}$, but it is equal to 1 in the topological phase. This is illustrated in Fig. 3.8 (b). Thus, for $T < T_{BKT}$, the I_d is a property of the manifold exclusively formed by configurations connected to neighbors with the same winding number.

In a nutshell, the underlying cause for the sensitivity of the I_d to phase transitions is that, both the symmetry-breaking and topological transitions, affect the neighboring configurations' connectivity. The

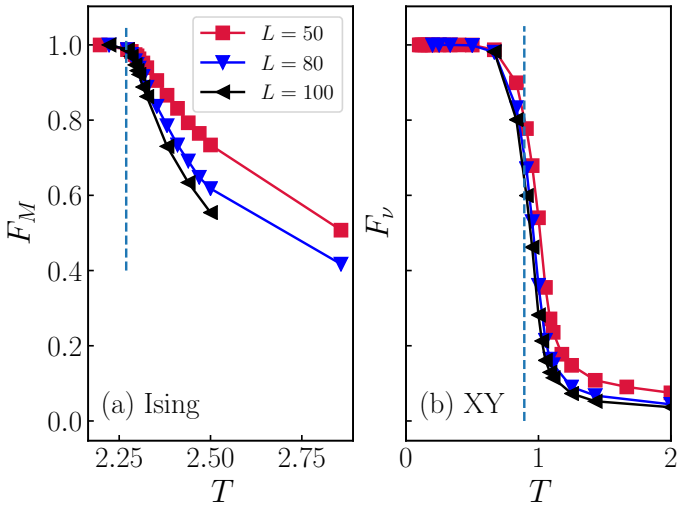

FIGURE 3.8: *Connectivity between neighboring points.* Panel (a) shows the fraction of points in the Ising data set whose first two nearest-neighbors have the same magnetization sign. Similarly, in panel (b), we show the fraction of points in the XY data set whose first two nearest-neighbors have the same winding number (see text).

key aspect is that nearest-neighbors configurations have identical physical properties (order parameter and winding number) when the system is in the ordered phases (symmetry-broken or quasi-long-range-ordered). By contrast, in the disordered phase, the first and second neighbors' physical properties are entirely random. At the data structure level, the phase transition represents a change of scale between those regimes.

3.5.2 Why I_d exhibit universal scaling behavior?

Based on the fact that I_d shows a characteristic minimum feature in the vicinity of phase transitions at $T_c(L)$, we now provide an argument in support of universal scaling of the latter temperature against system size. The key aspect of our argument is that the distances r_1 and r_2 are related with many-body correlation functions in the system, computed at equilibrium.

We analyze the curve $\ln(1 - P_i)$ versus $\ln \mu_i$ close to the origin. From Eq. (3.2), the slope of this curve is proportional to I_d. The curve starts at the origin; we assume that its slope can be correctly determined by sampling the first point of the curve several times (e.g., by sampling several independent Markov chains); this seems very well satisfied based on our earlier numerical observations (fluctuations and deviations from linear behavior typically appear only for very large values of μ). Within this assumption, one obtains the following estimate for I_d:

$$I_d = -\frac{\ln(1 - 1/N_r)}{\ln[r_2(1)] - \ln[r_1(1)]}. \tag{3.12}$$

We post-pone to the end of section an alternative justification for such a scaling behavior. From now on, we specifically consider the Euclidian distance function [see, Eq.(3.9)]; using the hamming distance will not affect the substance of our reasoning, but will change some of its details.

For the sake of simplicity, we can assume that the reference configuration $i = 1$ corresponds to the lowest energy state. This second assumption relies on the fact that such state is the one that has a higher probability of being sampled at any temperature, and, at least at sufficiently low temperatures, it is very likely to be the state with the lowest value of μ, as low-lying excitations do typically differ from the lowest energy states by a low amount of spin flips (representative of spin waves), when compared to the average distance between states. Within this approximation, we can fix the coordinates of the reference configuration: $s_j = s \quad \forall j$ for the Ising data set and $\theta_j = \theta \quad \forall j$ for the XY data set.

We can now proceed and analyze the denominator of Eq. (3.12). We define:

$$\alpha_{0f} = \sum_{j=1}^{N_s} S_0 S_{j,f}, \tag{3.13}$$

where S_0 represent the coordinates of the reference configuration; see Fig. 3.9 (c). Thus, the distance between two configurations reads:

$$r_f(1) = \sqrt{2N_s}\sqrt{1 - \frac{\alpha_{0f}}{N_s}} \tag{3.14}$$

We then get:

$$\ln[r_2(1)] - \ln[r_1(1)] = \frac{\ln(1 - \frac{\alpha_{01}}{N_s}) - \ln(1 - \frac{\alpha_{02}}{N_s})}{2}. \tag{3.15}$$

For $T \gg T_c$, the coordinates of neighboring configurations are expected to be completely random compared to S_0. Thus, it is reasonable to expect that $\alpha_{0f} \ll N_s$ (we will come back to this point below). Analyzing the transition from the disordered phase, we can expand the logarithms up to second order in α_{0f}/N_s and get:

$$\ln[r_2(1)] - \ln[r_1(1)] = \mathcal{F}_2 + \mathcal{F}_4 + ... \tag{3.16}$$

where the function $\mathcal{F}_p$ contains all p-spin correlation functions $S_{j_1,f} S_{j_2,f} ... S_{j_p,f}$ taken over the single states 1 and 2. In principle, one shall also retain other orders: in fact, the difference of the two distances depends parametrically on arbitrary body correlation functions.

Now, we make a third assumption, that is, that the correlations contained in $\mathcal{F}_p$ can be replaced by the corresponding thermal averages. The rationale behind this is that, based on our first assumption above, we are actually considering the states that have the highest weight in the partition function, so the ones that contribute the most to the computation of the correlation function. Here, temperature plays a clear physical role: higher temperature let us sample states that are (on average) at a larger distance from the lowest energy state when compare to lower temperatures. One can reformulate the above as follows. For any given Markov chain, we have a given $\mathcal{F}_p^{(k)}$, which depends on correlations on a single pair of configurations. Then, average over the various Markov chains gives us an averaged value, that depends on the average of correlations over the various configurations. This last formulation is closer to the numerical recipe that we utilize to estimate I_d, where, in fact, we obtain the latter from averaging the I_d resulting from several distinct simulations.

Now, since we are dealing with thermal averages, we can recall the finite-size scaling hypothesis. This hypothesis tells us that, if a quantity develops a singular behavior at the transition point (not necessarily a divergence), the temperature corresponding to such a feature T_{feat} shall be shifted according to finite-size scaling (FSS) theory as (for second order phase transitions):

$$(T_{\text{feat}} - T) \propto \frac{1}{L^\nu} \tag{3.17}$$

We are thus in a position to make a statement: if any of the arbitrary body correlation functions contained in the definition of our distance displays singular behavior at the transition point, those will dictate the scaling of the position of the minimum of I_d according to FSS, and reveal us the critical exponent ν (or, in case of BKT, they will be consistent with the logarithmic scaling expected there). The behavior of all other correlations is not expected to affect this scaling behavior at all, as those are not displaying any non-singular feature by definition.

We note that our reasoning and the validity of its assumptions can be *a posteriori* verified by noticing that it implies that features in the distribution of the distances r_1 will also be related to critical behavior. In particular, we consider the pivotal assumption that the correlation contained in Eq. (3.14) can be replaced by the corresponding thermal averages, and compare the predictions for $r_f(1)$ with our numerical results [1]. Fig. 3.9 shows this comparison for both the Ising and XY models. (i) In the disordered phases, $\alpha_{0,f} \ll 1$, due to the exponential decay of the correlations, and thus $r_f \approx \sqrt{2N_s}$. (ii) On the other hand, in the

[1] We note that, by verifying this assumption, we indirectly check the ones taken before as well

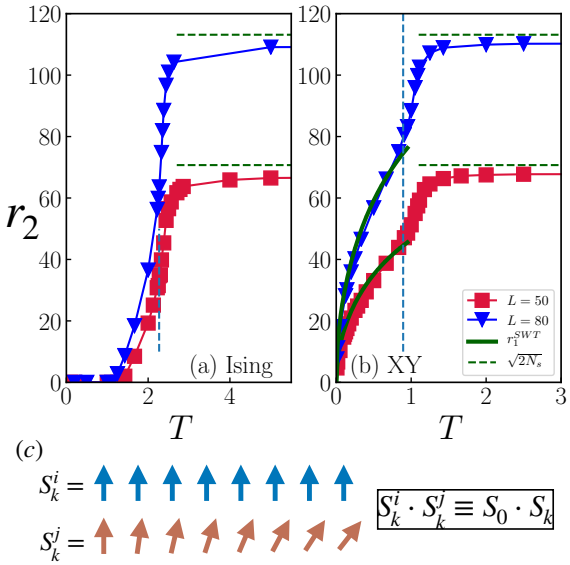

FIGURE 3.9: *Correlation functions and distance between neighboring configurations.* Temperature dependence of the smallest r_2 (this distance is representative of the lowest value of μ, see text) for the (a) Ising and (b) XY models. The lines (full and dashed) represent the predictions for r_2 based on Eq. (3.14) and the corresponding expressions of the asymptotic formula for the correlation functions in the high and low temperatures regimes (see text). The panel (c) illustrate the basic assumption behind Eq. (3.14), i.e, correlation between configurations are equivalent to correlation functions(see text).

symmetry- broken phases, $\alpha_{0,f} \approx O(N_s)$, given the long-range nature of the correlations; which implies that $r_f \ll 1$. (iii) Finally, in XY model's critical phase, the temperature dependence of the correlations is given by $S_0 \cdot S_{j,f} \sim |j|^{-T/2\pi}$ (where |j| represents the spatial distance from a reference site). By computing the corresponding $\alpha_{0,f}$, one can obtain the temperature dependence of r_f. The numerical results display very good agreement with our predictions; see Fig. 3.9 (a) and (b). It is worth noting that, while our argument justified critical scaling for $T_c(L)$ and does not justify the full collapse scaling observed for I_d, this is still directly informative about both critical temperature, and the critical exponent ν.

Before ending the section, we present a different approach to determining the dependence between I_d and the smallest value of μ as per Eq. (3.2). An alternative way to qualitatively estimate I_d from a data distributed according to Eq. (3.1) is to apply the maximum likelihood criterion. Utilizing the commonly used log-likelihood function $\ell_k = \log[f(\mu_k)]$, one obtains that, for data sets where $I_d \gg 1$, one has $I_D \simeq N_r/\ln(\mu_1)$. The scaling with N_r is different with respect to Eq. (3.12): this is not unexpected due to the fact that (1) we are considering sampling of few configurations in the previous approximation, and (2) maximum likelihood does not necessarily capture the correct scaling with the number of points in the set (as one may expect many of those do not contribute to the determination of the minimum). Nevertheless, this difference is irrelevant for the sake of our argument above, as we are not immediately interested in the N_r scaling. What is important is that maximum likelihood returns exactly the same functional dependence on μ_1, thus providing a data driven justification of the first assumption presented above.

3.6 Conclusions

We have shown that phase transitions can be learned through a single property of raw data sets of configurations - the intrinsic dimension - without any need to perform dimensional reduction. The key observation made here is that, in analogy to physical observables, the intrinsic dimension exhibits universal scaling behavior close to different classes of transitions: first-, second-order, and Berezinskii-Kosterlitz-Thouless (BKT). This indicates how the intrinsic dimension, in the vicinity of critical points, behaves as an order parameter in data space, showing how the latter undergoes a structural transition that parallels the phase transition identified by conventional order parameters.

At the practical level, we have shown that the finite-size analysis of intrinsic dimension allows not just to detect, but also to characterize critical points in an unsupervised manner. In particular, we have shown that the intrinsic dimension allows one to estimate transition temperatures and (critical) exponents of both first- and second-order transitions with accuracies ranging from 1% to 0.1% at very modest system sizes. In addition, the method is equally applicable to topological transitions, where we have demonstrated an accurate (with 1% of confidence) estimation of the BKT topological transition competitive with more traditional methods at the same system sizes. This latter result suggests that the lack of any dimensional reduction allows retaining topological information in the vicinity of the phase transition, which may instead be lost otherwise [28, 30].

A fundamental aspect of our approach is that it is based on a I_d-estimation method suitable to learn complex manifolds, such as the twisted XY manifold emerging at the BKT critical point. The results demonstrate the potential of state-of-the-art I_d-estimators [9, 65] methods to tackle many-body problems, and motivates an even stronger methodological connection between data mining techniques, and many-body physics. We also note that, in comparison with previous applications in other fields [33, 36, 66], the values of the intrinsic dimension reported here are considerably larger. For future applications, like combining our analysis with clustering methods that do not rely on dimension reduction[67], it may be interesting to develop novel estimators that focus on large values of I_d, potentially trading absolute accuracy with numerical efficiency (in the spirit of ref. 65). Another interesting question to address in the future is to assess the possibility of data lying in submanifolds with different I_d[68] and how it affects to our method. This is a plausible scenario in cases with co-existence of phases.

Some of the methods presented here may be applied to quantum mechanical objects, such as quantum partition functions, density matrices, and wave functions. It is an open challenge to determine whether the data mining of quantum objects can provide an informative perspective on the latter, such as, e.g., accessing entanglement or other more challenging forms of quantum correlations. Finally, while we focused on configuration generated by Monte Carlo sampling, our approach is equally applicable to experimentally generated data; it may be interesting to apply it to settings where raw data configurations are available, such as, e.g., quantum gas microscope experiments [19, 69, 70].

3.7 Appendix

3.7.1 The TWO-NN method and comparison with principal component analysis (PCA)

In this section, we provide more details about the two-NN method.

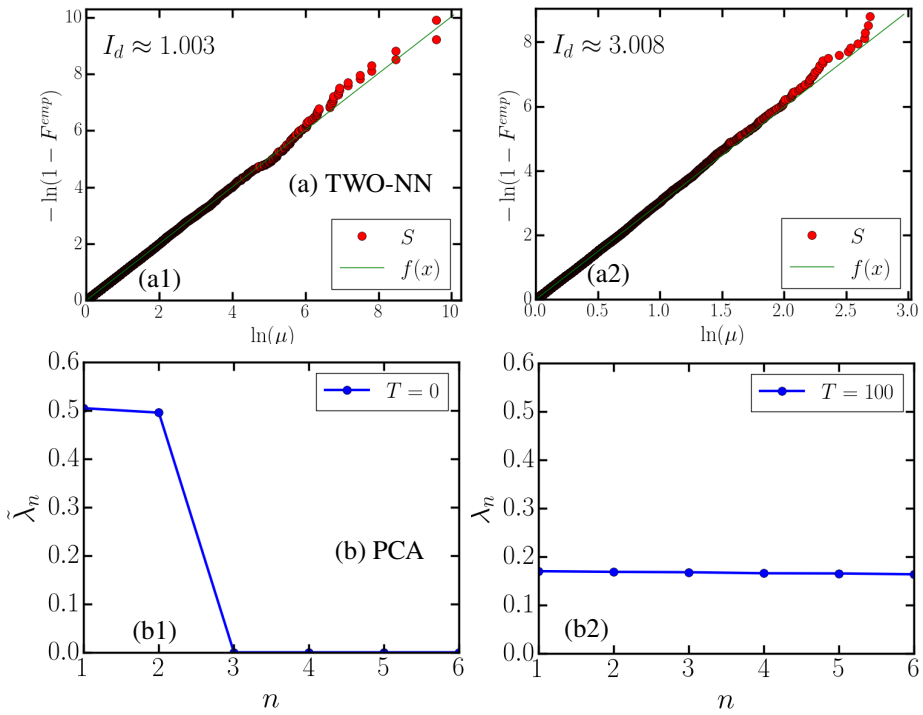

FIGURE 3.10: *3-site XY model.* Panels (a) show results of the TWO-NN method: fitting of the data points S for (a1) $T = 0$ and (a2) $T = 100$. The data set have $N_r = 10^3$ configurations. We obtain (a1) $I_d = 1$ and (a2) $I_d = 3$. Panels (b) show results of the PCA method: normalized eigenvalues of the covariance matrix, $\tilde{\lambda_n}$, obtained from the raw XY configurations. Here we use the same notation of ref. [28] For $n > I_d^{PCA}$, $\tilde{\lambda_n} \to 0$. PCA predicts (b1) $I_d^{PCA} = 2$ and (b2) $I_d^{PCA} = 6$, which is not in agreement with the exact results (see text)

As described in Ref. [9], the intrinsic dimension, I_d, can be obtained through the following steps:

1. For each point i of the data set ($i = 1, 2, ..., N_r$), compute its first- and second-nearest neighbor, $r_1(i)$, $r_2(i)$, respectively.

2. For each point i, compute the ratio $\mu_i = r_2(i)/r_1(i)$.

3. The empirical cumulate is defined as $P^{\text{emp}}(\mu) = i/N_r$, while the values of μ_i are sorted in an ascending order through a permutation, i.e., $(\mu_1, \mu_2, ...\mu_{N_r})$, where $\mu_i < \mu_j$, for $i < j$.

4. Finally, the resulting $S = \{(\ln(\mu), -\ln[1 - P^{\text{emp}}(\mu)]\}$ are fitted with a straight line passing through the origin. The slope of this line is equal to I_d (see Eq.(3.2)).

Fig. 3.10 shows the plot of S for the basic 3-site XY example presented in the Fig. 3.1 (B). It worth mentioning that while we depict the configurations $\vec{\theta} = (\theta_1, \theta_2, \theta_3)$ for clarity of illustration in Fig. 3.1 (B), in our calculations, $\vec{\theta}$ is defined as in Eq. (3.8). In this way, the distance between two configurations $\vec{\theta^i}$ and $\vec{\theta^j}$: $r(\vec{\theta^i}, \vec{\theta^j}) = \sqrt{2\sum_{k=1}^{N_s}(1-\vec{S_k^i}\cdot\vec{S_k^j})}$, properly takes into account the periodicity of the variables θ_k^i. Another important technical aspect is that the fit of S is unstable for larger values of μ. As is considered in ref. [9], we discard the 10% of points characterized by the highest values of μ. Based on this approach, we obtain

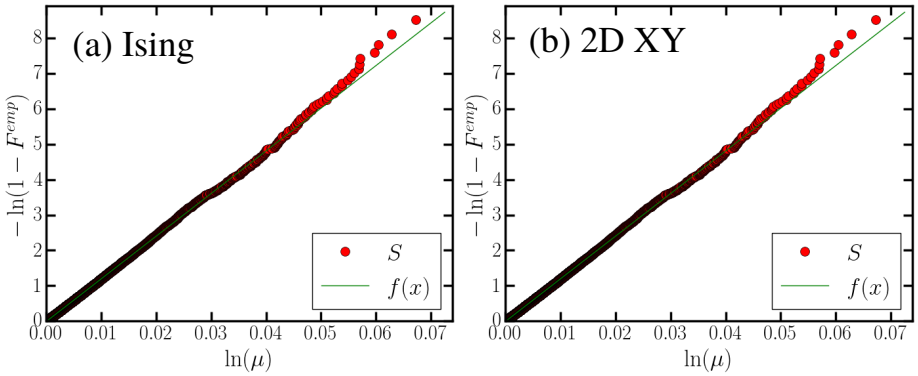

FIGURE 3.11: Results of the TWO-NN method: fitting of the data points S for (a) Ising and (b) 2D XY thermal data sets generated close to the critical point (in (a) $T \approx 2.2$, while in (b) $T \approx 0.89$); in both cases we consider $L = 40$, and the data set have $N_r = 10^4$ configurations. We obtain $I_d \approx 47$ and $I_d \approx 120$, respectively.

$I_d \approx 1$ and $I_d \approx 3$, for the zero and high temperature regimes, respectively, which is consistent with the value expected from physical reasonable assumptions (see Figs. 3.10 (a1) and (a2)).

We also show some examples of the plot of S for data sets generated in the vicinity of the critical points of the Ising and 2D XY models, see Fig. 3.11 (a) and (b), respectively. In both cases, the points S are well fitted by a straight line passing through the origin. We obtain similar results for the other system-sizes and values of T considered in this Chapter.

In contrast, simple linear dimension reduction methods, such as Principal Component Analysis (PCA), fails to describe the I_d of the XY data sets. To illustrate this point, we employ linear PCA in the same collection of configurations considered in the last paragraph. As can be seen from Figs. 3.10 (b1) and (b2), even for this simple example, PCA fails to obtain the true I_d; for $T = 0$, $I_d^{PCA} = 2$, while for $T = 100$, $I_d^{PCA} = 6$. This failure is related to the fact that the XY manifolds are curved [30].

However, PCA can describe the main features of the Ising data set. Based on this, we consider the PCA estimation of the I_d in Fig. 3.7 of the main text. Here, we give more details about the computation of $I_{d,PCA}$. First, we consider the eigenvalues of the covariance matrix $\mathbf{X^T X w_n} = \lambda_\mathbf{n} \mathbf{w_n}$ (we use the same notation of ref. [28]). We then define the normalized eigenvalues, $\tilde{\lambda_n} = \frac{\lambda_n}{\sum_i^{N_r} \lambda_i}$. The I_d is defined by choosing an *ad hoc* cut-off parameter for the integrated spectrum of the covariance matrix, i.e.,

$$\sum_{n=1}^{I_{d,PCA}} \tilde{\lambda}_n \approx f, \tag{3.18}$$

where f represents a fraction of the eigenvalues of the covariance matrix. In Fig. 3.7 (c), we consider $f = 0.6$. The value of $I_{d,PCA}$ depends on f. However, we observe that the qualitative behavior of the function $I_{d,PCA}(T)$ is not affected by the value of f (as long as $f \geq 0.5$). In particular, for all the values of f that we considered (i.e., $f = 0.5, 0.6, 0.7, 0.8$ and 0.9), the global $I_{d,PCA}(T)$ goes to 1 immediately below T_c, and that the local $I_{d,PCA}(T)$ exhibit a non-monotonic behavior.

3.7.2 Scaling of the I_d with the number of configurations

In this section we discuss the scaling of the I_d with the number of configurations, N_r, considered in the data set; for all the results shown in the main text, $N_r = 5 \times 10^4$. The first important aspect to consider is that the TWO-NN is a scale-dependent method. In other words, the estimation of the I_d is performed on a length scale that is related to the first and second neighbor distances of each point. Thus, by varying N_r, one is probing a different neighborhood size like, i.e., estimating I_d in different scales [9].

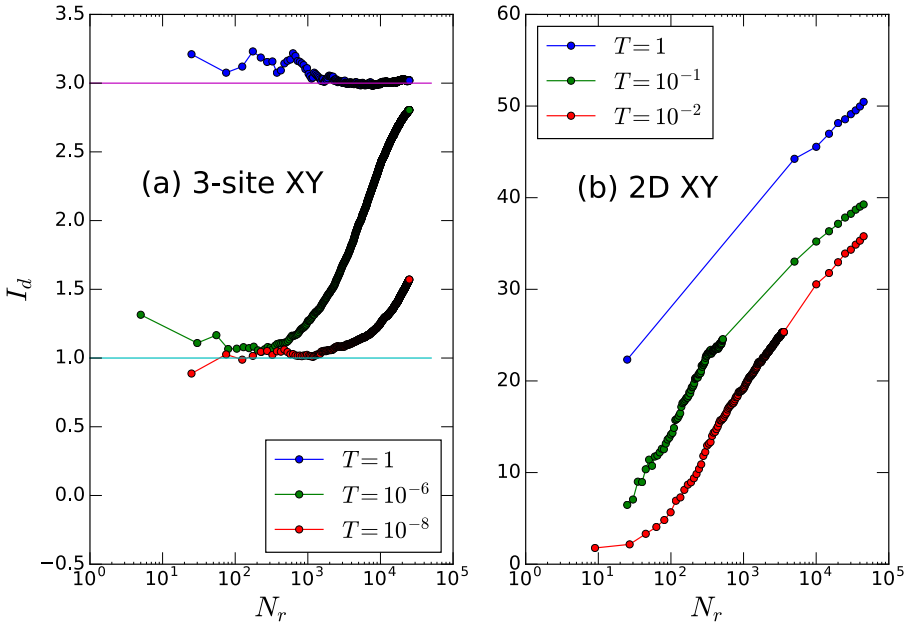

FIGURE 3.12: Scaling of the I_d with the number of configurations in the data set. In panel (a) is show the results for the 3-site XY model, while in panel (b) for the $2D$ XY model with $L = 10$.

To illustrate how this change in scale affects the I_d of the thermal data sets considered here, we first consider the 3-site XY model in Fig. 3.12 (a). For $T = 1$, the I_d converges to 3 as expected for the high-temperature regime of this model. In the low temperature regime $T \approx 10^{-6}$, however, $I_d(N_r)$ exhibit a plateau at $I_d = 1$ for $N_r \in [10^0, 10^3[$. As illustrate in Fig.3.1 (B) this simple data set is well described by a one-dimensional manifold. This plateau in $I_d(N_r)$ is a signature of this soft direction [9]. Nevertheless, by further increasing N_r, the I_d increases ($I_d \to 3$ in this case), as an effect of the decrease of the scale in which I_d is estimated. In this scale regime, the number of soft directions cannot be determined. We stress that the computation of the I_d of the high-dimensional data sets considered here is always performed in this regime. In this case, the I_d exhibit an exponential scaling with N_r, as exemplified in Fig. 3.12 (b).

We now discuss how the temperature dependence of I_d is affected by the change in N_r. Fig. 3.13 (a1) and (b1) shows $I_d(T)$ for different values of N_r for the Potts and 2D XY data sets, respectively. Despite the change of the absolute value of I_d with N_r, the qualitative behavior of $I_d(T)$ is not modified. Most importantly, we observe that the position of the local minimum at T^* does not shift with N_r for $N_r > 10^4$. Furthermore, as expected, the scaling of I_d with N_r is exponential, see Figs. 3.13 (a2) and (b2), at least in the vicinity of the phase transition. Similar results are obtained for other system sizes and for the Ising model. Summing up, our results indicate that, as long as $N_r > 10^4$, the universal scaling behavior exhibited by the I_d is not affected by the scale in which the I_d is measured.

3.7.3 Data collapse

In this section we discuss the finite size analysis employed for the estimates of the critical temperature and exponents presented in Sec. 3.4. Our procedure is a standard search of the minimal least-square difference fit between our data and an appropriately chosen scaling function hypothesis. Let us first focus on the second-order phase transitions, concerning the Ising and 3-state Potts models. The method is divided into four steps.

1 First we choose a suitable mesh for the parameter ranges for T_c, ν and α.

2 We compute from our data the scaling variables $x_{\text{dat}}(T_c, \nu) = (T - T_c)L^{1/\nu}$ and $y_{\text{dat}}(\alpha) = I_d(T)L^{-\alpha}$ for different R-range of system sizes $\{L_1, L_2, \ldots, L_R\}$.

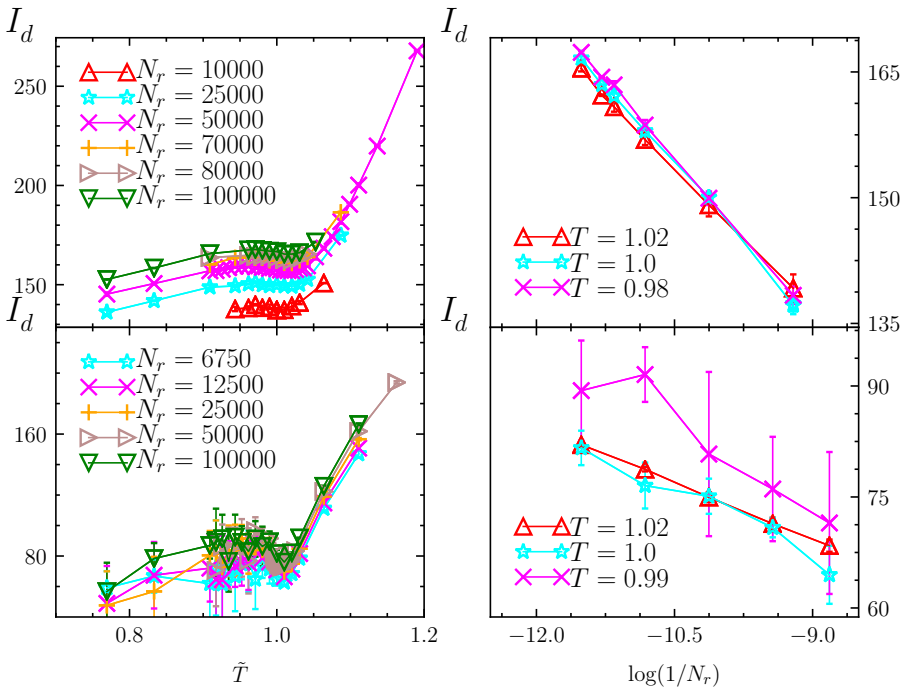

FIGURE 3.13: Panels (a): the temperature dependence of the I_d for different values of N_r for the (a1) 2D XY model and (b) 3-states Potts model, in both cases $L = 60$. For each point, we harvested approximated 10 instances of the data set and average the resulting estimates for the I_d. The error bars are the standard deviation of such set of results. Panels (b): the scaling of I_d with N_r for certain values of T.

3 We choose a parametric functional hypothesis $f(x; \{a\})$.

4 For each $(x_{\text{dat}}(T_c, \nu), y_{\text{dat}}(\alpha))$ we compute the best fit of the hypothesis function $\{a^\star\}$ through the Levenberg-Marquardt algorithm. We store the residuals as:

$$\epsilon(T_c, \nu, \alpha) = \frac{||f(x_{\text{dat}}(T_c, \nu); \{a^\star\}) - y_{\text{dat}}(\alpha)||}{||y_{\text{dat}}(\alpha)||} \tag{3.19}$$

The optimal set of parameters for each set $\{L_1, L_2, \ldots, L_R\}$ is located in the minimum $\epsilon(T_c, \nu, \alpha)$. In order to keep a low-bias on the hypothesis function $f(x, \{a\})$, we choose various k-degree polynomial $Q_k(x; a_0, a_1, \ldots, a_k)$. Thus, we obtain a set of optimal $\{T_c^\star\}$, $\{\nu^\star\}$, $\{\alpha^\star\}$ for each choice of degree k and each set of system sizes $\{L_k\}$. Our estimates and errors for the critical temperature and critical exponents are then estimated as the average and standard deviation of these sets, respectively.

The analysis for the BKT transition (XY model) is performed in a similar fashion. The only difference is the choice of scaling variable, which for this case is:

$$x_{\text{dat}}(T_c, a) = L \exp\left[-\frac{a}{\sqrt{T - T_c}}\right]. \tag{3.20}$$

For the Ising, 3-state Potts and XY models we select polynomials of degrees $k \in \{5, 6, 7, 8\}$ and different sets of system sizes among the $L \geq 70$ ones. For the XY model, we perform the data collapse within the range $T = [0.91, 1.10]$ and use a bin of $\Delta T \approx 0.005$. Our estimations for the XY model are $T_c = 0.92(1)$, $a = 1.4(1)$ and $\zeta = 0.40(1)$.

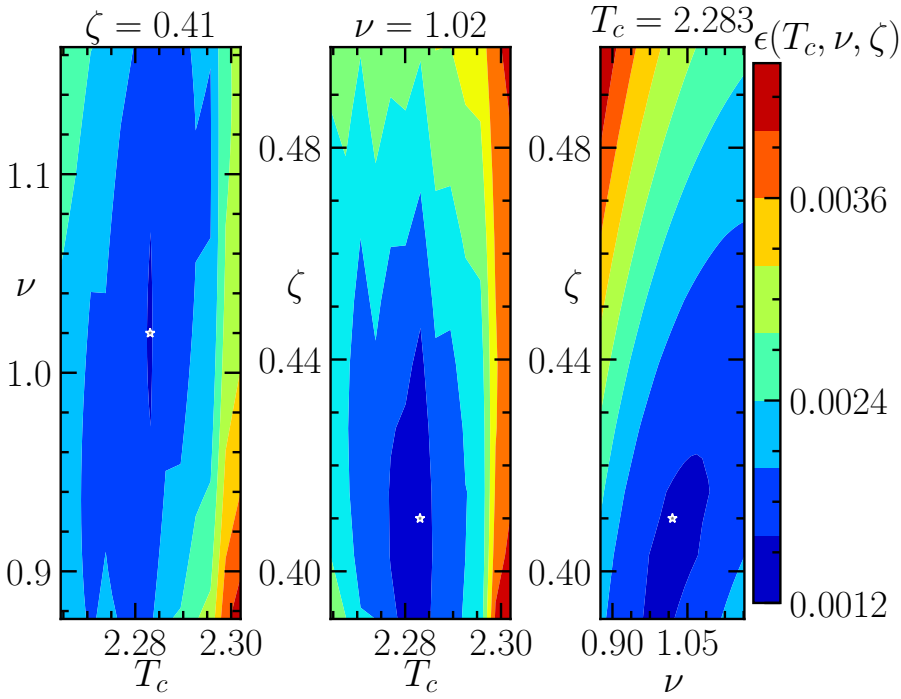

FIGURE 3.14: Contour plot of the average residuals projected on the direction of the optimal parameters for the Ising model. The white star points to the optimal parameters for our finite size analysis.

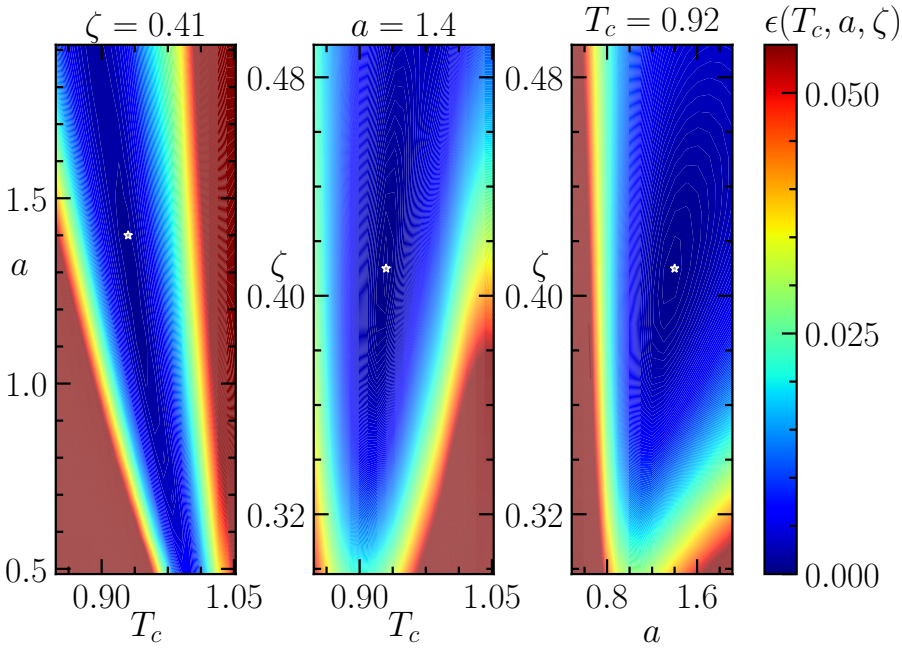

FIGURE 3.15: Contour plot of the average residuals projected on the direction of the optimal parameters for the XY model. The white star points to the optimal parameters for our finite size analysis.

We visualize the resulting residuals for both the ising and the XY models, see Fig. 3.14 and Fig. 3.15, respectively. Since the parameter space is 3D, for convenience we plot the projected directions along with the optimal critical parameters.

3.7.4 Definition of the winding number

We now discuss the definition of the winding number mentioned in Fig. 3.8 (b) of the main text. We consider a closed path along the x and y directions of the square lattice and define

$$w_x = \frac{1}{2\pi} \sum_{i=1}^{L_x} \Delta\theta_{(i,y=1)}, \tag{3.21}$$

and

$$w_y = \frac{1}{2\pi} \sum_{i=1}^{L_y} \Delta\theta_{(x=1,i)}, \tag{3.22}$$

where the angle difference is $\Delta\theta_{(x=1,i)} = \theta_{(i+1,y=1)} - \theta_{(i,y=1)}$; $\Delta\theta$ is rescaled into the range $(-\pi, \pi]$. We compute the $w = (w_x, w_y)$ for each configuration of the data set. We then define the total number of configurations whose first two nearest neighbors have the same w, N_w. Figure 3.8 (b) shows the fraction of those points $F_w = N_w/N_r$ as function of T.

Bibliography

[1] T. Mendes-Santos, X. Turkeshi, M. Dalmonte, and Alex Rodriguez. Unsupervised learning universal critical behavior via the intrinsic dimension. *Physical Review X*, 11(1):011040, Feb 2021.

[2] M. I. Jordan and T. M. Mitchell. *Machine learning: Trends, perspectives, and prospects*, volume 349. American Association for the Advancement of Science, 2015.

[3] Yann LeCun, Yoshua Bengio, and Geoffrey Hinton. *Deep learning*, volume 521. Nature Publishing Group, 2015.

[4] Pedro Domingos. *A few useful things to know about machine learning*, volume 55. ACM New York, NY, USA, 2012.

[5] Keith T Butler, Daniel W Davies, Hugh Cartwright, Olexandr Isayev, and Aron Walsh. *Machine learning for molecular and materials science*, volume 559. Nature Publishing Group, 2018.

[6] Elizaveta Levina and Peter J. Bickel. Maximum likelihood estimation of intrinsic dimension. In L. K. Saul, Y. Weiss, and L. Bottou, editors, *Advances in Neural Information Processing Systems 17*, pages 777–784. MIT Press, 2005.

[7] Sebastian Goldt, Marc Mézard, Florent Krzakala, and Lenka Zdeborová. *Modelling the influence of data structure on learning in neural networks: the hidden manifold model*. 2019.

[8] Sangmin Lee, P. Campadelli, E. Casiraghi, C. Ceruti, and A. Rozza. *Intrinsic Dimension Estimation: Relevant Techniques and a Benchmark Framework*, volume 759567. Oct 2015.

[9] Elena Facco, Maria d'Errico, Alex Rodriguez, and Alessandro Laio. *Estimating the intrinsic dimension of datasets by a minimal neighborhood information*, volume 7. Oct 2017.

[10] Giuseppe Carleo, Ignacio Cirac, Kyle Cranmer, Laurent Daudet, Maria Schuld, Naftali Tishby, Leslie Vogt-Maranto, and Lenka Zdeborová. *Machine learning and the physical sciences*, volume 91. American Physical Society, Dec 2019.

[11] Pankaj Mehta, Marin Bukov, Ching-Hao Wang, Alexandre G.R. Day, Clint Richardson, Charles K. Fisher, and David J. Schwab. *A high-bias, low-variance introduction to Machine Learning for physicists*, volume 810. 2019.

[12] Juan Carrasquilla. *Machine Learning for Quantum Matter*. mar 2020.

[13] Lei Wang. *Discovering phase transitions with unsupervised learning*, volume 94. American Physical Society, Nov 2016.

[14] Juan Carrasquilla and Roger G. Melko. *Machine learning phases of matter*, volume 13. Oct 2017.

[15] Evert P. L. van Nieuwenburg, Ye-Hua Liu, and Sebastian D. Huber. *Learning phase transitions by confusion*, volume 13. 2017.

[16] Yi Zhang and Eun-Ah Kim. *Quantum Loop Topography for Machine Learning*, volume 118. American Physical Society, May 2017.

[17] Kelvin Ch'ng, Juan Carrasquilla, Roger G. Melko, and Ehsan Khatami. *Machine Learning Phases of Strongly Correlated Fermions*, volume 7. American Physical Society, Aug 2017.

[18] Benno S. Rem, Niklas Käming, Matthias Tarnowski, Luca Asteria, Nick Fläschner, Christoph Becker, Klaus Sengstock, and Christof Weitenberg. *Identifying quantum phase transitions using artificial neural networks on experimental data*, volume 15. jul 2019.

[19] Annabelle Bohrdt, Christie S. Chiu, Geoffrey Ji, Muqing Xu, Daniel Greif, Markus Greiner, Eugene Demler, Fabian Grusdt, and Michael Knap. *Classifying snapshots of the doped Hubbard model with machine learning*, volume 15. 2019.

[20] Yuhong Zhang, Annamaria Mesaros, Kazuhiro Fujita, S D Edkins, M H Hamidian, Kelvin Ch'ng, Hiroshi Eisaki, Sohkichi Uchida, J C Séamus Davis, Ehsan Khatami, and Eun ah Kim. *Machine learning in electronic-quantum-matter imaging experiments*, volume 570. 2019.

[21] Dimitrios Bachtis, Gert Aarts, and Biagio Lucini. *Extending Machine Learning Classification Capabilities with Histogram Reweighting*. 4 2020.

[22] Giuseppe Carleo and Matthias Troyer. *Solving the quantum many-body problem with artificial neural networks*, volume 355. American Association for the Advancement of Science, 2017.

[23] Dong-Ling Deng, Xiaopeng Li, and S. Das Sarma. *Quantum Entanglement in Neural Network States*, volume 7. American Physical Society, May 2017.

[24] Mohammad H. Amin, Evgeny Andriyash, Jason Rolfe, Bohdan Kulchytskyy, and Roger Melko. *Quantum Boltzmann Machine*, volume 8. American Physical Society, May 2018.

[25] Markus Schmitt and Markus Heyl. *Quantum many-body dynamics in two dimensions with artificial neural networks*. 2019.

[26] Sebastian J. Wetzel. *Unsupervised learning of phase transitions: From principal component analysis to variational autoencoders*, volume 96. American Physical Society, Aug 2017.

[27] Kelvin Ch'ng, Nick Vazquez, and Ehsan Khatami. *Unsupervised machine learning account of magnetic transitions in the Hubbard model*, volume 97. American Physical Society, Jan 2018.

[28] Wenjian Hu, Rajiv R. P. Singh, and Richard T. Scalettar. *Discovering phases, phase transitions, and crossovers through unsupervised machine learning: A critical examination*, volume 95. American Physical Society, Jun 2017.

[29] Natanael C. Costa, Wenjian Hu, Z. J. Bai, Richard T. Scalettar, and Rajiv R. P. Singh. *Principal component analysis for fermionic critical points*, volume 96. American Physical Society, Nov 2017.

[30] Joaquin F. Rodriguez-Nieva and Mathias S. Scheurer. *Identifying topological order through unsupervised machine learning*, volume 15. May 2019.

[31] Yang Long, Jie Ren, and Hong Chen. *Unsupervised Manifold Clustering of Topological Phononics*, volume 124. American Physical Society, May 2020.

[32] Emmanuelle Abisset-Chavanne Elena Lopez, Adrien Scheuer and Francisco Chinesta. *On the effect of phase transition on the manifold dimensionality: application to the Ising model*, volume 6. mathematical sciences publishers, 2018.

[33] Elena Facco, Andrea Pagnani, Elena Tea Russo, and Alessandro Laio. *The intrinsic dimension of protein sequence evolution*, volume 15. Public Library of Science, 04 2019.

[34] N. Krueger and M. Felsberg. A continuous formulation of intrinsic dimension. In *Proceedings of the British Machine Vision Conference*, pages 27.1–27.10. BMVA Press, 2003.

[35] A Asensio Ramos, H Socas-Navarro, A López Ariste, and MJ Martínez González. *The intrinsic dimensionality of spectropolarimetric data*, volume 660. IOP Publishing, 2007.

[36] Alessio Ansuini, Alessandro Laio, Jakob H Macke, and Davide Zoccolan. Intrinsic dimension of data representations in deep neural networks. In *Advances in Neural Information Processing Systems*, pages 6109–6119, 2019.

[37] Daniel C. Laughlin. *The intrinsic dimensionality of plant traits and its relevance to community assembly*, volume 102. 2014.

[38] Svante Wold, Kim Esbensen, and Paul Geladi. *Principal component analysis*, volume 2. 1987.

[39] Ingwer Borg and Patrick JF Groenen. *Modern multidimensional scaling: Theory and applications*. Springer Science & Business Media, 2005.

[40] Mukund Balasubramanian and Eric L. Schwartz. *The Isomap Algorithm and Topological Stability*, volume 295. American Association for the Advancement of Science, 2002.

[41] Sam T. Roweis and Lawrence K. Saul. *Nonlinear Dimensionality Reduction by Locally Linear Embedding*, volume 290. American Association for the Advancement of Science, 2000.

[42] Mark A Kramer. *Nonlinear principal component analysis using autoassociative neural networks*, volume 37. Wiley Online Library, 1991.

[43] Laurens van der Maaten and Geoffrey Hinton. *Visualizing data using t-SNE*, volume 9. 2008.

[44] Leland McInnes, John Healy, and James Melville. *UMAP: Uniform Manifold Approximation and Projection for Dimension Reduction*. 2018.

[45] Francesco Camastra and Alessandro Vinciarelli. *Estimating the intrinsic dimension of data with a fractal-based method*, volume 24. IEEE, 2002.

[46] Dietrich Stauffer and Amnon Aharony. *Introduction To Percolation Theory*. London: Taylor and Francis, 1991.

[47] Ulli Wolff. *Collective Monte Carlo Updating for Spin Systems*, volume 62. American Physical Society, Jan 1989.

[48] D. P. Landau and K. Binder. *A Guide to Monte Carlo Simulations in Statistical Physics*. Cambridge: Cambridge University Press, 2005.

[49] Philippe Di Francesco, Pierre Mathieu, and David Sénéchal. *Conformal field theory*. Graduate texts in contemporary physics. Springer, New York, NY, 1997.

[50] Malte Henkel. *Conformal Invariance and Critical Phenomena*. Springer, Berlin, Heidelberg, 1999.

[51] F. Y. Wu. *The Potts model*, volume 54. American Physical Society, Jan 1982.

[52] Shumpei Iino, Satoshi Morita, Naoki Kawashima, and Anders W. Sandvik. *Detecting Signals of Weakly First-order Phase Transitions in Two-dimensional Potts Models*, volume 88. 2019.

[53] J M Kosterlitz and D J Thouless. *Ordering, metastability and phase transitions in two-dimensional systems*, volume 6. IOP Publishing, apr 1973.

[54] Rajan Gupta, Jerry DeLapp, George G. Batrouni, Geoffrey C. Fox, Clive F. Baillie, and John Apostolakis. *Phase Transition in the* 2DXY *Model*, volume 61. American Physical Society, Oct 1988.

[55] Yun-Da Hsieh, Ying-Jer Kao, and Anders W Sandvik. *Finite-size scaling method for the Berezinskii–Kosterlitz–Thouless transition*, volume 2013. IOP Publishing, sep 2013.

[56] Anders W. Sandvik. *Computational Studies of Quantum Spin Systems*, volume 1297. 2010.

[57] Ce Wang and Hui Zhai. *Machine learning of frustrated classical spin models. I. Principal component analysis*, volume 96. American Physical Society, Oct 2017.

[58] Matthew J. S. Beach, Anna Golubeva, and Roger G. Melko. *Machine learning vortices at the Kosterlitz-Thouless transition*, volume 97. American Physical Society, Jan 2018.

[59] Alexander Lidiak and Zhexuan Gong. *Unsupervised machine learning of quantum phase transitions using diffusion maps*. mar 2020.

[60] Quoc Hoan Tran, Mark Chen, and Yoshihiko Hasegawa. *Topological Persistence Machine of Phase Transitions*. apr 2020.

[61] David R. Nelson and J. M. Kosterlitz. *Universal Jump in the Superfluid Density of Two-Dimensional Superfluids*, volume 39. American Physical Society, Nov 1977.

[62] E Buddenoir and S Wallon. *The correlation length of the Potts model at the first-order transition point*, volume 26. IOP Publishing, jul 1993.

[63] Michael E. Fisher and A. Nihat Berker. *Scaling for first-order phase transitions in thermodynamic and finite systems*, volume 26. American Physical Society, Sep 1982.

[64] K. Binder and D. P. Landau. *Finite-size scaling at first-order phase transitions*, volume 30. American Physical Society, Aug 1984.

[65] Vittorio Erba, Marco Gherardi, and Pietro Rotondo. *Intrinsic dimension estimation for locally undersampled data*, volume 9. nov 2019.

[66] Alex Rodriguez, Maria d'Errico, Elena Facco, and Alessandro Laio. *Computing the Free Energy without Collective Variables*, volume 14. 2018.

[67] Maria d'Errico, Elena Facco, Alessandro Laio, and Alex Rodriguez. *Automatic topography of high-dimensional data sets by non-parametric Density Peak clustering*. 2018.

[68] Michele Allegra, Elena Facco, Francesco Denti, Alessandro Laio, and Antonietta Mira. *Data segmentation based on the local intrinsic dimension*, volume 10. Nature Publishing Group, 2020.

[69] Christian Gross and Immanuel Bloch. *MICROSCOPY OF MANY-BODY STATES IN OPTICAL LATTICES*.

[70] Ehsan Khatami, Elmer Guardado-Sanchez, Benjamin M. Spar, Juan Felipe Carrasquilla, Waseem S. Bakr, and Richard T. Scalettar. *Visualizing Correlations in the 2D Fermi-Hubbard Model with AI*. 2020.

Chapter 4

Measurement-Induced Criticality in Non-Unitary Quantum Systems

This chapter is based on the following pubblications:

[1] Xhek Turkeshi, Rosario Fazio, and Marcello Dalmonte,
Measurement-induced criticality in (2+1)-d hybrid quantum circuits,
Phys. Rev. B **102**, 014315 (2020)

[2] Xhek Turkeshi,
Measurement-induced criticality as a data-structure transition,
arXiv: 2101.06245.

[3] Xhek Turkeshi, Alberto Biella, Rosario Fazio, Marcello Dalmonte, and Marco Schiró,
Measurement-Induced Entanglement Transitions in the Quantum Ising Chain: From Infinite to Zero Clicks,
Phys. Rev. B **103**, 224210 (2021). *(Editor's Suggestion)*

4.1 Introduction

Watched pot never boils.

Recent years have seen major progress in the understanding of many-body quantum dynamics. Two well separated limits have been discussed extensively, the unitary dynamics of closed isolated systems [4, 5] and the dissipative dynamics of open quantum systems coupled to an external environment [6]. In the former case the system remains in a pure many-body state which, in the absence of ergodicity breaking [7, 8] and for sufficiently large system sizes, acts as an efficient bath for any of its subsystems, leading to the thermalization of local observables and a volume-law entanglement entropy. In the latter, the system is intrinsically mixed and described by a master equation for the density matrix. In this setting, the competition between unitary and dissipative couplings can lead to non-equilibrium phase transitions, but it is not expected to change the entanglement and structural properties of the system.

An intermediate situation which has recently attracted major attention is the one in which the external environment represents a measurement apparatus, which ceaselessly probes some local observable on the system. Here the key physics is encoded in stochastic quantum many-body trajectories (conditional states), which contain a much richer information on the system dynamics than the average state. Without loss of generality, a quantum trajectory [6, 9] can be formally denoted as

$$|\Psi(\xi_t;t)\rangle = \Phi(\xi_t;t)|\Psi_0\rangle, \tag{4.1}$$

where t is the time, and the map Φ preserve the purity of the state and is fixed by the history of some deterministic operator (e.g. an Hamiltonian), and a collection of stochastic processes ξ_t for each time step, which can be discrete or continuous. Two simple examples include the unitary evolution solely generated by an Hamiltonian, as well as measurement operations (projective or generalized). Specifically, given the

Hamiltonian H, the former is captured by $\Phi(\xi_t;t) = \exp(-iHt)$. Instead, the measurement operations depends on the results of one or multiple measurements drawn with the Born rule. To be concrete, we fix for simplicity a single projective measurement P_A over some hermitian operator A and consider discrete times; then the formula for a single time step $t \to t+1$ is

$$|\Psi(\xi_t;t)\rangle = \Phi(\xi_t;t)|\Psi(\xi_{t-1};t-1)\rangle = \frac{P_A}{||P_A|\Psi(\xi_{t-1};t-1)\rangle||}|\Psi(\xi_{t-1};t-1)\rangle. \tag{4.2}$$

(The generalization to multiple measurement, generalized measurement, as well as continuous monitoring follow a similar rationale). We note that the renormalization in Eq. (4.2) is crucial in the following discussion, as it introduces non-linear effects in the evolution.

If the trajectories Eq. (4.1) are unaccessible, the relevant physics is uniquely encoded in the average state

$$\rho_{\text{ave}} = \int \mathcal{D}\mu[\xi_t]|\Psi(\xi_t;t)\rangle\langle\Psi(\xi_t;t)|. \tag{4.3}$$

In Eq. (4.3), $\mathcal{D}\mu[\xi_t]$ is a path integral measure over the possible trajectories (occasionally denoted histories). Eq. (4.3) can be proven to follow a Kraus dynamical map evolution (see Ref. [6] for a general discussion). We note that in the ubiquitous case of a Markovian environment, the specific form of this map can be recasted in a Lindblad master equation.

However, when the trajectories are accessible, the conditional state itself $|\Psi(\xi_t;t)\rangle$ is physically relevant. Crucially, this difference is invisible to operators O which are linear in the density matrix

$$\text{tr}(\rho_{\text{ave}}O) = \int \mathcal{D}\mu[\xi_t]\text{tr}(O|\Psi(\xi_t;t)\rangle\langle\Psi(\xi_t;t)) = \int \mathcal{D}\mu[\xi_t]\langle\Psi(\xi_t;t)|O|\Psi(\xi_t;t)\rangle. \tag{4.4}$$

In Eq. (4.5) we have used the linearity of the path integral over the histories. However, when considering a non-linear functional $\mathcal{F}(\sigma)$ over density matrices σ, the two averages differ

$$\text{tr}(\mathcal{F}(\rho_{\text{ave}})) \neq \int \mathcal{D}\mu[\xi_t]\text{tr}\left(\mathcal{F}(|\Psi(\xi_t;t)\rangle\langle\Psi(\xi_t;t)|)\right). \tag{4.5}$$

A simple example is the purity of the state $\mathcal{F}(\sigma) = \sigma^2$. Since the average state is in general mixed $\mathcal{F}(\rho_{\text{ave}}) < 1$, whereas the right-hand-side in Eq. (4.5) is identically 1, by definition of quantum trajectory. A dramatic consequence is that quantum information tools such as the Rényi entanglement entropies, quantify entanglement for the conditional state Eq. (4.1) but not for the average state Eq. (4.3). More in general, the structural properties encoded at the level of the average density matrix exhibits different patterns compared to the quantum trajectories. Hence, the conditional state can host a variety of quantum phases of matter, exotic with respect to the ones present for isolated unitary evolution and for the dissipative average state.

In this Chapter we present three facets of such non-equilibrium phases and phase transitions. For a unitary dynamics generated by random gates, we present how the structure of the manifold encoding the state changes (Sec. 4.3). Always for unitary random gates coupled to a measuring environment, we present evidence that the phase transition differs from known classical equilibrium transitions, by studying the 2+1D Clifford random circuits (Sec.4.4). Lastly, in Sec. 4.5 we investigate the role of measurements for a unitary dynamics fixed by the quantum Ising Hamiltonian, and show that the entanglement phase transition is already captured by the limit of no-measurement, where the environment act as a back-reaction in the system Hamiltonian.

The remaining of this Section gives an overview of the relevant literature, the setting of the problems considered in this Chapter, and the summary of the results which we obtain.

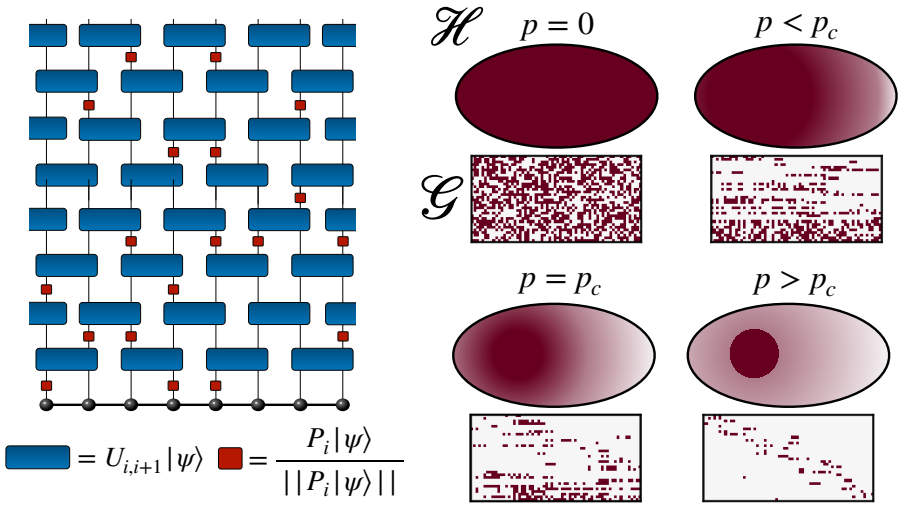

FIGURE 4.1: (Left) Cartoon of the hybrid quantum evolution. The brick-wall unitary is designed to let the qubits propagate correlations, while the measurement gates are randomly peaked with probability p. (Right) Pictorial representation of the phase transition: the explored Hilbert space $\mathcal{H}$ undergoes structural changes, reflected in the symplectic encoding $\mathcal{G}$.

4.1.1 Measurement-induced criticality in hybrid random circuits

Random unitary systems subject to repeated measurements of an environment are an ideal model to study the interplay between unitary evolution and stochastic local measurements [10–57]. This non-unitary framework is suitable for the description of noisy intermediate-scale quantum technologies (for a quantum simulation see Ref. [52]), and tackles fundamental questions of statistical physics, such as thermalization and ergodicity.

More concretely, the dynamical phases are controlled by the balance between the random unitary dynamics, which tries to relax the system toward the fully mixed density matrix $\rho_{\text{eq}} \propto \mathbf{1}$ ($\mathbf{1}$ is the identity matrix acting on the Hilbert space), and local measurements, which in contrast tend to localize the state to a restricted manifold fixed by the measurement outcomes. Rephrasing, the former spreads non-local correlations and generate entanglement throughout the system, while the latter typically destroy coherence and reduce the encoded quantum information, due to their local and collapsing nature.

At low measurement rate, the quantum information encoded in the state is robust against the environment probes, which acts as local errors in the dynamics. Hence this setting is labeled error-correcting phase [58–61], or *volume-law* phase, referring to the extensive system size scaling of the entanglement entropy in the stationary regime. At a high measurement rate, the state is constantly collapsed and is unable to escape a restricted manifold of the Hilbert space. This quantum Zeno phase [10] is characterized by local correlations and is dubbed *area-law* phase for its subextensive entanglement entropy scaling, proportional to the area of the subsystem boundary (with possible logarithmic corrections). Importantly, it has been shown that these phases are separated by a second-order transition at a critical measurement rate, with emerging conformal behavior for (1+1) dimensional circuits [10–12, 17, 18, 41].

Measurement-induced criticality as a data-structure transition

These results obtained through entanglement measures suggest a structural difference between the error-correcting and Zeno phases.

In Sec. 4.3, we propose a data-structure viewpoint, by directly analyzing the configurations encoding the state (datapoints), and show the measurement-induced criticality manifests as a geometric transition in the data-space. To this end, we consider principal component analysis and intrinsic dimension estimation, which, as unsupervised learning methods, provide an ideal framework to seek pattern in raw data. (See

Ref. [62–79] for applications of similar methods in statistical physics, and Ref. [80–82] for a general review of machine learning in physics.) As a proof of principle, we specialize in the study of (1+1) dimension Clifford hybrid circuits with local polarization measurements (see Fig. 4.1).

We show that the first quantified principal component is a robust order parameter for the transition, while the secondary quantified components present a change of pattern depending on the phase. The intrinsic dimension (see also Ch. 3), which is a measure of the effective dimensionality of the data space, scale differently with the system size at low and high measurement rate. It grows linearly in the error-correcting phase and logarithmically in the Zeno phase, reflecting the dimensionality of the explored Hilbert space, respectively exponential and polynomial in system size. We identify the transition as a local minimum of the intrinsic dimension. In fact, at the critical point, by virtue of universality, the system is parametrically simpler to describe compared to its vicinity.

Measurement-induced criticality in 2+1D hybrid random circuits

Despite the vast investigation in 1+1D, the nature of this transition is still subject to a debate. Motivated by numerical observations and analytical treatments, this critical point has been suggested to lie in the vicinity of a 2D classical percolation field theory [10–12]. Compared to the already rich (1+1)-d case, relatively little is instead known about their higher dimensional counterparts, where, even at equilibrium, entanglement properties are considerably different. For instance, the nature of a measurement-induced transition in two spatial dimensions could shed light on the relationship between HRC and percolation theories, and, potentially, give access to a new class of genuine out-of-equilibrium critical points.

In Sec. 4.4 we study the dynamics of (2+1)-d hybrid random circuit (HRC). We consider two measurement protocols, with rank-1 and rank-2 local projective measurements. In both cases, we find a volume-law phase at a slow rate of measurement, separated from an area-law phase at a high measurement rate via a measurement-induced transition (MIC). We perform a finite-size scaling (FSS) analysis to obtain accurate predictions of the correlation length critical exponent for the two cases. Our results suggest both critical points belong to the same universality class, which is distinct from that of percolation, similarly to the (1+1)-d case analyzed in Ref. [41]. This thesis is enriched by the presence of a violation of the area-law term in the entanglement entropy, that resembles those observed in Fermi liquids and $U(1)$ gauge fields coupled to fermionic matter [83–90].

4.1.2 Measurement-induced criticality in the quantum Ising chain

When instead the unitary dynamics is generated by an Hamiltonian, the properties of the system depend on the nature of the latter [26–30]. For instance, in the case of a free fermion Hamiltonian, the volume law is unstable for any measurement rate to a subextensive entanglement content [31, 54]. However, it has been shown that the average entanglement entropy can still show a transition between a logarithmic and area law phase at a critical measurement strength or to display a purely logarithmic scaling, depending on the stochastic protocol [32, 57]. A logarithmic growth of the entanglement entropy in an entire phase is particularly intriguing, given that the average state is expected to be effectively thermal, and it is reminiscent of a critical, conformally-invariant, phase whose origin has been so far elusive. Similar results have been obtained for free-fermion random circuits with temporal randomness [48], a setting that has been recently generalized to higher dimension [33], or for Majorana random circuits [91, 92].

A different take on measurement-induced transitions has instead focused on the limit of post-selection, also called forced measurement phase transitions [14], where only atypical trajectories with a particular outcome of measurement are retained. In this regime several works have discussed the relationship between measurement-induced transitions and the spectral properties of the associated non-Hermitian Hamiltonian [15, 34, 93]. More recently a non-Hermitian Hamiltonian has been also shown to emerge from the replica field theory associated to monitored Luttinger Liquids, leading to a Kosterlitz-Thouless transition between a gapless and a gapped phase [36].

In light of these developments it is interesting to compare the entanglement properties of stochastic quantum dynamics and non-Hermitian Hamiltonian, in a simple and paradigmatic setting. With such motivation, in Sec. 4.5 we consider the one-dimensional Quantum Ising model coupled to an environment which continuously measures its transverse magnetization. Specifically, we focus on two rather opposite limits of the measurement problem: the quantum state diffusion protocol [94, 95], a very clear, experimentally realizable measurement protocol in quantum optical systems [9], equivalent to homodyne trajectories [96, 97] and the quantum jump protocol in the so called no-click limit, corresponding to a purely deterministic non-Hermitian evolution, which amounts to post-select only trajectories without jumps.

Remarkably, despite describing rather different limits, show a very similar phenomenology in their entanglement properties. In particular, upon increasing the ratio γ between measurement rate and Hamiltonian coupling we find in both protocols a transition from a critical phase to an area law phase, the former characterized by a logarithmic scaling of the entanglement with time and system size. Right at the transition point γ_c, which we find numerically to coincide in the two protocols, the prefactor of the logarithmic entanglement contribution, interpreted as an effective central charge, vanishes continuously.

We note that an extended phase with logarithmic (critical) scaling of the entanglement was found also for other free-fermionic systems under monitoring, for example the XX chain of Ref. [32].

In this respect the no-click limit offers a natural explanation both for the critical entanglement scaling and for its transition towards an area law: these can be naturally understood by looking at the spectral properties of the non-Hermitian Quantum Ising chain which undergoes, right at γ_c, a subradiance transition from an extended critical phase with gapless decay modes, to a gapped phase which is smoothly connected to the dark state of the measurement operator.

In spite of the important similarities, the two protocols differ for the behavior of the effective central charge as a function of the measurement rate. In particular we find this quantity to be larger in the no-click limit, a signature of a noise-induced disentangling effect that appears clearly in the statistics of the entanglement entropy, which shows emergent bimodality upon approaching the critical point. Our results highlight the key role played by the non-Hermitian Hamiltonian for the qualitative understanding of entanglement transitions and suggest that different stochastic ensembles provide different universality classes of a common critical phenomenon.

Structure of the Chapter

The remaining of this Chapter is structured as follows. In Sec. 4.2 we introduce the stabilizer formalism, necessary for the investigation of measurement-induced transition in hybrid random circuits. In Sec. 4.3 we investigate measurement induced criticality on the perspective of data-space. In Sec. 4.4 we investigate the entanglement measurement-induced criticality for 2+1D hybrid circuits. In Sec. 4.5 we study the measurement-induced phase transition for the quantum Ising model coupled to a monitoring environment, and relate the results to the non-Hermitian Hamiltonian describing the post-selected trajectories with no-measurement events. For the latter Section, we detail derivations and numerical methods in the Appendix 4.6.

4.2 Stabilizer states and Clifford unitary gates

In this Section we review the stabilizer formalism. Truly generic random evolution would involve gates drawn with Haar measure from the full unitary group (Haar gates). However, the exponential scaling of the Hilbert space hinders classical computations beyond a few decades of spins. Despite the remarkable results in obtained (1+1)-d numerical investigations, Haar gates are inadequate to tackle thermodynamic limits, or higher dimensional systems.

Thus, in order to simulate large systems and have a consistent scaling analysis, throughout this Chapter we restrict our attention to the evolution of stabilizer states with unitary gates drawn from the Clifford group and projective measurement on Pauli strings. The Clifford group is an approximation to the Haar gates, which fully encode statistical properties up to the second moment (2-unitary design) [98]. The approximation is apparent in the investigation of complex operators, which involve a number of unitaries larger than 2. Important examples are out-of-time correlation (OTOC) functions, as they are one of the hallmarks of ergodicity in quantum systems. Simulations in (1+1)-d Haar circuits present evidence of exponential growth in time of the OTOC (signal of chaotic behavior), while analogous computations for Clifford circuits result in trivial time-scaling [99–101]. Nevertheless, the entanglement entropy exhibits qualitatively similar behavior, as illustrated for instance in Ref. [10].

For self-consistency, we give a technical summary on the stabilizer formalism and on the Clifford gates (we refer for a general review to Ref. [98, 102]). For readers already familiar with such formalism, the rest of the Section is hopefully useful to clarify notations. After general considerations, we recall the Gottesman-Knill theorem [98, 103] and the Hamma-Ionicioiu-Zanardi theorem [104, 105]. The former explains how polynomial classical computation resources are needed to simulate the HRC of interest, while the latter gives an efficient way to compute entanglement for stabilizer states.

Stabilizer states are vectors of the Hilbert space satisfying the condition:

$$O_i|\psi\rangle = +|\psi\rangle, \tag{4.6}$$

for some set of operators O_i (for spin-1/2 systems, we anticipate here these are Pauli strings that will be discussed below). This set, under matrix multiplication, forms a group $\mathcal{G} = \{O_i\}$. In principle, the vectors satisfying Eq. (4.6) form a vector space associated to the group G. However, if the number of generators of the group is equal to the number of sites $|\mathcal{G}| = N_s$, a unique state (up to normalization) is fixed by the knowledge of $\mathcal{G}$ (see Ref. [102]). Stabilizer formalism has been largely discussed in the context of quantum error correction (see Ref. [102] and reference therein), and have recently appeared [10–12, 17, 18, 39, 44, 58, 59, 106] in tailored non-unitary quantum dynamics as they can be efficiently simulated.

The key result behind the simulations of stabilizer states under the action of the Clifford group is the Gottesman-Knill theorem, which explains: (i) how unitary evolution affects stabilizer states, (ii) how projective measurements change the state within the stabilizer formalism. Let us briefly sketch the ideas behind this result. Under the unitary evolution, Eq. (4.6) holds for the evolved stabilizer:

$$O_i(t)|\psi(t)\rangle = +|\psi(t)\rangle, \quad O_i(t) = U(t)O_iU^\dagger(t). \tag{4.7}$$

In general, $O_i(t)$ is a linear combinations over exponentially many Pauli strings. However a major simplification occurs when the unitary U is drawn from the Clifford group. The latter is defined as the set of unitary operations that map a Pauli string into a *single* Pauli string. Since the number of stabilizers does not grow under Clifford gates, the knowledge of the system only requires keeping track of the evolution of N_s stabilizers at each time step. However, a Pauli string is totally given by a binary vector of exponents and a phase:

$$\begin{aligned} O_i &= e^{i\phi}(\sigma_1^x)^{v_1^x}(\sigma_1^z)^{v_1^z}(\sigma_2^x)^{v_2^x}(\sigma_2^z)^{v_2^z}\dots(\sigma_{N_s}^x)^{v_{N_s}^x}(\sigma_{N_s}^z)^{v_{N_s}^z} \\ &\equiv (v_1^x, v_1^z, v_2^x, v_2^z, \dots, v_{N_s}^x, v_{N_s}^z|\phi). \end{aligned} \tag{4.8}$$

As a consequence, the state evolution under Clifford circuits is encoded by a $N_s \times (2N_s + 1)$ matrix. The phase will be convenient in Sec. 4.3, but it is negligible for studies on the entanglement (as in Sec. 4.4,

where our configurations are encoded in a $N_s \times (2N_s)$ matrix with binary entries).

Throughout this Chapter we consider the Clifford group $\mathcal{C}_n$ acting on $n = 2$ or $n = 4$ sites. For an efficient algorithm on how to implement uniform peaking over the Clifford group we refer to Ref. [107].

Projective measurement on Pauli string is less intuitive, but easy to implement. Let us consider a Pauli string O_p we want to projectively measure on $|\psi\rangle$ a stabilizer state. Give its stabilizer group:

$$\mathcal{G} = \text{span}(O_1, O_2, \dots, O_k, O_{k+1}, \dots, O_{N_s}), \tag{4.9}$$

suppose that $[O_j, O_p] = 0$ for $j \leq k$ and $\{O_j, O_p\} = 0$ for $j > k$ (either one holds for Pauli strings). The wave-function get mapped after measurement to:

$$|\psi\rangle_\pm \mapsto \frac{1 \pm O_p}{2}|\psi\rangle. \tag{4.10}$$

The Gottesman-Knill theorem states that the measured state expressed in term of the stabilizer group is given by:

$$\mathcal{G}_\pm = \text{span}(O_1, O_2, \dots, O_k, O_{k+1} \cdot O_{k+2}, \dots O_{N_s-2} \cdot O_{N_s-1}, O_{N_s-1} \cdot O_{N_s}, \pm O_p). \tag{4.11}$$

The phase can be determined $\mathcal{O}(N_s^2)$ using a symplectic doubling trick (see Ref. [103] for details), or within $\mathcal{O}(N_s^3)$ using a Gauss-Jordan elimination. Throughout the Chapter, we specialize to $O_p = \sigma_i^z$, or $O_p = \sigma_i^z \sigma_j^z$ with j neighbor of i.

Lastly, entanglement entropy can be extracted directly from the binary submatrix $N_s \times (2N_s)$ obtained neglecting the phases. Given a bipartition $A \cup B$ of dimension respectively N_A and N_B, we extract the $N_s \times (2N_A)$ matrix $\mathcal{G}_A$ corresponding to the sites belonging in A. The Hamma-Ionicioiu-Zanardi theorem state the entanglement entropy for a stabilizer state is simply given by:

$$S_A(\rho_A) = \text{rank}(G_A) - N_A. \tag{4.12}$$

We conclude this Section by noticing that algebraic sums modulo 2 between the stabilizers in the tableau representation $\mathcal{G}$ do not change the entanglement. This gauge degree of freedom is irrelevant for our discussion, but can be used to introduce a quasi-particle picture for the 1+1D hybrid Clifford circuits [11]

4.3 Measurement-induced criticality as a data-structure transition

4.3.1 Hybrid non-unitary dynamics

We consider the quantum trajectories of a system under the combined action of a unitary protocol and stochastically distributed local measurements. At every time step, each qubit is picked with probability p and measured:

$$|\psi(\tilde{k_t};t)\rangle_{t+1} = \frac{P_i|\psi(k_t;t)\rangle_t}{||P_i|\psi(k_t;t)\rangle_t||}, \tag{4.13}$$

and afterward the system is unitary evolved $|\psi(k_t;t)\rangle_{t+1} = U|\psi(\tilde{k_t};t)\rangle_{t+1}$. Here, k_t encodes the history of the quantum trajectory, both for the type unitary gates applied, and for the stochastic measurements (see Sec. 4.1). Mathematically, it can be represented by a tensor with $\mathcal{O}(L)$ entries. Occasionally we omit k_t if no confusion arises.

The rate of measurement p controls the dynamical phases of the system. When local measurements are suppressed $p \to 0$, the dynamics is governed mostly by the unitary part. For generic initial conditions, the system explores a large portion of the Hilbert space, and reaches extensive bipartite entanglement entropy, hence the name of volume law phase. In the opposite regime $p \to 1$, the system is constantly projected. Non-local correlations are suppressed, thus effectively localizing the state into a restricted manifold of the Hilbert space, and the entanglement entropy is subextensive (area law phase).

For concreteness, we consider a stabilizer circuit where local measurements involve the local polarization $P_i = (1 \pm \sigma_i^z)/2$, while the unitary gates are randomly drawn from the Clifford group and structured in a brick-wall fashion (Fig. 4.1):

$$|\psi\rangle_{t+1} = \prod_{i=\mathrm{mod(t,2)}}^{L/2} U_{2i-1,2i}|\tilde{\psi}\rangle_{t+1}. \tag{4.14}$$

In the last equation, the nearest-neighboring gates alternate depending on the parity of t, that in this setup has integer values.

Stabilizer states on L qubit are fully characterized by L independent Pauli strings (see Sec. 4.2). Consequently, the stabilizer group is represented by a binary matrix $\mathcal{G} \equiv [n_j^i]_{L\times 2L+1}$. This encoding fixes uniquely the state [1]

$$\rho = |\psi\rangle\langle\psi| = \frac{1}{2^L}\sum_{g\in\mathcal{G}} g. \tag{4.15}$$

As discussed in Sec. 4.2, the Gottesmann-Knill theorem provides a set of rules for implementing Eq. (4.13) and Eq. (4.14) directly on the matrix $\mathcal{G}$. In this way, the dynamics $|\psi\rangle \mapsto |\psi\rangle_t$ is converted into $\mathcal{G} \mapsto \mathcal{G}_t$.

Our implementation follows the lines of Ref. [103] and uses the package in Ref. [107] to simulate the random Clifford gates. The system it is known to present a criticality at $p = 0.16(1)$, with a correlation length critical exponent around $\nu = 1.30(5)$ [10, 11, 17, 18]. We use this model to benchmark our approach described in the next sections.

4.3.2 Principal component analysis

We begin by considering principal component analysis (PCA) [62–64, 80, 108], which is a linear transformation of the data space basis. Given a dataset G, that is a matrix $N \times d$ in which each row is a configuration of the system (feature), PCA rotates it, such that the greatest variance of the dataset lies in the first component, the second greatest variance in the second component, *etc.*.

The method consists of three steps:

i Define the centered dataset X, whose elements are $X_{i,j} = G_{i,j} - (1/N)\sum_i G_{i,j}$. This procedure guarantees that $\Sigma = X^T X/(N-1)$ is the covariance matrix of the dataset.

[1] We shall interchangeably denote $\mathcal{G}$ the symplectic representation, i.e. the generators $[n_j^i]_{L\times 2L+1}$, and the generated group $\mathcal{G} = \mathrm{span}\{O_i\} \simeq \mathrm{span}[n_j^i]$. Here $\simeq$ is a group isomorphism.

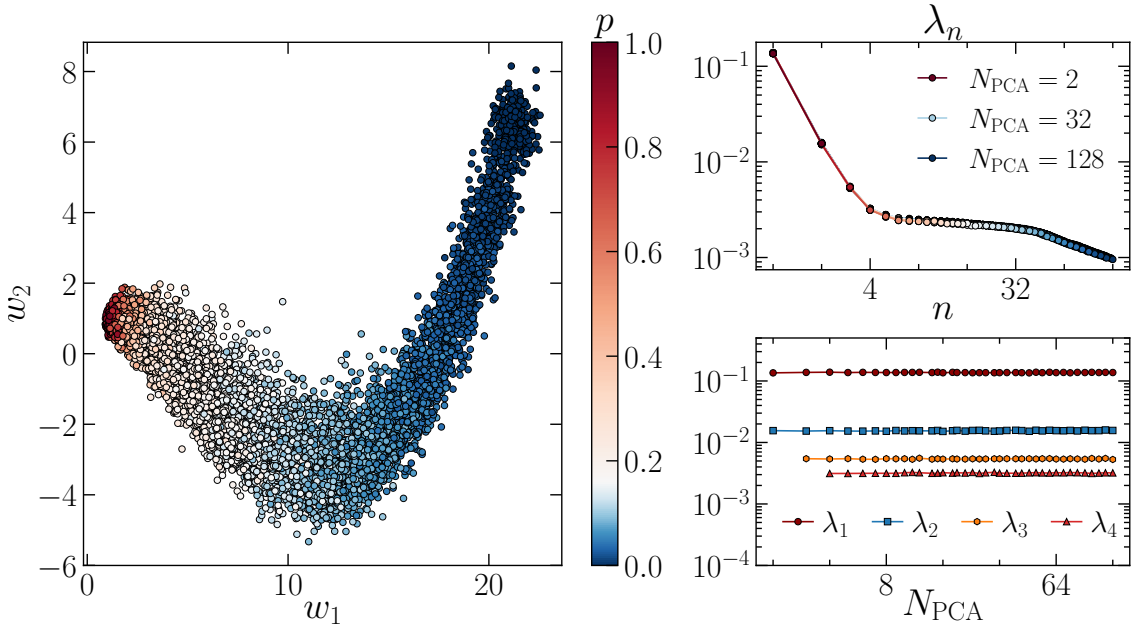

FIGURE 4.2: *Principal components for a stabilizer group* — (Left) Results for the principal components w_1 and w_2 at $L = 32$. The data organize in separate regions for different measurement rates. (Right) Explained variance ratios λ_n for the most relevant components. The relative relevance of the directions does not change upon increasing the number of components $N_{\rm PCA} = 2 \div 128$.

ii Perform a singular value decomposition of the centered dataset $X = V'DV$.

iii Apply the rotation $V = [v_1, \dots, v_d]$ to the original dataset G (in matrix form $W = GV$). The vectors w_j along the direction v_j are termed principal component. (In practice, one fixes a restricted number of components in the analysis, to gain computational efficiency.)

The PCA is particularly effective in cases where few principal components are most relevant. The relevance is obtained from the singular values d_n corresponding to the weight vectors v_n, as they quantify the variance of the dataset along the n-th direction. In fact, the covariance matrix Σ is diagonalized by the weight vectors:

$$\Sigma v_n = d_n^2 v_n. \tag{4.16}$$

Rescaling these quantities to $\lambda_n = d_n^2/(\sum_n d_n^2)$, we obtain the so-called explained variance ratios [80], that is, a measure of relative weights of the principal directions. Notice that by definition $\sum_n \lambda_n = 1$, hence λ_n are percentage of encoded information along the n-th direction.

In our implementation (which is based on `sklearn` [109]), for each system size L, we construct the dataset G, where each row contains the $d = L(2L+1)$ elements of the binary matrix $\mathcal{G}_t$. We draw these configuration within the stationary regime $t \geq 8L$, with $\Delta t = L/2$ waiting time between snapshots. The total number of configurations obtained is $N = N_p N_s$, and consists of N_p number of values $p \in [0, 1]$ considered, and N_s snapshots for each value of p [2].

As an illustrative example, we present the results of the PCA for $L = 32$ in Fig. 4.2. We can see that the first component alone captures around 16% of the dataset, and within the first 4 components the cumulative encoding reaches 20%. This fact is unaffected by varying the number of directions required by the algorithm, as the explained variance ratios remain qualitatively unchanged. Conversely, λ_n distribute

[2] We fix $N_p = 43$, with $p \in [0.0, 0.01, \dots, 0.29] \cup [0.35, 0.4, 0.45, \dots, 0.95]$, and vary $N_s = 200, 400, 800, 1600$. We present data only for $N_s = 400$, as we find no qualitative behavior on the results. The system size considered for the PCA range between $L = 16 \div 320$.

into the same curve over the range of considered principal directions N_{PCA}. We stress that the dataset considered in each case is different, and the small fluctuations are related to the specific realizations.

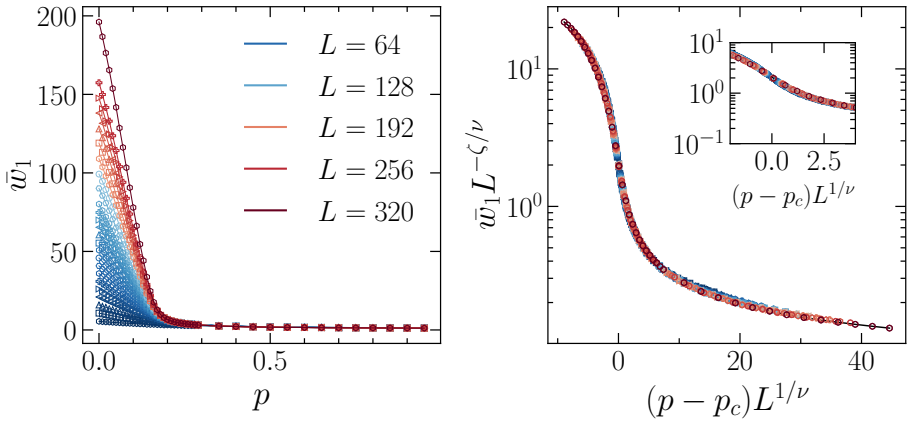

FIGURE 4.3: (Left) Quantified principal component $\bar{w}_1$ for different system sizes L, and (Right) its data collapse. The results show the order parameter nature of $\bar{w}_1$. The estimated $p_c = 0.16(1)$, $\nu = 1.4(1)$, and $\zeta = 0.51(3)$ are in agreement with the results in literature.

The principal components w_j contain all the relevant information of the dataset: knowing the full distribution of w_j as stochastic variable is equivalent in the reconstruction of the dataset. It is however suitable to consider a single proxy which is able to capture relevant information on the system. Therefore, here we specialize to the quantified principal components, defined as the conditional averages

$$\bar{w}_j = \frac{1}{N_s} \sum_{i(p)} w_j(i), \tag{4.17}$$

where the mean is over N_s configurations sharing the same measurement rate p. This quantity is plotted in Fig. 4.3 (left). Remarkably, under the finite-size scaling hypothesis:

$$\bar{w}_1 = L^{\zeta/\nu} f_1((p - p_c)L^{1/\nu}), \tag{4.18}$$

we find a data collapse which correctly identify the transition [110]. Our estimate for the critical point and exponents are: $p_c = 0.16(1)$, $\nu = 1.4(1)$ and $\zeta = 0.51(3)$. In Fig. 4.3 (right) we can appreciate the quality of the collapse in the whole range of considered measurement rates. Notice that $\bar{w}_1$ lacks a straightforward physical interpretation, and is a non-local order parameter, as it corresponds to a rotation of arbitrary length Pauli strings. (Differently, for instance, from the equilibrium 2D Ising model, where $\bar{w}_1$ is proportional to the magnetization [64]).

Next, we consider the subsequent, less relevant, components. We discover that oscillations appear in the error-correcting phase ($p < p_c$), while they saturate toward a $\mathcal{O}(1)$ value in the Zeno phase ($p > p_c$). These fluctuations feature off the critical point feature non-universal information. Nonetheless, they encode universal information close to criticality. For instance, we apply the finite-size scaling also to a restriction of the dataset for the quantified principal component $\bar{w}_2$, cutting off values $p < 0.11$. Then, assuming the same ansatz as in Eq. (4.18), we again identify the correct critical behavior within error bars (the data collapse for the second component in the inset of Fig. 4.4). A similar analysis has not been applied to further components, as a more refined resolution of measurement rates is required to correctly perform the finite-size scaling. However, we expect similar results to hold.

4.3.3 Intrinsic dimension

The limitation of the principal component analysis is rooted in the linear nature of the transformation. Hence, when the dataspace has a non-linear, complex geometry, PCA needs further analysis to give meaningful

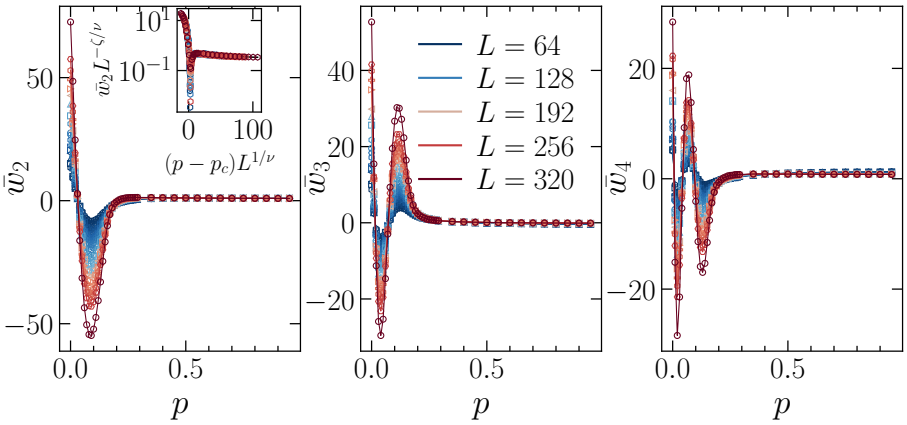

FIGURE 4.4: Secondary quantified principal component for different system sizes L. Oscillations appear in the error-correcting phase. (Inset) Data collapse for $\bar{w}_2 = L^{\zeta/\nu} f_2((p - p_c)L^{1/\nu})$, in a restricted region close to criticality. The estimated $p_c = 0.16(1)$, $\nu = 1.4(1)$, and $\zeta = 0.48(3)$ are compatible with the analysis for $\bar{w}_1$ (see Fig. 4.3).

information. To overcome these limitations, we consider the intrinsic dimension [111–114]. The intrinsic dimension I_d is the effective dimension of a dataset. We discuss in depth the intrinsic dimension in Ch. 3 of this thesis, but to preserve a self-consistency of the Chapter, we provide a brief summary in the following, and specify our dataset. The I_d can be estimated using different techniques [80], but here we specialize in the two nearest-neighboring technique (TWO-NN), which has been recently applied to equilibrium statistical physics [115]. The TWO-NN: (i) is independent of the density pattern of the whole dataset, (ii) applies also to non-linear complex geometries.

The main assumption of the method is that the dataset is *locally* uniform. Here, locality is related to the scale at which we look at the data: the larger the dataset, the more resolved is the distance between points. (Empirically, a finer scale is inversely proportional to the dataset size N^{-1} in one-dimensional systems.) In this approach, differently from the PCA, we restrict the dataset to a given system size L, and a given rate measurement rate p: $G = G(L, p)$. The goal is to find the dimension of the space explored, pictorially represented in Fig. 4.1. The technique is described in Ch. 3, but to keep the Chapter selfconsistent, we briefly summarize the key points here.

The method is based on computing the distribution functions of neighborhood distances. For each configuration $x = G(i; L, p)$, we compute the first and second nearest-neighboring distances $r_1(x)$ and $r_2(x)$, respectively. Under the assumption of locality, we may represent the dataset as a uniform hypersphere; then the distribution function of $\mu = r_2/r_1$ is:

$$f(\mu) = I_d \mu^{-I_d - 1}. \tag{4.19}$$

We can derive a formula for the I_d for the cumulative distribution $P(\mu) = \int^{\mu} d\mu' f(\mu')$:

$$I_d = -\frac{\ln(1 - P(\mu))}{\ln \mu}. \tag{4.20}$$

We estimate the intrinsic dimension by Eq. (4.20), where the cumulative distribution is substituted with the empirical distribution of the data.

It is important to stress that the local uniformity is but an approximation for discrete datasets. For this reason, we collect $N_{\text{data}} = 30$ datasets of $N = 5000$ for each value of L and p considered, compute the intrinsic dimension over each dataset, and average the results to obtain the final estimate [3].

[3] We fix $N_s = 5000$, with $p \in [0.0, 0.01, \ldots, 0.98, 0.99]$, and vary the system size in $L = 16 \div 128$. Furthermore, see Ref. [115] for a discussion on complementary methods and limitations. The research of more refined algorithms to estimate the intrinsic dimension in discrete systems is an active topic of research in the field.

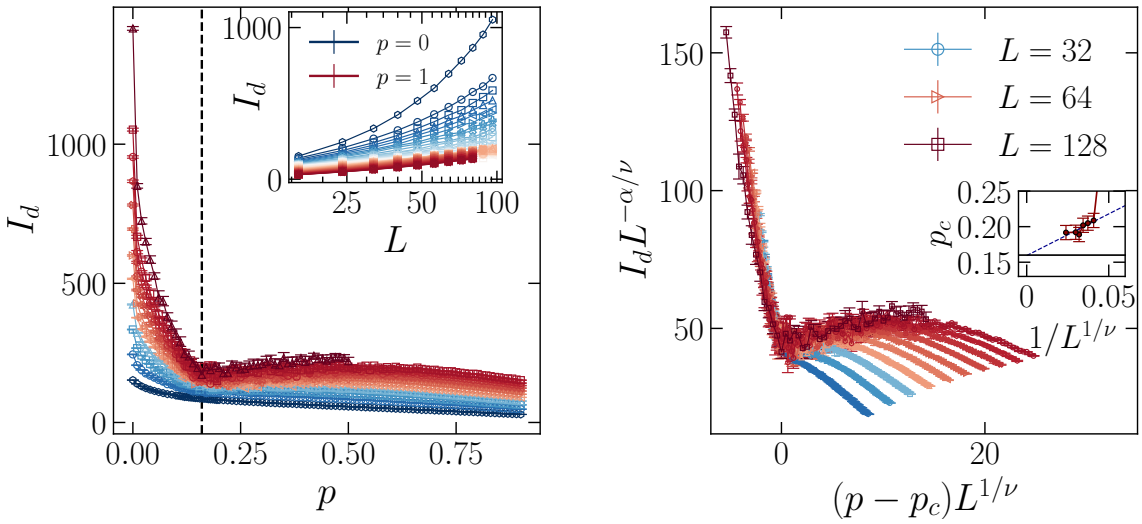

FIGURE 4.5: (Left) Intrinsic dimension for different system sizes L. Notice the non-monotonic behavior, with a minimum close to criticality. (Inset) Scaling of the intrinsic dimension with the system size for various values of the measurement rate. We distinguish a linear region for $p < p_c$, and a logarithmic one for $p > p_c$. (Right) Data collapse after a finite-size scaling analysis. The estimated $\nu = 1.3(1)$, $p_c = 0.16(2)$, and $\alpha = 0.3(1)$, are in agreement with the previous analysis (Fig. 4.3 and Fig. 4.4). (Inset) Estimation of the critical point through the minimum of the ID. The points are obtained by fitting a third-order polinomial and locating the minimum. The dashed line is the optimal linear fit in $1/L^{1/\nu}$, where we excluded small system sizes. The intersection $p_c(L \to \infty) = 1.6(2)$ is in agreement with the data collapse.

The results are plotted in Fig. 4.5. We find a linear growth of the ID for $p \lesssim 0.16$, while a logarithmic one at $p \gtrsim 0.16$. The physical interpretation of these results is based on the dimensionality of the Hilbert space. Since the quantum state ρ is obtained by summing over all Pauli strings generated by $\mathcal{G}$ (cfr. Eq. (4.15)), we have $\dim\mathcal{H} \simeq 2^{I_d}$. When I_d scales linearly with system size, the Hilbert space explored is exponentially large and the stationary state is a random stabilizer state. Conversely, deep in the Zeno phase, the Hilbert space explored is polynomial in system size. In particular, in the thermodynamic limit, the system is localized in a zero-measure manifold. As remarked before, these considerations are consistent with the results obtained using the entanglement measures [10]. Let us stress an important difference: while the entanglement entropy in the Zeno phase saturates, the intrinsic dimension scales logarithmically. This is because the intrinsic dimension is not a measure of entanglement, and include also classical correlations in the encoding dataset.

The intrinsic dimension develops a non-monotonic behavior close to criticality. We identify the transition as the local minimum of the intrinsic dimension (see Fig. 4.5 (right,inset)). Physically, the critical point is parametrically simpler to describe compared to its vicinity. In fact, the collective behavior at criticality is captured by few relevant effective fields, in the renormalization group sense. Instead, the off-critical region requires additional information on the irrelevant operators, which increases the number of parameters close to the transition. This picture is *a fortiori* confirmed in the present setup by the presence of a conformal field theory [11, 41], but holds on general ground. Besides, the intrinsic dimension in the vicinity of the transition manifests universal behavior. We use the finite-size scaling ansatz:

$$I_d = L^{\alpha/\nu} h((p - p_c)L^{1/\nu}), \tag{4.21}$$

adapting the analysis to values of $p \in [p_c^{\text{est}} - \delta p, p_c^{\text{est}} + \delta p]$ close to the empirically estimated critical point $p_c^{\text{est}} = 0.17$, $\delta p = 0.15$. We obtain $p_c = 0.16(2)$, $\nu = 1.3(1)$ and $\alpha = 0.3(1)$, compatibly with the literature and the PCA analysis. This critical change of the intrinsic dimension is the hallmark of a geometric transition in the data space. The dimensionality of Hilbert manifold describing the late time state $|\psi\rangle$ undergoes an

abrupt and critical change, intimately related to the change of scaling for the entanglement measures.

4.3.4 Conclusion

In this Section, we used principal component analysis and intrinsic dimension estimation to describe the phases and locate the transition of hybrid random circuits directly in the data space. In particular, we have shown that measurement-induced criticality reveals as a structural transition in the encoding data manifold.

Similarly to the case of equilibrium classical physics [62–64], the PCA captures the critical behavior and the structural change of phase for the hybrid random circuits. In particular, the first quantified principal component $\bar{w}_1$ gives an alternative order parameter for the transition. The data space transition is also manifest in the change of intrinsic dimension, which develops a minimum at criticality. Here, the representative space is parametrically simpler, signaling the presence of emerging collective behavior with fewer effective degrees of freedom compared to the neighboring region. Overall our results show full compatibility with the data present in the literature while giving a complementary viewpoint on the nature of the transition.

The unsupervised nature of the considered methods, which require no a priori knowledge of the phase space, and the simplicity of their computation, make these attractive tools to investigate hybrid dynamical systems. It would be interesting to apply and extend this toolbox to more complex setups, such as high dimensional hybrid circuits, or to tackle experimental data. As recently shown in Ref. [116] for the many-body localization transition, it is possible to reconstruct a dynamical phase diagram directly from experimental data and using machine learning tools: applying similar methods to the measurement-induced transition may resolve the problem of entanglement measurements, which are notably hard.

4.4 Measurement-induced criticality in 2+1D hybrid random circuits

4.4.1 Model and observables

System dynamics

We consider a two-dimensional square lattice model of spin-1/2 qubits. The system is initialized in a low-entanglement state [4] and let evolve through a hybrid quantum circuit where unitary dynamics is alternated to layers of randomly picked local projective measurements (see cartoon in Fig. 4.6).

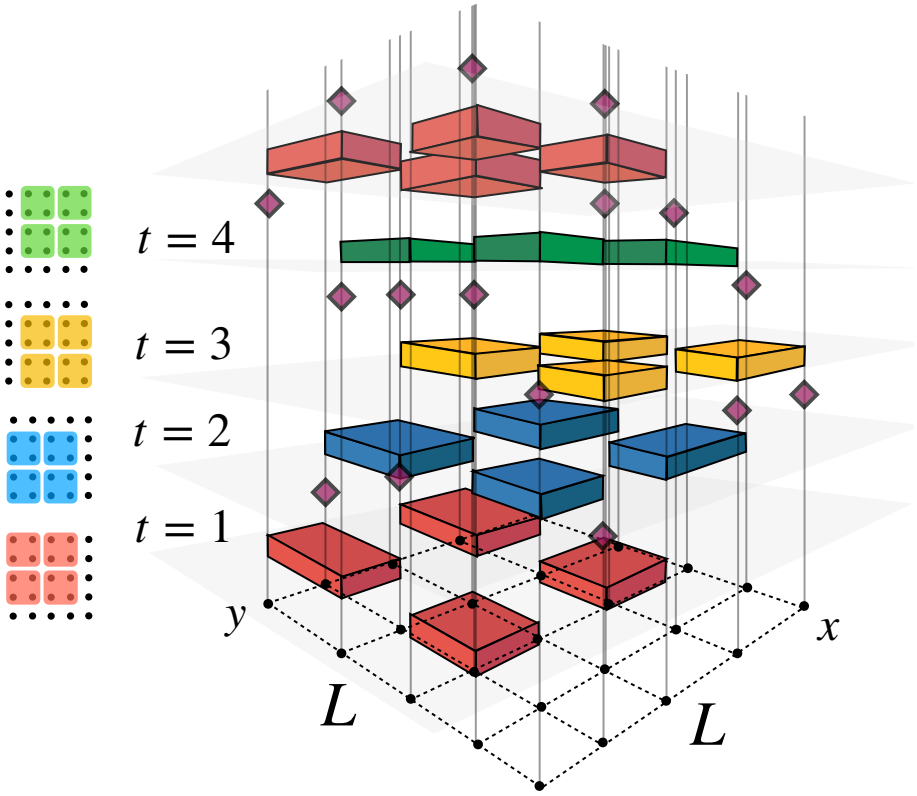

FIGURE 4.6: Graphical scheme of the system dynamics with measurement protocol in Eq. (4.28). Spins are arranged on a square lattice ($x-y$ plane) of size $L \times L$. The time evolution is a stroboscopic sequence of random Clifford unitaries (colored rectangles) acting on plaquettes, and layers of random local projections (diamond symbols) acting on single spins. Different colors identify different unitary layers (see Eq. (4.22)).

The unitary operations are given by random gates acting on four neighboring sites and structured in a brick-layer pattern. These gates have a periodic space-time pattern: depending on the value of the discrete time t, the operations are padded in the x and y directions. Given the elementary gate:

$$U(x,y,t) \equiv U_{(x,y),(x+1,y),(x,y+1),(x+1,y+1)}(t), \tag{4.22}$$

[4] The choice of low-entanglement state is unimportant for our purposes, as the stationary regime is independent of the initial state.

each unitary layer is given by:

$$U(t) = \prod_{x=1}^{L_x/2} \prod_{y=1}^{L_y/2} U(2x - r_x(t), 2y - r_y(t), t) \tag{4.23}$$

$$r_x(t) = \begin{cases} 1, & \text{if } t \mod 4 = 1, 2 \\ 0, & \text{otherwise,} \end{cases} \tag{4.24}$$

$$r_y(t) = \begin{cases} 1, & \text{if } t \mod 4 = 0, 1 \\ 0, & \text{otherwise.} \end{cases} \tag{4.25}$$

The different shifts guarantees that the dynamics correlates all spins. The above operators act linearly on the state:

$$|\psi(k_t; t+1)\rangle = U(t)|\psi(k_t; t)\rangle, \tag{4.26}$$

and generate entanglement throughout the system.

Measurements are randomly picked with probability p throughout the circuit. Together with the random unitary gates, they are responsible for the stochastic variable k_t in Eq. (4.26), which fix the trajectory as it labels both the type of unitary gates, and of space-time measurement events. (In practice, this can be though as a tensor with $\mathcal{O}(L^2)$ elements.)

Given an evolution up to time T, for a square lattice of side L, the average number of measurements in the circuit is the fraction $N_{\text{meas}} = pL^2T$, where $0 \leq p \leq 1$. These operations induce a non-linearity in the dynamics, as the wave function is renormalized after each collapse:

$$|\psi(k_t; t)\rangle \mapsto |\psi(k_t; t+1)\rangle = \frac{P^\alpha|\psi(k_t; t)\rangle}{||P^\alpha|\psi(k_t; t)\rangle||}. \tag{4.27}$$

In the last equation, α is a multi-index label of the measurement type and of the measurement position. In this Section we consider the following rank-1 and rank-2 projective measurement (see Fig. 4.7):

$$P^{(1)}_{(x,y)} = \frac{1 \pm \sigma^z_{(x,y)}}{2}, \tag{4.28}$$

$$P^{(2)}_{\langle(x_1,y_1),(x_2,y_2)\rangle} = \frac{1 \pm \sigma^z_{(x_1,y_1)}\sigma^z_{(x_2,y_2)}}{2}. \tag{4.29}$$

Here the single site measurement Eq. (4.28) acts on site (x, y), while Eq. (4.29) acts on neighboring sites (x_1, y_1), (x_2, y_2) and project the state onto a Bell pair. Furthermore, the dynamics can be tailored conditionally on the measurement outcomes. In the present setting, we consider only unconditioned measurement layers, as the dynamic of entanglement for stabilizer states, is unaffected by the measurement outcomes. To obtain larger system sizes we restrict to stabilizer states, so that Gottesmann-Knill theorem and the Hamma-Ionicioiu-Zanardi theorem can be used (see Sec. 4.2).

For each trajectory, we compute the entanglement entropy as a function of time. Given a bipartition of the system $A \cup B$, the entanglement entropy is defined as the Von Neumann entropy of the reduced density matrix $\rho_A(k_t; t) = \text{tr}_B|\psi(k_t; t)\rangle\langle\psi(k_t; t)|$:

$$S_A(k_t) = -\text{tr}_A\rho_A(k_t; t) \log \rho_A(k_t; t). \tag{4.30}$$

This quantity is an operational measure of entanglement, and in the present setting, serves as an order parameter characterizing distinct dynamical phases. The latter are a consequence of the competing tendencies of the unitary evolution and the local projective measurements, whose balance is controlled by the rate p. A qualitative understanding of these dynamical phases is captured in the extreme limits [10–12]. When $p \sim 0$, the evolution is largely unitary and the system is driven toward generic ("infinite temperature") wave-functions. For any given basis, the number of components of the Hilbert space required to sensibly capture this stationary regime scales exponentially with the subsystem volume, thus resulting in

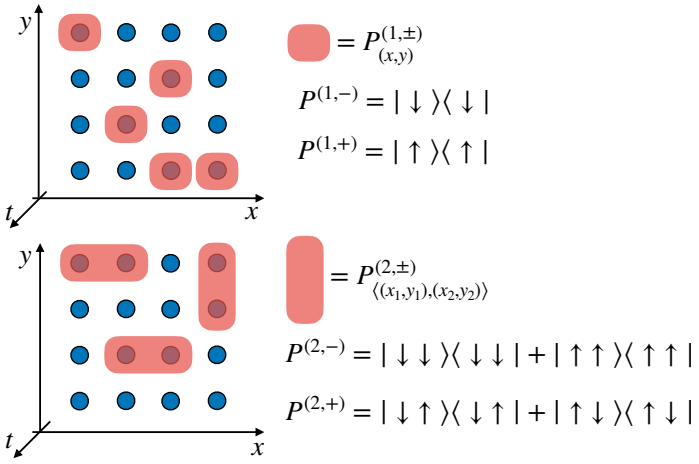

FIGURE 4.7: Local projection operator employed in the two dynamics.

an extensive entanglement entropy $S_A(k_t) \propto \text{vol}(A)$. On the other hand, when measurements are frequent $p \lesssim 1$, the projections impede information spreading beyond arbitrary distant regions of the system. In this regime, spins are correlated on a length-scale proportional to the domain of the projective measurement. As a consequence, the stationary wave-function is localized in a smaller subspace, resulting in an entanglement entropy scaling with the area of the subsystem boundary $S_A(k_t) \propto \text{area}(\partial A)$. Finally, entanglement entropy is able to capture also a transition point between the aforementioned volume-law and area-law phases (see Sec. 4.4.2).

We are interested in the average values of the late time $t \to \infty$ over many realizations for the hybrid circuits

$$S_A(p, L) = \lim_{t\to\infty} \overline{S_A(k_t)} = \lim_{t\to\infty} \int \mathcal{D}\mu[k_t] S_A(k_t), \tag{4.31}$$

where we denote as $\overline{B}$ the average of a given quantity B over the trajectories. In practice, we wait for the stationary regime up to times $t \sim \mathcal{O}(L^2)$, when the time evolution fluctuation of the entanglement are contained. We conclude with two remarks: (i) the path integral in Eq. (4.31) is discrete and hence convergent, and (ii) the average density matrix $\rho_{\text{ave}} = \overline{\rho_A(k_t)}$ always presents a volume-law compatible with that of thermal systems [10].

4.4.2 Entanglement dynamical phases and universal criticality

We simulate the model in Sec. 4.4.1 and compute the entanglement entropy averaged over $\mathcal{N} = 10^4$ circuit realizations for each system size and each measurement rate considered. We consider periodic boundary conditions and consider a bipartition for strips between $N_A = L \times L_A$ and $N_B = L \times (L - L_A)$. The latter choice allows us to isolate boundary contributions and neglect effects due to corners. We vary both L and L_A and store, after convergence is reached, the stationary value of the entanglement entropy $S(p, L_A)$.

We have checked, but not reported here, that in the stationary regime our results are independent of the initial state chosen. Below we separately discuss the numerical results for rank-1 and rank-2 measurement considered (see Sec. 4.4.1). We find that for both protocols, a volume-law phase is separated by an area-law phase via a second-order phase transition (at a point p_c which depends on the projector operator used). This point exhibits a universal behavior, in the sense that the computed correlation length critical exponents are compatible in the two cases within one error bar.

Rank-1 measurements

We consider the local projectors $P^{(1)}_{\mathbf{i}}$ (cfr. (4.28)). We simulate for various $p \in [0, 1)$, expecting a volume-law average entanglement entropy for $p \simeq 0$ and an area-law for $p \lesssim 1$. The case $p = 1$ is fine tuned, as

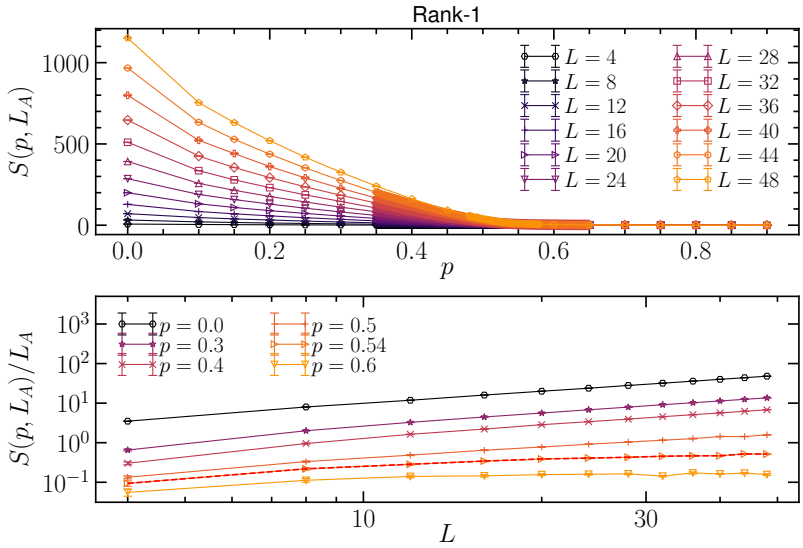

FIGURE 4.8: Entanglement for various linear system sizes L and for various rates p, with $L_A = L/2$. We can see that the values $p < 0.54$ present a volume-law entanglement $S(p, L_A) \propto L_A^2$, while for values $p > 0.54$ we have a quantum Zeno phase, with entanglement saturating to an area-law $S(p, L_A) \propto L$. The line $p_c = 0.54$ characterize the critical point, which exhibits a scaling $S(p_c, L_A) \propto L \log(L_A)$. The slope for a volume-law phase is provided in blue to guide the eye; this is quantitatively accurate for purely unitary dynamics. All error bars are smaller than the size of the symbols.

the local projections applied to each sites project the state after each time step in a product state, hence not considered here.

In Fig. 4.8 (top panel) we show the average entanglement entropy at half-system $S(p, L_A = L/2)$ for various values of system sizes L and different measurement rates p. Here, errorbars are present, but are smaller than the size of the markers; hence they are undistinguishable by the markers. Since in two spatial dimensions the area-law is proportional to the entanglement cut length L_A, it is instructive to analyze $S(p, L_A)/L$, as this quantity saturates to a constant for an area-law phase and scale linearly with the system size in the volume-law phase. In Fig. 4.8 (bottom panel) we plot $S(p, L_A)/L$ for $L_A = L/2$. In the figure, it is possible to identify two distinct scaling regimes: For $p \lesssim 0.54$, the entropy increases linearly with the volume of the system. For $p \gtrsim 0.54$, after an initial growth for small sizes, the entropy saturates to a size-independent value. These results are expected from our previous discussion, except for the exact location of the critical point, which is extracted from a careful finite-size scaling analysis (presented below).

Furthermore, in order to gain more information on the critical regime, we investigate the ratio $S(p, L_A)/L$ for a fixed system size, and varying the subsystem dimension. Specifically, we consider a lattice with side of length $L = 64$, and consider a subsystem of dimension $N_A = L \times L_A$, with $L_A = 4, 8, \ldots, L/2$. Also in this case, our simulations distinguish between the volume-law, area-law, and critical regimes, as presented in the Main panel of Fig. 4.9. To clearly characterize the critical line and its scaling, in the inset of Fig. 4.9 we plot the results in a semi-logarithmic scale. Our data strongly support scaling at the transition of type $S(p_c, L_A) \propto L \ln L_A$.

As remarked earlier, a correction of this kind has been, at present, observed only in Fermi liquids and in $U(1)$ gauge field coupled with matter. For Fermi liquids, the origin is hidden in the peculiar Fermi surface of the models [84, 88, 89], and the entanglement scaling can be obtained analyzing the entanglement Hamiltonian. Similarly, the scaling of entanglement of critical spin liquids ($U(1)$ gauge fields coupled to fermions), has been observed numerically in Ref. [87]. The authors suggest this may be related to the fermionic matter of the theory, and their Fermi surface. In the present setting, the appearance of logarithmic corrections $\propto L \ln L_A$ is puzzling as: (i) the transition point is out-of-equilibrium, (ii) the system does not transparently have a Fermi surface. We postpone a discussion on the emergence of this scaling at the end of

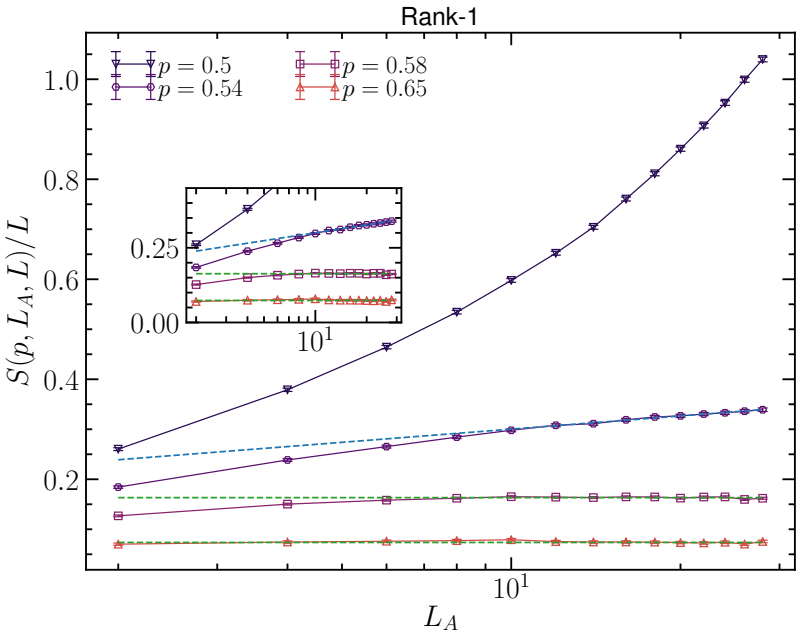

FIGURE 4.9: (Main) Stationary entanglement entropy near the critical point as a function of L_A. To spot the correct scaling, we divide the entanglement entropy by the uncut system size $S(p, L_A)/L$. Clearly one can distinguish three regimes: one super-logarithmic (volume-law), one logarithmic (critical point), and one sub-logarithmic (area-law). (Inset) Scaling of entanglement entropy close to the transition in logarithmic scale. To guide the eye, we plot the fitted $\log L_A$ for the ratio of interest. All error bars are smaller than the size of the symbols.

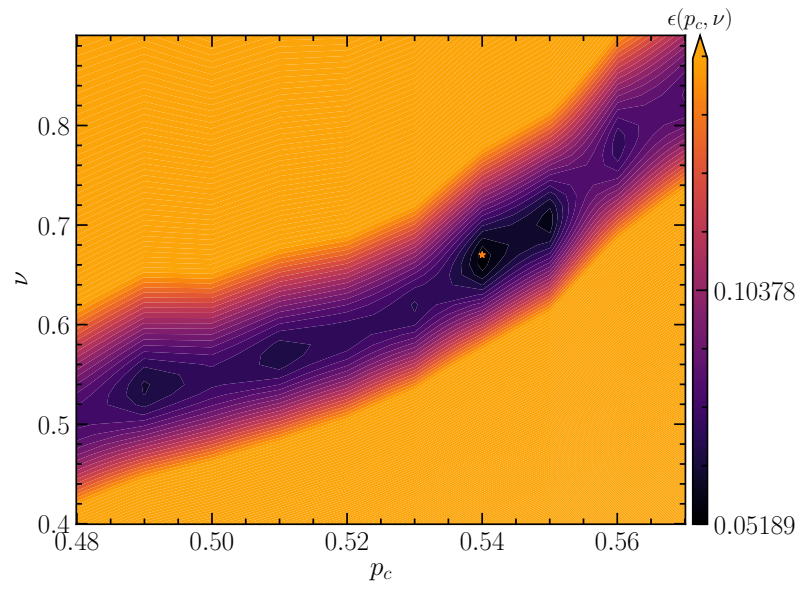

FIGURE 4.10: Finite size analysis for the model of interest. The landscape of the residual is plotted for a suitable range of ν and p_c considered in the FSS. The orange star locate the optimal parameters $\nu = 0.67(1), p_c = 0.54(1)$.

this section.

To access the correlation length critical exponent, we perform a finite-size scaling analysis (FSS) around the critical point. To compare with the literature in (1+1)-d HRC and the critical exponents of percolation

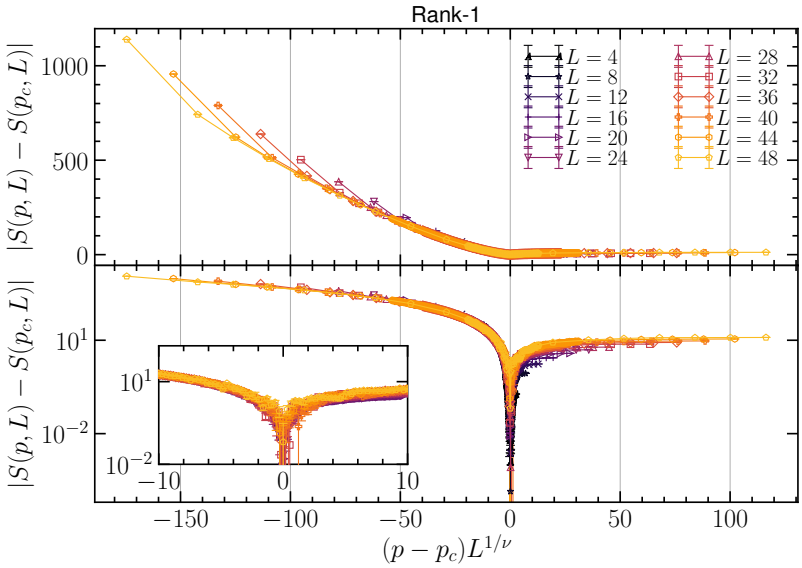

FIGURE 4.11: Data collapse for the hybrid circuit with rank-1 projective measurements. Here $p_c = 0.54(1)$ and $\nu = 0.67(1)$. In the inset, we present a closer look on the critical point.

theory, we use the scaling ansatz:

$$S(p, L_A) - S(p_c, L_A) = F((p - p_c)L_A^{1/\nu}). \tag{4.32}$$

Specifically, given the scaling variables:

$$x_{\text{dat}}(p_c, \nu) = (p - p_c)L^{1/\nu}, \tag{4.33}$$

$$y_{\text{dat}}(p_c) = S(p, L) - S(p_c, L), \tag{4.34}$$

we implement polynomial fits for different degree polynomials and different subsets of system sizes. Given a fixed polynomial $P_m(x)$ of degree m and given a subset of lengths $\{L_1, L_2, \ldots, L_k\}$, the best fit is obtained minimizing the normalized least-square distance between the data and the polynomial computed on the scaling variable x_{dat}:

$$\varepsilon = \sqrt{\frac{\sum_i |y^2_{\text{dat}}(i) - P^2_m(x_{\text{dat}}(i))|}{\sum_i y^2_{\text{dat}}(i)}}. \tag{4.35}$$

Our final results are obtained averaging over different values of the degree m and different subsets of system sizes; similarly, the error is the propagated error. In Fig. 4.10 we present the landscape of the residual for the optimal fit varying ν and p_c. The estimated critical parameters $\nu = 0.67(1)$ and $p_c = 0.54(1)$, give us the data collapse in Fig. 4.11, presented in both linear and logarithmic scale.

Let us conclude this subsection by comparing our results with the critical exponents of percolation theory. If a quantum-to-classical similarity has to hold in higher dimension (with respect to the results of (1+1)-d HRC), we should test our findings against 3D percolation on a cubic lattice. Here the correlation length critical exponent is $\nu^{3D}_{\text{perc}} = 0.877(1)$, more than 30% different from our estimate. Consequently, this quantum critical point is sensibly different from the percolation one for the same space-time dimension.

4.4.3 Rank-2 measurements

These circuits have local projectors $P^{(2)}_{\langle \mathbf{i},\mathbf{j} \rangle}$ (cfr. (4.29)). In this case, the measurement projects the neighboring qubits into a Bell pair. We proceed in full analogy with Sec. 4.4.2. In Fig. 4.12 we show the bare data for the circuit. We see that for $p \lesssim 0.84$ the system displays a volume law, whereas for $p > 0.84$ the system

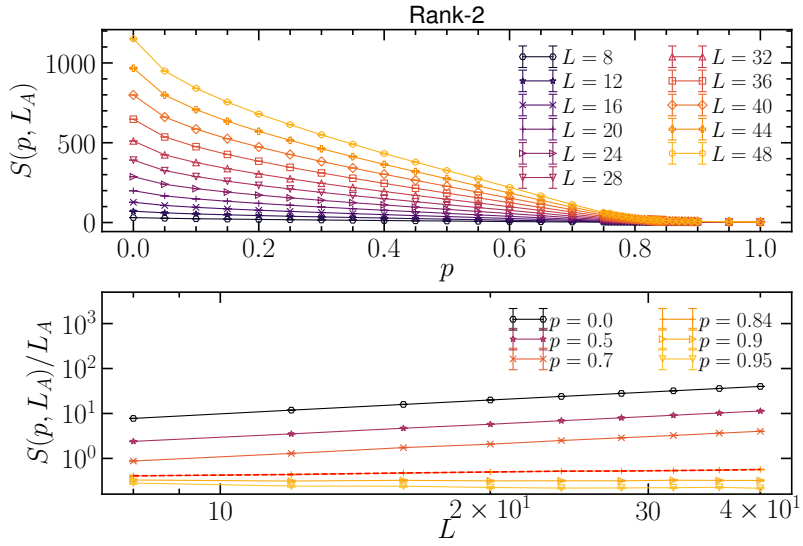

FIGURE 4.12: Entanglement for various linear system sizes L and for various rates p, with $L_A = L/2$. We can see that the values $p < 0.84$ present a volume-law entanglement $S(p, L_A) \propto L_A^2$, while for values $p > 0.84$ we have a quantum Zeno phase, with entanglement saturating to an area-law $S(p, L_A) \propto L$. The line $p_c = 0.84$ characterize the critical point, which exhibits a scaling $S(p_c, L_A) \propto L \log(L_A)$. The slope for a volume-law phase is provided in blue to guide the eye; this is quantitatively accurate for purely unitary dynamics. All error bars are smaller than the size of the symbols.

shows an area law. In the vicinity of the critical point, we investigate up to $L = 64$ to benchmark and check this analysis, as reported for S_A/L in Fig. 4.13.

We perform a finite-size analysis analogous to the previous subsection. The landscape of the residual Eq. varying the parameters p_c and ν is plotted in Fig. 4.14.

The critical point in this case is shifted to higher values (the estimated $p_c = 0.84(1)$). This is not a surprise, as the rank-2 projectors have less disentangling power than the correspondent rank-1 measurements, and the critical point is affected by changes in the microscopic physics of the system. Nevertheless, the universal information contained in the critical exponent is preserved, as we estimate $\nu = 0.68(1)$ (see Fig. 4.15 for the data collapse). This robust check confirms our previous analysis, in particular the distinction between this critical point and the percolation theory one.

4.4.4 Discussion and open questions

The obtained numerical results leave us with open questions. To which, if any, universality class do the measurement induced critical points belong? For $D > 1$ hybrid quantum circuits, is there a classical effective model or any mean-field theory? Which is the origin of the area-law violation at the critical point? We conclude this subsection addressing these issues with speculative arguments based on our numerical observations.

Our estimate of the critical exponents (mutually compatible within $\%2$ error in both the considered models), suggest both critical points belong to the same universality class. However, we do not have enough information to fully characterize the nature of such a universality class. A naive comparison with $D = 3$ classical percolation theory rule out a quantum-to-classical analogy between entanglement and percolation in (2+1)-d circuits. In fact, our estimated critical exponent $\nu \simeq 0.67$ is incompatible from the $\nu_{\text{perc}} \simeq 0.87$ of percolation theory in $3D$.

A key feature here is that the critical point exhibits an area-law violation. Such violation is common to gapless fermionic systems, such as free theories and Fermi liquids. It is however very unusual for spin systems: in these cases, such violations to area-law contributions are typically associated with the emergence of

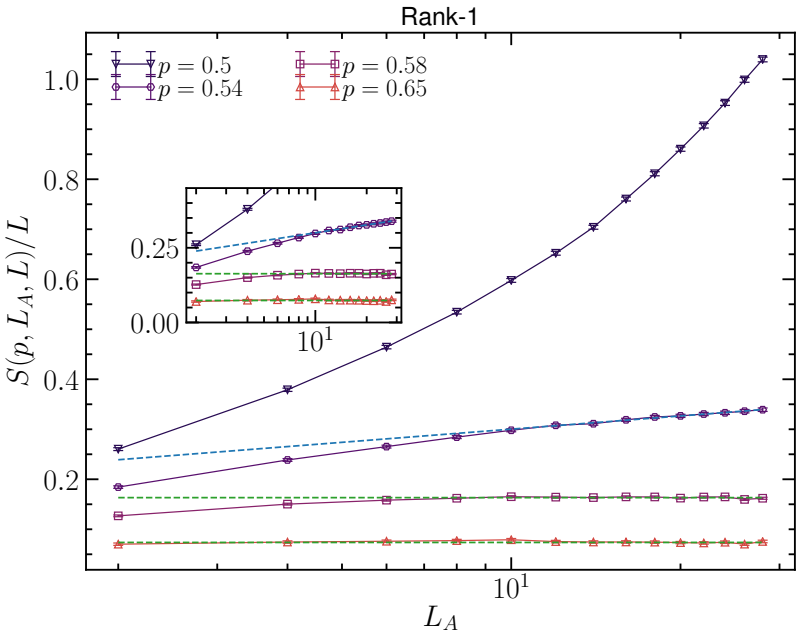

FIGURE 4.13: (Main) Stationary entanglement entropy near the critical point as a function of L_A. To spot the correct scaling, we divide the entanglement entropy by the uncut system size $S(p, L_A)/L$. Clearly one can distinguish three regimes: one super-logarithmic (volume-law), one logarithmic (critical point), and one sub-logarithmic (area-law). (Inset) Scaling of entanglement entropy close to the transition in logarithmic scale. To guide the eye, we plot the fitted $\log L_A$ for the ratio of interest. All error bars are smaller than the size of the symbols.

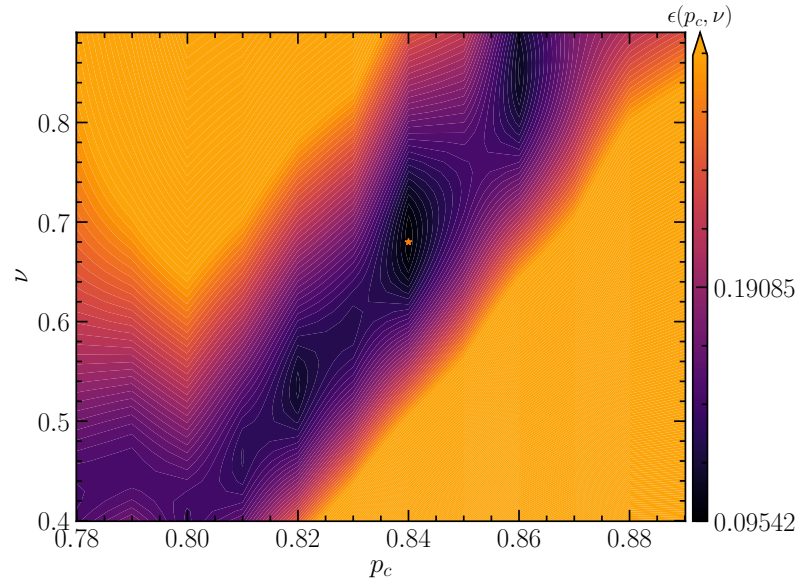

FIGURE 4.14: Finite size analysis for the model of interest. The landscape of the residual is plotted for a suitable range of ν and p_c considered in the FSS. The orange star locate the optimal parameters $\nu = 0.68(1), p_c = 0.84(1)$.

an underlying $U(1)$ gauge theory descriptions, with emergent fermionic excitations responsible for the logarithmic corrections [**?**]. We note that some classes of these gauge theories - directly connected to $\mathbb{C}P(N)$ models - have been reported to have critical exponents compatible with the one observed here [85]. This

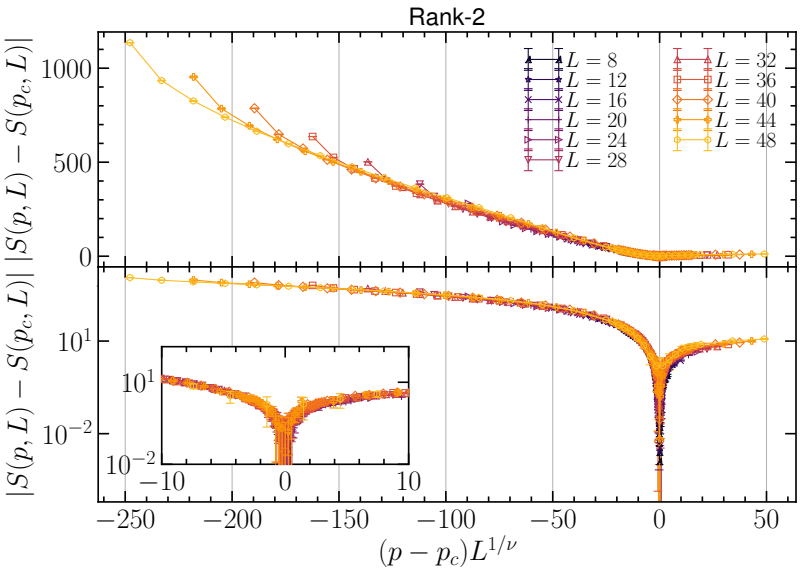

FIGURE 4.15: Data collapse of hybrid circuits with rank-2 projective measurements. Here $p_c = 0.84(1)$ and $\nu = 0.68(1)$. The inset shows a closer look to the critical point.

analogy in terms of entanglement scaling suggests that either the present critical regime has no-equilibrium analog, or that emergent fractionalization of quantum numbers might be taking place. The formulation of a rigorous statistical mechanics mapping as done in the (1+1)-d case, or the investigation of gauge-invariant quantum circuits may resolve this issue.

From a complementary, microscopically oriented viewpoint, the logarithmic area-law violation we observe may be justified from the stabilizer size distribution. In one-dimensional systems, this quantity is defined in terms of the length of stabilizers, i.e. the distance between the edge Pauli matrices of a Pauli string. This has been related to entanglement entropy in Ref. [11, 13], where the authors deduce the following scaling in one spatial dimension:

$$S_A^{1+1d}(p,L) = \begin{cases} \alpha(p)\log L + \beta(p)L & p < p_c, \\ \alpha(p)\log L & p = p_c, \\ \alpha(p)\log \xi & p > p_c. \end{cases} \tag{4.36}$$

Heuristically this argument extends to two spatial dimension, with the important caveat that here, for lattice models, a clear definition of stabilizer *area* distribution is missing. (It is likely that corner effects may roughen a proper scaling limit). Nonetheless, from our numerical data we conjecture this is the case, and correspondingly the entanglement entropy behaves as:

$$S_A^{2+1d}(p,L) = \begin{cases} \tilde{\alpha}(p)L\log L + \tilde{\beta}(p)L^2 & p < p_c, \\ \tilde{\alpha}(p)L\log L & p = p_c, \\ \tilde{\alpha}(p)L\log \xi & p > p_c, \end{cases} \tag{4.37}$$

with $\tilde{\alpha}$ and $\tilde{\beta}$ system-size independent. We leave for future work elaborating a proper definition of the stabilizer area and its implication on the hybrid quantum circuits dynamics.

4.4.5 Conclusion

We investigated the measurement-induced criticality in two-dimensional hybrid quantum circuits generated by Clifford random unitary gates. Our findings reveal that the entanglement transition separating area and

volume-law phases present universal features: those are signaled by the correlation length critical exponent being insensitive to the choice of the measurement, and by the same functional form of the entanglement entropy at criticality, showing logarithmic violations of the area-law. This universality class is distinct from that of 3D percolation theory.

Concerning the nature of the critical point, at equilibrium, the entanglement scaling we report has been previously observed only in systems with fermionic excitations, such as Fermi liquids and $U(1)$ gauge theories coupled to fermionic matter. Recently, monitored (2+1)D fermionic systems have been reported in Ref. [33], where a stable $L \log L$ phase was found. It would be interesting to investigate monitored gauge-invariant (2+1)D circuits, where an effective lattice gauge field theory may be present, and hence it may exhibits a similar $L \log L$ phase.

For 1+1D Haar random circuits with local unitary gates, there exists a map to a classical statistical mechanics model in a replica space. A key factor for this analytic analysis, is that the interactions in this analog lattice are replica index invariant, and hence enable to a simple replica limit to recast physical quantities (such as the entanglement entropy). We leave for future work to generalize these results in higher dimension, and check if an emergent gauge symmetry acts on the replica space.

From the computational side, additional insights may be gathered via the computation of other observables, such as the scaling of corner contributions in the entanglement entropy, and equal-time correlation functions. Regarding the latter, the challenge is to implement these quantities within the stabilizer formalism, thus preserving the technical advantage over full (Haar) quantum dynamics. Moreover, it would be interesting to seek the upper critical dimension of the system of interest, and in particular, if a "mean-field" regime can be captured by a classical statistical mechanics model. In fact, our estimate of the critical exponent $\nu \simeq 0.67$ is close to the mean-field limit $\nu_{\text{MFT}} = 1/2$ of statistical field theory. It is possible that already HRC in 3+1d saturate this limit, a fact that might be detectable already at modest system sizes due to its mean-field origin.

We conclude this section by a comparison with the results in Ref. [40], where the authors study a similar 2+1D quantum circuit, and report a different set of critical exponents (for instance the correlation length critical exponent is $\nu \simeq 0.8$). We attribute the differences to the limited sizes considered in their paper. In fact, in our analysis, the inclusion/exclusion of smaller system sizes in the finite size scaling gives considerably different results. In particular, restricting the finite size analysis to the same sizes $L \leq 32$ we find a correlation length critical exponent compatible to the one they report.

4.5 Measurement-induced entanglement transition in the monitored quantum Ising chain

In this section we discuss the Ising chain coupled to a monitoring environment.

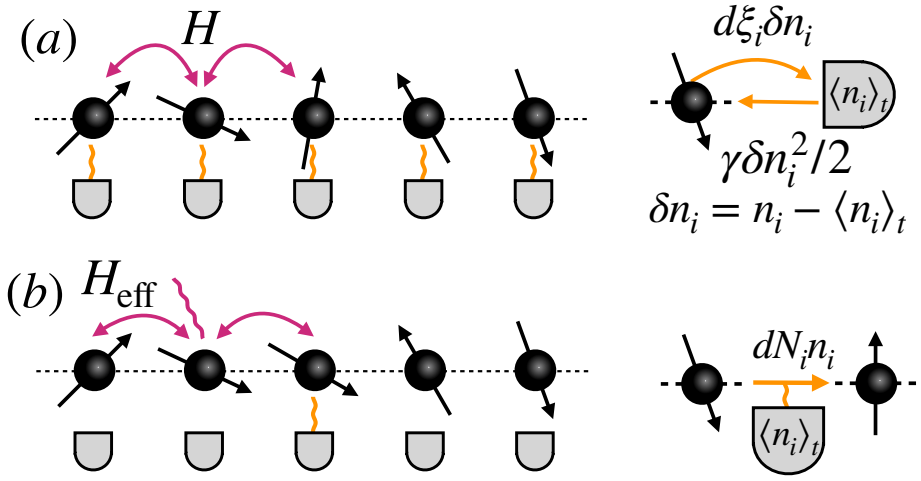

FIGURE 4.16: Cartoon of the monitored Quantum Ising Chain. (a) Quantum state diffusion protocol: on each lattice site a two-level system (Ising spin) interacts with its neighbors and is subject to a weak-continuous measurement of the up-polarized state. (b) Quantum jump protocol: the spins in the chain interact through a non-Hermitian Hamiltonian. Occasionally a quantum jump take place, projecting the measured degree of freedom in the up-polarized state. The no-click limit corresponds to post-selecting only trajectories without jumps. (See text for details).

4.5.1 Model and Measurement Protocols

We consider a one dimensional Quantum Ising chain with Hamiltonian

$$H = J \sum_{i=1}^{L-1} \sigma_i^x \sigma_{i+1}^x \tag{4.38}$$

with open boundary conditions, evolving under the competing effect of its own unitary dynamics and the measurement of the up-polarized state $n_i \equiv (\sigma_i^z + 1)/2 = |1\rangle\langle 1|$ (pictorially illustrated in Fig. 4.16). Here σ^α are the Pauli matrices. We now introduce the two measurements protocols that will be considered in this work, namely the quantum state diffusion and the quantum jumps with post-selection, corresponding to the non-Hermitian Hamiltonian.

Stochastic Quantum Dynamics with Continuous Monitoring

Due to the monitoring, the evolution is captured by quantum trajectories $|\psi(\vec{\xi}_t)\rangle$ which follow the quantum state diffusion (QSD) equation

$$\begin{aligned} d|\psi(\vec{\xi}_t)\rangle = -iHdt|\psi(\vec{\xi}_t)\rangle + \sum_{i=1}^{L}(n_i - \langle n_i\rangle_t)d\xi_t^i|\psi(\vec{\xi}_t)\rangle \\ - \frac{\gamma}{2}\sum_{i=1}^{L}(n_i - \langle n_i\rangle_t)^2 dt|\psi(\vec{\xi}_t)\rangle. \end{aligned} \tag{4.39}$$

(See Appendix 4.6.1 for a brief derivation of the above stochastic Schrödinger equation). The first term in Eq. (4.39) represents the unitary evolution, while the remaining encode the noise effects. The $d\xi_t^i$ are Îto increments of a Wiener process $\vec{\xi}_t = (\xi_t^1, \xi_t^2, \dots, \xi_t^L)$, responsible for the stochastic nature of the trajectories, with zero mean $\overline{d\xi_t^i} = 0$ and fulfilling the exact property $d\xi_t^i d\xi_t^j = \gamma dt \delta^{ij}$. The last term in Eq. (4.39) describes a deterministic back-action from the measuring environment.

We note the presence of a feedback mechanism in Eq. (4.39), as the noise contributions couple to the fluctuations of the measured operator $\delta n_i = n_i - \langle n_i \rangle_t$ where $\langle \circ \rangle_t = \langle \psi(\vec{\xi}_t)| \circ |\psi(\vec{\xi}_t)\rangle_t$ is the average over the quantum state. The role of this feedback is to preserve the norm of the state (and any of its cumulant) for any realization of the noise.

Recalling the general discussion on the difference between conditional and average states (see Sec. 4.1), we comment on the average state following the Lindblad master equation and on the quantum trajectories being unravelling of the latter. In the present setting, the conditional state is $\rho_t(\vec{\xi}_t) = |\psi(\vec{\xi}_t)\rangle\langle\psi(\vec{\xi}_t)_t|$, while the mean state is

$$\overline{\rho_t} = \int \mathcal{D}\vec{\xi}_t P(\vec{\xi}_t) |\psi(\vec{\xi}_t)\rangle\langle\psi(\vec{\xi}_t)| \tag{4.40}$$

with $P(\vec{\xi}_t)$ the probability distribution of the noise. Despite the conditional state is always pure, the mean state is mixed. A simple Îto calculus computation shows that the average state follows the Lindblad master equation

$$\frac{d}{dt}\overline{\rho_t} = -i[H, \overline{\rho_t}] - \frac{\gamma}{2}\sum_i [n_i, [n_i, \overline{\rho_t}]]. \tag{4.41}$$

This difference is crucial, and highlights how the two states $\overline{\rho_t}$ and $\rho_t(\vec{\xi}_t)$ provide rather different information on the statistical properties of the system.

After this digression, we introduce the main observable of interest: the (von Neumann) entanglement entropy [117–120]. Given a partition $A \cup B$, the (conditional) reduced density matrix $\rho_A(\vec{\xi}_t) = \mathrm{tr}_B \rho(\vec{\xi}_t)$ encodes the bipartite entanglement. The entanglement entropy is defined as

$$S(\vec{\xi}_t) = -\mathrm{tr}_A \left[\rho_A(\vec{\xi}_t) \ln \rho_A(\vec{\xi}_t)\right]. \tag{4.42}$$

We note that this is a well defined measure of entanglement provided that the overall state is pure, in which case it yields the amount of Bell pairs that can be distilled from the quantum state. This is not the case for an overall mixed state, such as the averaged state, where also classical correlation enters into this quantity [121]. For this reason, throughout this Section we only consider the conditional state and the conditional average of the entanglement entropy. To simplify the notation, we furthermore omit the conditional specification. After evolving the state under Eq. (4.39), we compute the entanglement entropy. Its average is given by

$$\overline{S} = \int \mathcal{D}\vec{\xi}_t P(\vec{\xi}_t) S(\vec{\xi}_t), \tag{4.43}$$

as well as its full probability distribution is

$$P(S_t) = \int \mathcal{D}\vec{\xi}_t P(\vec{\xi}_t)\ \delta\left(S - S(\vec{\xi}_t)\right) \tag{4.44}$$

Throughout this Section we set $J = 1$ and study the problem by varying the strength of the measurement γ and for different system sizes L.

Non-Hermitian Hamiltonian

When the measurements act occasionally but abruptly on the quantum state, the quantum trajectories are described by the following stochastic Schrödinger equation

$$d|\psi(\vec{N}_t)\rangle = -iHdt|\psi(\vec{N}_t)\rangle - \frac{\gamma}{2}dt\sum_i (n_i - \langle n_i\rangle_t)\,|\psi(\vec{N}_t)\rangle + \sum_i \left(\frac{n_i}{\sqrt{\langle n_i\rangle_t}} - 1\right)\delta N_t^i|\psi(\vec{N}_t)\rangle, \tag{4.45}$$

where $\vec{N}_t$ is a Poisson process, with $\delta N_t^i = 0, 1$, $(\delta N_t^i)^2 = \delta N_t^i$, and $\overline{\delta N_t^i} = \gamma dt\langle n_i\rangle_t$. (A derivation of Eq. (4.45) is given in Appendix 4.6.1). The dynamics generated by Eq. (4.45) preserves the purity of the state for each trajectory, and gives an alternative unravelling of the average dynamics in Eq. (4.41).

When $\delta N_t^i = 0$ on every site, the evolution is driven by the non-Hermitian Hamiltonian

$$H_{\text{eff}} = J\sum_{i=1}^{L-1}\sigma_i^x\sigma_{i+1}^x - i\frac{\gamma}{2}\sum_{i=1}^{L} n_i, \tag{4.46}$$

while when any $\delta N_t^i = 1$, the last term in Eq. (4.45) dominates and projects the measured degree of freedom onto the up-polarized state $|1\rangle_i$. The feedback constant $\propto i\gamma\sum_i\langle n_i\rangle_t$ enters as a renormalization of the wavefunction within the non-Hermitian evolution driven by Eq. (4.46). In the following we consider a post-selection of the stochastic dynamics, which arises when, among the experimental runs, we select a portion of trajectories where measurements do not take place (no-click limit). The evolution is therefore deterministic, and driven by the non-Hermitian Hamiltonian in Eq. (4.46). In particular, the effect of the environment enters the imaginary part of Eq. (4.46). Here we notice that this limit captures different aspects of the weak measurement-induced dynamics compared to the quantum state diffusion. In the framework of quantum jumps, the latter arise in the limit of infinite measurement events, and hence correspond to an infinite-click dynamics [122].

The dynamics of this non-Hermitian Hamiltonian has been considered previously in Ref. [34], where a subradiant transition has been observed in relationship to a quantum-Zeno effect. Here we study its entanglement properties, namely we evolve the initial density matrix $\rho_0 = |00\ldots0\rangle\langle 00\ldots0|$ according to

$$\rho(t) = \frac{e^{-iH_{\text{eff}}^\dagger t}\rho_0 e^{iH_{\text{eff}}t}}{\text{Tr}\left(\rho_0 e^{iH_{\text{eff}}t}e^{-iH_{\text{eff}}^\dagger t}\right)}, \tag{4.47}$$

where the denominator take into account the term proportional to $\gamma dt\sum_i\langle n_i\rangle_t$ in Eq. (4.45). Then, given a partition $A\cup B$, we construct the reduced density matrix $\rho_A(t) = \text{tr}_B\rho(t)$ which encodes the bipartite entanglement. As stressed before, the non-Hermitian Hamiltonian provide a deterministic protocol, hence the entanglement entropy is deterministic

$$S(t) = -\text{tr}_A\left[\rho_A(t)\ln\rho_A(t)\right]. \tag{4.48}$$

To explore the stationary regime, in order to avoid residual dynamical oscillations, we consider

$$S(\infty) \equiv \lim_{t\to\infty}\frac{1}{t - t_{\text{sat}}}\int_{t_{\text{sat}}}^{t} dsS(s). \tag{4.49}$$

As for the monitoring case we make use of the Jordan-Wigner mapping to write down the non-Hermitian Ising model in Eq. (4.46) in terms of a quadratic fermionic model (see Appendix 4.6.2).

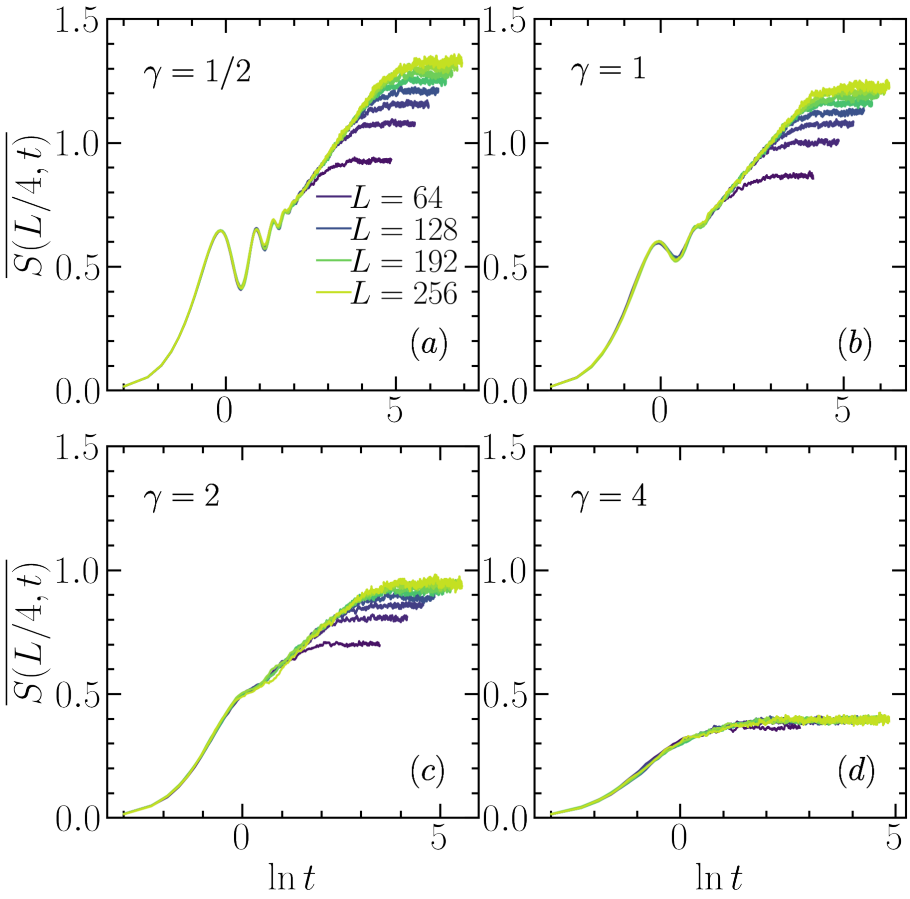

FIGURE 4.17: Dynamics of the entanglement entropy averaged over $N = 2000$ trajectories for different values of the measurement strength γ, different system sizes L and fixing $L_A = L/4$. (a-c) We see a logarithmic growth in time of the entanglement (note the log scale for the time axis) with a saturation to a size-dependent plateau, for $\gamma < 4$ and a much slower growth to a value independent from system size, for $\gamma > 4$.

4.5.2 Results

In this section we present the results of the numerical simulations for the quantum state diffusion and the non-Hermitian Hamiltonian. After discussing the entanglement growth within both paradigms, we compare the entanglement scaling in the stationary state. Finally, we investigate the entanglement statistics of the quantum state diffusion protocol, and relate it to the non-Hermitian results.

Entanglement Growth

We start considering the initial state $|\psi_0\rangle = |00\ldots0\rangle$ and evolve the system according to the QSD protocol defined in Eq. (4.39). This setup is suitable to investigate the entanglement generation in the system, as the initial state has zero entanglement being a product state. (We have checked that our results are robust against a different choice of initial product state.) We make use of the Jordan-Wigner mapping to write the monitored Ising model as a quadratic model of spinless fermions, which can be solved efficiently. (Details on the free fermion techniques, and on the numerical implementation are given in Appendix 4.6.2). For the computation of entanglement, we choose a subsystem A of L_A contiguous sites. The average entanglement evolution is shown in Fig. 4.17. For small to intermediate values of γ (see panels a-c) we find a logarithmic

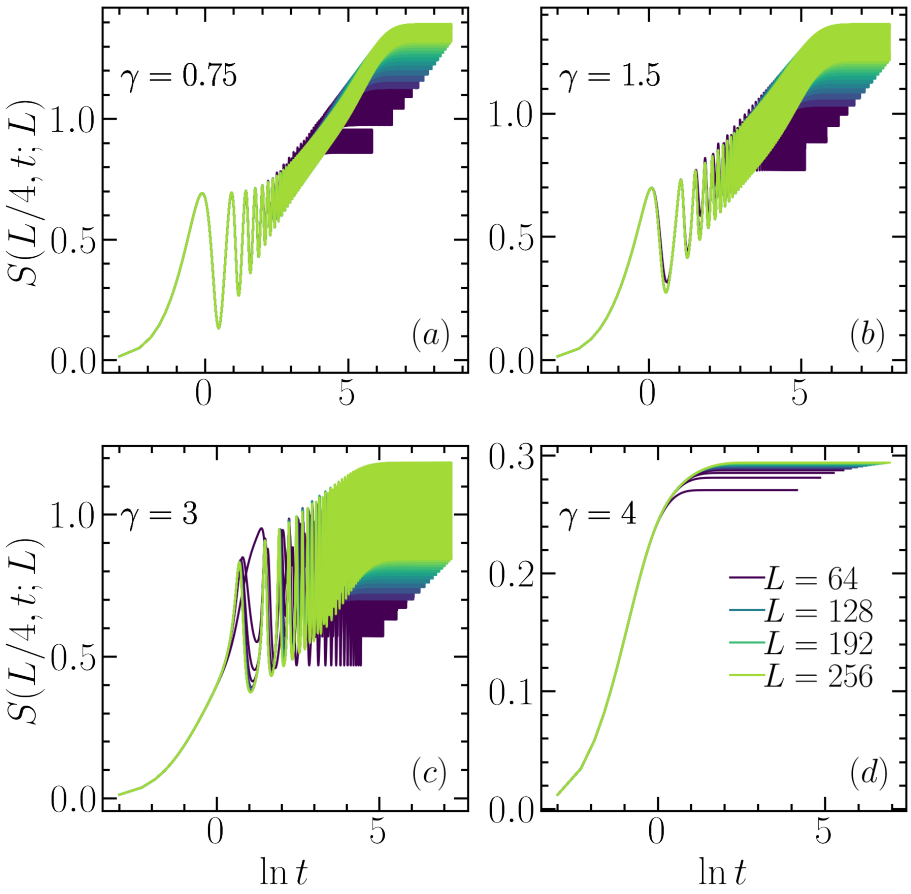

FIGURE 4.18: Entanglement dynamics for the non-Hermitian Hamiltonian for different values of the measurement rate γ and different system sizes. For small γ (panel a) we see a logarithmic growth in time and a saturation to a plateau that depends on system sizes. For large γ (panel b) the entanglement rapidly saturates to a value that does not depend on size. Approaching the transition point we see strong oscillations in the dynamics.

growth in time of the entanglement,

$$\overline{S(t)} \sim \ln t, \tag{4.50}$$

which ultimately saturates at times $t_{\text{sat}} \sim L/\gamma$. It is worth emphasizing that already a small monitoring rate γ is enough to give rise to a non-trivial entanglement dynamics compared to the isolated system oscillation (generated by $H = \sum_i \sigma_i^x \sigma_{i+1}^x$). In other words the interplay between measurements and unitary evolution can increase the entanglement production, at least in a certain region of the parameters, as also noted in Ref. [34]. However, upon further increasing the measurement rate we see a substantial change of the entanglement growth which already for $\gamma = 4$ shows a rapid saturation to a plateau that is almost independent from the size, a trend that continues for larger values of γ.

The results of the entanglement dynamics for the non-Hermitian Ising model (cfr. Eq. (4.48)) are given in Fig. 4.18. For small values of γ (panels a-c), we see that the entropy exhibits an overall logarithmic growth, which resembles the result for the QSD protocol, but has the important difference of exhibiting residual oscillations which dress both the growth and the saturation regimes. Upon further increasing the measuring strength γ the entanglement dynamics in the non-Hermitian case displays a sharp transition towards a regime characterized by a fast approach to a stationary value, with no oscillations. Our numerics locate the boundary between these dynamical regimes around $\gamma \sim 4$, an estimate compatible with what

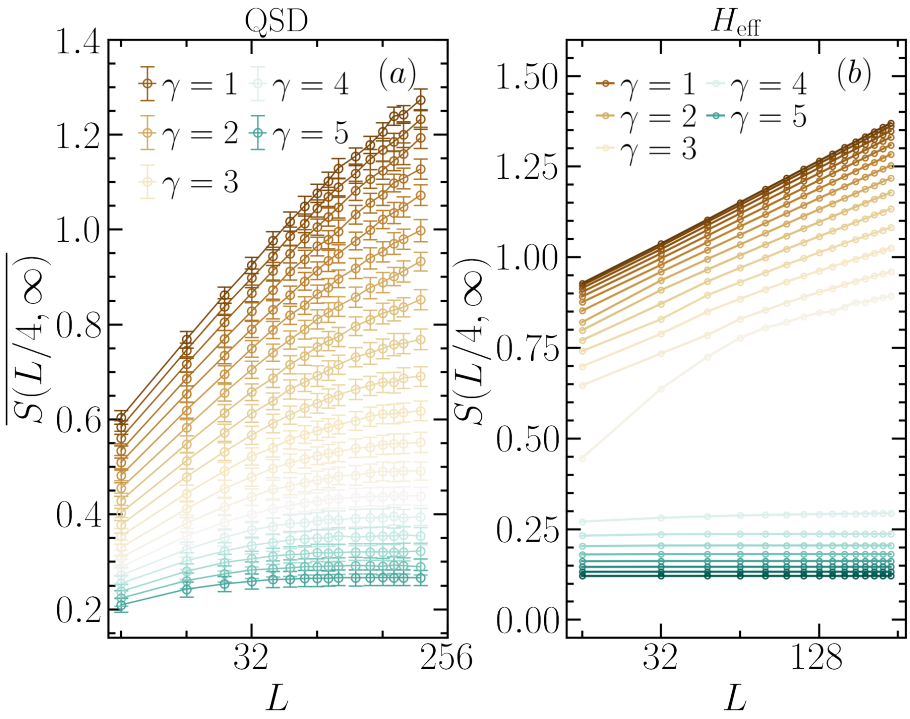

FIGURE 4.19: Stationary-state entanglement entropy as a function of the length of the chain. (a) Average entanglement entropy for the QSD protocol. (b) Long-time entanglement entropy for the non-Hermitian dynamics. In both cases we see a transition from a logarithmic *critical* scaling, for small γ to an area law (constant) scaling at large γ. Different curves in the two panels correspond to increasing values of γ, from $\gamma = 0.25$ (top curve) to $\gamma = 6$ (bottom curve) with a $\Delta\gamma = 0.25$.

found for the QSD protocol. As we will discuss in the next section we can understand the origin of this sharp transition by looking at the spectral properties of the non-Hermitian Hamiltonian.

Entanglement Scaling and Effective Central Charge

As we have seen, at long enough times the entanglement reaches a stationary value in both protocols. We first discuss the scaling of this stationary entanglement with system size. This usually provides key insights on the properties of the system at long-times. To this extent we chose a subsystem of $L_A = L/4$ contiguous spins and plot in Fig. 4.19 the long-time entanglement as a function of L and different values of γ.

For the quantum state diffusion protocol, we can clearly distinguish a regime of logarithmic entanglement growth with system size for small γ, which eventually evolves into a much weaker dependence, an almost constant plateau for large measurement rates (see Fig. 4.19 (a)). As we are going to discuss further below those two regimes are separated by a sharp entanglement transition.

We note that a logarithmic scaling of the average entanglement in an extended region of parameters is a particularly intriguing result which was obtained before in free-fermion models with a continuous $U(1)$ symmetry [32] and more recently in connection with a BKT transition [36, 92]. Here we find this result for a model which only features a discrete Z_2 symmetry and whose ground-state would show logarithmic scaling of the entanglement only at the critical point. This suggests that a different mechanism, not directly related to the microscopic symmetries of the problem, could be behind the origin of this seemingly *critical* phase.

Interestingly, the finite-size scaling of the entanglement entropy for the non-Hermitian Hamiltonian shows a behavior which is qualitatively similar to the QSD protocol, as we show in Fig. 4.19 (b), including a logarithmic scaling for small γ and an area-law (constant) scaling for large measurement rates, separated by

a sharp transition. We also note that the two scaling regimes are connected by a finite-size crossover, absent in the stochastic QSD protocol, whose characteristic scale we found to diverge at the transition (not shown).

For equilibrium quantum critical systems the prefactor of the logarithmic scaling of the entanglement entropy is controlled by the central charge of the associated Conformal Field Theory(CFT) [117], a universal quantity which roughly measures the number of degrees of freedom in the CFT. Following this analogy Ref. [32] introduced an *effective central-charge* for an XX spin-chain under continuous monitoring, which turned out to be a non-universal function of the measurement rate. Here we follow this route and define an effective central charge for both the QSD protocol and the non-Hermitian Hamiltonian by fitting the data in Fig. 4.19 according to the ansatz

$$\begin{aligned} &\text{QSD} && \overline{S} = \frac{1}{3} c_{\text{QSD}}(\gamma) \ln L + a\,, \\ &H_{\text{eff}} && S = \frac{1}{3} c_{H_{\text{eff}}}(\gamma) \ln L + b\,. \end{aligned} \tag{4.51}$$

Here a and b are two system-size independent quantities.

We plot the result in Fig. 4.20 and find that $c(\gamma)$ decreases with γ and, quite remarkably, vanishes for both protocols around the same value of measurement strength $\gamma_c \simeq 4$, that we therefore establish as critical value for the entanglement transitions between logarithmic and area law regimes. Our results are consistent with the unbiased fit on the region $\gamma > 4$, which, for the investigated values, is compatible with zero within errorbar. Despite this similarity we notice that the effective central charge shows a rather different dependence from γ in the QSD and in the non-Hermitian Hamiltonian protocols. In particular, a direct comparison in Fig. 4.20 shows that the effective central charges coincide at small and large values of γ, while deviate in a region before the critical point. Here the non-Hermitian effective central charge turns out to be larger than the one associated to the QSD protocol, a point on which we will come back in the next section.

Before closing this section we note that many of the properties found for the entanglement dynamics of the non-Hermitian Hamiltonian can be naturally understood in terms of the spectral properties of the non-Hermitian Ising model in Eq. (4.46). In fact this can be easily diagonalized once written in fermionic language [34, 123, 124], and takes the form

$$H_{\text{eff}} = \sum_{k>0} \Lambda_k \left(\bar{\eta}_k \eta_k + \eta_{-k} \bar{\eta}_{-k}\right) + E_0, \tag{4.52}$$

where $\bar{\eta}_k, \eta_k$ are fermionic operators obtained from a non-Hermitian Bogolyubov rotation, E_0 is an additive constant fixing the energy zero, and Λ_k are the quasiparticle energies. We note that these are in general complex, as the model lacks any PT symmetry and read

$$\Lambda_k = 2\sqrt{1 - \frac{\gamma^2}{16} + i\frac{\gamma}{2}\cos k} \tag{4.53}$$

The non-Hermitian Ising model features a subradiance transition at a critical value of the measurement rate, given exactly by $\gamma_c = 4$, at which the state with smallest imaginary part changes in a non-analytic way [34]. For small $\gamma < \gamma_c$ the imaginary part of the spectrum in Eq. (4.53) is *gapless* and, consistently, the correlation functions in this phase decay as a power-law [124], a result which is at odds with a model possessing only a discrete symmetry.

From this point of view the logarithmic scaling of the entanglement entropy can be naturally understood, since the entire phase $\gamma < \gamma_c$ has soft-modes with small quasi-degenerate lifetime, which are responsible for the slow growth of the entanglement. On the other hand the real-part of the spectrum is gapped for $\gamma < \gamma_c$, leading to residual oscillations in the entanglement dynamics.

Above the subradiance transition for $\gamma > \gamma_c$ a gap opens up in the imaginary part of the spectrum Λ_k, which is consistent with the fast entanglement dynamics found in this regime. The correlation functions in this phase are expected to decay exponentially over a length diverging as $\gamma \to \gamma_c^+$, a fact that can naturally explain the emergence of a crossover in the finite-size entanglement scaling. We note that in the subradiant

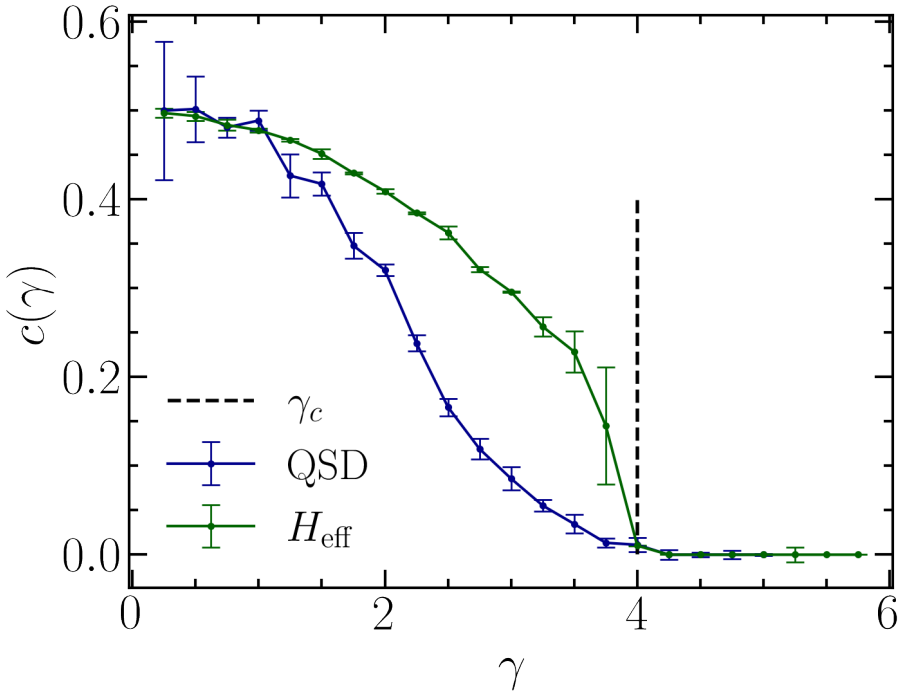

FIGURE 4.20: Effective central charge as a function of the measurement rate γ, for the QSD protocol and the non-Hermitian dynamics. In both cases we find that $c(\gamma)$ decreases monotonously and vanishes around $\gamma_c \simeq 4$, which locates the entanglement transition between logarithmic scaling and area law. Interestingly the two central charges coincide at small and large values of γ, while approaching the critical point we find the non-Hermitian one to be larger, possibly vanishing at γ_c in a non-analytic way.

phase the long-time dynamics is controlled by a pair of states with the smallest non-zero imaginary part. These in the strong measurement limit coincide with the dark states of the measurement operator, which are factorized (uncorrelated) eigenstates of the transverse magnetization, therefore justifying the small, system-size independent entanglement entropy.

We note that the non-Hermitian protocol can be also easily generalised to an Ising model evolving in presence of a real transverse field h, in addition to the imaginary-one due to the measurement rate. In this case we expect, from the analysis of the quasiparticle spectrum, that a spectral and entanglement transition would occurr at a field-dependent rate $\gamma_c(h)$. A complete analysis of the dynamics in this case is however beyond the scope of this work and left for future works.

Finally, the insights on the non-Hermitian Hamiltonian could suggest that an effective field theory description could be possible for $\gamma < \gamma_c$ and that the effective central charge could be computed using field theory replica techniques [125], which however we do not attempt here. We also note that, in this perspective, an effective central charge which depends from a parameter in a non-universal way seems very natural, and in fact several non-unitary field theories have been shown to enjoy this property [48, 126, 127].

Entanglement Statistics

Additional insights are given by the statistical fluctuations of the entanglement in the quantum state diffusion protocol, a feature that goes beyond the simple average so far discussed and that is encoded in the full probability distribution, $P(S_t)$, defined in Eq. (4.44). Concretely, we investigate this distribution at stationarity and evaluate $P(S_\infty) = \lim_{t\to\infty} P(S_t)$.

As we see in Fig. 4.21, the statistics of entanglement shows a rather rich evolution with γ. In particular we see that in the logarithmic phase ($\gamma < \gamma_c$), the statistics changes dramatically, much more than what one

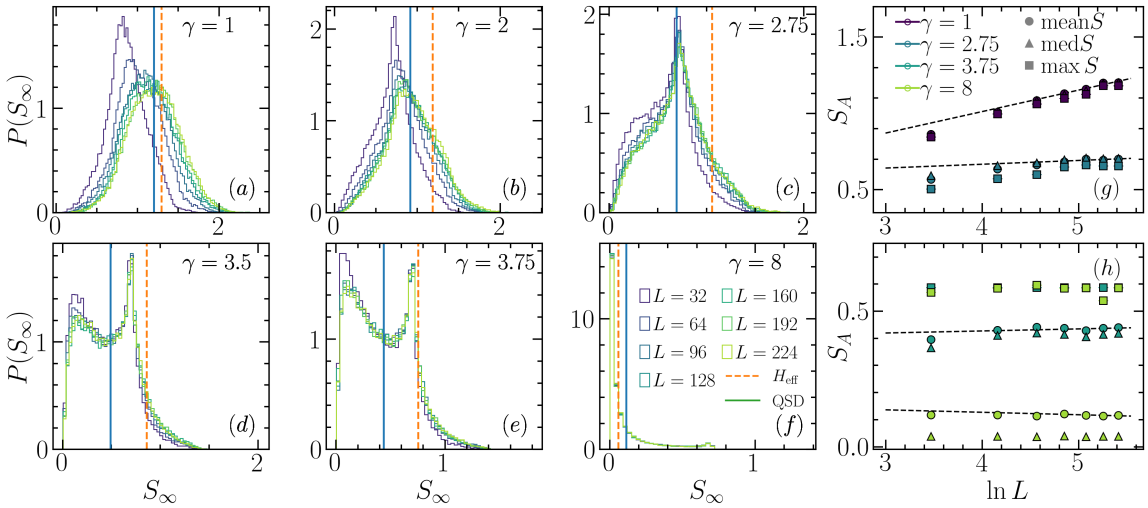

FIGURE 4.21: (a-f) Probability distribution of the entanglement entropy for different values of γ and different system sizes. The realization collected for these functions are $N = 64000$. We see that upon increasing γ, the statistic evolves from a simple Gaussian (panel a-b) to a skewed distribution (panel c-e), with emergent bimodality. At large γ, the distribution is peaked at $S_\infty \simeq 0$ (panel f). The solid line show the average (blue line) over the trajectories for the quantum state diffusion, and the stationary value of the non-Hermitian Hamiltonian (orange line). (g-h) Different statistical estimators $\langle\langle S \rangle\rangle$ versus system size for different values of γ. Note the logarithmic scaling in the L-axis.

could have guessed from the average value, whose dependence from γ can be reabsorded in a renormalization of the central charge. For small values of the measurement rate, $\gamma \lesssim 1$ (panel a), the entanglement distribution is a normal Gaussian which broadens asymmetrically for $\gamma \sim 2$ (panel b) and develops an emergent bimodality as the critical point γ_c is approached (panels c-e). Specifically we see that already for $\gamma = 2.75$ a secondary peak, for lower values of the entanglement, starts to emerge. Upon further increasing γ we see a transfer of weight between the high-entanglement and low-entanglement peaks, with the latter ultimately becoming the dominant one as the system enters the area-law phase. Here, for $\gamma > \gamma_c$ the entanglement distribution is strongly skewed and peaked around small values of the entropy.

It is interesting to discuss the size dependence of the histograms, which is rather different depending on the value of γ. In particular, as we show in Fig. 4.21 (g), where we plot the average, median and typical entanglement for different L and γ, we find that for $\gamma \lesssim 2.5$ all indicators scale logarithmically with L. Instead, Fig. 4.21 (h) shows that approaching the critical point ($\gamma = 3.75$) and above it ($\gamma = 8$) the statistical estimators deviate from each others, a signature of the non-gaussianity of the entanglement distribution. In the area-law phase for $\gamma > \gamma_c$ the scaling of all the statistical proxies considered becomes independent on the system size.

The emergence of bimodality in the entanglement statistics is an interesting result, which suggests that within the log-phase the entanglement is not a self-averaging quantity, and that limiting the discussion to the average value could hide important features of the problem. A similar result was found in the monitored XX model under QSD protocol [32] and, in Ref. [34] for the statistics of the return probability and the local transverse magnetization under a quantum jump stochastic protocol. In this latter case it was shown that the non-Hermitian Hamiltonian captured a secondary peak in the distribution of the relevant observables.

It is therefore interesting to compare the statistical properties of the entanglement in the QSD protocol with the non-Hermitian Hamiltonian. This comparison is proposed in Fig. 4.21, where we indicate with a dashed line the long-time entanglement in the non-Hermitian case and with a blue line the average entanglement of the QSD protocol. We see that indeed the non-Hermitian Hamiltonian provides a good proxy for the average entanglement both for small γ, when entanglement fluctuations are gaussian, as well as for large γ when the statistics is dominated by small values of the entanglement entropy. For intermediate values of γ instead, when the statistics becomes strongly bimodal and fluctuations due to the noise are more relevant,

the entanglement content of the non-Hermitian Hamiltonian is systematically larger than the average, reflecting the atypical nature of the no-click process. This is not surprising in retrospect, as the QSD protocol contains randomness which is expected to decrease the entanglement content of the system as opposed to the translational-invariant non-Hermitian protocol. We note also that in addition to the leading scaling behavior of the entanglement, captured by the effective central charge, there is also a non-universal correction to the entanglement that depends in principle on γ and could play a role in the precise comparison between the two protocols.

4.5.3 Conclusion

In this Section we have discussed measurement-induced criticality in a Quantum Ising chain coupled to a monitoring environment. We have focused on two different limits of the measurement problem, corresponding respectively to the quantum state diffusion protocol and the no-click dynamics, the latter described by a non-Hermitian Ising model.

In both cases we found a sharp phase transition in the entanglement properties of the system, as a function of the measurement rate γ. The entanglement dynamics out of an initial product state evolves from a slow logarithmic growth at small measurement rates to a fast approach to a stationary value at large γ. The stationary state entanglement shows a *critical* logarithmic scaling with respect to system size, with an effective central charge which changes continuously with γ and vanishes at a critical strength γ_c, indicating a transition towards an area-law scaling which we found numerically to coincide in the two protocols. The existence of an extended critical phase with logarithmic scaling of the average entanglement is particularly surprising for our Ising model which, differently from others stochastic measurement problems considered recently in the literature, lacks a continuous symmetry usually associated with gapless critical behavior. The no-click limit and associated non-Hermitian evolution provides a natural mechanism for this phenomenology, in terms of a spectral (subradiant) phase transition from a critical phase with gapless decay modes at small measurements to a gapped area-law phase. We also find important differences between the two protocols, in particular in the behavior of the effective central charge as a function of the measurement strength which turns out to be larger in the non-Hermitian case. This effect, which seems to suggest different universality classes depending on the specific measurement ensemble, can be understood in terms of a disentangling effect of the noise.

4.6 Appendix

4.6.1 Continuous measurements and stochastic Schrödinger equations

This section is an overview of stochastic quantum dynamics in the Hilbert space (see Ref. [95, 122, 128, 129] for general review). We first introduce the positive-operator value measurements (POVM), which arise naturally when system and environment interact for a finite time. In the limit of weak measurement, the system evolve through a stochastic Schrödinger equation, the details of which depend on the environment specifics. We consider two possible choices of system-environment setups which naturally translate, respectively, in the quantum state diffusion Eq. (4.39) and in the quantum jump equation Eq. (4.45). From the latter, the non-Hermitian quantum Hamiltonian Eq. (4.46) is obtained through post-selection. These equations correspond to different unravelling of the same master equation, highlighting the independence of the mean state Eq. (4.40) from the stochastic protocols.

Weak measurements and quantum trajectories

Measurement lies at the core of quantum mechanics. Given a state $|\psi\rangle$, and an observable O, the von Neumann postulate states that, when a measurement takes place, the wavefunction collapses in the eigenvector $|n\rangle$ of O corresponding to the measurement outcome o_n. This can be seen as the transformation

$$|\psi\rangle \mapsto |\psi'\rangle = \frac{P_n|\psi\rangle}{||P_n|\psi\rangle||}. \tag{4.54}$$

Here $P_n = |n\rangle\langle n|$ is the projector to the eigenspace of o_n (the observable is resolved as $O = \sum_n o_n P_n$), and $p_n \equiv \langle\psi|P_n|\psi\rangle$ is the measurement probability.

These projective measurements are an idealization: they are implicitly instantaneous, and they collapse a pure state into a pure state. In contrast, real world experiments are imperfect: they require a finite time of interaction with the system, and in general the outcome state is mixed. Positive operator-value measurements represent a generalization of projective measurements, which are suitable to treat situations where the interaction time between system and ancilla is comparable to the energy-scale of the system.

Given a set of positive operators E_n which sum to the identity $\sum_n E_n = 1$, it is possible to define the probabilities $p_n = \mathrm{tr}(\rho E_n)$. Differently from the projective case, these operators are not orthogonal, hence the knowledge of E_n does not fix the state after the measurement. It is necessary to know a set of operators $A_{n,k}$ such that $E_n = \sum_k A_{nk}^\dagger A_{nk}$ (dubbed Kraus operators). Then, the state after the measurement outcome corresponding to E_n is

$$\rho \mapsto \rho' = \frac{\sum_k A_{nk}\rho A_{nk}^\dagger}{\mathrm{tr}(\rho E_n)}. \tag{4.55}$$

It is clear that in general, given a pure density matrix ρ, the outcome measurement in Eq. (4.55) is mixed. The condition to preserve purity is that $E_n = A_n^\dagger A_n$, *i.e.*, there is only one Kraus operator per measurement. In this case Eq. (4.55) can be recast in a wave-function perspective

$$|\psi\rangle \mapsto |\psi'\rangle = \frac{A_n|\psi\rangle}{\sqrt{\langle\psi|E_n|\psi\rangle}}. \tag{4.56}$$

POVM can be implemented by allowing the system to interact with an ancilla for a finite time, and apply afterward a projective measurement to the ancilla. The limit when this interaction is small is the weak measurement, when typically the state of the system is mildly perturbed.

As an example, we consider the toy model of a two-level system $|\psi\rangle = \sum_{n=0,1} c_n^S |n\rangle_S$ which interacts with a two-level ancilla initialized in a state $|a\rangle = \sum_{k=0,1} c_k^A |k\rangle_A$. If their interaction is infinitesimal, the

unitary evolution of the combined system initialized in $|\Psi\rangle = |\psi\rangle \otimes |a\rangle$ is given by

$$U(\epsilon) = \exp\left[-i\epsilon \sum_j O_j^S \otimes O_j^A\right]. \tag{4.57}$$

After the unitary transformation, entanglement is generated, and the state up to first order in ϵ is given by

$$\begin{aligned} |\Psi'\rangle(\epsilon) &= \sum_{m,n} (c_n^S c_m^A - i\epsilon c_{nm}^{\text{ent}})|n\rangle_S \otimes |m\rangle_A \\ c_{nm}^{\text{ent}} &= \sum_j \sum_{n',m'=0,1} O_{j,n',n}^S O_{j,m',m}^A c_{n'}^S c_{m'}^A \\ O_{j,k,k'}^{\mu} &\equiv \langle k|O^{\mu}|k'\rangle_{\mu}, \quad \mu = S, A. \end{aligned} \tag{4.58}$$

Rearranging the above equation, the system is given by

$$|\Psi'\rangle(\epsilon) = \alpha(\epsilon)|\phi_0\rangle_S \otimes |0\rangle_A + \beta(\epsilon)|\phi_1\rangle_S \otimes |1\rangle_A, \tag{4.59}$$

where the constants α, β and ϕ_k are read out matching Eq. (4.58) and Eq. (4.59). If a measurement is now performed on the ancilla along the z-direction, one obtains

$$|\psi\rangle = \begin{cases} |\phi_0\rangle, & \text{with probability} \quad p_0 = |\alpha(\epsilon)|^2, \\ |\phi_1\rangle, & \text{with probability} \quad p_1 = |\beta(\epsilon)|^2. \end{cases} \tag{4.60}$$

Hence, POVM can be implemented by carefully designing the system-ancilla interaction, the ancilla initial state, and the projective measurement on the ancilla. To conclude, let us notice that, in the case of two-level ancilla, the Kraus operator are one for each measurement type. Hence, the measurements are generated by $E_k = A_k^\dagger A_k$ $k = 0, 1$. This is a convenient, but not unique, setting to guarantee the purity-preservation of the state. Furthermore, as stressed, the precise form of the operators A_k depends on the microphysics of system and ancilla. As we shall see, to derive a stochastic Schrödinger equation it is usually necessary to expand up to second order in the parameter ϵ. (Nonetheless, the above argument is still valid.) In the following we shall assume that the Kraus operators (and hence the POVM) are given by the problem, thus simplifying the discussion.

Quantum state diffusion

We consider the following Kraus operators

$$A_0 = \sqrt{\frac{1}{2}}|0\rangle\langle 0| + \sqrt{\frac{1}{2} - \epsilon}|1\rangle\langle 1| \tag{4.61}$$

$$A_1 = \sqrt{\frac{1}{2}}|0\rangle\langle 0| + \sqrt{\frac{1}{2} + \epsilon}|1\rangle\langle 1|. \tag{4.62}$$

Starting from the state $|\psi\rangle = \alpha|0\rangle + \beta|1\rangle$, after the measurement the state is in one of the following two states

$$|\phi_0\rangle = \frac{A_0|\psi\rangle}{\sqrt{p_0}} = \alpha\left(|\beta|^2\epsilon + \frac{3}{2}|\beta|^4\epsilon^2\right)|0\rangle + \beta\left(\epsilon(1-|\beta|^2) + \frac{\epsilon^2}{2}(-1-2|\beta|^2+3|\beta|^4)\right)|1\rangle \tag{4.63}$$

$$|\phi_1\rangle = \frac{A_1|\psi\rangle}{\sqrt{p_1}} = \alpha\left(-|\beta|^2\epsilon + \frac{3}{2}|\beta|^4\epsilon^2\right)|0\rangle + \beta\left(-\epsilon(1-|\beta|^2) + \frac{\epsilon^2}{2}(-1-2|\beta|^2+3|\beta|^4)\right)|1\rangle, \tag{4.64}$$

with probability respectively $p_0 = 1/2 - |\beta|^2\epsilon$ and $p_1 = 1/2 + |\beta|^2\epsilon$. The above post-measurement state can be collected into a compact differential form, by introducing the random binomial variable $dW = \mp\epsilon$, and the operator $n = |1\rangle\langle 1|$. We have

$$d|\psi\rangle = |\psi'\rangle - |\psi\rangle = 2\epsilon^2(\langle n\rangle^2 - 2\langle n\rangle n)|\psi\rangle + dW(n-\langle n\rangle)|\psi\rangle - \frac{\epsilon^2}{2}(n-\langle n\rangle)^2|\psi\rangle, \tag{4.65}$$

where $\langle\circ\rangle = \langle\psi|\circ|\psi\rangle$ is the state average. The expression can be simplified by centering the random variable $dW \mapsto d\xi = dW - \overline{dW}$, since the average $\overline{dW} = 2\beta^2\epsilon^2 = 2\langle L\rangle\epsilon^2$ due to the $\mathcal{O}(\epsilon)$ unbalance in the outcome probability. The variance is preserved at leading order $d\xi^2 = \epsilon = dW^2$, and the equation reads

$$d|\psi\rangle = d\xi(n-\langle n\rangle)|\psi\rangle - \frac{\epsilon^2}{2}(n-\langle n\rangle)^2|\psi\rangle. \tag{4.66}$$

Eq. (4.66) gives one interaction with a single ancilla qubit. In order to derive a stochastic Schrödinger equation we subsequently couple a series of identically prepared ancillas with the same paradigm. Hence, Eq. (4.66) is iterated multiple time. Taking the scaling limit, with infinitesimal time step we have

$$\frac{d|\psi(\xi_t)\rangle}{dt} = \frac{d\xi_t}{dt}(n-\langle n\rangle_t)|\psi(\xi_t)\rangle - \frac{\epsilon^2}{2dt}(n-\langle n\rangle_t)^2|\psi(\xi_t)\rangle. \tag{4.67}$$

Fixing the scaling $\epsilon^2 = \gamma dt$ reduce this equation to

$$d|\psi(\xi_t)\rangle = d\xi_t(n-\langle n\rangle_t)|\psi(\xi_t)\rangle - \frac{\gamma}{2}dt(n-\langle n\rangle_t)^2|\psi(\xi_t)\rangle. \tag{4.68}$$

This is the quantum state diffusion equation for a two-level qubit.

Let us make some final comments. (i) The scaling $\epsilon = \sqrt{\gamma dt}$ is typical when dealing with Kraus operators (for instance, see Ref. [6, 95, 122] for an indepth discussion). This is due to a Markovian approximation, which is assumed to hold for the systems of interest. (ii) The generalization to multiple qubits is trivial. Recovering the noise terms in Eq. (4.39) require the introduction of L uncorrelated Îto terms $d\xi_i$ with $\overline{d\xi} = 0$ and $d\xi_i d\xi_j = \gamma dt\delta_{ij}$. (iii) For the time evolution in the limit $dt \to 0$, the binomial variable can be approximated by a Gaussian increment, in the same spirit as obtaining a Wiener process from a random walk.

Quantum jumps and non-Hermitian Hamiltonian

We consider the following Kraus operators

$$A_0 = |0\rangle\langle 0| + \cos\epsilon|1\rangle\langle 1| \tag{4.69}$$
$$A_1 = \sin\epsilon|1\rangle\langle 1|. \tag{4.70}$$

In this situation, given the state $|\psi\rangle = \alpha|0\rangle + \beta|1\rangle$, the measurements E_0 and E_1 are unbalanced, with probability $p_0 = 1 - |\beta|^2\epsilon^2$ and $p_1 = |\beta|^2\epsilon^2$, respectively. As in the previous section, we introduce the operator $n = |1\rangle\langle 1|$. The state after the measurement is in either of the following states

$$\begin{aligned} |\phi_0\rangle &= |\psi\rangle + \frac{1}{2}\alpha\langle n\rangle\epsilon^2|0\rangle + \frac{1}{2}\beta(\langle n\rangle - 1)\epsilon^2|1\rangle \\ &= |\psi\rangle - \frac{1}{2}\left(n - \langle n\rangle\right)\epsilon^2|\psi \end{aligned} \tag{4.71}$$
$$|\phi_1\rangle = |1\rangle. \tag{4.72}$$

In differential form, we have

$$d|\psi\rangle = -\frac{1}{2}\left(n - \langle n\rangle\right)\epsilon^2|\psi\rangle + \left(\frac{n}{\sqrt{\langle n\rangle}} - 1\right)\delta N|\psi\rangle. \tag{4.73}$$

Here δN is a Poisson process: $\delta N = 0(1)$ with probability $p_0(p_1)$. Since $\overline{\delta N} = |\beta|^2\epsilon^2$, the state is unlikely to experience a measurement and usually is affected only by the Kraus operator A_0. However, when $\delta N = 1$, the second term in Eq. (4.73) dominate the infinitesimal one, and project the state onto $|1\rangle$. Notice that in this case $\delta N^2 = \delta N$.

Suppose that the system interacts with n ancilla qubits. As previously discussed, the stochastic Schrödinger equation is given once the scaling $\epsilon^2 = \gamma dt$ is set

$$\begin{aligned} d|\psi(N_t)\rangle = &-\frac{1}{2}\left(n - \langle n\rangle_t\right)\gamma dt|\psi(N_t)\rangle \\ &+ \left(\frac{n}{\sqrt{\langle n\rangle_t}} - 1\right)\delta N_t|\psi(N_t)\rangle. \end{aligned} \tag{4.74}$$

This is the so-called quantum jump equation. The first term is a non-Hermitian Hamiltonian, while the second term is the quantum jump. When the event happens, the state is projected to $|1\rangle\langle 1|$. It is interesting to ask how much is the probability that the state does never jump? The probability of this no-click dynamics for one-qubit is given by

$$P_{\text{no-click}} = \Pi_{n=0}^{\infty} p_0 \simeq |\alpha|^2. \tag{4.75}$$

Thus, the number of trajectories with no-jump effect is substantial.

We conclude with few remarks. (i) The generalization to many-body is trivial, once L uncorrelated variables are included, and the Hamiltonian H of the system is added. The final equation for the quantum jumps is Eq. (4.45). The non-Hermitian Hamiltonian in Eq. (4.46) is recasted when post-selecting the trajectories without jumps. Notice that the contribution $\propto \gamma dt\sum_i\langle n_i\rangle_t$ factorize as an overall rescaling of the wavefunction, and cancels out in the average. (ii) In the situation of a spin-chain, the probability of no-click dynamics (hence non-Hermitian generated dynamics) depends on the system size. In practice, one chooses among all the trajectories the portion where no jump has occurred. This post-selection process is key in investigating non-Hermitian physics in experimental setups. (ii) Both the quantum jump and the quantum state diffusion equations induce the same Lindblad evolution Eq. (4.41) for the mean state. This difference highlights how quantum trajectories contain substantial more information than the average state. Importantly, the non-Hermitian Hamiltonian coincide with the non-coherent term of the Lindblad

equation (4.41).

4.6.2 Free fermion techniques and numerical implementation

In this section we present a summary of the simulation techniques used in Sec. 4.5. (For a general reference on the ideas used here, see Ref. [130]). These methods are based on the fermionic representation of the Ising model, which can be applied also to Eq. (4.39) (Eq. (4.46)), as the noise (non-Hermitian) term preserve the quadratic structure. We first review the Jordan-Wigner transformation, and explain how the time-evolution reads in fermionic variables. Due to the Gaussian preservation of both quantum state diffusion and non-Hermitian Hamiltonian, the state is fully characterized by its two point function. Afterwards, we show how the entanglement entropy is derived from the correlation matrix. Finally, we give some detail of the numerical implementation.

Jordan-Wigner mapping

The Jordan-Wigner transformation is defined by

$$\sigma_i^x = K_i(c_i + c_i^\dagger), \quad K_i = \prod_{j<i}(2n_i - 1) \tag{4.76}$$

$$n_i = c_i^\dagger c_i. \tag{4.77}$$

Here, the string operator K_i ensure the fermionic algebra. For the quantum state diffusion Eq. (4.39), the dynamics maps to

$$\begin{aligned} d|\psi(\vec{\xi}_t)\rangle = &-i\sum_{i=1}^{L-1}(c_i^\dagger c_{i+1} + c_i^\dagger c_{i+1}^\dagger + \text{h.c.})dt|\psi(\vec{\xi}_t)\rangle \\ &+ \sum_{i=1}^{L}(n_i - \langle n_i\rangle_t)d\xi_t^i|\psi(\vec{\xi}_t)\rangle \\ &- \frac{\gamma}{2}dt\sum_{i=1}^{L}(n_i - \langle n_i\rangle_t)^2|\psi(\vec{\xi}_t)\rangle. \end{aligned} \tag{4.78}$$

Instead for the non-Hermitian Hamiltonian Eq. (4.46), we have

$$\begin{aligned} d|\psi\rangle = &-i\sum_{i=1}^{L-1}(c_i^\dagger c_{i+1} + c_i^\dagger c_{i+1}^\dagger + \text{h.c.})dt|\psi\rangle \\ &- \frac{\gamma}{2}dt\sum_{i=1}^{L} n_i|\psi\rangle. \end{aligned} \tag{4.79}$$

Within this formalism, if the initial state of the system is Gaussian, then the state is Gaussian at each time step. In particular, all the observables are encoded in the correlation matrix

$$G_{ij} = \begin{pmatrix} \langle c_i^\dagger c_j\rangle & \langle c_i^\dagger c_j^\dagger\rangle \\ \langle c_i c_j\rangle & \langle c_i c_j^\dagger\rangle. \end{pmatrix} \tag{4.80}$$

In the next subsection, we show how the dynamics can be reduced to the time-evolution of a $2L \times 2L$ matrix.

Dynamics in the fermionic formalism

The equation of motion for both the protocol can be written as $d|\psi(\vec{\xi}_t)\rangle = dZ_t|\psi(\vec{\xi}_t)\rangle$, where dZ_t is quadratic in the creation/destruction fields. For the quantum state diffusion

$$dZ_t = dt\left(-iH - \frac{\gamma}{2}\sum_i (n_i - \langle n_i\rangle_t)^2\right) + \sum_i d\xi_t^i (n_i - \langle n_i\rangle_t), \tag{4.81}$$

while for the non-Hermitian Hamiltonian we have

$$dZ_t = dt\left(-iH - \frac{\gamma}{2}\sum_i n_i\right) = -idtH_{\text{eff}}. \tag{4.82}$$

Both these instances can be treated on the same foot, once the operator dZ_t is specified. From the operator dZ_t, it is possible to write down an equation of motion for the correlation matrix Eq. (4.80). (This is obtained by taking the differential of Eq. (4.80), simplifying the fermionic algebra, and expanding up to order $\mathcal{O}(dt)$).

However, in practical implementation, this method is not the most efficient. A better strategy, which we follow here, is the route pioneered in Ref. [31]. Since the system is Gaussian, for any t, there exist a unitary matrix

$$\mathcal{U}_t = \begin{pmatrix} U_t & V_t^\dagger \\ V_t & U_t^\dagger, \end{pmatrix} \tag{4.83}$$

such that

$$|\psi\rangle_t = \frac{1}{\sqrt{|\det U_t|}} \exp\left(-\frac{1}{2}\sum_{i,j,k}(U_t)_{i,k}(V_t^\dagger)_{k,j}c_i^\dagger c_j^\dagger\right)|0\rangle. \tag{4.84}$$

This condition is equivalent to finding a unitary transformation that maps the original fermionic fields $(c_i, c_j^\dagger)$ to a new set $(\chi_i, \chi_j^\dagger)$ such that $\chi_i|\psi\rangle_t = 0$ for all i. Explicitly, labelling a vector of fermionic field as $\mathbf{c} = (c_1, c_2, \ldots, c_L)$,

$$\begin{pmatrix} \chi \\ \chi^\dagger \end{pmatrix} = \mathcal{U}_t \begin{pmatrix} \mathbf{c} \\ \mathbf{c}^\dagger. \end{pmatrix} \tag{4.85}$$

From the definition of the correlation matrix and Eq. (4.84), and after few manipulation in fermionic algebra, we have the relationship

$$G(t) = \mathcal{U}_t \begin{pmatrix} \mathbf{1}_{L\times L} & \mathbf{0}_{L\times L} \\ \mathbf{0}_{L\times L} & \mathbf{0}_{L\times L} \end{pmatrix} \mathcal{U}_t^\dagger. \tag{4.86}$$

Hence, the full evolution is encoded in $\mathcal{U}_t$. The equation of motion for this object are easily derived from Eq. (4.85) and using the annihilation condition $\chi_i|\psi\rangle_t = 0$. In practice it can be implemented into two steps. (i) Integrate the Heisenberg equation of motion between t and $t + dt$ (with initial condition $\mathcal{U}_{t=0} = \mathcal{U}_0$ given)

$$d\mathcal{U}_t = 2d\mathcal{Z}_t\mathcal{U}_t. \tag{4.87}$$

(ii) Apply a renormalization to guarantee that U_{t+dt} is unitary (for instance a QR decomposition). This guarantees that $|\psi\rangle_{t+dt}$ is in the form Eq. (4.84) with the operators given in U_{t+dt}. For concrete details on the numerical implementation, see Sec. 4.6.2.

Majorana fermions and entanglement entropy

For a Gaussian state, Wick's theorem reduce the computation of entanglement from diagonalizing a $2^L \times 2^L$ matrix to a $2L \times 2L$ linear problem. For this goals, it is convenient to introduce two species of Majorana fermions

$$a_{j,1} = c_j + c_j^\dagger, \qquad a_{j,2} = i(c_j^\dagger - c_j). \tag{4.88}$$

Then the matrix

$$V = \begin{pmatrix} \mathbf{1}_{L\times L} & \mathbf{1}_{L\times L} \\ -i\mathbf{1}_{L\times L} & i\mathbf{1}_{L\times L} \end{pmatrix}, \tag{4.89}$$

transforms the correlation function from Dirac fermions to Majorana $W = VGV^\dagger$. Due to the Majorana algebra $\{a_{i,p}, a_{j,q}\} = \delta_{i,j}\delta_{p,q}$, the Majorana correlation can be decomposed into $W = \mathbf{1} + i\tilde{W}$. The matrix $\tilde{W}$ is real and anti-symmetric, and is the key actor in computing any observable. In particular, entanglement entropy on a bipartition $A \cup B$ is obtained by diagonalizing $\tilde{W}|_{A(B)}$, that is restricting the indices of the Majorana fermions within either partition. If the eigenvalues of $\tilde{W}|_A$ are λ_k, then the entanglement entropy is given by

$$S = -\sum_k \left(\frac{1+\lambda_k}{2} \ln \frac{1+\lambda_k}{2} + \frac{1-\lambda_k}{2} \ln \frac{1-\lambda_k}{2} \right). \tag{4.90}$$

Numerical implementation

The numerical implementation can be adapted to the protocol considered. For the quantum state diffusion, it is practical to divide the unitary step from the noise term $d\mathcal{Z}_t = -i\mathcal{H}dt + dT$. The Hamiltonian H can be stored and exponentiated only once, while the noise term dT is diagonal, with elements $dT_{ij} = \delta_{ij}(d\xi^i + \gamma dt(2\langle n_i\rangle - 1))/2$ that needs to be computed repeatedly at each time step.

The resulting evolution then is

$$\tilde{\mathcal{U}}_{t+dt} = \mathcal{N} e^{2dT} e^{2i\mathcal{H}dt} \mathcal{U}_t, \tag{4.91}$$

where we have neglected higher order terms $\mathcal{O}(d\xi dt)$ (Trotter approximation). The normalization $\mathcal{N}$ is unimportant, as Eq. (4.91) is followed by a QR decomposition $\tilde{\mathcal{U}}_{t+dt} = \mathcal{Q}_{t+dt}\mathcal{R}_{t+dt}$, and by setting $\mathcal{U}_{t+dt} = \mathcal{Q}_{t+dt}$. As previously discussed, this condition guarantees the state is in the form Eq. (4.84) and the correlation function is obtained through Eq. (4.86).

For the non-Hermitian quantum evolution, it is sufficient to exponentiate once the operator $d\mathcal{Z}_t = -i\mathcal{H}_{\text{eff}}dt$ and apply it subsequently to generate the evolution

$$\tilde{\mathcal{U}}_{t+dt} = \mathcal{N} e^{2i\mathcal{H}_{\text{eff}}dt} \mathcal{U}_t. \tag{4.92}$$

After each time step, the QR decomposition is implemented to normalize the state. In both situations, the entanglement entropy is computed as described in Sec. 4.6.2.

Bibliography

[1] Xhek Turkeshi, Rosario Fazio, and Marcello Dalmonte. Measurement-induced criticality in (2+1) -dimensional hybrid quantum circuits. *Physical Review B*, 102(1):014315, Jul 2020.

[2] Xhek Turkeshi. Measurement-induced criticality as a data-structure transition. 2021.

[3] Xhek Turkeshi, Alberto Biella, Rosario Fazio, Marcello Dalmonte, and Marco Schiro. Measurement-induced entanglement transitions in the quantum ising chain: From infinite to zero clicks. 2021.

[4] A. Polkovnikov, K. Sengupta, A. Silva, and M. Vengalattore. colloquium*: nonequilibrium dynamics of closed interacting quantum systems*. *Rev. Mod. Phys.* ***83****, 863 (2011).*

[5] L. D'Alessio, Y. Kafri, A. Polkovnikov, and M. Rigol. *From quantum chaos and eigenstate thermalization to statistical mechanics and thermodynamics*. *Advances in Physics* ***65****, 239 (2016).*

[6] H. P. Breuer, and F. Petruccione. *The theory of open quantum systems*. *Oxford University Press, Oxford (2002).*

[7] R. Nandkishore, and D. A. Huse. *Many-body localization and thermalization in quantum statistical mechanics*. *Annu. Rev. Condens. Matter Phys.* ***6****, 15 (2015).*

[8] D. Abanin, E. Altman, I. Bloch, and M. Serbyn. *Colloquium: Many-body localization, thermalization, and entanglement*. *Rev. Mod. Phys.* ***91****, 021001 (2019).*

[9] C. W. Gardiner, and P. Zoller. *Quantum noise*. *Springer-Verlag Berlin Heidelberg, Berlin (2000).*

[10] Y. Li, X. Chen, and M. P. A. Fisher. *Quantum Zeno effect and the many-body entanglement transition*. *Phys. Rev. B* ***98****, 205136 (2018).*

[11] Y. Li, X. Chen, and M. P. A. Fisher. *Measurement-driven entanglement transition in hybrid quantum circuits*. *Phys. Rev. B* ***100****, 134306 (2019).*

[12] B. Skinner, J. Ruhman, and A. Nahum. *Measurement-induced phase transitions in the dynamics of entanglement*. *Phys. Rev. X* ***9****, 031009 (2019).*

[13] A. Chan, R. M. Nandkishore, M. Pretko, and G. Smith. *Unitary-projective entanglement dynamics*. *Phys. Rev. B* ***99****, 224307 (2019).*

[14] A. Nahum, S. Roy, B. Skinner, and J. Ruhman. *Measurement and entanglement phase transitions in all-to-all quantum circuits, on quantum trees, and in Landau-Ginsburg theory*. *arXiv: 2009.11311.*

[15] Shao-Kai Jian, Zhi-Cheng Yang, Zhen Bi, and Xiao Chen. Yang-lee edge singularity triggered entanglement transition. 2021.

[16] O. Shtanko, Y. A. Kharkov, L. P. García-Pintos, and A. V. Gorshkov. *Classical Models of Entanglement in Monitored Random Circuits*. *arXiv: 2004.06736 (2020).*

[17] M. J. Gullans, and D. A. Huse. *Scalable Probes of Measurement-Induced Criticality*. *Phys. Rev. Lett.* ***125****, 070606 (2020).*

[18] M. J. Gullans, and D. A. Huse. *Dynamical Purification Phase Transition Induced by Quantum Measurements*. *Phys. Rev. X* ***10****, 041020 (2020).*

[19] A. Zabalo, M. J. Gullans, J. H. Wilson, S. Gopalakrishnan, D. A. Huse, and J. H. Pixley. *Critical properties of the measurement-induced transition in random quantum circuits*. *Phys. Rev. B* ***101****, 060301 (2020).*

[20] M. Szyniszewski, A. Romito, and H. Schomerus. *Entanglement transition from variable-strength weak measurements*. *Phys. Rev. B* ***100****, 064204 (2019).*

[21] K. Snizhko, P. Kumar, and A. Romito. *Quantum Zeno effect appears in stages*. *Phys. Rev. Research* ***2****, 033512* .

[22] C.-M. Jian, B. Bauer, A. Keselman, and A. W. W. Ludwig. *Criticality and entanglement in non-unitary quantum circuits and tensor networks of non-interacting fermions*. *arXiv:2012.04666.*

[23] S. Sang, Y. Li, T. Zhou, X. Chen, T. H. Hsieh, and M. P. A. Fisher. *Entanglement Negativity at Measurement-Induced Criticality*. *arXiv:2012.00031.*

[24] B. Shi, X. Dai, and Y.-M. Lu. *Entanglement negativity at the critical point of measurement-driven transition*. *arXiv:2012.00040.*

[25] Matteo Ippoliti and Vedika Khemani. Postselection-free entanglement dynamics via spacetime duality. *Phys. Rev. Lett.*, 126:060501, Feb 2021.

[26] Y. Fuji, and Y. Ashida. *Measurement-induced quantum criticality under continuous monitoring*. *arXiv: 2004.11957 (2020).*

[27] D. Rossini, and E. Vicari. *Measurement-induced dynamics of many-body systems at quantum criticality*. *arXiv: 2001.11501 (2020).*

[28] O. Lunt, and A. Pal. *Measurement-induced entanglement transitions in many-body localized systems*. *arXiv: 2005.13603 (2020).*

[29] S. Goto, and I. Danshita. *Measurement-Induced Transitions of the Entanglement Scaling Law in Ultracold Gases with Controllable Dissipation*. *arXiv: 2001.03400 (2020).*

[30] Qicheng Tang and W. Zhu. Measurement-induced phase transition: A case study in the nonintegrable model by density-matrix renormalization group calculations. *Phys. Rev. Research*, 2:013022, Jan 2020.

[31] X. Cao, A. Tilloy, and A. De Luca. *Entanglement in a fermion chain under continuous monitoring*. *SciPost Phys.* ***7****, 024 (2019).*

[32] O. Alberton, M. Buchhold, and S. Diehl. Entanglement transition in a monitored free-fermion chain: From extended criticality to area law. *Phys. Rev. Lett.*, 126:170602, Apr 2021.

[33] Q. Tang, X. Chen, and W. Zhu. *Quantum criticality in non-unitary dynamics of 2+1d free fermions*. *arXiv:2101.04320.*

[34] A. Biella, and M. Schiró. *Many-Body Quantum Zeno Effect and Measurement-Induced Subradiance Transition*. *arXiv:2011.11620.*

[35] Sarang Gopalakrishnan and Michael J. Gullans. Entanglement and purification transitions in non-hermitian quantum mechanics. *Phys. Rev. Lett.*, 126:170503, Apr 2021.

[36] M. Buchhold, Y. Minoguchi, A. Altland, and S. Diehl. *Effective Theory for the Measurement-Induced Phase Transition of Dirac Fermions*. *arXiv:2102.08381.*

[37] Raimel Medina, Romain Vasseur, and Maksym Serbyn. Entanglement transitions from restricted boltzmann machines. 2021.

[38] Tsung-Cheng Lu and Tarun Grover. Entanglement transitions via space-time rotation of quantum circuits. 2021.

[39] N. Lang, and H. P. Büchler. *Entanglement Transition in the Projective Transverse Field Ising Model*. *arXiv: 2006.09748 (2020)*.

[40] O. Lunt, M. Szyniszewski, and A. Pal. *Dimensional hybridity in measurement-induced criticality*. *arXiv:2012.03857*.

[41] Y. Li, X. Chen, A. W. W. Ludwig, and M. P. A. Fisher. *Conformal invariance and quantum non-locality in hybrid quantum circuits*. *arXiv: 2003.12721 (2020)*.

[42] Ali Lavasani, Yahya Alavirad, and Maissam Barkeshli. Topological order and criticality in (2+1)d monitored random quantum circuits. 2021.

[43] Shengqi Sang and Timothy H. Hsieh. Measurement-protected quantum phases. *Phys. Rev. Research*, 3:023200, Jun 2021.

[44] Ali Lavasani, Yahya Alavirad, and Maissam Barkeshli. Measurement-induced topological entanglement transitions in symmetric random quantum circuits. *Nature Physics*, 17(3):342–347, Jan 2021.

[45] Maxwell Block, Yimu Bao, Soonwon Choi, Ehud Altman, and Norman Yao. The measurement-induced transition in long-range interacting quantum circuits. 2021.

[46] Stefanie Czischek, Giacomo Torlai, Sayonee Ray, Rajibul Islam, and Roger G. Melko. Simulating a measurement-induced phase transition for trapped ion circuits. 2021.

[47] L. Zhang, J. A. Reyes, S. Kourtis, C. Chamon, E. R. Mucciolo, and A. E. Ruckenstein. *Non-universal Entanglement Level Statistics in Projection-driven Quantum Circuits*. *Phys. Rev. B* ***101***, *235104 (2020)*.

[48] X. Chen, Y. Li, M. P. A. Fisher, and A. Lucas. *Emergent conformal symmetry in non-unitary random dynamics of free fermions*. *arXiv: 2004.09577 (2020)*.

[49] Piotr Sierant, Giuliano Chiriacò, Federica M. Surace, Shraddha Sharma, Xhek Turkeshi, Marcello Dalmonte, Rosario Fazio, and Guido Pagano. Dissipative floquet dynamics: from steady state to measurement induced criticality in trapped-ion chains. 2021.

[50] Jason Iaconis and Xiao Chen. Multifractality in non-unitary random dynamics. 2021.

[51] Aidan Zabalo, Michael J. Gullans, Justin H. Wilson, Romain Vasseur, Andreas W. W. Ludwig, Sarang Gopalakrishnan, David A. Huse, and J. H. Pixley. Operator scaling dimensions and multifractality at measurement-induced transitions. 2021.

[52] Crystal Noel, Pradeep Niroula, Daiwei Zhu, Andrew Risinger, Laird Egan, Debopriyo Biswas, Marko Cetina, Alexey V. Gorshkov, Michael J. Gullans, David A. Huse, and Christopher Monroe. Observation of measurement-induced quantum phases in a trapped-ion quantum computer. 2021.

[53] Matteo Ippoliti, Tibor Rakovszky, and Vedika Khemani. Fractal, logarithmic and volume-law entangled non-thermal steady states via spacetime duality. 2021.

[54] Lukasz Fidkowski, Jeongwan Haah, and Matthew B. Hastings. How dynamical quantum memories forget. *Quantum*, 5:382, Jan 2021.

[55] Utkarsh Agrawal, Aidan Zabalo, Kun Chen, Justin H. Wilson, Andrew C. Potter, J. H. Pixley, Sarang Gopalakrishnan, and Romain Vasseur. Entanglement and charge-sharpening transitions in u(1) symmetric monitored quantum circuits. 2021.

[56] T. Boorman, M. Szyniszewski, H. Schomerus, and A. Romito. Diagnosing entanglement dynamics in noisy and disordered spin chains via the measurement-induced steady-state entanglement transition. 2021.

[57] Thomas Botzung, Sebastian Diehl, and Markus Müller. Engineered dissipation induced entanglement transition in quantum spin chains: from logarithmic growth to area law. 2021.

[58] S. Choi, Y. Bao, X.-L. Qi, and E. Altman. *Quantum Error Correction in Scrambling Dynamics and Measurement-Induced Phase Transition*. *Phys. Rev. Lett.* ***125****, 030505 (2020).*

[59] Y. Bao, S. Choi, and E. Altman. *Theory of the phase transition in random unitary circuits with measurements*. *Phys. Rev. B* ***101****, 104301 (2020).*

[60] Y. Li, and M. P. A. Fisher. *Statistical Mechanics of Quantum Error-Correcting Codes*. *arXiv:2007.03822.*

[61] R. Fan, S. Vijay, A. Vishwanath, and Y. -Z. You. *Self-Organized Error Correction in Random Unitary Circuits with Measurement*. *arXiv: 2002.12385 (2020).*

[62] L. Wang. *Discovering phase transitions with unsupervised learning*. *Phys. Rev. B* ***94****, 195105 (2016).*

[63] Sebastian J. Wetzel. *Unsupervised learning of phase transitions: From principal component analysis to variational autoencoders*, volume 96. American Physical Society, Aug 2017.

[64] Wenjian Hu, Rajiv R. P. Singh, and Richard T. Scalettar. *Discovering phases, phase transitions, and crossovers through unsupervised machine learning: A critical examination*, volume 95. American Physical Society, Jun 2017.

[65] K. Ch'ng, N. Vazquez, and E. Khatami. *Unsupervised machine learning account of magnetic transitions in the Hubbard model*. *Phys. Rev. E* ***97****, 013306 (2018).*

[66] Natanael C. Costa, Wenjian Hu, Z. J. Bai, Richard T. Scalettar, and Rajiv R. P. Singh. *Principal component analysis for fermionic critical points*, volume 96. American Physical Society, Nov 2017.

[67] Joaquin F. Rodriguez-Nieva and Mathias S. Scheurer. *Identifying topological order through unsupervised machine learning*, volume 15. May 2019.

[68] M. Cristoforetti, G. Jurman, A. I. Nardelli, C. Furlanello. *Towards meaningful physics from generative models*. *arXiv: 1705.09524 (2017).*

[69] Y. Long, J. Ren, and H. Chen. *Unsupervised manifold clustering of topological phononics*. *Phys. Rev. Lett.* ***124****, 185501 (2020).*

[70] E. A.-C. Elena Lopez, Adrien Scheuer and F. Chinesta. *On the effect of phase transition on the manifold dimensionality: application to the ising model*. *MEMOCS* ***6****, 251 (2018).*

[71] Ce Wang and Hui Zhai. *Machine learning of frustrated classical spin models. I. Principal component analysis*, volume 96. American Physical Society, Oct 2017.

[72] Ehsan Khatami, Elmer Guardado-Sanchez, Benjamin M. Spar, Juan Felipe Carrasquilla, Waseem S. Bakr, and Richard T. Scalettar. *Visualizing Correlations in the 2D Fermi-Hubbard Model with AI*. 2020.

[73] Matthew J. S. Beach, Anna Golubeva, and Roger G. Melko. *Machine learning vortices at the Kosterlitz-Thouless transition*, volume 97. American Physical Society, Jan 2018.

[74] Alexander Lidiak and Zhexuan Gong. *Unsupervised machine learning of quantum phase transitions using diffusion maps*. mar 2020.

[75] Quoc Hoan Tran, Mark Chen, and Yoshihiko Hasegawa. *Topological Persistence Machine of Phase Transitions*. apr 2020.

[76] D. R. de Assis Elias, E. Granato, M. de Koning. *Unsupervised learning the phase diagram of frustrated Ising models*. *arXiv: 2012.11529 (2020).*

[77] G. Torlai, C. J. Wood, A. Acharya, G. Carleo, J. Carrasquilla, and L. Aolita. *Quantum process tomography with unsupervised learning and tensor networks*. *arXiv: 2006.02424 (2020).*

[78] S. Martiniani, P. M. Chaikin, and D. Levine. *Quantifying Hidden Order out of Equilibrium*. *Phys. Rev. X* ***9****, 011031 (2019).*

[79] A. A. Bagrov, I. A. Iakovlev, A. A. Iliasov, M. I. Katsnelson, and V. V. Mazurenko. *Multiscale structural complexity of natural patterns*. *PNAS* ***117****, 30241 (2020).*

[80] P. Mehta, M. Bukov, C.-H. Wang, A. G. Day, C. Richardson, C. K. Fisher, and D. J. Schwab. *A high-bias, low-variance introduction to machine learning for physicists*. *Phys. Rep.* ***810****, 1 (2019).*

[81] Giuseppe Carleo, Ignacio Cirac, Kyle Cranmer, Laurent Daudet, Maria Schuld, Naftali Tishby, Leslie Vogt-Maranto, and Lenka Zdeborová. *Machine learning and the physical sciences*, volume 91. American Physical Society, Dec 2019.

[82] Juan Carrasquilla. *Machine Learning for Quantum Matter*. mar 2020.

[83] M. M. Wolf. *Violation of the Entropic Area Law for Fermions*. *Phys. Rev. Lett.* ***96****, 010404 (2006).*

[84] D. Gioev, and I. Klich. *Entanglement Entropy of Fermions in Any Dimension and the Widom Conjecture*. *Phys. Rev. Lett.* ***96****, 100503 (2006).*

[85] O. I. Motrunich and A. Vishwanath. *Comparative study of Higgs transition in one-component and two-component lattice superconductor models*. *arXiv:0805.1494 (2008).*

[86] B. Swingle. *Entanglement Entropy and the Fermi Surface*. *Phys. Rev. Lett.* ***105****, 050502 (2010).*

[87] Y. Zhang, T. Grover, and A. Vishwanath. *Entanglement Entropy of Critical Spin Liquids*. *Phys. Rev. Lett.* ***107****, 067202 (2011).*

[88] B. Swingle, and J. McGreevy. *Area law for gapless states from local entanglement thermodynamics*. *Phys. Rev. B* ***93****, 205120 (2016).*

[89] A. C. Potter. *Boundary-law scaling of entanglement entropy in diffusive metals*. *arXiv:1408.1094 (2014).*

[90] M. Pouranvari, Y. Zhang, and K. Yang. *Entanglement Area Law in Disordered Free Fermion Anderson Model in One, Two, and Three Dimensions*. *Adv. Condens. Matter Phys.* ***2015****, 397630 (2015).*

[91] A. Nahum, and B. Skinner. *Entanglement and dynamics of diffusion-annihilation processes with Majorana defects*. *Phys. Rev. Research* ***2****, 023288 (2020).*

[92] Y. Bao, S. Choi, and E. Altman. *Symmetry enriched phases of quantum circuits*. *arXiv:2102.09164.*

[93] S. Gopalakrishnan, M. J. Gullans. *Entanglement and purification transitions in non-Hermitian quantum mechanics*. *arXiv:2012.01435.*

[94] N. Gisin, and I. C. Percival. *The quantum-state diffusion model applied to open systems*. *J. Phys. A: Math. Gen.* ***25****, 5677 (1992).*

[95] T. A. Brun. *A simple model of quantum trajectories*. *Am. J. Phys.* ***70****, 719 (2002).*

[96] H. M. Wiseman, and G. J. Milburn. *Quantum theory of field-quadrature measurements*. *Phys. Rev. A* ***47****, 642 (1993).*

[97] D. Yang, C. Laflamme, D. V. Vasilyev, M. A. Baranov, and P. Zoller. *Theory of a Quantum Scanning Microscope for Cold Atoms*. *Phys. Rev. Lett.* ***120****, 133601 (2018).*

[98] D. Gottesman. *The Heisenberg Representation of Quantum Computers*. *arXiv: 9807006 (1998).*

[99] V. Khemani, A. Vishwanath, D. A. Huse. *Operator spreading and the emergence of dissipative hydrodynamics under unitary evolution with conservation laws*. *Phys. Rev. X* ***8****, 031057 (2018).*

[100] A. Nahum, S. Vijay, and J. Haah. *Operator Spreading in Random Unitary Circuits*. *Phys. Rev. X* ***8****, 021014 (2018).*

[101] C. W. von Keyserlingk, T. Rakovszky, F. Pollmann, and S. L. Sondhi. *Operator Hydrodynamics, OTOCs, and Entanglement Growth in Systems without Conservation Laws*. *Phys. Rev. X* ***8****, 021013 (2018).*

[102] Michael A. Nielsen and Isaac L. Chuang. *Quantum Computation and Quantum Information*. Cambridge University Press, 2009.

[103] S. Aaronson, and D. Gottesman. *Improved simulation of stabilizer circuits*. *Phys. Rev. A* ***70****, 052328 (2004).*

[104] A. Hamma, R. Ionicioiu, and P. Zanardi. *Ground state entanglement and geometric entropy in the Kitaev's model*. *Phys. Lett. A* ***337****, 22 (2005).*

[105] A. Hamma, R. Ionicioiu, and P. Zanardi. *Bipartite entanglement and entropic boundary law in lattice spin systems*. *Phys. Rev. A* ***71****, 022315 (2005).*

[106] M. Ippoliti, M. J. Gullans, S. Gopalakrishnan, D. A. Huse, and V. Khemani. *Entanglement phase transitions in measurement-only dynamics*. *Phys. Rev. X* ***11****, 011030 (2021).*

[107] R. Koenig, and J. A. Smolin. *How to efficiently select an arbitrary Clifford group element*. *J. Math. Phys.* ***55****, 122202 (2014).*

[108] Svante Wold, Kim Esbensen, and Paul Geladi. *Principal component analysis*, volume 2. 1987.

[109] F. Pedregosa, G. Varoquaex, A. Gramfort, V. Michel, B. Thirion, O. Grisel, M. Blondel, P. Prettenhofer, R. Weiss, V. Dubourg, J. Vanderplas, A. Passos, D. Cournapeau, M. Brucher, M. Perrot, and E. Duchesnay. *Scikit-learn: Machine Learning in Python*. *JMLR* ***12****, 2825 (2011).*

[110] A. Sorge. *pyfssa*. *pyfssa 0.7.6. Zenodo (2015).*

[111] E. Levina, and P. J. Bickel. *Maximum likelihood estimation of intrinsic dimension*. *in NIPS* ***17****, 777 (2004), edited by L. K. Saul, Y. Weiss, and L. Bottou, MIT Press (Cambridge, MA).*

[112] S. Goldt, M. Mézard, F. Krzakala, and L. Zdeborová. *Modelling the influence of data structure on learning in neural networks: the hidden manifold model*. *Phys. Rev. X* ***10****, 041044 (2020).*

[113] S. Lee, P. Campadelli, E. Casiraghi, C. Ceruti, and A. Rozza. *Intrinsic dimension estimation: relevant techniques and a benchmark framework*. *Math. Probl. Eng* ***759567****, 1024 (2015).*

[114] E. Facco, M. d'Errico, A. Rodriguez, and A. Laio. *Estimating the intrinsic dimension of datasets by a minimal neighborhood information*. *Sci Rep* ***7****, 12140 (2017).*

[115] T. Mendes-Santos, X. Turkeshi, M. Dalmonte, and A. Rodriguez. *Unsupervised learning universal critical behavior via the intrinsic dimension*. *arXiv:2006.12953 (2020).*

[116] A. Bohrdt, S. Kim, A. Lukin, M. Rispoli, R. Schittko, M. Knap, M. Greiner, and J. Léonard. *Analyzing non-equilibrium quantum states through snapshots with artificial neural networks*. *arXiv: 2012.11586 (2020).*

[117] Pasquale Calabrese and John Cardy. Entanglement entropy and quantum field theory. *Journal of Statistical Mechanics: Theory and Experiment*, 2004(06):P06002, Jun 2004.

[118] L. Amico, R. Fazio, A. Osterloh, and V. Vedral. *Entanglement in many-body systems*. *Rev. Mod. Phys.* ***80****, 517 (2008).*

[119] R. Horodecki, P. Horodecki, M. Horodecki, and K. Horodecki. *Quantum entanglement*. *Rev. Mod. Phys.* ***81****, 865 (2009).*

[120] Nicolas Laflorencie. Quantum entanglement in condensed matter systems. *Physics Reports*, 646:1–59, Aug 2016.

[121] V. Alba, and F. Carollo. *Spreading of correlations in Markovian open quantum systems*. *Phys. Rev. B* ***103****, 020302 (2021).*

[122] M. B. Plenio, and P. L. Knight. *The quantum-jump approach to dissipative dynamics in quantum optics*. *Rev. Mod. Phys.* ***70****, 101 (1998).*

[123] J. M. Hickey, S. Genway, I. Lesanovsky, and J. P. Garrahan. *Time-integrated observables as order parameters for full counting statistics transitions in closed quantum systems*. *Phys. Rev. B* ***87****, 184303 (2013).*

[124] T. E. Lee, and C.-K. Chan. *Heralded Magnetism in Non-Hermitian Atomic Systems*. *Phys. Rev. X* ***4****, 041001 (2014).*

[125] P. Calabrese, J. Cardy and B. Doyon. *Entanglement entropy in extended quantum systems*. *J. Phys. A* ***42****, 500301 (2009).*

[126] D. Bianchini, O. Castro-Alvaredo, B. Doyon, E. Levi, and F. Ravanini. *Entanglement entropy of non-unitary conformal field theory*. *J. Phys. A: Math. Theor.* ***48*** *04FT01 (2014).*

[127] R. Couvreur, J. L. Jacobsen, and H. Saleur. *Entanglement in Nonunitary Quantum Critical Spin Chains*. *Phys. Rev. Lett.* ***119****, 040601 (2017).*

[128] K. Jacobs, and D. A. Steck. *A straightforward introduction to continuous quantum measurement*. *Contemporary Physics* ***47****, 279 (2006).*

[129] H. M. Wiseman, and G. J. Milburn. *Quantum Measurement and Control*. *Cambridge University Press, Cambridge (UK) (2009).*

[130] G. B. Mbeng, A. Russomanno, and G. E. Santoro. *The quantum Ising chain for beginners*. *arXiv:2009.09208.*

Acknowledgments

I would like to conclude this thesis by expressing my gratitude to my mentors and the people close to me in the last four years. I wish to thank Marcello Dalmonte for the guidance over the years, providing me with continuous supervision, support, and, more importantly, freedom. I thank Pasquale Calabrese and Rosario Fazio for the unvaluable insights on the topics I studied in my thesis. I also thank the collaborators over the years: Marco Schiró, Paola Ruggiero, Giuliano Giudici, Tiago Santos-Mendes, Alex Rodriguez, Giuliano Chiriacó, Vincenzo Alba, Alberto Biella, Piotr Sierant. Among them, I'm indebted to Giuliano for introducing me to coding, with now is an active part of my life also outside accademia, and to Paola for teaching me "Il mestiere". I wish to thank all my friends, many of them SISSA students as well. I thank my family Kujtim Turkeshi and Anila Progeri, for support. Lastly, the special thank goes to Silvia: my partner, my friend, my ally in life.